Centre for Computational Geostatistics (CCG)
Monograph Series Vol. 1

Integration of Production Data in Generating Reservoir Models

X.H. Wen

C.V. Deutsch

A.S. Cullick

Z.A. Reza

August 2005

Integration of Production Data in Generating Reservoir Models

Centre for Computational Geostatistics (CCG)
Monograph Series

Volume 1: Integration of Production Data in Generating Reservoir Models

Volume 2: Geostatistical Characterization of the Alberta Oil Sands

Integration of Production Data in Generating Reservoir Models

Xian-Huan Wen
Chevron Energy Technology Company

Clayton V. Deutsch
University of Alberta

A. Stan Cullick
Landmark, Halliburton Digital and Consulting Solutions

Zulfiquar A. Reza
University of Colorado, Boulder

Published by Centre for Computational Geostatistics
3-133 Markin/CNRL Natural Resources Engineering Facility,
University of Alberta
Edmonton, AB, Canada T6G 2W2

http://www.uofaweb.ualberta.ca/ccg/

Cataloging in Publication Data:

Wen, X. H., Deutsch, C.V., Cullick, A.S., and Reza, Z.A. Integration of Production Data in Generating Reservoir Models / Wen, X. H., Deutsch, C.V., Cullick, A.S., and Reza, Z.A. Centre for Computational Geostatistics, publishers.

ISBN 0-9738460-0-3

Printed by Riley's Reproductions & Printing Ltd., Edmonton, AB, www.rileys.com

Preface

This Monograph is essentially a compilation of published technical papers that grew from a research collaboration by the authors initiated between Stanford University and Mobil Technology Corporation in early 1996.

In early 1996, the methods described here were just so many ’brainstormed’ items on a whiteboard at Stanford, which attempted to solve the long-standing problem of generating reservoir models that by construction honor production data. By mid-1998, the ideas had been brought to completed computer codes and successful tests on example data. During the same two-year period, many other researchers were advancing technologies to solve this difficult problem, and the literature has become very rich in this area since 1996. This monograph, however, by capturing the work of the authors, provides an important foundation for those who want to familiarize themselves with this field, whether they want to practice the art or develop the science.

Acknowledgements

The authors want to thank those who helped make this work possible. Mobil Technology Company funded the postdoctoral fellowship of X. H. Wen at Stanford, and Robert Heinemann provided the leadership to enable this industry-academic collaboration. Mobil granted permission to publish the research results as papers and professional society presentations. The Stanford Center for Reservoir Forecasting supported the research and provided the facilities, and Andre Journel was always available to provide insight, discussion, criticism, support, and encouragement. Chevron Technology Company, with the leadership of T. T. Tran and R. A. Behrens, has provided support and encouragement for the publication of this Monograph.

Finally, we would like to thank Prof. Jaime J. Gomez-Hernandez, Prof. Jose E. Capilla and Prof. Andres Sahuquillo at the Technical University of Valencia, Spain for their generous support during the development and extension of the SSC method, which was originally developed by them in the area of subsurface hydrology for conditioning pressure data.

Contents

Chapter 1

Introduction

Optimal reservoir management requires reliable reservoir performance forecasts with as little uncertainty as possible. Incomplete data and inability to model the physics of fluid flow at a suitably small scale lead to uncertainty. Subsurface reservoir models that "by construction" honor the historical production data should yield significantly more accurate predictions of reservoir performance with reduced uncertainty than those that do not. This monograph aims to present a few recently developed methods to link temporal production data and static spatial constraints on the distribution of permeability in reservoir models. This compilation does not bring forth the entire technology being used in the science or craft, as one might argue, of data integration in reservoir characterization. The methods discussed here establish the "missing link" in reservoir characterization for three important types of dynamic data: (1) single-phase well test data, (2) single-phase pressure and rate data, and (3) multiphase (incompressible fluid), multiple-well pressure and fractional flow rate data from wells. These techniques yield relatively coarse spatial representations of permeability that recognize the resolution of the data. The coarse scale representations are then used to constrain fine scale reservoir models when integrated with seismic, geologic, and petrophysical data.

1.1 Motivation for the Monograph

The motivation for this monograph was the recognition that although rapid development is being made on dynamic data integration in reservoir characterization, there exists no concise text on this active area of research. This monograph should help the researchers and professionals in comprehending the problem better with simple illustrated examples and exercises. The methods discoursed here will prepare them to address more complicated reservoir scenarios. Reliable predictions of future reservoir performance require reservoir models that honor all available data including conceptual geological data, seismic data, core data, well log data, DST/RFT data, well test data, and historical production data. Each source of data carries information at different scales and with varying levels of precision, related to the true distribution of petrophysical and fluid properties in the reservoir. The challenge of subsurface prediction is to integrate all data sources. Integrating all the available data in numerical geological models will make it possible for reservoir engineers to much more quickly perform flow simulation studies. Reducing the calendar and engineering time for flow studies will add significant value by providing more time to optimize reservoir management plans.

The honoring of historical production data has been a missing component of this process. Early approaches to numerical history matching by a single-stage mathematical inversion have been hampered by the following difficulties: (1) excessive CPU execution time for even relatively small reservoir models, (2) limiting, simplifying assumptions, e.g., linear relationship between pressure and reservoir properties, Gaussian distribution, small variability, and/or uniform flow, used in order to speed up the computations of the inversion process; these assumptions are often inconsistent with real complexity, (3) often only one type of data can be considered at a time, at the expense of information coming from other data sources such as seismic and geology, and (4) there was a significant difficulty with multiphase flow data, leading to unconstrained, nonunique, and computationally intensive methods. So that even today, the most common history matching technique practiced is manual iteration.

More recent numerical methods have combined the nonlinear inverse calculation with stochastic modeling or streamlines for multiphase in various ways, and although much progress has been reported, almost all have suffered from many of the limitations of the early techniques. In essence, there has been a continuing attempt to invert the production data directly to a detailed three-dimensional reservoir model. One must recognize that the production data measurement at each well is essentially a single-point in space which by itself can only yield effective properties over a large volume. Attempts to build a detailed subsurface model from that data alone do not have a high chance of success.

Figure 1.1 shows a conceptual illustration of the approach. The production data, as well as various other data, each yield a prior model. Each prior model is the best interpretation of the data and preserves the resolution and uncertainty inherent in the data. Ultimately, the prior models are integrated into unified predictive reservoir models using optimization techniques. Production data at wells are inverted to a coarse scale maps of permeability. These maps are then used as constraints along with those from other available data in an optimization procedure. It is this step of building a prior model from production data that is the focus of this monograph.

1.2 Problem Description

Reservoir development planning using detailed 3D reservoir models requires models of structure, stratigraphy, and properties. Interpretive, deterministic and geostatistical techniques for constructing models of lithofacies and properties are used that constrain the models to static data from core, logs, seismic, and geologic interpretation. In general, however, honoring all data including the dynamic pressure or historical production data is quite difficult. In practice, trial-and-error history matching is still the most common approach at the final stage of modeling. The problem of fully integrating production and pressure data in the construction of reservoir models lends itself to a variety of approaches. Property models within the volume of influence of a well are generated through a one-step mathematical inversion of the pressure response. The problems with these techniques are the intense computations needed to generate a solution that is not unique and may be inconsistent

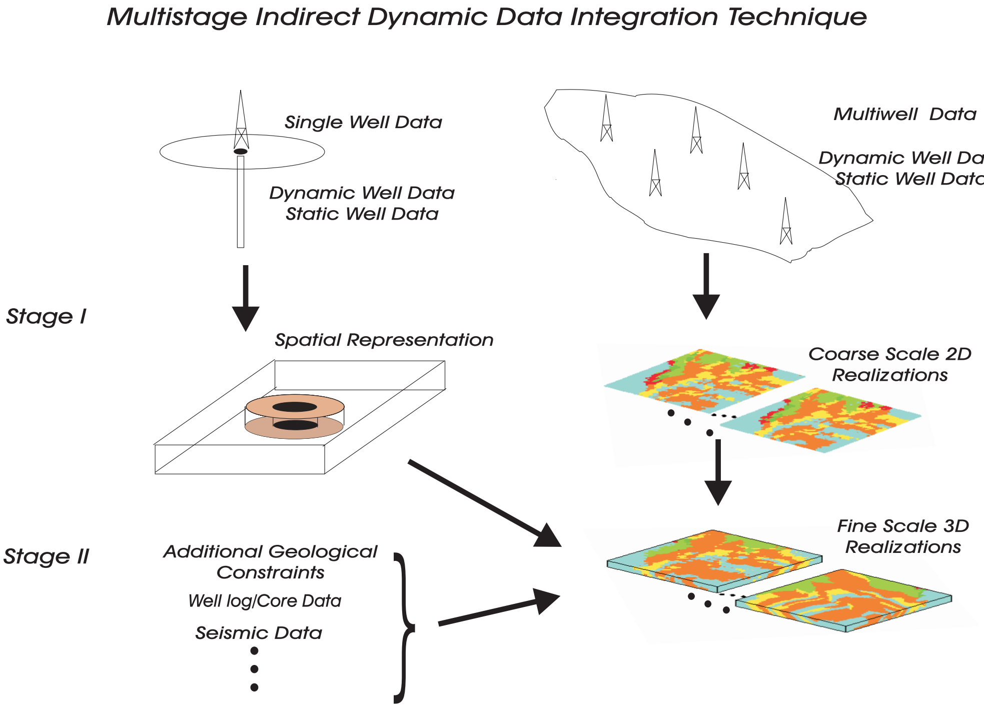

Figure 1.1: A conceptual illustration of the multistage indirect inversion technique.

with some of the static data. In other approaches, the property models are generated in several steps with a first-step coding of the well-derived data into a spatial property representation. A detailed classification of the techniques available for dynamic data integration is discussed in Chapter 2.

1.2.1 Limitations of Single-stage Methods

Mathematical inversion techniques have been applied primarily to transient well pressure data. The approach formulates an inverse problem with the intent to explicitly honor raw pressure data, and by doing so, completely generate a property model that reproduces the data explicitly. In general, some assumptions about flow equations (e.g., linear), covariance, or cross-covariance of reservoir and flow parameters are needed. The mathematical inversion method is attractive in the sense that production data are explicitly honored in the reservoir model.

There are, however, a number of limitations with these techniques. Usually they are CPU intensive, and are thus limited to relatively small model sizes. Moreover, almost all these approaches call for simplifying assumptions in order to speed up the computations. Apart from such simplification, it has been found quite difficult to handle production data for multiphase flow conditions, multiple data types and other data such as geophysical data and geological knowledge, without having inconsistent results.

1.2.2 Improvement with Multistage Approaches

The multistage approaches rely on inversion of the production data into a spatial representation of reservoir attributes that impact flow, e.g. lithofacies, permeability, or barriers. By "multistage" we mean than there is first step of inverting the production data to a "coarse-scale" spatial representation. A second step follows that integrates the coarse model with other data (e.g., seismic) through optimization or cosimulation.

Multistage approaches have great flexibility to account for different data types and to integrate reservoir characteristics that contributed most to the raw production data. These approaches utilize single-stage mathematical inversion techniques to provide coarse-scale spatial representations that are grounded in flow processes and yet honor preservation of geological and other data at appropriate scale. However, the resulting reservoir model may not reproduce the production data exactly after the interpretation stage.

1.2.3 Improving the Estimation of Global Reservoir Parameters

Production data can be used to improve the estimation of global reservoir parameters, such as the mean and covariance of reservoir properties. Once estimated, such statistical parameters are used as inputs in geostatistical techniques to construct reservoir models. The contribution of production data lies in the improvement in the estimation of statistical parameters describing the reservoir heterogeneity. In a few cases, such as when the reservoir parameters are Gaussian, and the relationship between the reservoir parameter and pressure data are linear, the constructed geostatistical reservoir model may also directly honor the pressure data.

In addition to facies, porosity and permeability distributions, production data have an imprint on the communication between the wells, connectivity between and within reservoir strata, presence of structures like sealing faults, connectivity across the faults, etc. With additional evidence to corroborate such presence or quantification as applicable, each of these features can be captured in the reservoir models through production data integration. A plausible approach may be construction of some probabilistic maps and incorporation of such maps into detailed reservoir models in the optimization or annealing stage, which will be discussed later.

1.3 Inversion Methodology

The inversion methodology adapted here can be considered as a multistage indirect inversion technique. It is believed that each type of dynamic well data contains information about some subset of the spatial property distribution, for example, facies proportion or permeability anisotropy. Thus, by taking a process-specific approach, one should be able to interpret dynamic data as some spatial representation.

The approach is more attractive because of its ability to account for different types of production data and the coding of these data into spatial data through some interpretive basis on different flow processes. Also, this method integrates only the "actual" information behind the raw production data. Hence, this provides greater insight into reservoir systems and can better capture structures. Techniques for computing kh from pressure response and flow pathways from tracer data, developed from inversion methods, are used to assist in the geological coding.

The central idea behind this monograph is to assemble and test a set of analytical and numerical tools to extract the spatial "essence" from production data and then to integrate these data in detailed reservoir models. A multistage geological coding technique is developed as a viable and more accurate reservoir modeling tool. There were significant technical issues in making this a reality. Inversion methods applicable to limited regions (e.g., the influence area of a well-test) had to be extended to larger interwell region. Interpretive tools were developed for a variety of production data to translate the production data into spatial representations of reservoir heterogeneities. Tools were devised to integrate production data consistently with other information such as seismic data. Consistency and validity of production data constraints were checked by comparing with data from different sources.

This indirect multistage approach could significantly enhance reservoir management and development planning by building geologic models that are more predictive, and significantly reduce the resources required to achieve history match. More specifically, enhanced predictive ability of flow simulation is possible by providing a quantitative geological description consistent with historical flow data. Also, reservoir management is improved by allowing a greater number of development options to be considered. More importantly, production data is integrated in a spatial context that is consistent with all geological information.

1.4 Types of Production Data and their Spatial Representation

In general, from a provenance perspective, production data may be summarized into three main groups: single-well test data, multiple-well test data, and historical production data. From a process perspective, each data type has the potential to inform us about some subset of spatial characteristics. In the following sections, the spatial representations from each data type and some issues concerning our ability to extract these spatial data are listed.

1.4.1 Single-well Test Data

Mathematical inversion methods for single well test pressure data (see Table 1.1) and interpretive tools are largely in place [64, 94, 150, 162]. This is perhaps the subject of most well test analyses research. Well test interpretation is a standard reservoir engineering practice. Some of the typical single-well test data are RFT data, drawdown/buildup test data, variable rate test data, production logs and permanent pressure gauges. For instance, interpretation of RFT data is quite useful particularly for decisions like production strategy, change in well configurations, well workovers or perforation jobs.

1.4.2 Multiple-well Test Data

Compared to single-well test data, multiple-well test data (see Table 1.2) are more extensive in terms of areal coverage and provide specific connectivity information between wells. Data sufficiency, i.e., whether sufficient data are available to establish significant contributions, is an important issue. Suitable method to quantify connectivity between two locations is

Data Available	**Spatial Representation**
Pressure as function of depth (e.g., RFT)	- Communication between strata - Communication across faults - Location of fluid contacts
Buildup/drawdown test $p(t)$	- Distance to boundaries - Effective kh - Flow regime (e.g., fractures) - Aquifer influx/fluid extent
Multirate test data	- More details - Layer productivity
Production logging (q(depth))	- Permeability of different layers/strata (ratio or "relative" k between layers)
Permanent pressure gauges ($p(t)$, t from 0 to present)	- kh for coarse grid or information between wells - "Map" interwell region - Boundaries and interwell communication

Table 1.1: Typical single-well test data with their spatial representation

Data Available	**Spatial Representation**
Interference tests $p(\mathbf{u}, t)$, $q(\mathbf{u}, t)$ and $p(\mathbf{u}', t)$, $q(\mathbf{u}', t)$	- Presence of sealing faults - Fault transmissibility - Qualitative measure of connectivity - Effective k - Flow/pressure pathways
Tracer data	- More unique model - Tell how a well is isolated or connected with other wells

Table 1.2: Typical multiple-well test data with their spatial representation

Data Available	**Spatial Representation**
P, q_o, q_g as functions of dimensionless time at each well	- kh at each well (relatively larger areas) - Drainage volume for each well - Local facies information indirectly through k_{ro}/k_{rg} ratios - $\overline{k}_{coarse\ scale}$ effective permeability - Interwell communication from fractional flow/pressure data

Table 1.3: Typical historical production data with their spatial representation

imperative. The approach of geo-objects, collections of locations/blocks connected to each other, is used for this purpose.

1.4.3 Historical Production Data

According to production mechanisms, historical production data (see Table 1.3) may be from different sources. The classification can be with respect to reservoir depletion with or without water drive, with gas-cap drive, water injection or gas injection. Each of these has unique implementation and interpretive issues.

Depletion without water drive

Expansion drive and gravity segregation drive are the main sources of reservoir potential in these situations. Estimation procedure of drainage volume for each well should be properly devised. Relative permeability ratios (gas to oil), $\frac{k_{ro}}{k_{rg}}$, may also explain something about the lithofacies proportions within drainage area, since different facies usually have different $\frac{k_{ro}}{k_{rg}}$ ratios.

Depletion with water drive

Before breakthrough of water, no new information on the spatial distribution of heterogeneities than that from single-well test or multiple-well test data is available. The data reveal almost same information as in the case of depletion without water drive. After water breakthrough fractional recovery data (q_w, q_o) are available. Original water contact data (e.g. surface-point connectivity), $\overline{k}_{coarse\ scale}$ effective permeability distribution may be obtained from the available data. Also, $\frac{\overline{k_{ro}}}{k_{rw}}$ may indicate facies proportion in the "contacted region".

Depletion with gas-cap drive

These data are similar to those available from water-drive depletion, except between production wells and original gas-cap, instead of aquifer. Interwell connectivity data and the stratigraphic surface correlation can be established. Fractional recovery data ($\frac{k_{ro}}{k_{rg}}$) may indicate facies proportion. Distribution of $\overline{k}_{coarse\ scale}$ may be derived from well and drive data.

Injection (of water or gas)

More definitive determination of $\overline{k}_e$ between wells, particularly after breakthrough, is possible. Flow capacity (kh) around injection wells, connected volume between injector/producer pairs can be estimated. Breakthrough times may explain anisotropic variogram, interwell facies connectivity, and permeability distribution. Measurement of heterogeneities, calibration and calculation of connected volume from the 3D reservoir model are crucial issues.

1.5 Data Developed in this Monograph

The three different types of production data are considered in this monograph:

- Single-well test data: In the radial flow regime of a well test, one calculates permeability values representing weighted averages of permeabilities within dimensionless time-dependent annular reservoir volumes around the well. The approach discussed here uses two parameters to represent the volume-of-averaging and the type of averaging. Both parameters are derived by a simple calibration process. The method is tested with a number of 2D and 3D examples of varying size, grid discretization, anisotropy, permeability heterogeneity, and lithofacies architecture. The limitations and range of applicability have been documented.

- Multiple-well single-phase rate and pressure data provide more information on the spatial variations of reservoir properties than single-well test data, especially on the spatial connectivity between wells. Deriving the spatial constraints due to such data is more complex in the sense that inverse solutions of flow equations are needed. This inverse problem is tackled with the sequential self calibration (SSC) method: a hybrid technique using an iterative approach coupled with the analytical calculation of sensitivity coefficients. Results from a number of synthetic examples show flexibility, efficiency and robustness of the SSC method.

- Integration of multiphase multiwell data presents unique challenges because it additionally requires additional knowledge of the sensitivity coefficients of fractional flow rate to perturbations to permeability. A streamline-based method is applied for efficient calculation of such sensitivity coefficients. This method adapts the concept of decoupling multiple-dimensional full flow problem into multiple 1D problems along streamlines. The sensitivity of fractional flow rate with respect to the reservoir property change is then directly related to the sensitivity of time-of-flight of each individual streamline and the sensitivity of pressure at cells along the streamline. The sensitivity of time-of-flight of each streamline can be obtained analytically assuming constant streamline geometry. While the sensitivity of pressure can be obtained as part of single phase flow simulation, which is computationally fast.

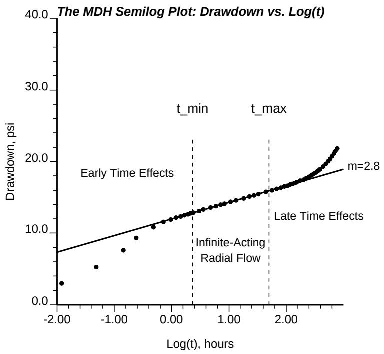

Figure 1.2: Typical semilog plot of pressure drawdown from a well test.

1.6 Data-specific Approaches in this Monograph

1.6.1 Technique for Single-well Single-phase Well Test Data

A single-well pressure transient well test consists of imposing some flow rate and measuring the consequent change in pressure. The change of pressure evolves over an initial near wellbore effects dominant period, a middle radial flow period, and ultimately boundary dominant or late-time period. A schematic illustration of a pressure drawdown is shown in Figure 1.2. Chapter 3 will present the technique in greater detail.

Infinite acting central flow period is considered to bear most of the information regarding the actual reservoir properties. Early time effects relate to the condition of the wellbore and not the vast interwell region which is the main concern here. Moreover, there exist well understood interpretive tools for late-time boundary effects such as faults and stratigraphic barriers. The time limits, $t_{\min}$ and $t_{\max}$, of infinite acting radial flow can be established by examining the pressure transient data $p(t)$ (see Figure 1.2). The derivative of pressure with respect to time can be calculated within these time limits, $(t_{\min}, t_{\max})$. A time-dependent permeability, $k_e(t)$, is linearly related to this derivative given estimates of fluid and reservoir parameters such as viscosity, formation thickness, porosity, formation volume factor, and single phase flow rate. The problem is to identify the volume informed by the time dependent effective permeabilities. Using perturbation analysis, Oliver [138] investigated the annular reservoir region that influences pressure derivative, and thus effective permeability at a given time. Under the assumption of small variation of permeability, an analytical weighting function was derived to specify the relative contribution of the permeability of various regions to the estimation of effective permeability, $k_e(t)$. There is a smooth transition between the minimum and maximum times. This normalized weighting function is remarkably robust with respect to departures from the assumptions used to derive it [194]. A scaling parameter, A, is introduced to correct for departures. This parameter is calibrated by flow simulations. The time-dependent permeability $k_e(t)$ is modeled by a weighted power average. The weighting function is the corrected version of Oliver's weighting function and the averaging power is based on calibration (see Figure 1.3). As a first approximation, the averaging power most often leads to geometric averaging. This basic model was tested using synthetic and real reservoir examples to establish its domain of applicability and limitations.

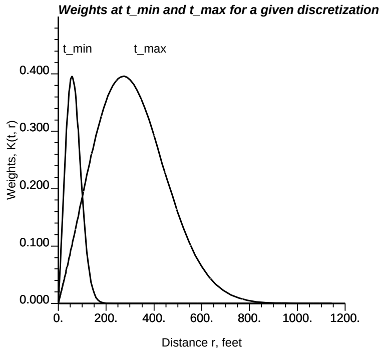

Figure 1.3: Normalized weighting function for the start and end of the central infinite-acting radial flow region.

1.6.2 Technique for Multiple-well Single-phase Data

The goal is to quantify the relatively coarse spatial information on petrophysical properties contained in multiple-well single-phase production data. In case of a single well, inversion to the spatial constraints was established through an analytical derivation and calibration procedure. However, the situation is significantly more complex considering the irregular distribution of multiple wells producing at different times and flow rates. A more elaborate inversion scheme must be considered. The Sequential Self-Calibration (SSC) method is used as a starting point to derive an inversion scheme for multiple-well single-phase data. The SSC method is an iterative geostatistics-based method coupled with an optimization procedure developed for steady state single phase flow [194]. Chapter 4 presents the technique in detail.

The SSC method is adapted to unsteady single-phase and also to multiphase flow (see Figure 1.4). For single-phase case, multiple initial realizations of permeability fields are created using the most suitable geostatistical techniques to honor all available static data. Imposing time-dependent flow rates, numerical flow simulation is performed to establish the "calculated" pressures from the model at all wells at all time. The sum of squared differences between these pressures measures the mismatch of the current permeability realization and one that would honor the production data. Modifications to the permeability field are determined that allow the production data to be honored more closely. A number of assumptions are required to calculate these "perturbations" to the permeability field. However, recurring the entire procedure allows convergence in most cases. The optimal perturbations are determined for a limited number of "master points" rather than every grid cell in the field. This makes the method more computationally efficient and is consistent with the relatively large scale nature of pressure transient data. An optimization problem is solved to search for the optimal perturbation values at the master point locations These optimal perturbation values are propagated through the entire field by kriging to obtain a smooth perturbation field. A variogram appropriate to the geological setting of the reservoir is used for the kriging. This smooth perturbation field is then added to the previous permeability field to obtain an updated permeability field. Flow equations are again solved using the updated permeability field with the same boundary and production rate conditions and the entire procedure is repeated until convergence. This procedure can

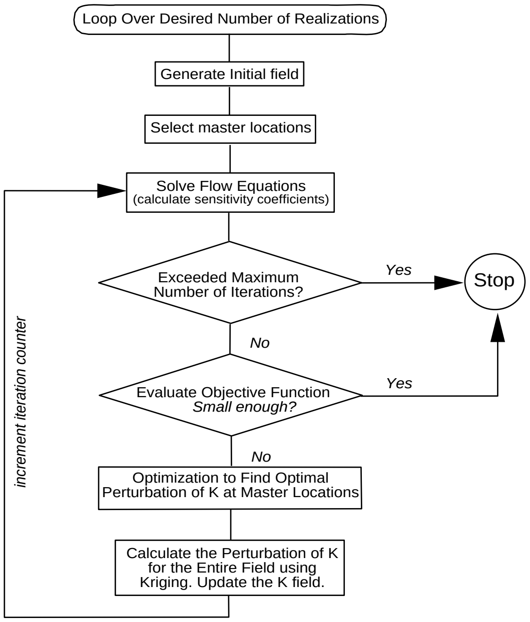

Figure 1.4: Flowchart of the Sequential Self-Calibration method.

be repeated as necessary to obtain multiple realizations.

Deterministic-type permeability distributions with large-scale heterogeneities and stochastic-type permeability distributions are investigated. Large features are "captured" by the multiple well pressure/rate data and appear in the final SSC realizations. The presence of small stochastic features may be detected but their precise location is not necessarily established. The convergence properties of the method were also explored by using an increasing number of wells and a longer historical production time. As expected, more wells and longer duration measurements lead to more constrained results. The CPU efficiency of the method was also explored and documented. In general, the method is significantly more efficient than direct single-step inversion methods.

The approach was also tested in prediction mode. One set of reservoir models was constructed without production data and another set was constructed with production data. Integrating the production data led to significantly improved predictions of future performance. The multiple-well single-phase data technique is now well established.

A spin-off of the SSC technique was the capability to obtain facies proportions. The method proceeds as follows. Facies proportions are calibrated against permeability honoring core, logs, seismic data. Master point method is used to compute coarse scale permeability maps for multiple initial models. Coarse scale models are merged to local distributions of facies proportions.

1.6.3 Technique for Multiple-well Multiphase Data

Integrating multiphase data such as fractional flow rate data (e.g., watercut or GOR) is extremely challenging. This information carries valuable information on the spatial distribution of reservoir properties. The SSC method is extended to multiphase data with additional calculation of sensitivity coefficients of the rate of change in the fractional flow at a well at a given time with respect to the perturbation of permeability. The calculation of these sensitivity coefficients is essential in order to update permeability to honor production data. The brute force method to get these sensitivity coefficients based on full flow simulation is prohibitive due to CPU cost. A streamline-based simulator is used by perturbing the permeability, recalculating the streamlines and fractional flow curves, and finally estimating the sensitivity coefficients. This approach requires a single-phase flow simulation for each permeability. Practical integration of multiphase production data requires an even faster approach.

To achieve a significant improvement, the streamline locations are assumed not to be changing for a permeability perturbation. Of course, the velocity along each streamline changes hence the fractional flow response at each well changes. Moreover, the streamlines are changed for each iteration of the SSC method. An analytical approach to calculate the sensitivity coefficients was developed with this key assumption. Only one single-phase flow simulation is required to calculate all sensitivity coefficients. Responses indicate that the "fixed location" assumption is not limiting. In fact, the analytical approach relaxes two assumptions of earlier approaches: (1) the permeability perturbations are now considered jointly rather than one at a time, and (2) there is no need to choose a specific permeability before calculating the sensitivity coefficients. However, the implementation to date is limited to two-phase flow. Technique has been implemented to compute sensitivity of fractional flow rate at wells and saturations at given locations with respect to the change of permeabilities at selected master locations. A variety of deterministic and stochastic permeability fields with different configurations of production or injection wells have been considered. These techniques are discussed in detail in Chapter 5.

1.7 Characterization with Different Types of Spatial Data

Characterization of detailed 3D reservoir models entails working in an almost infinite dimensional space with a multitude of parameters to be estimated. There are various reservoir model properties for which inversion techniques, mentioned earlier, are applied. In most cases, these reservoir parameters include communication between strata and across faults through transmissibility, distance to boundaries, effective flow capacities in the vicinity of wells, productivity of wells, measures of interwell communication (absolute/relative kh), coarse grid representation of kh, or ϕ, facies connectivity between wells, drainage volumes around wells, facies proportions around/between wells, connectivity between wells and connected surfaces,local measures of heterogeneity (e.g., variogram, covariance, mean and variance of permeability and porosity), etc.

The problem of constructing reservoir models that honor the above spatial data is an inverse problem. Essentially, solution of inverse problem means making inference of a physical system from real data. Issues regarding the solution algorithm of inverse problems may be: dimensionality, non-uniqueness, consistency, robustness and so forth.

Characterizing any physical system such as a petroleum reservoir is an infinite dimensional problem. Properties at an infinite number of points are to be identified. Solution of this infinite dimensional problem is out of the question. The problem is thus redefined in a finite-dimensional setup.

There are many models in the solution space (model space) that can match the system performance. Non-uniqueness may arise because of attempting to derive a large number of essentially continuous parameters from a limited number of responses. Also, identifiability of the physics, mechanisms or even procedures may lead to a loss of uniqueness. For instance, one may often have to correlate some calculated or estimated parameters like acoustic impedance from seismic with other variables such as porosity, permeability, and fluid saturations affecting these measurements. The choice of variables may lead to non-uniqueness.

Reservoir characterization, like most inverse problems, entails numerous data of different types and information content. There is often some inconsistency due to different levels of accuracy within the same data type or different types of data. Also, some data may be in the time domain while some in the space domain.

Moreover, the scales or volumetric supports of various data may lead to inconsistencies. For example, well logs have a different volumetric support than well test data or core plug data. Inconsistency may also arise through application of different methods.

Many of these issues are still to be resolved to a satisfactory level in dynamic data integration. This is one reason that this field is an active area of research. Most methods attempt to reduce the non-uniqueness. However, it is difficult to agree on a suitable measure of such reduction. Consistency is a difficult issue especially in the presence of sparse data and many degrees of freedom. This monograph explores the issue of robustness to some extent. Due to its infinite dimensionality, it is not possible to completely deal with the robustness issue. At the end, one should be reminded that there is a need to explore more efficient reservoir characterization techniques with dynamic data. This monograph is only one step towards the goal of full data integration and uncertainty quantification.

Chapter 2

Literature Review

This is not an exhaustive documentation of the literature on dynamic data integration. The authors have restricted their literature review to relevant studies documented in public domain up to mid 1998. Notwithstanding the attempt to be thorough, there is always some possibility of missing valuable research endeavors.

2.1 Brief Description

Production data integration is an inverse problem, that is, a parameter estimation problem. The dynamic production data contain important information about petrophysical properties (e.g. permeability, porosity). Any reliable reservoir characterization study should account for these dynamic data. The objective here is to generate reservoir models that reproduce these dynamic together with static data and measures of spatial continuity.

The classification of the techniques presented in this review is subjective. The chronology of the methods, their distinctness and salient aspects were the criteria for the classification. The methods overlap, which would be true of any possible classification. A common ground of almost all the approaches is the notion of formulating a misfit or mismatch function on which some minimization algorithm is imposed. Furthermore, in many formulations, the problem is ill-posed particularly because of the non-uniqueness of the solution space (model space) and the lack of continuous dependence. A natural consequence in many of these techniques is an exertion to make the problem well-posed, or in mathematical parlance, regularized.

A thorough review of the subject of parameter identification in reservoir simulations is also given by, for instance, Jacquard and Jain [102], Gavalas et al. [71], Watson et al. [186], Feitosa et al. [69, 70], or Oliver [141]; and by Yeh [203] and Carrera and Neuman [25] in groundwater hydrology.

2.1.1 Classical Inversion Techniques

Early approaches to the integration of pressure transient data in geological modeling used inverse techniques for parameter identification or history matching. Probably the most naive and primitive approach to tackle this kind of problem is the trial and error method. Because of its simplicity in formulation, trial and error methods are still widely used for history matching. However, a notable limitation of such methods is the inefficiency, i.e., enormous professional and computation time.

Automatic history matching addresses this inverse problem. The objective of history matching is to estimate reservoir petrophysical parameters from pressure and/or flowrate data [5, 15, 16, 28, 31, 32, 41, 65, 66, 78, 103, 147, 169, 171]. Most methods are based on the premise that the best spatial distribution of reservoir parameters minimizes the difference between observed and calculated pressure data at well locations. These techniques seek direct spatial distributions of reservoir parameters that honor the pressure measurements through pressure response simulation.

Most automatic history matching techniques are based on gradient method or streamline based methods [65]. One of the important aspects of the gradient based history matching techniques is computation of the gradients or sensitivity coefficients. Schemes like perturbation methods, rigorous finite differencing of the physical flow equations [5, 15], convolution integral method [28, 102], optimal control theory [31, 32, 185, 186], have been utilized. Up to 1972, most of the work done had been based on perturbation methods. In perturbation-based methods, the gradients are calculated by first making an initial simulator base run and then repeating the simulator run each time after perturbing each parameter to be estimated. In the finite difference based approaches, the sensitivity coefficients are derived by setting up new equations from the original partial differential equations describing the physical flow system; the new set of equations are then finite differenced. A close alternative approach to this is to derive the gradients directly from the finite-difference form of the physical flow equations. In convolution integral methods, a convolutional method is applied for computing the sensitivity coefficients of the linear system relating the difference between the calculated and the observed parameters. Optimal control theory based methods use the physical system of equations as equality constraints for the minimization problem of the misfit function with the unknown parameters serving as control variables.

2.1.2 Generalized Pulse-Spectrum Techniques and Other Regularization Based Techniques

The inverse problem is often ill-posed partly due to the lack of continuous dependence, that is, small variation in data may result in unbounded changes in the model estimates, and also to the non-uniqueness of the solution space, which means, more than one estimate can satisfy the same set of observed data [165, 201, 203]. To tackle the stability and efficiency problem, a versatile technique was devised by Tsien and Chen [179]. Since its inception in 1974, the technique has been subsequently modified and improved further by Chen and his colleagues [33, 34, 35, 36, 37, 38, 83, 127, 128, 129, 170]. Essentially the Generalized Pulse-Spectrum Technique (GPST) is a combination of a Newton-like iterative algorithm and the Tikhonov regularization method. The capability of GPST has been demonstrated in performing history matching for one-dimensional single-phase reservoir simulators in [34], for two-dimensional single-phase simulators in [127] and for two-dimensional two-phase models in [170]. Hierarchical multigrid approach, in which the estimation is performed on successively finer grids until convergence is reached, is applied to improve the efficiency of GPST further [33, 38]. Landa et al. [120] used a similar technique to integrate well test, production, shut-in pressure, log, core, and geological data.

Another promising numerical method based on regularization techniques proposed by Kravaris and Seinfeld [115, 116, 117] appears particularly suitable for two-dimensional single-phase simulator models [124] and for two-phase models [125]. These methods apply Tikhonov regularization method first and then the well-posed problem is solved by the partial conjugate gradient method of Nazareth [135]. Cubic spline function is used in these methods to approximate the unknown parameters. Makhlouf et al. [131] extended this numerical algorithm to estimate absolute permeability in multiphase, multilayered petroleum reservoirs based on noisy observed data, such as pressure, water cut, gas-oil ratio and rates of liquid and gas production from individual layers.

Both these groups of techniques do not require any *a priori* information on the parameters to be estimated.

2.1.3 Bayesian and MultiGaussian Approaches with *A Priori* Information

A Bayesian estimation framework was proposed by Gavalas et al. in 1976 [71] for reservoir modeling using dynamic production data. The underlying theory behind this technique is to reduce the statistical uncertainty by using additional prior information, for instance autocorrelation and mean values of permeability and porosity. Shah et al. [165] showed that if reliable prior information particularly about permeability or porosity is available, Bayesian estimation will improve the variance of the estimation error. Similar Bayesian approach was used much later by the workers at the Norwegian University of Science and Technology to integrate historical production data [89, 177]. The problem of integrating production data is formulated in a lower dimensional parameter space where, for the sake of mathematical tractability, the parameters are often assumed multivariate Gaussian.

Neuman and Yakowitz [136] used an extended Bayesian approach to estimate actual values of transmissivity in two dimensional study and covariance functions. Clifton and Neuman [40] demonstrated the importance of jointly inverting permeability and pressure data through conditional simulation. They found that the conditioning effect of the pressure data in a full inversion is much greater than that of kriging.

Cooley proposed a method to incorporate prior information having unknown reliability into the nonlinear regression model by adding a penalty function [42]. The resulting composite objective function consists of two terms: the weighted sum of squared errors in the pressure and the sum of weighted errors in the parameters. Dagan [44] used an *a priori* selected analytical technique and Gaussian conditional mean for the inverse problem.

Maximum likelihood methods [24, 25, 26, 27, 68] have long been used for parameter estimation with dynamic data. This is a general non-linear technique that estimates reservoir parameters using prior estimates along with transient or steady state pressure data. Early development of this method is presented in Carrera and Neuman [25, 26] and Feinerman et al. [68]. Parameter estimation is performed using the maximum likelihood theory, incorporating the prior information into the likelihood function. The nonlinear flow equation is solved by a numerical method. Both steady-state and transient pressure data can be integrated into the model. However, this method is computationally intensive.

Oliver [141] used Gauss-Newton method to obtain the maximum *a posteriori* estimate (mean and covariance) that minimizes the objective function derived directly from the *a* *posteriori* probability density function. Multiwell pressure data and prior information are honored in this technique, however, at each iteration of Gauss-Newton method, the forward problem is solved using a reservoir simulator. Chu et al. [39] presented an efficient method of computing sensitivity coefficients required in the approach. This method yields a smoothed version of the true distribution. Conditional realizations with given variability are constructed using Cholesky decomposition of the covariance matrix estimated by assuming that permeability distribution is Gaussian and pressure data is a linear function of permeability. Reparameterization based on spectral decomposition reduces the number of the parameters to be estimated by the Gauss-Newton procedure [39, 141]. More recently, a reparameterization technique based on subspace method was presented to further improve the computational efficiency in the Gauss-Newton procedure by Reynolds et al. [155]. He et al. [87] extended this method for a three dimensional reservoir model. In another effort, the same authors [86] developed a multistep procedure to generate reservoir models conditioned to well test data. The ensemble realizations by this method provides a good empirical approximation to the posteriori probability density function for the reservoir model, which can be used for Monte Carlo inference. Oliver et al. [144] concluded that the frequency of occurrence of parameter values within an interval of values must be approximately proportional to the conditional probability density function for the parameter. Consecutive sampling from a small neighborhood will cause artifact. Abacioglu et al. [1] used a similar technique to a field example in estimation of heterogeneous anisotropic permeability fields from multiwell interference.

Wu et al. [196] developed a discrete adjoint method for generating sensitivity coefficients related to two-phase flow production data. The method directly generates the sensitivity of the calculated data to the model parameters. Using these sensitivity coefficients, an efficient Gauss-Newton algorithm is applied to generate maximum a posteriori estimates and realizations of the rock property fields.

Cunha et al. [43, 143] used a hybrid Markov Chain Monte-Carlo algorithm to generate realizations of permeability conditioned to prior mean, variance and multiwell pressure data. These realizations represent samples from the correct a posteriori probability distribution.

Ates and Kelkar [6] devised a two-stage multiphase production data inversion technique. The method is based on an analytical sensitivity equations for two-phase flow which can be coupled to both streamline and finite-difference simulators. The most probable models were constructed using dual-loop technique, which combines Gauss-Newton and Conjugate Gradient algorithms.

Rogerro [156] used a Bayesian inversion technique and an efficient optimization algorithm to integrate multiple well historical data and prior geostatistical information. The procedure permits direct selection of particular constrained model realization within a confidence level of the parameter space.

2.1.4 Zonation Methods

All numerical reservoir characterization models, irrespective of static or dynamic nature, should fall into this category inasmuch as the original problem is infinite-dimensional but is modeled by a finite number of parameters. Notwithstanding this fact, the authors have grouped the subsequent methods in this category because of the utility and emphasis of the zonation approach.

Some of the early methods [25, 40, 65, 102, 136] have already been grouped as the classical techniques for a historical perspective. While the zonation method is effective in reducing the number of unknowns, sufficient *a priori* information is not usually available to enable specification of the zones on any physical basis. Zonation methods are active research area. Amongst the newer methods are pilot point method, sequential self-calibrated method, and others.

Pilot point method [50, 122, 154] is a zonation method that starts by simulating a conditional transmissivity field. The generated field is then modified by adding additional or fictional transmissivity data at some selected locations, termed pilot points, to improve the calibration of the pressure data. Adjoint sensitivity analysis is used to determine the locations where additional transmissivity data should be included [121]. The additional transmissivity data at the selected pilot points are treated as local data, a new conditional realization of transmissivity is then generated, and, the flow model is run again. The iteration of adding pilot points is continued until the least-squared error criterion is met or the addition of more pilot points does not improve the calibration. This method is, however, computationally inefficient and cannot efficiently handle pressure data from multiple hydraulic tests at different times. Fasanino et al. [67] applied this model in inverse modeling of a gas reservoir. Bissell et al. [14] evaluated pilot point method it to an alternative gradzone method, where groups of grid cells in the model are modified.

Sequential self-calibrated method [22, 73] combines geostatistical and optimization techniques. A geostatistical technique is used to generate a reservoir parameter model conditioned to local measurements of parameters. Initial model is modified to minimize the misfit function through an optimization procedure. In order to reduce the parameter dimension, the optimization is parameterized as a function of the perturbations of permeability at a few selected locations, called master points. The perturbation values at the master locations are determined from the optimization procedure by minimizing the squared difference of the simulated and observed pressures. The resulting perturbations are propagated throughout the entire reservoir domain by kriging to obtain the perturbation field that is subsequently added to the initial field. The flow equation is linearized to obtain fast solution in the optimization process. Alternatively, an iterative process is used in order to avoid the errors in the linear approximation of the flow equation, that is the modified reservoir model is input again into the reservoir simulator and the squared difference of simulated and observed pressures is reevaluated until the actual solution of pressure from the numerical reservoir simulator is close to the observed data. This approach accounts for measurement errors in the data and the uncertainty in flow boundary conditions. It is computationally efficient. Promising results were obtained by using this approach in groundwater hydrology [188, 194, 195, 204].

Blanc et al. [17] presented a solution to the problem of constraining geostatistical models by well test pressure data similar to the pilot point method or sequential self-calibrated method. In this method, a well test simulator is coupled with a nonlinear constrained optimization program for an inversion loop so that a set of optimal facies or rock-type properties and well-skin that give best fit between the simulated and measured pressure data are obtained. Sensitivity coefficients are computed numerically, and in each iteration, full numerical solution of well test pressures are computed by a well test simulator. The method is thus computationally inefficient.

Xue and Datta-Gupta [198] developed a two stage approach for a structure preserving inversion technique similar to pilot-point technique but incorporates the prior information in a different way. The covariance matrix is embedded in the parameterization of the permeability field.

2.1.5 Cokriging Based Methods

Kitanidis and his colleagues [92, 114] applied cokriging to simulate transmissivity and pressure fields using covariance or cross-covariance models based on field measurements of transmissivity and pressure. The cross-covariance between transmissivity and pressure is developed through linearization of the single phase steady state flow equation. Parameters in the covariance and cross-variance are estimated from the measured data and the linearized flow equation using a maximum likelihood method. Realizations are then constructed using Cholesky decomposition of the covariance matrix, which is computationally efficient. However, the steady-state pressure data are reproduced only under the assumptions that the relationship between transmissivity and pressure is linear which is valid only for small variance of transmissivity, the permeability distribution is Gaussian, and flow is uniform.

In linearized semi-analytical cokriging method [160, 161], a linearized form of the single phase steady-state flow equation is used to develop analytical expressions of cross-covariances of permeability and pressure assuming uniform flow and infinite domain. Transient pressure is accounted for with the linearity assumption between change of pressure and time.

Harvey and Gorelick [82] presented a cokriging method, combining numerical simulation of flow and tracer transport with a linear estimation, to construct permeability field that sequentially accounts for permeability, pressure and tracer arrival times. Integrating tracer arrival time data improves the accuracy of the permeability estimation. Tracer arrival time quantiles are found to be robust indicators of flow paths and flow barriers.

Yeh et al. [202] applied a similar but iterative technique to account for the nonlinear relationship between permeability and pressure in the estimation through successive linear approximation. It first estimates a permeability field by cokriging from the available permeability and steady-state pressure data. The flow equation is then solved numerically to obtain a pressure field, which is computationally intensive. The covariance and cross-covariance of permeability and pressure are then updated and a new permeability field can be obtained by again cokriging using the updated covariance and cross-covariance. This process is continued until the variance of estimated permeability stabilizes.

In another cokriging based method, fast Fourier transform method [79, 80] is applied to the linearized steady-state flow equation. Transmissivity and pressure perturbations are represented in the spectral domain as Fourier integrals in two dimension. The covariance and cross-covariance are represented as functions of the spectral and cross-spectral density. Transmissivity realizations conditioned to the pressure data are constructed by adding the difference between the unconditional simulation and kriged values of the unconditional simulation to the kriged values using the field data [51, 108]. This method is computationally fast when there are a large number of pressure data.

Huang et al. [99, 100] integrated time-lapse seismic and production data in reservoir characterization. The uncertainty was quantified by the statistics on reservoir-scale 3D acoustic impedance blocks. Using collocated cokriging the impedances were transformed into reservoir parameter through a petrophysical relationship while respecting the well information. The results are finally transferred from the time domain to a spatial one for flow simulation.

Hu et al. [95] proposed a new kriging algorithm to estimate lithofacies proportions in well test areas of investigation. Method consists in kriging jointly the proportions of all lithofacies in the area through a weighted power averaging of lithofacies permeabilities. For multiple well tests, an iterative process is used to account for their interaction.

Srinivasan and Journel [166] interpreted well test derived effective permeability as linear average of small scale permeability values indexed with a power. A kriging on the power transformed permeability fields followed by an inverse power transform allows generating estimated permeability fields over the drainage area.

2.1.6 Simulated Annealing Based Techniques

Ouenes and his colleagues [145, 146, 167] employed simulating annealing for automatic history matching. Petrophysical and reservoir engineering parameters are estimated through an automatic and multiwell history matching using simulated annealing method. A least-square error objective function defined by the oil, gas, and water productions at each well is minimized by the simulated annealing method. At each iteration in the simulated annealing method, a limited number of reservoir parameters are adjusted. The impact of these new parameters on the objective function is evaluated by forward reservoir simulation, which is too costly for routine application for large number of parameters and iteration steps used in this approach.

In another simulated annealing approach proposed by Tauzin [172], the objective function is evaluated analytically which improves the computational time. An analytical influence function is defined to approximate the perturbation on the pressure transient due to a local heterogeneity. This influence function is derived from the analytical solution of transient pressure in an infinite homogeneous reservoir containing a single circular discontinuity from Rosa and Horne [159]. This approximation is usually sufficiently accurate to predict the direction and the order of magnitude of the pressure perturbation caused by the permeability perturbation.

Tracer data reveal important information on the interwell connectivity. Datta-Gupta et al. [48, 49] sequentially applied the simulated annealing method to account for both pressure and tracer data in the construction of reservoir permeability model. A semi-analytical transient time algorithm was used for fast calculation of tracer travel time in the simulated annealing [46]. Vasco et al. [183] first attempted to integrate multiphase production history data using 3D multiphase semi-analytical streamline model based on simulated annealing technique.

Maroongroge et al. [132] investigated the effectiveness of vertical tracer profiling for determining reservoir zonation. Tracer history is used to condition the permeability model using a simulating annealing method and a least square history matching method. Conditioning to tracer history substantially constrains the model and it is particularly important when the horizontal variogram is unknown. The use of vertical tracer profiling can substantially improve the results compared to the case when the integrated breakthrough curve is used. However, this would be quite difficult and costly to implement in the field.

2.1.7 Inversion Techniques for Statistical Parameters or Constraints

Most modern indirect inversion techniques fall into this category. Production data can be used to estimate statistical parameters, such as the mean, covariance, or the fractal dimension that describe the spatial distribution of reservoir properties. These parameters are subsequently used to characterize the reservoir.

These indirect techniques seek to construct geological models that honor critical features interpreted from the production data. Some relationship is first established between the production data and some reservoir parameters or their spatial variation. This relationship then serves as a constraint in the construction of the geological model so that the production data are indirectly integrated into the reservoir model.

The first step is to analyze transient production data and infer spatial heterogeneity features of the underlying reservoir model. These heterogeneity features may be in the forms of general information on the degree of heterogeneity, anisotropy and zonation of the reservoir properties; the presence of internal or external reservoir boundaries such as faults, lithofacies changes, water-oil contacts, stratigraphic pinchouts; the presence of high flow channels or low permeable zones in an area and the distance to these zones; in multiple well systems, water breakthrough time and recovery efficiencies inform connectivity between wells; effective transmissivity and facies proportions in the wellbore vicinity, etc.

Chang et al. [30] give an example of the connection between different engineering data including well test data, production data, production performance data, hydrogeochemical data and the geological model. Other references include [7, 8, 20, 85, 88, 93, 126, 130, 184].

Yadavalli et al [199, 200] used pressure transient data from single or multiple sets of well tests to estimate permeability variograms, and they were able to obtain reliable horizontal variogram models in cases where no information is available on the short scale structure of the variogram. Chang and Yortsos [29] and Beier [12, 148] showed that pressure transient field data could indicate fractal reservoir structure and the parameters of the fractal model. Grindrod and Impey [76, 77] also estimated fractal geometry parameters from permeability and pressure data using a maximum likelihood method.

Once the statistical parameters are estimated, they are used in geostatistical techniques to construct reservoir models. The contribution of production data lies in the improvement in the estimation of statistical parameters describing the reservoir heterogeneity. In some cases, such as when the reservoir parameters are Gaussian, and the relationship between the reservoir parameter and pressure data are linear, the constructed geostatistical reservoir model may also directly honor the pressure data.

Another approach is to infer parameters of the heterogeneous reservoir model from the production data and then constrain the reservoir models to those inferred parameters.

Effective permeability within the drainage area of the well obtained from well test data [94, 162] does not resolve local details of the spatial distribution of permeability. However, well-derived effective permeability can be regarded as the average value of the heterogeneous permeability values in the vicinity of the test well [2, 138]. Deutsch [55, 57, 58, 60, 61] presented an approach, based on simulated annealing, that integrates well test-derived effective permeabilities in stochastic reservoir models. The volume and type of averaging formed by the well test are first calibrated by forward simulating the well test on a number of stochastic reservoir models that are consistent with the geological interpretation, core, well log, and seismic data. The effective permeability from the well-test is assumed to be the power average of the heterogeneous permeability within the influence volume of the well test [2]. The optimal volume and power parameter for the averaging process are obtained from the calibration as suggested by Alabert [2]. Stochastic reservoir models are then constructed with simulated annealing to honor the well-derived average permeabilities. Results showed the improvement in characterizing permeability heterogeneity and waterflooding predictions when the effective permeabilities are constrained in the model.

A similar approach was presented by Sagar et al. [163] but using a geometric average of permeability values within the influence region. The approach of Deutsch was extended by Tauzin [172] to directly integrate the pressure transient data using a simple analytical algorithm based on Rosa and Horne [158, 159] to quickly evaluate the objective function due to the single perturbation of permeability.

Hird et al. [90, 91] used reservoir connectivity parameters as indirect well-performance constraints in the conditional simulation of a stochastic reservoir model. Reservoir connectivity parameter was defined by a functional relationship between fractional area connected and permeability percentile cutoffs. This connectivity parameter is found to be strongly correlated to the well performance, such as secondary recovery efficiency, drainable hydrocarbon pore volume, floodable hydrocarbon pore volume and also water breakthrough time. Based on a strong correlation between the spatial reservoir properties and the reservoir performance, they suggested use of the connectivity parameter to constrain the reservoir model using simulated annealing. Alabert and Modot [4] also defined connectivity of a permeability field in terms of the connected pore volume.

Holden et al. [93] presented an approach to indirectly account for well test data to improve the simulation of lithofacies and petrophysics under the framework of two-stage stochastic simulation as suggested by Haldorsen [45, 81]. Using an analytical tool, the pressure data is used to estimate pressure support and then the shortest distance from the well to a possible channel boundary, connection between two wells by a high permeable zone and channel geometry. The channel structure is then simulated using these interpretations with a marked point process model. Average permeability in the part of the channel intersected by the well is estimated from the well test data. The permeability field was then generated together with the core/log data using stochastic Gaussian model. Alabert and Massonnat [3] used well test data to infer information on channels and lobe dimensions in addition to average permeability.

Britto and Grader [19] applied transient pressure data to identify local impermeable regions or high-flow channels. Vashist et al. [184] presented a technique for defining reservoir facies which incorporates the geological features of deposition and diagenesis with the dynamic flow capacity (kh) of the reservoir. The ranges of permeability for different reservoir facies are determined through multiple regression analysis based on their dynamic flow capacity (kh) data in tested wells.

Benkendorfer et al. [13] presented a different approach to indirectly integrate production data using a two-step approach. That is, the permeability values estimated from well-test data are regarded as the sum of a core-based permeability and a large-scale permeability. The core-based permeability and the large scale permeability are constructed separately. The final model is the sum of the two models. This two-step approach is applicable when a significant difference exists between core-based permeability and production-scale permeability.

Feitosa et al. [69, 70] presented a new inversion solution, called Inverse Solution Algorithm (ISA) based on Oliver's perturbation solution [138]. Based on the pressure data from drawdown and buildup tests, the absolute permeability is estimated as a function of distance from the well [70, 139], or a function of both distance and angle from the well [69].

Huang and Kelkar [98] presented a procedure for integrating three dimensional seismic data and production data to develop a detailed reservoir description. Impedance distribution is constructed by the inversion of the seismic data, then porosity field, consistent with the impedance data, is simulated, and finally permeability field, consistent with porosity and dynamic well test data, is constructed. The initial permeability field is then perturbed randomly until the simulated well test data match the measured data. Forward simulator is used to calculate the pressure or flowrate response after each perturbation of permeability, thus it is computationally inefficient. To improve the efficiency, for a highly correlated porosity and permeability, the bound can be narrowed. The same authors have in another paper [97] discussed dynamic data integration in frequency domain. The spatial relationship-variogram is represented by power spectra and self-correlation in the frequency domain. Huang et al. [96] also explore the impact of dynamic data integration in the uncertainty of prediction of the multiphase systems.

Deng [52] and Deng and Horne [53] presented an analytical approach to interpret pressure and tracer data from multiple wells simultaneously to characterize the two dimensional permeability distribution in heterogeneous reservoir. The correlation between permeability and dispersivity is sought, and the convection-dispersion equation and diffusion equation to a system of first-order equations in permeability are reformulated. The system of equations is then solved to yield the permeability distribution for appropriate boundary conditions.

Several other authors have examined the sensitivity of transient pressure response to the spatial distribution of permeabilities, such as McElwee [134] and Sykes et al. [168]. The pressure response for a multirate test was found more sensitive to reservoir heterogeneities than a single flowrate test [158]. The effectiveness of the data in estimating local-scale permeability can be measured by its spatial resolution [46, 140, 142]. The higher the resolution of a data to a given parameter, the more information this data carries on the spatial variation of the parameter. Datta-Gupta et al. [46] used the concept of resolution matrix to give information on the spatial averaging involved in the parameter estimation due to limited sampling, as well as quantitatively evaluate the relative worth of additional data. The resolution of pressure data in constraining local permeability variations in heterogeneous media is limited. Oliver [142] showed that interference tests are generally more effective than single-well tests at improving the resolution. On the other hand, interwell tracer data can be very sensitive to local heterogeneities [47, 53]. Also, both transient pressure data and tracer data appear to resolve flow barriers better than flow channels [46].

Rahon et al. [151, 152, 153] developed geological shape inversion technique with improved gradient computation. The devised method is capable of identifying the limits of the reservoir, position of the faults, thickness and dimensions of channels. Geological shapes are modeled by triangulation as a 2D or 3D surface. A finite element structure is associated to each object and the Cartesian coordinates of the nodes in this triangulation are matched in the inversion process.

Jensen and Kelkar [105, 106] employed cross-correlation between pairs of wells production to determine the inter-well relationships, preferential flow directions and flow barriers. They incorporated Wavelet transformation tools in reservoir characterization technique in the form of a better search neighborhood definition. In an earlier paper [104] by the same authors, exploratory data analysis of production data was performed. A local and global analysis along both the temporal and spatial axis were considered.

Rogerro and Hu [157] used gradual deformation method to continuously modify geostatistical model while respecting its global mean and variogram. This method was coupled with an efficient optimization algorithm. Different strategies are used to obtain optimal efficiency by selecting the number of deformation parameters in the model and the optimization sequences.

Landa and Horne [119] devised a procedure to integrate well test data, reservoir performance history and 4D seismic information into reservoir characterization. Both cell-based and object-based modeling were formulated. Sensitivity coefficients were calculated with a multiphase extension of the Jacobian method. 4D seismic information was considered to be in the form of maps of change of saturation in the reservoir. The value of data integration was evaluated with the variance analysis.

Indirect methods provide flexibility to account for production data in the construction of reservoir models with less computational effort than full inversion. However, the success of these techniques in constraining reservoir models essentially relies on the quality of the interpretation of production data in retaining reservoir heterogeneous features.

Chapter 3

Single Well - Single Phase

This chapter provides the details of an approach to integrate dynamic production and well test data in reservoir model building. The technique discussed builds on the works of Wen and his colleagues [190]. First, a spatial representation of permeability is interpreted from the well test data. Single-well pressure responses are interpreted as a set of spatially varying average permeabilities. These parameters are utilized directly as input constraints along with other data in reservoir model building.

Within the radial flow domain, spatially varying permeability can be derived as weighted power averages of permeability values within a dimensionless time-dependent annular reservoir volume around the well. Two parameters represent the volume-of-averaging and the power average exponent, which can be derived by a simple calibration process.

A number of synthetic examples of varying grid size, anisotropy, permeability heterogeneity, dimensionality, and lithofacies architecture have been tested to develop a sense of the limitations and the range of applicability of the method. The methodology is also demonstrated on two segments from a real clastic reservoir.

3.1 Problem Statement

Single well pressure transient test data are common source of engineering data. The available data consist of time dependent pressure $p(t)$ and flow rate $q(t)$ observed at the testing well. Traditionally, single well tests are designed to analyze well performance and determine a single effective permeability of the drainage region around the well [94, 162].

With the introduction of high accuracy and high resolution pressure gauges, well tests are also used to evaluate reservoir heterogeneity. The pressure derivatives, coupled with non-linear regression, are used as interpretive tools. Time-dependent changes in pressure provide information on the spatial distribution of reservoir petrophysical properties. The analysis of pressure time derivative may identify some important heterogeneities in the reservoir, such as faults, stratigraphic pinch-outs, reservoir boundaries, facies boundaries, layered systems, fractured reservoirs, and other barriers. Since pressure is observed at only a single point, that is, at the testing well, a single well test can only provide information on the radial distribution of reservoir properties, no directional information can be retrieved.

Figure 3.1 summarizes the method for obtaining spatial representation of permeability from single-well pressure response. The procedure is divided into three phases: interpretation, calibration, and model-building.

The interpretation phase is based on a radial flow analysis as described in Section 3.4. This phase provides interpretation of the flow regime and the overall effective permeability. Second phase is the calibration phase described in Section 3.5. Two parameters, A and ω, defining the volume of averaging and the exponent of the power average, respectively, are obtained by a simple calibration process with the step-by-step procedure presented in this section. A and ω are determined from the pressure data and a prior approximate permeability description, for example, a descriptive geologic model. For practical applications in which no prior description of permeability is known, these optimal parameters may be calibrated from forward simulation with a small number (<10) of permeability realizations with the same heterogeneous features observed in the field.

Limitations and range of applicability of the method are addressed in Section 3.6, which discusses the dependence on grid size, dimensionality, boundary effects, lithofacies architecture, anisotropy, and flow regime. Guidelines are established to determine the time interval within which the simulated well test pressure data are reliable for analysis. Presented in this section are realistic synthetic reservoir models representing a heterogeneous single facies, a multi-facies carbonate, a high net-to-gross braided stream deposit, and a low net-to-gross fluvial reservoir.

Section 3.7 presents an example analysis for two segments from a real near-shore reservoir. The resulting spatial representation parameter set (A, ω) and the dimensionless time-dependent effective permeability are presented.

3.2 Background

This section discusses the basic mathematics involved in pressure transient analyses and the interpretations to be made from such analyses. The mathematical equation describing pressure transmission in a porous medium filled by slightly compressible fluid in cylindrical coordinates is given by [94]:

$$\frac{\partial^2 p}{\partial r^2} + \frac{1}{r}\frac{\partial p}{\partial r} = \frac{\phi \mu c}{k}\frac{\partial p}{\partial t} \tag{3.1}$$

where p is pressure, r is the radial distance from the wellbore, ϕ is the porosity, μ is the viscosity, c is the fluid compressibility, k is the absolute permeability, and t is time. Assumptions inherent in this equation are:

- Darcy's law is applicable and the flow is single phase.
- Flow is radial into the well penetrated over the entire vertical thickness of the formation.
- Formation is homogeneous and isotropic with constant porosity and constant permeability.
- Fluid has a small and constant compressibility and a constant viscosity.

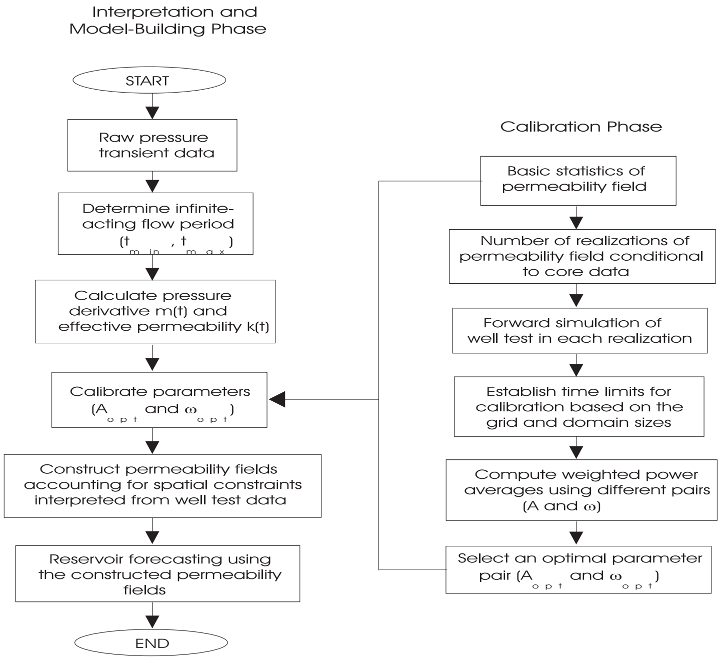

Figure 3.1: Flowchart of overall procedure of integrating well test pressure data in reservoir modeling.

- Pressure gradients are small and gravity and thermal effects are negligible.

For an infinite reservoir and a line source well with a constant flow rate q, the pressure solution to this equation may be written as:

$$p(r,t) = p_i - \frac{q\mu}{2\pi kh}\left\{-\frac{1}{2}E_i\left(-\frac{\phi\mu c r^2}{4kt}\right)\right\} \tag{3.2}$$

where E_i is the exponential integral function given by,

$$-E_i(-x) = \int_x^\infty \frac{e^{-u}}{u}du \tag{3.3}$$

The exponential integral function can be well approximated by a log function for all but early times,

$$p(r,t) = p_i - \frac{q\mu}{4\pi kh}\left[\ln\frac{kt}{\phi\mu c r^2} + 0.80907\right] \tag{3.4}$$

where:
k = permeability (md)
h = thickness (ft)
p_i= initial reservoir pressure (psi)
$p(r,t)$ = pressure at radial distance r (ft) and time t (hours).
q = flow rate (STB/d)
ϕ = porosity (pore vol/bulk vol)
c = fluid compressibility (1/psi)
μ = viscosity (cp)

In many situations, dimensionless variables are used to simplify the notation and to provide solutions that are independent of any particular unit system. The dimensionless pressure p_D is defined in oilfield units as:

$$p_D = \frac{kh}{141.2qB\mu}(p_i - p_{wf}) \tag{3.5}$$

where p_{wf} is the well flowing pressure and B is the formation volume factor (res vol/std vol).

The dimensionless time t_D is defined in oilfield units as:

$$t_D = \frac{0.000264kt}{\phi\mu c_t r_w^2} \tag{3.6}$$

where c_t is the total compressibility (1/psi) and r_w is the wellbore radius (ft).

The dimensionless radius r_D is defined as:

$$r_D = \frac{r}{r_w} \tag{3.7}$$

Reservoir parameters such as wellbore skin effect, wellbore storage, and effective permeability can be determined from well test analyses, provided the well test data, that is, flow rate q and corresponding pressure transient at the well $p(r_w,t)$, and the estimates for μ,

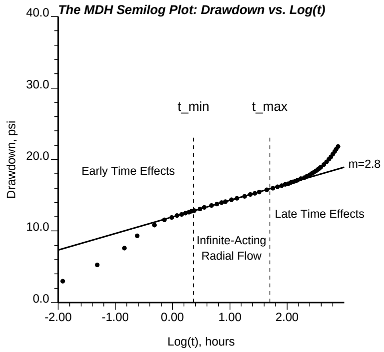

Figure 3.2: A typical semilog plot of pressure drawdown from a well test.

h, ϕ, and c are available. One widely used well test analysis is the Miller-Dyes-Hutchinson (MDH) method. In this method, pressure drawdown is plotted against the logarithm of time (see Figure 3.2). A straight line is then fitted to the pressure drawdown data during the infinite acting transient radial flow portion. The early-time effects are due to wellbore storage and skin effect, whereas the late-time effects are attributed to the reservoir boundaries. The slope of the semilog straight line m is linearly related to the effective permeability, k_e, by the following equation.

$$k_e = 162.6 \frac{qB\mu}{|m|\, h} \tag{3.8}$$

Traditionally, only a single effective permeability k_e is estimated. This effective or apparent permeability is considered to be representative of the reservoir permeability within the radius of investigation of the test, or the annular reservoir volume informed by the infinite acting radial flow period defined by $r(t_{\min})$ and $r(t_{\max})$, with $r(t)$ being the radius of investigation at time t.

In practice, the time interval that the pressure response resembles infinite-acting radial flow ($t_{\min}$ and $t_{\max}$) can be easily determined. However, evaluating the radius of investigation corresponding to a given time of test, $r(t)$, is not straightforward. The classical approaches proposed by van Poollen [182], Johnson [107], and Lee [123] give rise to similar expressions which can be written as:

$$r(t) = A\sqrt{\frac{k_e t}{\phi \mu c_t}} \tag{3.9}$$

or in dimensionless units as:

$$r_D(t) = A\sqrt{t_D} \tag{3.10}$$

where A, a constant, varies from 0.023 to 0.07 for oilfield units depending on the definition chosen for $r(t)$. Equation 3.9 assumes that the permeability field near the well is constant at k_e and independent of time.

For a heterogeneous permeability field, the radius of investigation is ill-defined. Alabert [2] proposed to calibrate the radius of investigation by repeated Monte-Carlo forward flow simulation. Using Equation 3.9, an optimal A was determined for a given spatial variation pattern of heterogeneous permeability field. A robust A_{opt} value of 0.010 in oilfield units was obtained for specified levels of discretization and well test durations used in his study. Alabert [2] also stated that the effective permeability determined by Relation 3.9 using time interval ($t_{\min}$, $t_{\max}$) can be expressed as power average of heterogeneous block permeabilities in an annular volume $V(A_{opt})$ defined by $r_{\min}(A_{opt},\, t_{\min})$ and $r_{\max}(A_{opt},\, t_{\max})$,

$$k_e \cong \overline{k}(\omega) = \left[\frac{1}{N} \sum_{\mathbf{u}_i \in V} k(\mathbf{u}_i)^{\omega} \right]^{1/\omega} \tag{3.11}$$

where $\overline{k}(\omega)$ is the ω-power average permeability of the N permeability values $k(\mathbf{u}_i)$, $i = 1, \ldots, N$, at location $\mathbf{u}_i$ within the volume of A. The optimal averaging power parameter, ω, can also be determined jointly with parameter A through calibrations by repeated flow simulation and it has been shown to be remarkably robust [54, 110]. $\omega = -1$ and 1 correspond to harmonic and arithmetic averages respectively, whereas geometric average is obtained as $\omega \rightarrow 0$. In many cases, ω is close to the geometric average ($\omega = 0$). Alabert [2] and Butler [21] also showed that the type of averaging can differ significantly from the geometric average for particular test durations and for complex permeability heterogeneities.

With these two calibrated parameters (A and ω) and the infinite acting radial flow interval ($t_{\min}$ and $t_{\max}$), Equation 3.11 describes the relationship between the effective permeability estimated from well test (k_e) and the smaller scale permeability values ($k(\mathbf{u}_i)$) within the annular volume centered at the wellbore. The inner and outer radii of the annular ($r_{\min}(A,\, t_{\min})$ and $r_{\max}(A,\, t_{\max})$) are determined by Equation 3.9.

The approach of Alabert [2] was successfully implemented by Deutsch [55, 57]. The constraints on the spatial distribution of permeability, defined by Equation 3.11, were integrated in the construction of heterogeneous permeability fields using simulated annealing. Results showed improvement in characterizing permeability heterogeneity and waterflooding predictions due to the integration of well test data. A similar approach was used by Sagar et al. [163, 164] but simply using the geometric average of the permeability values within the influence region to approximate the well-test-derived effective permeability.

The single effective permeability as in Equation 3.8, does not reflect the radial variation of permeabilities. At any instant in time t within infinite acting radial flow period, the pressure derivative ($\frac{d\triangle p}{d\log(t)} = m(t)$), the slope of pressure drawdown in the MDH plot, may be computed from high resolution pressure measurements during the well test. Thus, an effective permeability $k_e(t)$ as a function of time t can be obtained according to Equation 3.8. For each time (t_i, $i = 1, \ldots, N_t$), a corresponding effective permeability ($k_e(t_i)$, $i = 1, \ldots, N_t$) is obtained (see Figure 3.3). Pressure derivative, $m(t)$, is informed by a particular annular volume centered at the wellbore [138]. Hence, the corresponding effective permeability at time t, $k_e(t)$, is also informed by the permeability values in that annular volume. As a consequence, a series of time-dependent effective permeabilities ($k_e(t_i)$, $i = 1, \ldots, N_t$) can be inferred. These effective permeabilities refine the traditional single effective permeability and more importantly, provide additional information on the radial variation of averaging permeability values, which a single effective permeability can not provide.

Under the assumption of small variation of permeability, an analytical weighting function is derived to specify the relative contribution of the permeability of various regions to the estimation of effective permeability, $k_e(t)$ [138]. Figure 3.4 shows the normalized weighting

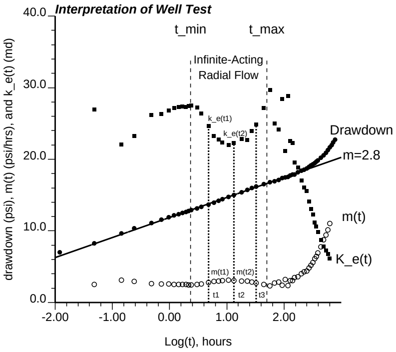

Figure 3.3: Interpretation of well test data for time-dependent effective permeabilities.

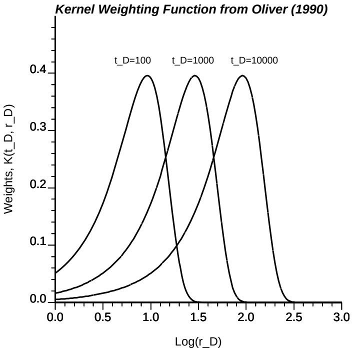

Figure 3.4: Kernel weighting at different times based on Oliver [138].

function for dimensionless time $t_D = 100$, 1000, and 10000, respectively. The inner and outer radii of the annular region for a given time can be taken as $0.12\sqrt{t_D}$ and $2.34\sqrt{t_D}$, which contain 98% of the contribution.

Based on above analytical results of Oliver [138], Feitosa et al. [69, 70] developed an analytical inversion approach, called Inverse Solution Algorithm (ISA) to estimate the radial distribution of permeability. On the basis of the same analytical weighting function, Sagar [163, 164] used simulated annealing to integrate the pressure derivatives at different time computed from well test into the permeability modeling.

3.3 The Inversion Approach

In multistage indirect inversion techniques, the well test data are first coded into spatial representations of reservoir parameters for example permeability. The spatial representation retained from the well test is then honored in model construction. One approach is to retain a single effective permeability (k_e) from the well test data, relate this effective permeability to the spatial distribution of permeability as in Equation 3.11, then constrain the permeability values within the calibrated annular region to that single effective permeability [2, 55, 57, 59, 163, 164]. This approach is simple and computationally fast; however, not all information from the well test is used.

This monograph emphasizes a new approach to integrate single well test data [193]. In this approach (see Figure 3.3), pressure transient data $p(t)$ is first interpreted to establish the limits to infinite acting radial flow, that is, $t_{\min}$ and $t_{\max}$. Pressure derivatives, $m(t_i) = \frac{d\triangle p}{d\log(t)}\Big|_{t=t_i}$, are computed at a number of times, $t_i, i = 1, \ldots, N_t$ (see Horne [94]). Effective permeabilities, $k_e(t_i)$, are then determined at these times t_i based on estimates of μ, h, B, q, and $m(t_i)$ according to Equation 3.8. The volume of investigation ($V \propto t$) and the type of averaging (ω) are calibrated. These parameters relate the effective permeabilities $k_e(t_i)$ to power averages of permeability values within annular regions $V(t_i)$ weighted by the kernel function of Oliver [138] (see Figure 3.4). Thus, the permeability fields are constrained to the well test "data".

In the following sections, these steps are discussed in detail along with some important implementation issues and applications to different types of heterogeneous reservoirs.

3.4 Interpretation of Pressure Transience

Early time effects, wellbore storage and near wellbore effects such as the skin effect, are not relevant to reservoir petrophysical properties. Thus, early time pressure transient data ($t < t_{\min}$) are usually excluded from well test analysis. Similarly, late time effects such as boundary effects are also not relevant to the type of reservoir heterogeneity considered here. Boundary effects such as faults can usually be accounted for deterministically in reservoir modeling. Hence, late time pressure transient data ($t > t_{\max}$) are also usually excluded from well test analysis. Figure 3.3 shows a typical MDH plot of pressure transient from a single well test.

The pressure transient data within time interval $[t_{\min},\ t_{\max}]$ represent infinite acting radial flow condition. This reflects easily understood responses of the reservoir system to the flow rate change used in the well test. Well test is interpreted using only pressure transient data in the infinite acting flow region. Within this region, the derivatives of pressure drawdown can be calculated as (Horne [94], p79-80):

$$m(t_i) = \left(\frac{d \triangle p}{d\log(t)}\right)_i = \left[\frac{\log(t_i/t_{i-k}) \triangle p_{i+j}}{\log(t_{i+j}/t_i)\log(t_{i+j}/t_{i-k})} + \frac{\log(t_{i+j}t_{i-k}/t_i^2) \triangle p_i}{\log(t_{i+j}/t_i)\log(t_i/t_{i-k})}\right.$$
$$\left. - \frac{\log(t_{i+j}/t_i) \triangle p_{i-k}}{\log(t_i/t_{i-k})\log(t_{i+j}/t_{i-k})}\right] \tag{3.12}$$

with $\ln(t_{i+j}/t_i)$ and $ln(t_i/t_{i-k})$ greater than 0.2.

Given the constant flow rate q, the estimates of μ, B, and h, and the derivatives of pressure drawdown $m(t_i)$ at time t_i, an effective permeability corresponding to time t_i, can be obtained according to (3.8), that is:

$$k_e(t_i) = 162.6\frac{qB\mu}{|m(t_i)|\,h} \tag{3.13}$$

For each time $t_i, i = 1, \ldots, N_n$, a time-dependent effective permeability is obtained (see Figure 3.3). The idea here is to link this effective permeability to a power average of permeability values weighted by the kernel function of Oliver [138] within a time-dependent annular reservoir region (see Figure 3.4). The annular volume and the type of averaging are calibrated by repeated forward flow simulations.

3.5 Calibration of Volume and Type of Averaging

3.5.1 Volume of Averaging

Oliver [138] showed that, at given time t, the pressure derivative, $m(t)$, hence also $k_e(t)$, is a weighted average of permeability values in the reservoir. The weighting function $K(r_D, t_D)$ was derived as:

$$\sqrt{t_D}K(r_D,t_D) = 0.5\sqrt{\frac{\pi r_D^2}{t_D}}\exp\left(-\frac{r_D^2}{2t_D}\right)W_{1/2,1/2}\left(\frac{r_D^2}{t_D}\right) \tag{3.14}$$

where $W_{1/2,1/2}(z)$ is Whittaker's function with expression as the following:

$$\begin{aligned} W_{1/2,1/2}(z) = \frac{z\exp(-z/2)}{2\pi}\Bigg\{\sum_{k=0}^{\infty}\frac{\Gamma(k+1/2)}{k!(k+1)!}z^k[\Psi(k+1)+\Psi(k+2) \\ -\Psi(k+1/2)-\ln(z)] + \frac{2\sqrt{\pi}}{z}\Bigg\} \end{aligned} \tag{3.15}$$

where $\Gamma(k+1/2)$ is Gamma function and $\Psi(k)$ is Euler's Psi function. For small z (≤ 2.0), good results can be obtained by using the first nine terms of Equation 3.15. When z is large ($z > 2.0$), Equation 3.15 can be well approximated by the following series:

$$W_{1/2,1/2}(z) = \sqrt{z}\exp(-z/2)\left(1+\frac{1}{4z}-\frac{3}{32z^2}+\frac{15}{128z^3}-\frac{525}{2048z^4}\dots\right) \tag{3.16}$$

The weighting function for three dimensionless times $t_D = 10^2$, 10^3 and 10^4 are shown in Figure 3.4. This weighting function specifies the relative contribution of permeability of various regions to the effective permeability at a given time. Based on the weighting function, for a given time t_D, an annular region that influences effective permeability estimate can be determined, for example an annular region $V(t_D)$ can be selected that includes 98% of the contribution with an inner radius $r_{D\,\min} = 0.12\sqrt{t_D}$ and an outer radius $r_{D\,\max} = 2.34\sqrt{t_D}$ (see Figure 3.5). It is considered that the permeabilities outside this annular region do not contribute to the estimation of effective permeability.

Oliver's analytical solution clearly defines the time-dependent reservoir volume informed by the effective permeability for a given time. As the time increases, the radii and the volume of the annular region increase. The main assumptions behind the analytical expression of Oliver [138] are that permeability variation is small about its mean, permeability is hydraulically and spatially isotropic, and ideal radial flow conditions exist around the well.

In general, these assumptions are not met. Therefore, the actual volume of investigation is not defined. Nevertheless, calibration of a scaling parameter (A) that accounts for any deviations of reality from the assumptions, should be done. This parameter is defined by the following equation.

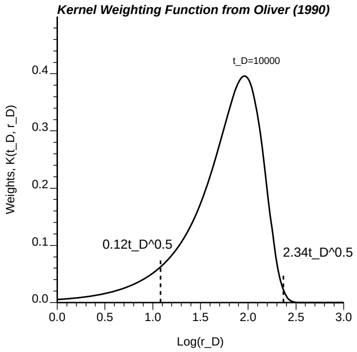

Figure 3.5: Defination of the inner and outer radii of a annular region based on the weighting function of Oliver [138].

$$t_D = A \cdot \frac{0.000264 k_e t}{\phi \mu c_t r_w^2} \tag{3.17}$$

where, the parameter A is different from the parameter A defined in Equation 3.9, although both are used to define the volume of averaging. Parameter A in Equation 3.17 serves as a scaling factor to shift the annular region at a given time defined by the kernel weighting function (Equation 3.14).

3.5.2 Type of Averaging

Type of averaging must also be defined along with volume of averaging to calculate the effective permeability. The averaging process within the annular region, $V(t_D)$, depends on the details of reservoir heterogeneity. Studies indicate that simple averages such as arithmetic, geometric, harmonic, or geometric (in θ)-harmonic (radially) averages are not applicable. The power average by Journel et al. [110] and Deutsch [54] expressed in Equation 3.11, is used in this approach.

The power parameter ω defines the type of averaging. This can be calibrated by forward flow simulation. Studies have shown that the value of ω depends on the "nature" of the heterogeneity such as spatial variation patterns and anisotropy, and it is quite robust [54, 55, 56].

3.5.3 Example calibration

The detailed calibration procedure for A and ω is demonstrated using the following synthetic example. The permeability field for this example is shown in Figure 3.6. A low permeability ring of 6 md is embedded in an otherwise homogeneous permeability field of 30 md. Size of the field is 2020 ft × 2020 ft, which is discretized into 101 × 101 cells of dimension 20 ft × 20 ft. Width of the low permeability ring is 20 ft or one cell and its inner radius is 140 ft. The well is located at the center of the ring, also the center of the field, with a constant flow rate of $q = 10$ STB/day. Other related parameters are constant: $\phi = 0.2$, $h = 10$ ft, $\mu = 0.3$ cp, $r_w = 0.33$ ft, $B = 1.4$ and $c_t = 5 \times 10^{-6}$ 1/psi.

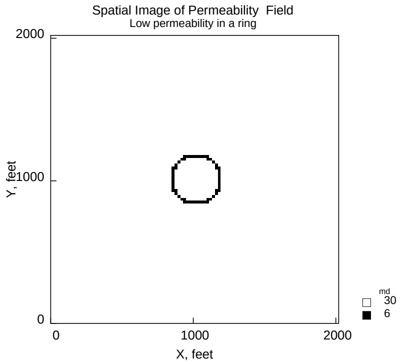

Figure 3.6: A low permeability ring embedded in a homogeneous permeability field

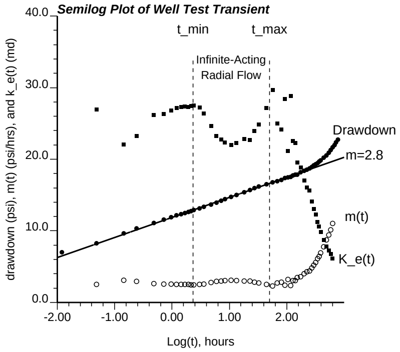

Figure 3.7: Semilog plot of well test transient pressure data performed in the permeability field shown in Figure 3.6

The well test is simulated using *Eclipse* with no-flow boundaries. Figure 3.7 shows the semilog plot of pressure drawdown ($\triangle p$), derivative of pressure drawdown ($\frac{d\triangle p}{d\log(t)}$), and the corresponding effective permeabilities (k_e). The pressure transient data within the time interval [$t_{\min} = 2.24$ hrs, $t_{\max} = 50.12$ hrs] are used for calibration for the infinite acting flow region. Effective permeability values are computed at some (14) points within this interval. The variation of effective permeabilities reflect the radial variation in the permeability field, which is smoothed by the weighting kernel. This information helps in identifying the location of the low permeability ring. If a single straight line is fitted for the pressure transient data as in traditional well test analysis, a slope of 2.8 (see Figure 3.7), hence a single effective permeability of 24.3 md is obtained. However, this single effective permeability does not give any indication of the radial variation of the permeability field.

Figure 3.8 shows the arithmetic, geometric, and harmonic averages of permeability within the annular regions defined by the weighting kernel. None of these simple averages matches the well test-derived effective permeabilities, although their variation patterns are similar. The correct type of averaging seems to be between the geometric and harmonic averages.

Based on the well test-derived effective permeabilities within the selected time interval, $k_e(t_i)$, $i = 1, \ldots, N_t$ ($N_t = 14$ in this example), the calibration procedure for A and ω is as follows:

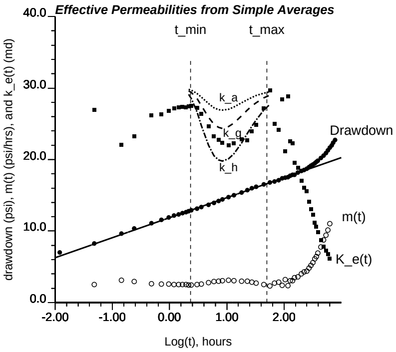

Figure 3.8: Comparison of the well test-derived effective permeabilities with simple average results

1. A number of (A, ω) pairs are selected and the radii of each annular region computed according to A. Then, power average permeabilities $\overline{k}(A,\omega)_i$, $i = 1, \ldots, N_t$ are computed using permeability values in the annular region of each time, weighted by the weighting function. For instance, $Log(A)$ increments of 0.05 and ω increments of 0.05 can be chosen for the calibration.

2. The mean normalized absolute deviation ($mNAD$, which measures correlation) and the mean normalized error (mNE, which measures bias) are computed as the following (Alabert, 1989; Deutsch, 1992):

$$mNAD(A,\omega) = \frac{1}{N_t} \sum_{i=1}^{N_t} \frac{\left|\overline{k}(A,\omega)_i - k_e(t_i)\right|}{k_e(t_i)} \tag{3.18}$$

$$mNE(A,\omega) = \left| \frac{\sum_{i=1}^{N_t} \overline{k}(A,\omega)_i - \sum_{i=1}^{N_t} k_e(t_i)}{\sum_{i=1}^{N_t} k_e(t_i)} \right| \tag{3.19}$$

3. A pair (A_{opt}, ω_{opt}) is selected that jointly minimizes the values of $mNAD$ and mNE.

Experience shows that the range of $Log(A)$ is from -0.5 to 0.5. Figure 3.9 shows the gray level maps of $mNAD$ and mNE for values $Log(A)$ ranging from -0.5 to 0.35 and values ω ranging from -1 to 1. The optimal pair $Log(A_{opt}) = -0.05$ and $\omega_{opt} = -0.8$ jointly minimizes both error terms.

The quality of the weighted power averages can be judged by plotting the average permeabilities with well test-derived effective permeabilities (see Figure 3.10). It is shown that the weighting power averages match the well test-derived effective permeabilities with a 0.95 correlation coefficient. The calibrated optimal power $\omega = -0.8$ indicates that the type of averaging is close to harmonic average, which makes sense for this particular example where the heterogeneity is caused by a ring. Also, considering the type of heterogeneity cited in this example, in which the weighted average is very sensitive to the volume of averaging, the agreement between the average permeabilities and the well test-derived effective permeabilities is quite good.

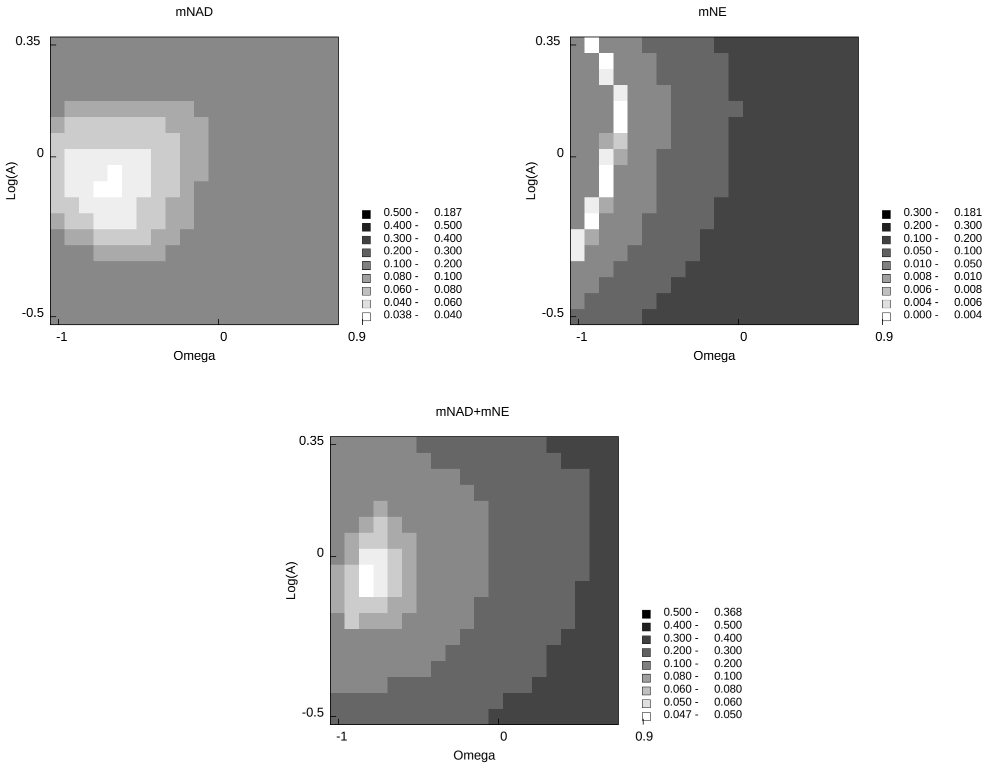

Figure 3.9: Gray level maps of the Calibration errors for $Log(A)$ ranging from -0.5 to 0.35 and ω ranging from -1 to 0.9.

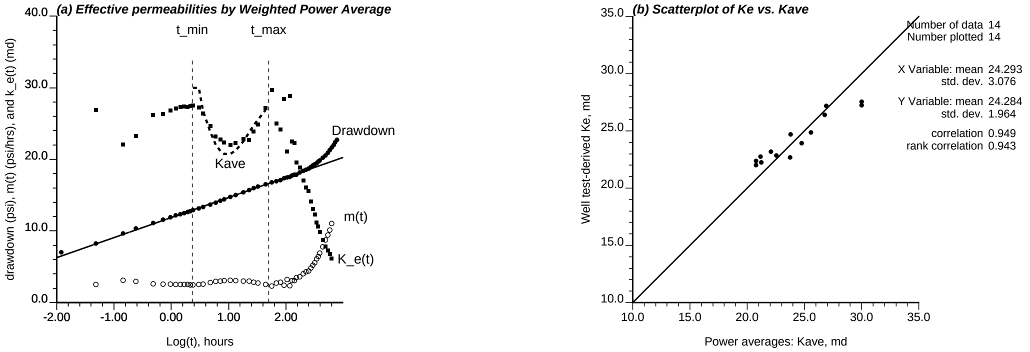

Figure 3.10: Comparison of well test-derived effective permeabilities and weighted power averages using the calibrated parameters $Log(A_{opt})$ and ω_{opt}.

3.6 Implementation Issues

This section discusses a number of implementation issues and documents more applications in realistic heterogeneous permeability fields.

3.6.1 Spatial Discretization

Calibration of the parameters A and ω requires forward flow simulation. Spatial and time discretizations are needed for numerical flow simulation, and there exist numerical errors in simulation due to these discretizations. In general, early time well test responses from numerical simulation are unreliable. Local refinement around the well location can improve the early time results. Notwithstanding the ability to refine the grid, in practice, early time pressure transient data of a given well test are usually associated with wellbore storage and skin effects. Thus, "clean" early time data are difficult to acquire in reality. A common practice in well test analysis is to disregard the early time data. A guideline will be established to determine the early time limit after which results are not affected by numerical errors.

To determine this early time limit, a numerical experiment is performed in a 2D square domain with size of 2020 ft × 2020 ft and a constant permeability of 30 md. This domain is discretized with different levels ranging from 31×31 cells to 161×161 cells with cell sizes ranging from $\triangle x = \triangle y = 65.2$ ft to 12.5 ft. A well test is performed at a well located at the center of the domain with a constant flow rate $q = 10$ STB/day. *Eclipse* [101] is used to calculate the pressure transient at the wellbore without grid refinement. Other reservoir parameters are: $\phi = 0.2$, $h = 10$ ft, $\mu = 0.3$ cp, $r_w = 0.33$ ft, $B = 1.4$, $c_t = 5 \times 10^{-6}$ 1/psi.

Figure 3.11 shows the semilog plots of results from the numerical simulations using different discretization levels. Because permeability is constant within the domain, the effective permeabilities computed from the numerical results should reproduce the constant permeability of 30 md. Apparently, due to numerical errors, early time results are not correct. Increasing the level of spatial discretization reduces the value of the earliest time $t_{\min}$ when the effective permeability reaches 30 md. Figure 3.12 shows the relationship between square of dimensionless cell size ($r_D = \triangle x / r_w$) and dimensionless early time limit $t_{D\min}$. It is apparent that $t_{D\min}$ increases exponentially with the dimensionless cell size. This implies that the local refinement may be of little help in improving the numerical well test pressure solutions.

Another issue in the numerical well test simulation is the late time effects due to the limited size of the simulation domain. Boundary effects should not be used in the calibration. Increasing the size of the simulation domain increases the time range for reliable calibration. A numerical experiment is also carried out to establish guidelines for the selection of late time limits.

Using a fixed cell size of $\triangle x = \triangle y = 20$ ft, the number of cells used in this experiment ranges from 31×31 to 161×161 resulting in the size of the simulation domain ranging from 620 ft × 620 ft to 3220 ft × 3220 ft. Well test is performed at the center of the domain with the same conditions as in the previous experiment. Figure 3.13 shows the semilog plots of simulated well test results using different sizes of domain. Clearly, increasing the domain size increases the late time limit ($t_{\max}$). Figure 3.14 shows the relation between the

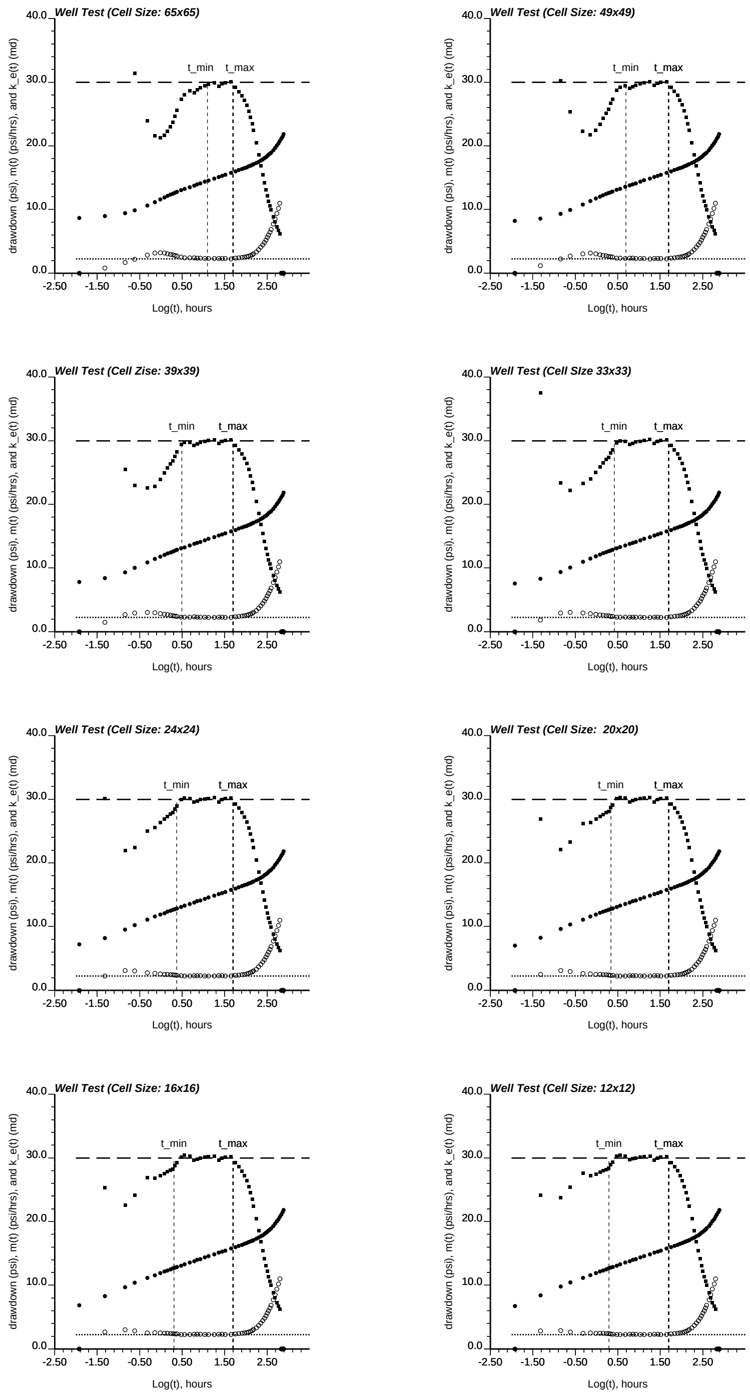

Figure 3.11: Semilog plots of well test results in a given domain using different discretization levels.

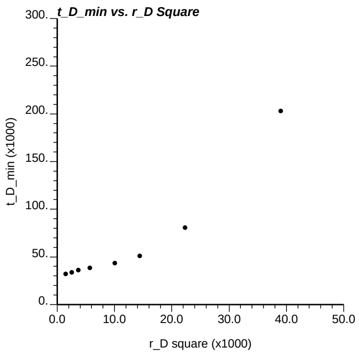

Figure 3.12: Relationship between the early time limit and the discretized cell size.

dimensionless late time limit ($t_{D\max}$) and the square of dimensionless half domain size (L_D^2, $L_D = L/r_w$ with L being the half domain size). It is approximately a straight line which is consistent with the traditional definition of radius of investigation as given in Equation 3.9.

For a given discretization level and a given size of domain in the numerical flow simulation, the time interval [$t_{\min}$, $t_{\max}$] can then be selected based on Figures 3.12 and 3.14. Figure 3.15 shows the weighting functions used for the time limits ($t_{\min} = 2.23$ hrs, $t_{\max} = 50.12$ hrs) for a 2020 ft × 2020 ft domain discretized by 20 ft × 20 ft grid. It should be noted that the radius of informed reservoir region at $t_{\max} = 50.12$ hrs is about one half of the domain size.

3.6.2 Anisotropy

Previous studies on integrating well test constraints mostly considered isotropic permeability field and a circular annular region as the volume of averaging [2, 55, 163, 164]. It is suggested here to use the same circular annular volume of averaging, calibrated by the above procedure, for permeability fields with moderate anisotropy ratio (say $< 10 : 1$). Here, "anisotropy" refers to the spatial variation of permeability. Whereas the permeability values at a given location is assumed directionally independent, that is, hydraulically isotropic.

An elliptical annular volume, oriented in the same direction as that of the permeability and with the same anisotropy ratio, could also be considered. However, this implicitly assumes that pressure "diffusion" due to well test has the same anisotropy. This concept was found inappropriate since pressure "diffusion" in anisotropic permeability fields appears more isotropic.

Figures 3.16 and 3.17 give two sets of permeability fields and corresponding pressure distributions at selected times. The anisotropy ratio of the permeability field (λ_1/λ_2) ranges from 1 to 10, λ_1 being the correlation length of maximum continuity ($-30°$ from the x-axis), λ_2 being the correlation length of minimum continuity ($60°$ from the x-axis). From these figures, it can be seen that pressure diffusion has much weaker anisotropy than the permeability. Ideally, an anisotropy ratio corresponding to the pressure anisotropy should be used for calibrating the averaging volume. However, there is no easy way to estimate pressure anisotropy from permeability anisotropy. Furthermore, pressure anisotropy may

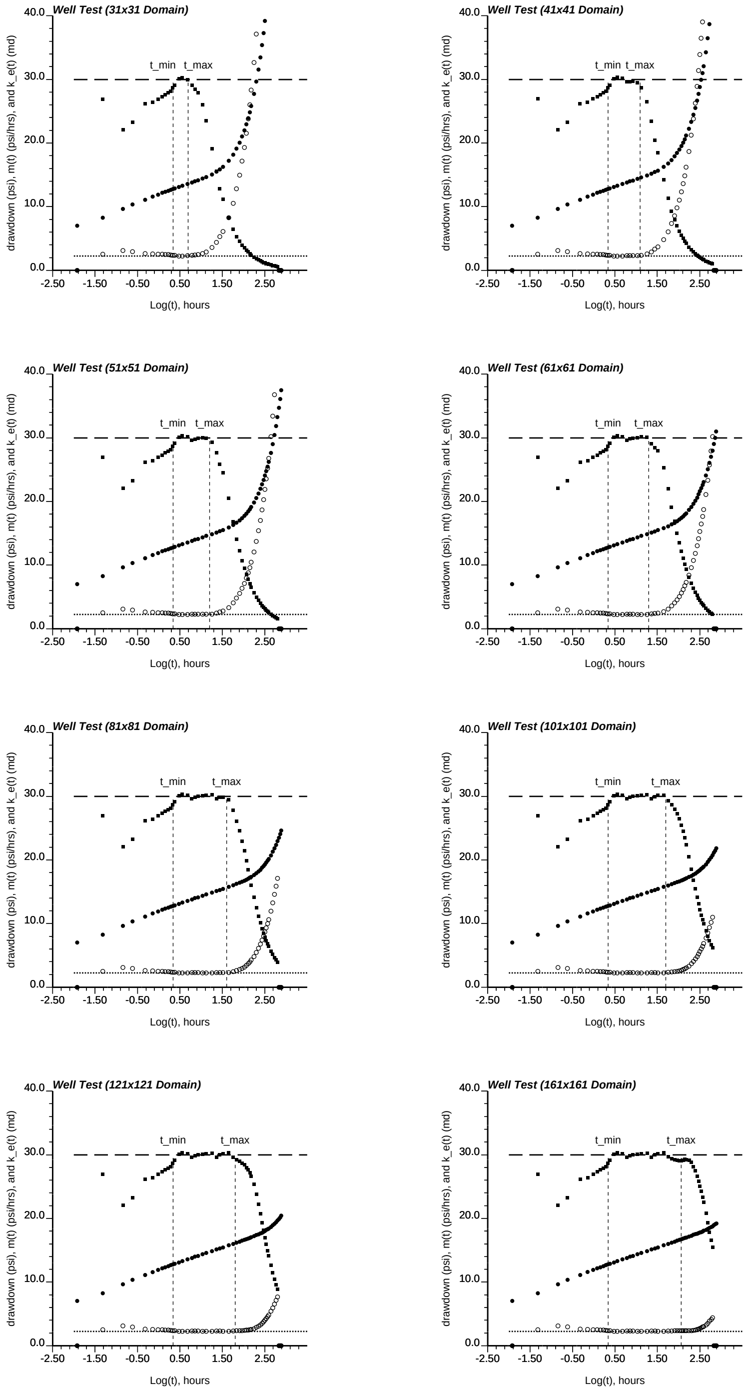

Well Test (31x31 Domain)

Well Test (41x41 Domain)

Well Test (51x51 Domain)

Well Test (61x61 Domain)

Well Test (81x81 Domain)

Well Test (101x101 Domain)

Well Test (121x121 Domain)

Well Test (161x161 Domain)

Figure 3.13: Semilog plots of well test results using different domain size with a fixed discretized cell size.

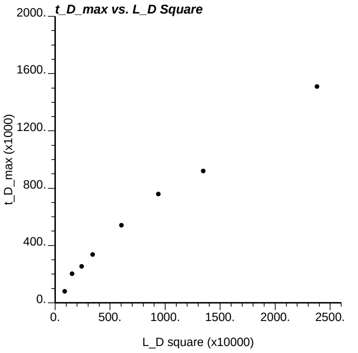

Figure 3.14: Relationship between the late time limit and the domain size.

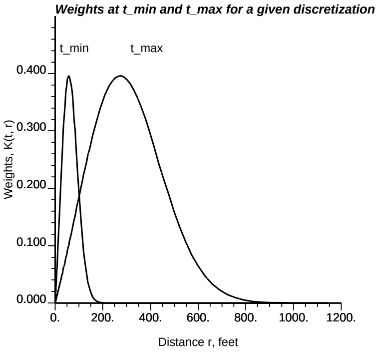

Figure 3.15: Weighting functions for the early time and late time limits for a 2020 ft × 2020 ft domain discretized by 20 ft × 20 ft square cell.

change with time. Therefore, an isotropic averaging volume is chosen even when the permeability field is anisotropic. This approximation appears appropriate when the permeability anisotropy ratio is less than 10:1 as shown in Figures 3.16 and 3.17.

To demonstrate this further, an example is given next to show the calibration quality of well test-derived effective permeability in an anisotropic field using isotropic and anisotropic averaging volumes. Figure 3.18 shows a 2020 ft × 2020 ft square domain which is discretized into 101×101 cells by a 20 ft × 20 ft square grid. The anisotropy ratio in this synthetic field is 5:1 with the direction of maximum continuity being -30° from the x-axis.

A well test at the center of the domain provides the semilog plot of the pressure transient shown in Figure 3.19. The constant flow rate used in the well test is: $q = 10$ STB/d, other parameters are: $\phi = 0.2$, $h = 10$ ft, $\mu = 0.3$ cp, $r_w = 0.33$ ft, $B = 1.4$, $c_t = 5 \times 10^{-6}$ 1/psi. The well test-derived effective permeabilities, within the selected time interval, indicate increase and then decrease of permeability in the radial direction as the test duration increases (see Figure 3.18).

In order to approximate the well test-derived effective permeabilities using weighted power averages, the volume of averaging (A) and the type of averaging (ω) are calibrated as discussed in Section 3.5. Two types of averaging volumes are used for comparison: an elliptical annular volume and a circular annular volume. Figure 3.20 shows the weighting functions at time $t = 13.2$ hrs. The averaging volume in Figure 3.20a has the same anisotropy ratio as the permeability anisotropy ($5 : 1$) and is oriented to the same direction as the permeability anisotropy (-30° from the x-axis). Figures 3.21 and 3.22 show the gray maps of errors ($mNAD$ and mNE) using different values of (A, ω) and different averaging volumes. The optimal pairs obtained are $Log(A_{opt}) = 0.25$, $\omega_{opt} = 0.2$ using elliptical volume, and $Log(A_{opt}) = 0.3$, $\omega_{opt} = 0.3$ using circular volume.

The quality of calibration can be seen from Figures 3.23 and 3.24 which show the comparisons and scatterplots of well test-derived effective permeabilities and the corresponding weighted power averages based on the parameters calibrated using two types of averaging volume. Clearly, better calibration results are obtained by using circular averaging volume ($\rho = 0.9$) than elliptical volume ($\rho = 0.7$). This encourages the use of isotropic averaging volumes.

As indicated in Figures 3.16 and 3.17, pressure “diffusion” is less anisotropic than permeability. From the pressure distributions at different times, shown in Figure 3.25, it appears that anisotropy ratio of $2 : 1$ is appropriate for the pressure “diffusion” in this field. So, an elliptical volume with a $2 : 1$ anisotropy ratio was tried to calibrate the effective permeabilities, resulting in an optimal pair of parameters: $Log(A_{opt}) = 0.45$, $\omega_{opt} = 0.2$. Figure 3.26 shows the values of the weighting function at time $t = 13.2$ hrs. The weighted average values of permeability using this anisotropic averaging volume and the calibrated parameters are compared with the well test-derived effective permeabilities in Figure 3.27. Better approximations are obtained ($\rho = 0.96$). However, in practice, information on the pressure anisotropy is usually not available.

3.6.3 3D versus 2D

3D reservoir models are usually required for reservoir simulation. Applicability of this approach to 3D models is demonstrated in this section through an example, and the results

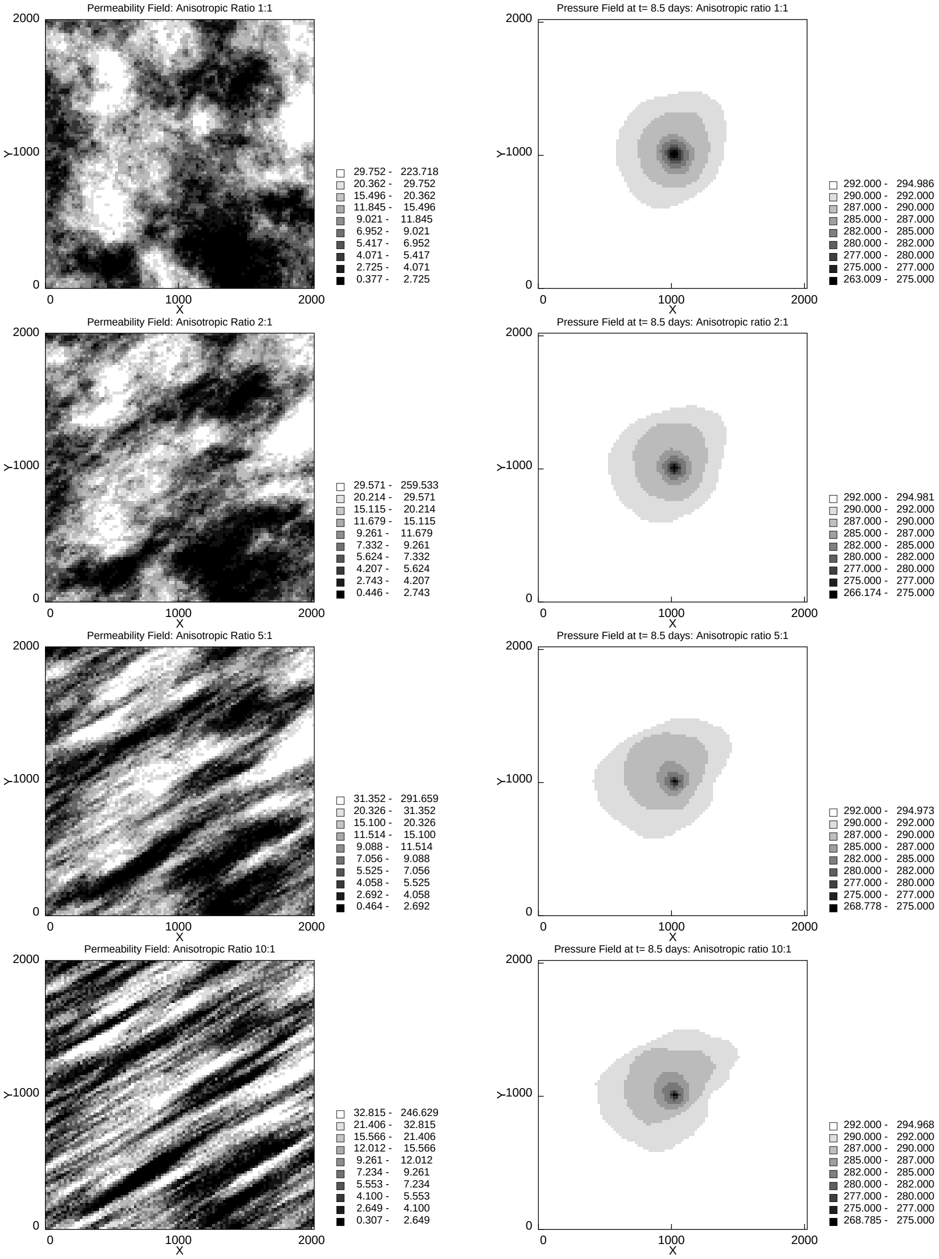

Figure 3.16: Permeability fields and the corresponding pressure distributions due to a well test at time $t = 8.5$ days. The permeability anisotropy varies from 1:1 to 10:1 from the top to the bottom: the first set.

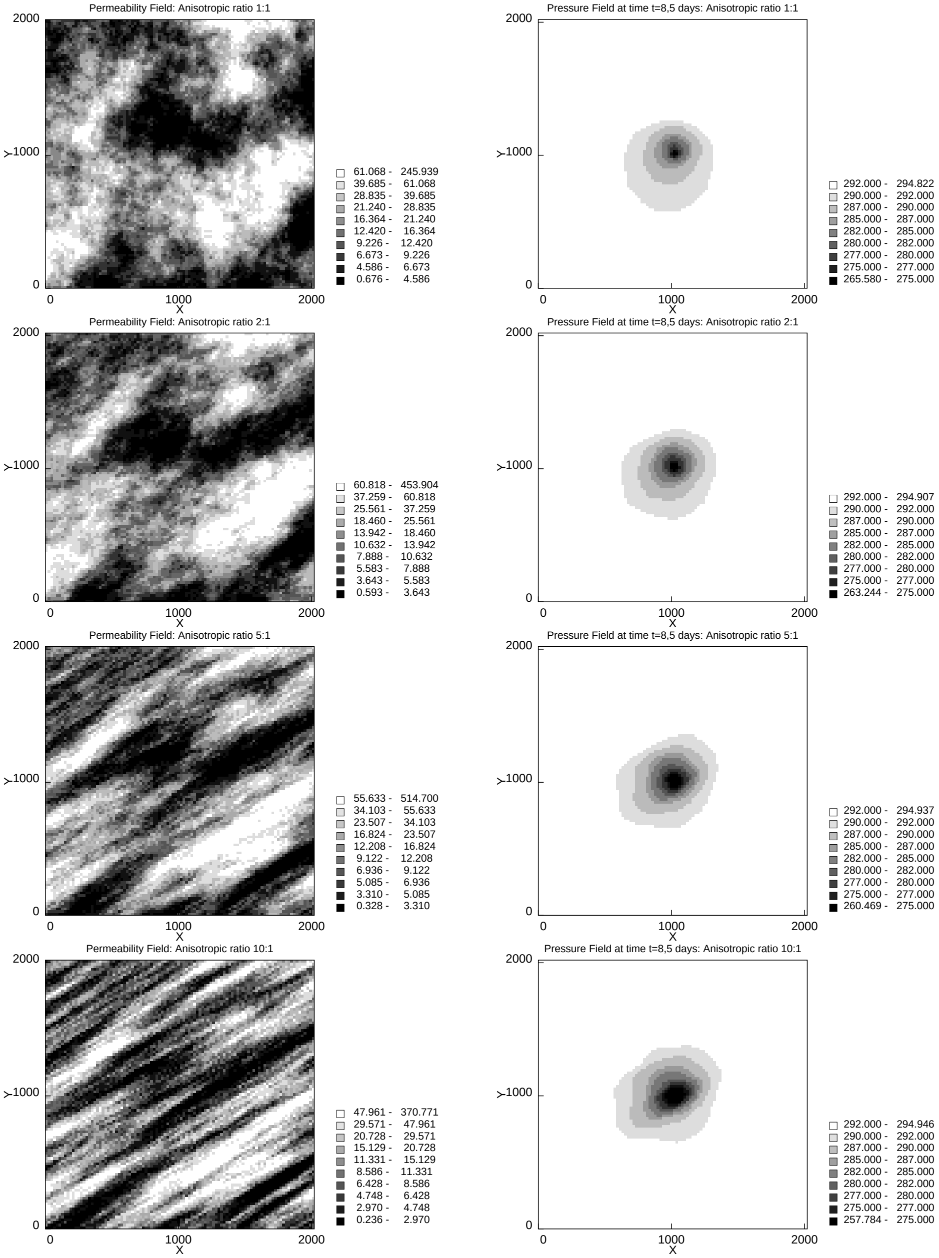

Figure 3.17: Permeability fields and the corresponding pressure distributions due to a well test at time $t = 8.5$ days. The permeability anisotropy varies from 1:1 to 10:1 from the top to the bottom: the second set.

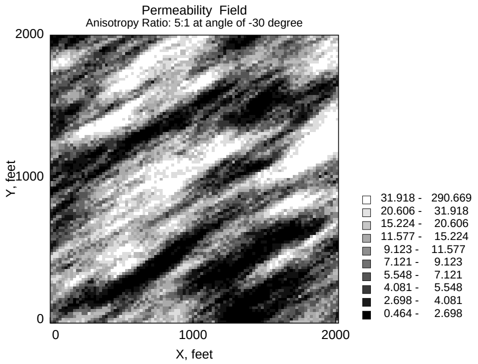

Figure 3.18: A heterogeneous permeability field with anisotropic spatial variation patterns.

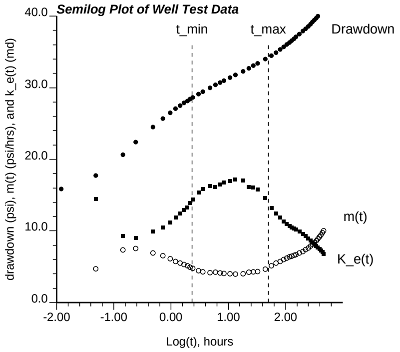

Figure 3.19: The semilog plot of well test data performed in the anisotropic permeability field shown in Figure 3.18.

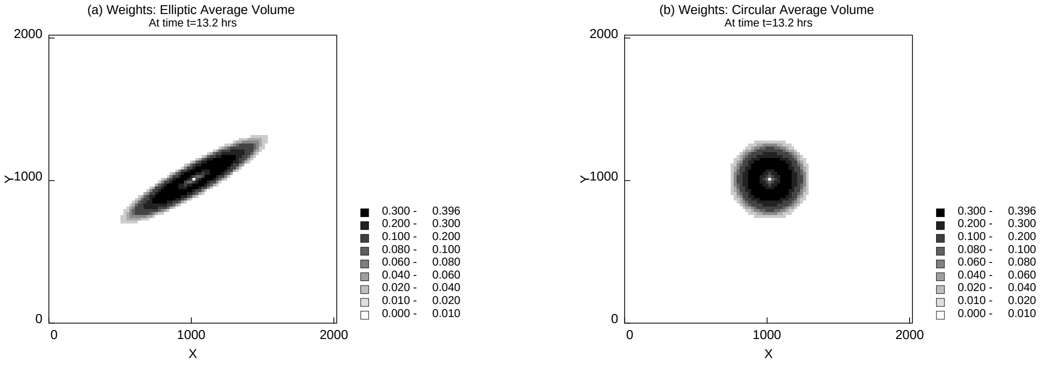

Figure 3.20: The weighting functions corresponding to an elliptical annular volume and a circular annular volume at time $t = 13.2$ hours.

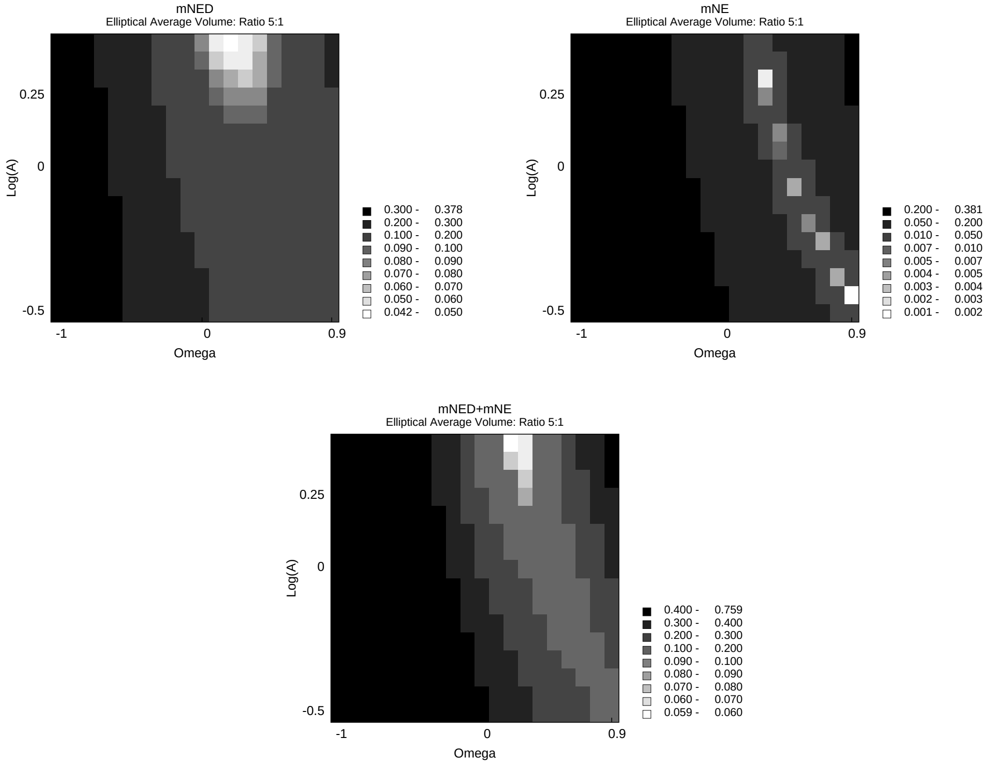

Figure 3.21: Gray level maps of calibrated error terms using different values of parameters $Log(A)$ and ω: Elliptical average volume.

compared with those of 2D models.

Figure 3.28 shows a 3D permeability field in a 1830 ft × 1830 ft × 10 ft domain which is synthetically generated by sequential Gaussian simulation method (Deutsch and Journel, [61]). The domain is discretized into 61 × 61 × 8 cells with the size of each cell being 30 ft × 30 ft × 1.25 ft. The correlation lengths used to generate this permeability field are: $\lambda_x = 900$ ft, $\lambda_y = 300$ ft, and $\lambda_z = 2.5$ ft. A well test at the center of the domain is performed with a constant flow rate $q = 10$ STB/d. The well is perforated over the entire thickness of the reservoir. Figure 3.29a displays the semilog plot of the well test results computed by *Eclipse*. Other parameters used are $\phi = 0.2$, $\mu = 0.3$ cp, $r_w = 0.33$ ft, $B = 1.4$, and $c_t = 5 \times 10^{-6}$ 1/psi.

The optimal pair of parameters (A, ω) are calibrated using a annular cylindrical volume of averaging centered at the wellbore, that is, the same weight is used for all cells with the same radial distance from the wellbore. These optimal parameters, minimizing $mNAD$ and mNE, are $Log(A_{opt}) = 0.2$ and $\omega_{opt} = 0.7$. The scatterplot of the weighted power average approximation and the true well test-derived effective permeabilities reveals an excellent correlation ($\rho = 0.98$) (see Figure 3.29b).

Permeability values in the above 3D model are averaged in vertical direction to obtain a 2D permeability model as shown in Figure 3.30. Figure 3.31 shows the semilog plot of well test data performed at the center of the model with the same conditions as used in the 3D model. Results in Figures 3.29a and 3.31a are quite similar, indicating a nearly 2D radial flow pattern in the 3D model. The optimal parameters calibrated using circular annular

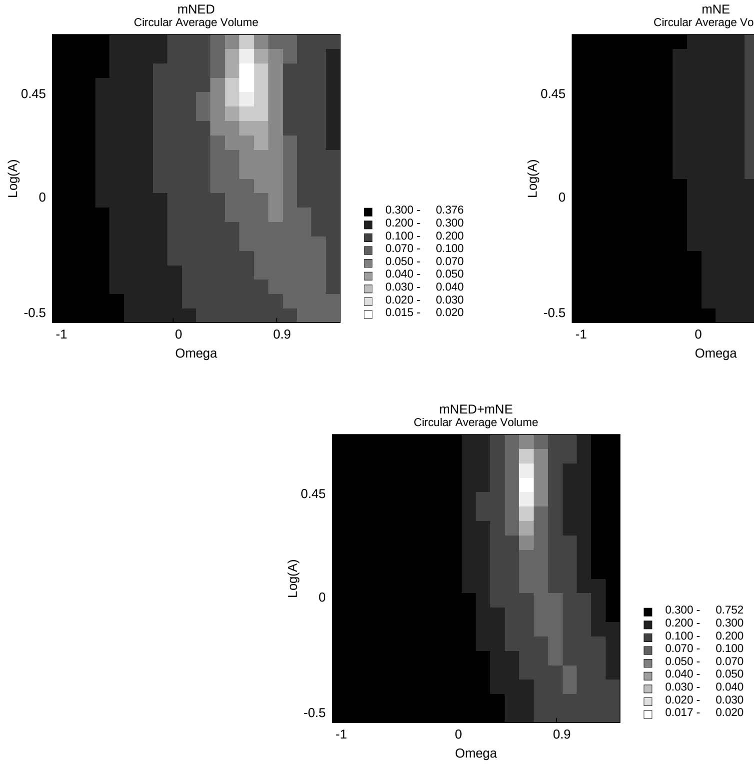

Figure 3.22: Gray level maps of calibrated error terms using different values of parameters $Log(A)$ and ω: Circular average volume.

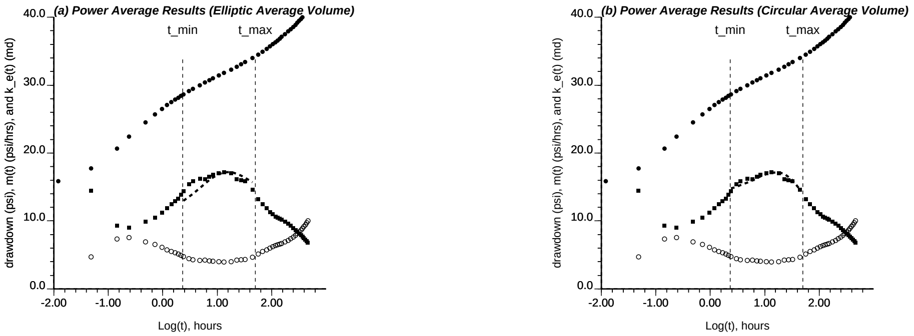

Figure 3.23: Comparisons of the well test-derived effective permeabilities and the weighted power averages using different types of average volumes.

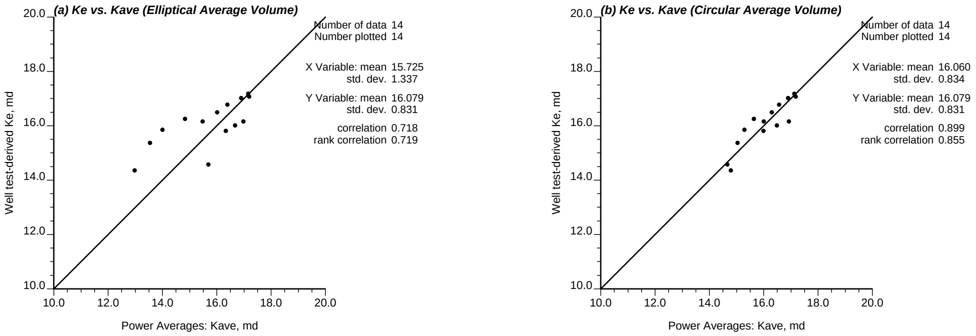

Figure 3.24: Scatterplots of the well test-derived effective permeabilities and the weighted power averages using different types of average volumes.

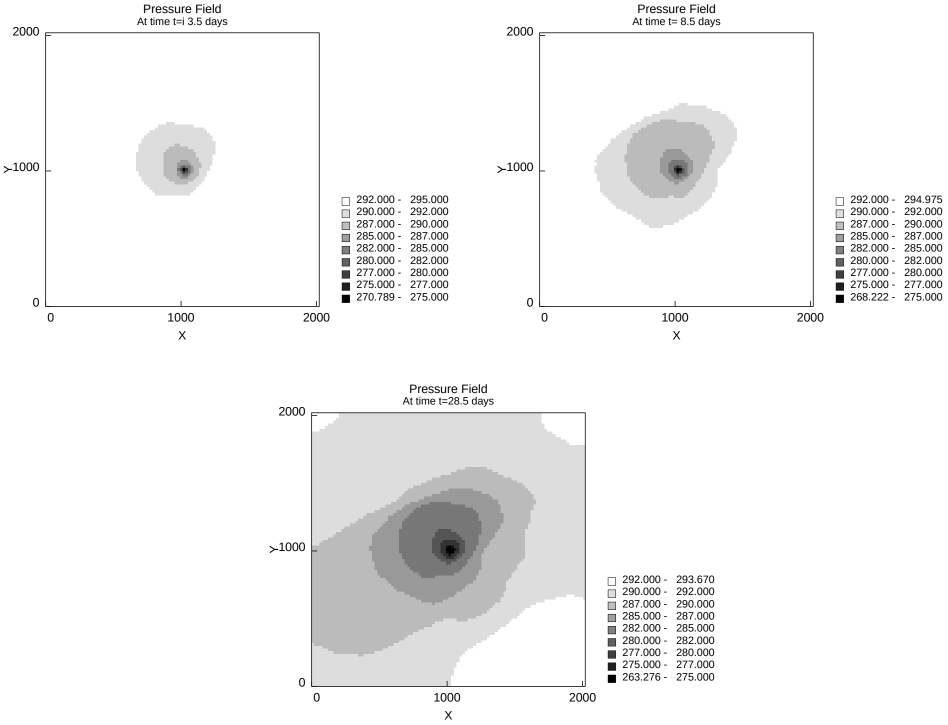

Figure 3.25: Pressure distributions due to the well test at different times.

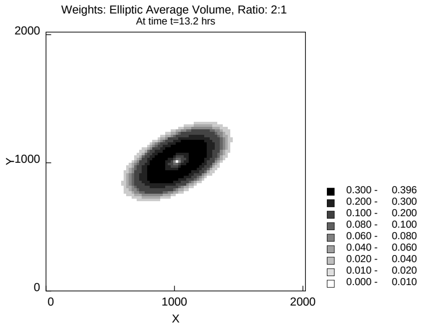

Figure 3.26: Weighting function at time $t = 13.2$ hours using an elliptic average volume with anisotropy ratio 2:1.

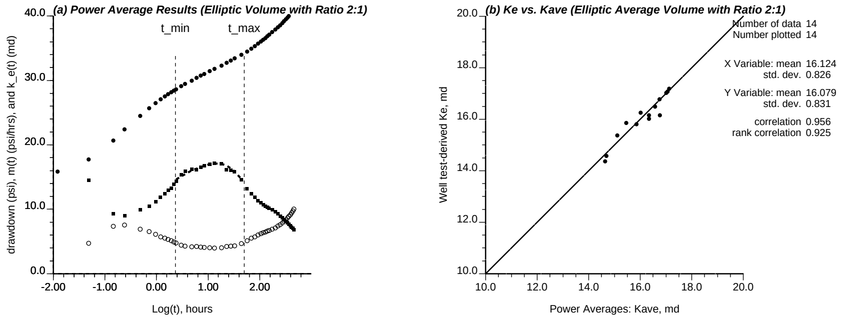

Figure 3.27: Comparisons of well test-derived effective permeabilities and the weighted power averages using the calibrated parameters.

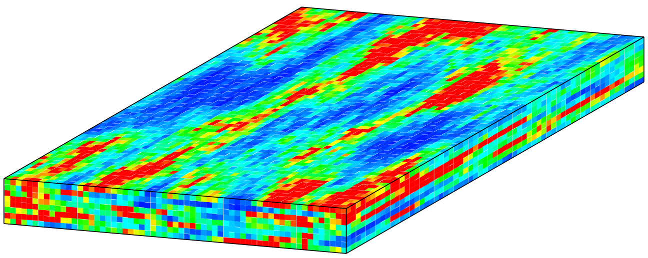

Figure 3.28: A 3D heterogeneous permeability field.

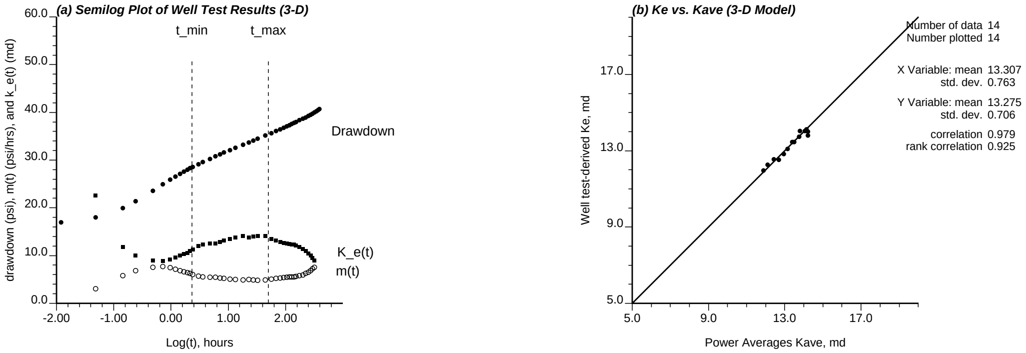

Figure 3.29: Semilog plot of well test result and scatterplot of well test-derived effective permeabilities with weighted power averages for the 3D permeability shown in Figure 3.28.

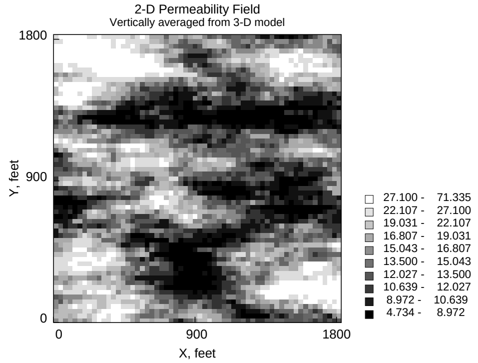

Figure 3.30: The 2D permeability field obtained by vartically averaging the 3D field shown in Figure 3.28.

volume of average are: $Log(A_{opt}) = 0.15$, $\omega_{opt} = -0.7$. The scatterplot of the weighted power average approximation and the true well test-derived effective permeabilities is given in Figure 3.31b. An excellent correlation coefficient value of 0.982 is obtained, which is even better than that of the 3D model.

Essentially, these results indicate that the calibration works well for 3D models. Parameter A seems to be almost similar for both 2D and 3D models. While parameter ω is higher in 3D models than in 2D models, which is consistent with the study of Noetinger and Haas [137]. Thus in 3D, the type of averaging is closer to arithmetic averaging, whereas in 2D, it is closer to harmonic. The higher ω values for 3D may be explained by the fact that in 3D flow toward the wellbore has more freedom than in 2D.

Multiple Realizations to Calibrate Parameters A and ω

In the above examples, synthetic permeability fields are used where permeability values are known exhaustively to calibrate optimal parameters (A_{opt}, ω_{opt}), so that the weighted power averages best approximate the well test-derived effective permeabilities. In practice, however, there is no access to the exhaustive permeability field. Only the pressure transient

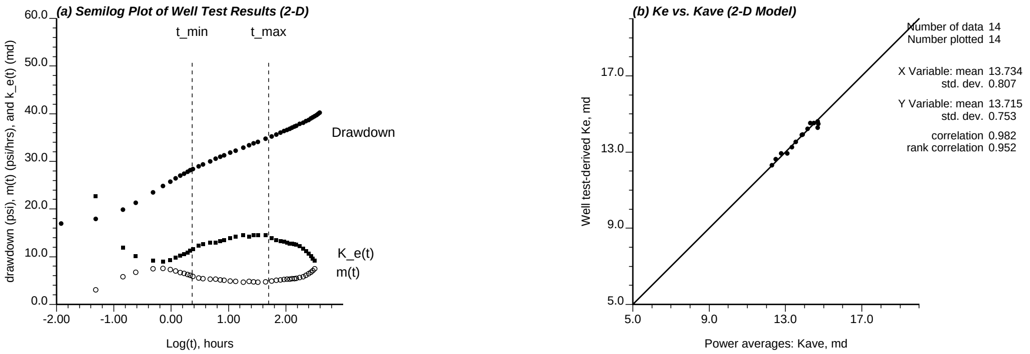

Figure 3.31: Semilog plot of well test result and scatterplot of well test-derived effective permeabilities with weighted power averages for the 2D permeability shown in Figure 3.30.

data and some knowledge about the "nature" of heterogeneity in the reservoir system are available.

One way to solve this problem is to calibrate the parameters (A, ω) by repeated Monte-Carlo flow simulation [2, 55]. First, multiple realizations of the permeability field are generated with relevant statistical properties. Next with conditions as close as to those used in the field, the well test is simulated in each realization to obtain effective permeabilities. Thus for each realization, available are the exhaustive permeability values and the corresponding well test-derived effective permeabilities, $k_e(i,j)$, $i = 1, \ldots, L$ and $j = 1, \ldots, N_t$. Here, L and N_t are the realization number and the number of time-dependent effective permeabilities, respectively. Finally, using the simulated effective permeabilities from the whole set of realizations, a pair of optimal parameters (A_{opt}, ω_{opt}) can be calibrated following the same procedure as in Section 3.5.

An important issue related to the above calibration procedure is the sensitivity of parameters A and ω to different realizations with the same heterogeneous features, that is, the robustness of the optimal parameters. To test this, two sets of 20 permeability realizations are generated with different spatial variation features: set A is isotropic with correlation lengths = 900 ft, set B is anisotropic with maximum correlation length 1500 ft in the direction of -30° and minimum correlation length 300 ft in the direction of 60°. The domain sizes in both cases are 2020 ft × 2020 ft, which are discretized into 101 × 101 cells with the size of each cell being 20 ft × 20 ft. Figure 3.32 shows 4 realizations from each set. The permeability value at the center of the field is fixed at 12.5 md in all realizations.

A well test with constant flow rate $q = 10$ STB/d is simulated on each realization of permeability, and an optimal parameter pair (A_{opt}, ω_{opt}) is calibrated for each realization. Figure 3.33 shows the histograms of 20 optimal A's and ω's from 20 permeability fields. The values of $Log(A_{opt})$ calibrated from individual realizations range from -0.4 to 0.4, whereas the values of ω_{opt} vary from -0.6 to 0.6.

A single pair of parameters (A_{opt}, ω_{opt}) is established for the two sets from the multiple (20) realizations. The resulting optimal parameters are $Log(A_{opt}) = 0.0$, $\omega_{opt} = -0.1$ for set A, and $Log(A_{opt}) = -0.1$, $\omega_{opt} = 0.0$ for set B. The scatterplots of power average approximations and the simulated well test-derived effective permeabilities for all 20 real-

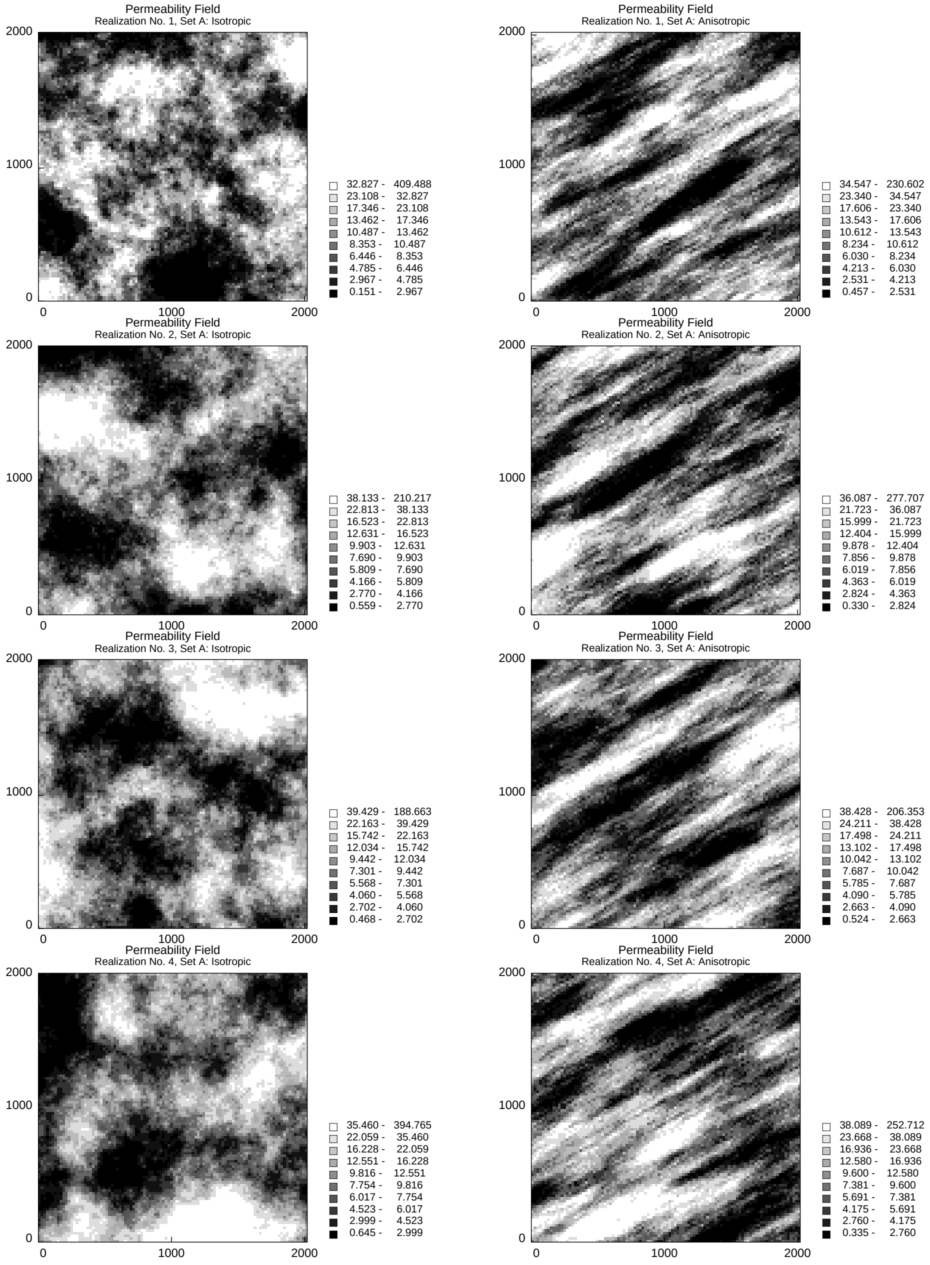

Figure 3.32: Four realizations of isotropic (set A) and anisotropic (set B) permeability fields.

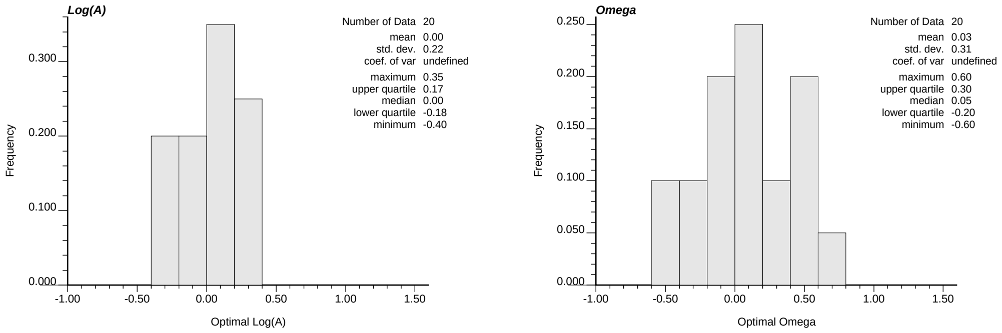

Figure 3.33: Histograms of calibrated parameters $Log(A)$ and ω from 20 realizations of isotropic (set A) and anisotropic (set B) permeability fields.

izations of both permeability sets are given in Figure 3.34. The effective permeabilities are unbiased and there is an excellent correlation values for both sets (> 0.93), implying that the optimal parameters calibrated from multiple realizations are quite robust and can be used to approximate the well test-derived effective permeabilities from any single realization. The average permeability values calculated using these parameters can be used to approximate the true well test-derived effective permeabilities. Also, the calibration quality in isotropic permeability fields (set A) is higher than in anisotropic fields (set B), indicating that the calibrated parameters may be more robust in isotropic permeability field than in anisotropic permeability fields.

In summary, it appears that the optimal parameters calibrated from multiple realizations are insensitive to the details of the realization and can be used to approximate the well test-derived effective permeabilities from any single realization. The parameter values ($A = 1.0$ and $\omega = 0.0$) seem to be fairly good first approximations for 2D isotropic or anisotropic permeability fields. The value of $\omega = 0.0$ corresponds to geometric average of permeability values within the time-dependent annular reservoir volume. It should be noted that this geometric average is different from geometric average of well permeability data. The quality of calibration in isotropic permeability fields appears better than in anisotropic fields, indicating the calibrated parameters to be more robust in isotropic permeability fields than in anisotropic permeability fields. This can be seen from the larger scatter in Figure 3.34b than in Figure 3.34a.

3.6.4 Calibration on Realistic Heterogeneities

A number of realistic, but synthetic, reservoir models are used here to illustrate the limitations and range of applicability of this approach.

Lithofacies control: carbonate reservoir analogue

Fluid flow in a carbonate reservoir is typically controlled by the lithology distribution. The variations of reservoir petrophysical properties within each lithofacies are relatively small. In this model, a 2D permeability field in a 2020 ft × 2020 ft square domain essentially

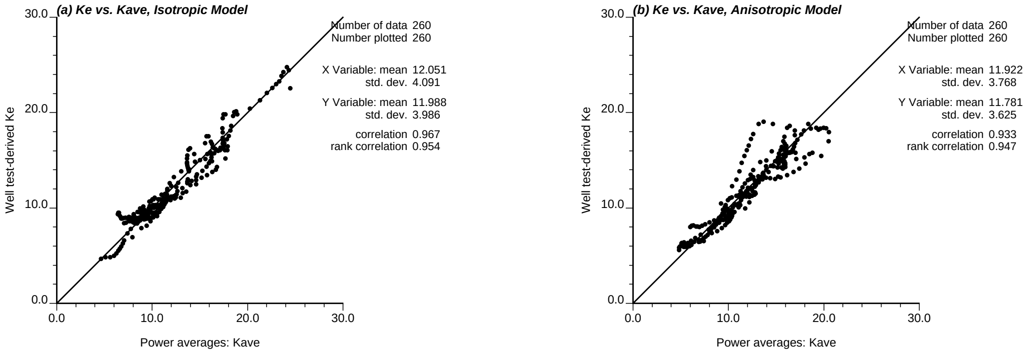

Figure 3.34: Scatterplots of the well test-derived effective permeabilities of 20 realizations and the weighted power averages using a single pair of optimal parameters $Log(A_{opt})$ and ω_{opt}, (a) isotropic field, (b) anisotropic field.

Facies	**1**	**2**	**3**	**4**
Proportion	0.15	0.35	0.35	0.15
Permeability, md	1	10	50	200
Porosity	0.15	0.20	0.25	0.30
Variogram type	Exp.	Exp.	Exp.	Exp.
Max. correlation length, ft	1600	160	160	1600
Min. correlation length , ft	40	80	80	40
Angle of max. continuity	-30	-90	-90	-30
Relative nugget effect	0.1	0.0	0.0	0.1

Table 3.1: Statistics and properties of four facies used to construct lithofacies model.

controlled by 4 lithofacies is considered. The statistics and properties of these 4 facies are listed in Table 3.1.

Based on the properties in Table 3.1, a lithofacies distribution model is generated using sequential indicator simulation [61]. Figure 3.35 shows the resulting lithofacies model. The petrophysical properties, i.e., permeability and porosity, of different facies are different, but constant within the same facies.

A well test performed at the center of the domain with a constant flow rate $q = 10$ STB/day is simulated using *Eclipse*. Figure 3.36 shows the semilog plot of the transient pressure data, the drawdown derivatives and the corresponding effective permeabilities. The well test-derived effective permeabilities in the time interval $[t_{\min} = 2.51 \text{ hrs}, t_{\max} = 100 \text{ hrs}]$ are used to calibrate the circular volume of averaging and the type of averaging, resulting in optimal parameter pair $Log(A_{opt}) = -0.4$, $\omega_{opt} = 0.0$.

The weighted power averages of permeability and the true well test-derived effective permeabilities are compared in Figure 3.36. Again, excellent approximations are obtained from weighted power averages using the calibrated parameters. This example also shows that the approach works when porosity is spatially variable, although this variability is ignored when calibrating the parameters.

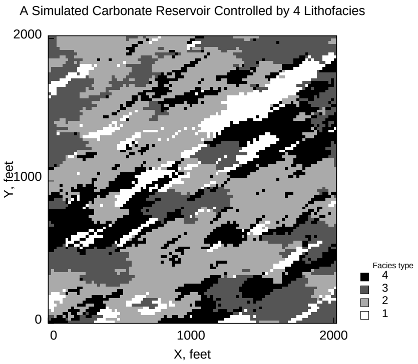

Figure 3.35: A synthetic carbonate reservoir analogue with 4 types of lithofacies.

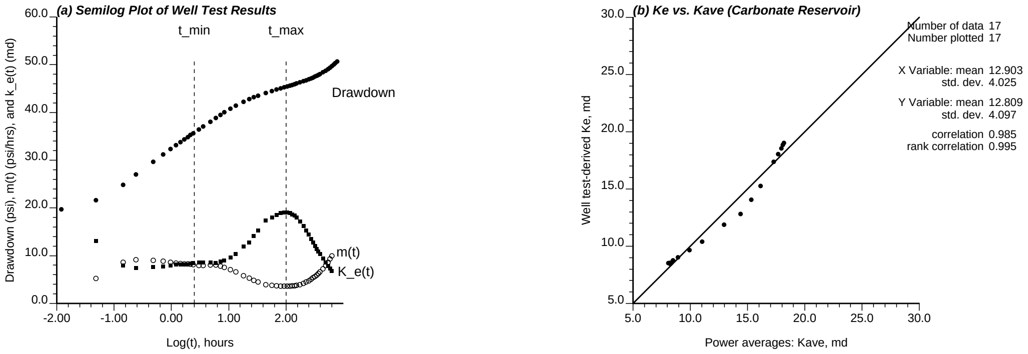

Figure 3.36: Semilog plot of well test result and scatterplot of well test-derived effective permeabilities with weighted power averages for the 2D carbonate reservoir model shown in Figure 3.35.

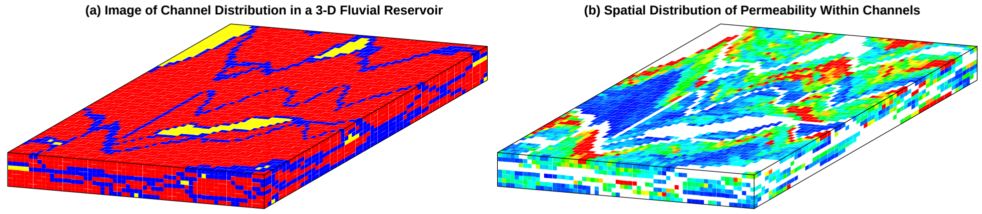

Figure 3.37: A 3D fluvial reservoir model constructed by a hierarchical object-based geostatistical method and the corresponding permeability distribution. In (a) channel is colored red, whereas shale is colored yellow. The bottom cell of every channel is colored blue. The permeability is color coded with blue being low permeability and red high permeability.

Fluvial Reservoir Analogue

Another typical reservoir is a braided stream fluvial reservoir. A characteristic feature of many fluvial reservoirs is the presence of sinuous sand-filled channels within a background of floodplain shale.

A 3D fluvial reservoir model is generated using a recently developed hierarchical object-based geostatistical method [62]. Figure 3.37 shows the resulting channel model and the permeability distribution with the channels. The size of the model is 61 × 61 × 8 with cell size of 30 ft × 30 ft × 1.25 ft. The spatial distribution of permeability within channels is generated using the sequential Gaussian simulation (`sgsim`, Deutsch and Journel [61]) with geometric mean 30 md and anisotropic spherical variogram (with correlation lengths 750 ft, 150 ft and 1.25 ft for $x-$, $y-$ and $z-$ directions, respectively). In this reservoir model, 86 % of the domain is filled by channels, whereas 14 % is filled by floodplain shale. The bottom cells of each channel (see Figure 3.37a) account for 28 % of the entire reservoir model. A very small permeability value (0.001 md) is assigned to all shale cells and a relatively small permeability value (0.1 md) is assigned to all bottom cells of the channels which account for the reduction of permeability between the channels and shale facies. The porosity is assumed constant within each facies: $\phi = 0.1$ for shale, $\phi = 0.15$ for bottom cells of channels, and $\phi = 0.2$ for channels.

A well test is performed at the center of the domain with a constant production rate $q = 10$ STB/day. The well is completed and perforated over the entire thickness of the reservoir. Other parameters used are $\mu = 0.3$ cp, $r_w = 0.33$ ft, $B = 1.4$, and $c_t = 5 \times 10^{-6}$ 1/psi. Figure 3.38a shows the semilog plot of the resulting pressure transient from the well test and the well test-derived effective permeabilities. The effective permeabilities decrease with time. The parameters for weighted power averaging are calibrated using pressure transient data within time interval $t_{min} = 3.16$ hours and $t_{max} = 39.8$ hours. Resulting optimal parameters are $Log(A_{opt}) = 0.0$ and $\omega_{opt} = 0.4$. Figure 3.38b shows the scatterplot of the well test-derived effective permeabilities and the weighted power averages computed by using the calibrated parameters. A good correlation is observed implying excellent calibration quality.

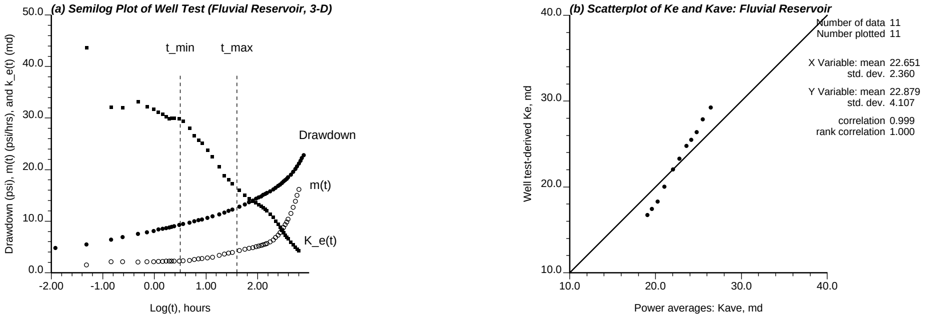

Figure 3.38: Semilog plot of well test result and scatterplot of well test-derived effective permeabilities with weighted power averages for fluvial reservoir model shown in Figure 3.37.

To test the applicability of the technique in low net-to-gross fluvial reservoirs, another fluvial reservoir model is constructed as shown in Figure 3.39. In this model, only 56 % of the field is filled by channels and 44 % by shale. The bottom cells of channels account for 24 % reservoir domain. This reservoir model shows clear linear features.

Again, a well test is performed at the center of the domain with a constant production rate $q = 10$ STB/day. Other parameters are kept same as in the previous example. Figure 3.40a shows the semilog plot of the resulting pressure transient from the well test and the well test-derived effective permeabilities. Linear flow behavior is observed in this figure due to the effects of channel distribution, that is, the pressure drawdown derivatives show two distinct relatively constant values: a smaller value at early time and a larger value at later time (see Horne [94]). The parameters for weighted power averaging are calibrated using pressure transient data within time interval $t_{min} = 3.16$ hours and $t_{max} = 39.8$ hours. Resulting optimal parameters are $Log(A_{opt}) = -0.1$ and $\omega_{opt} = 0.6$. Figure 3.38b shows the scatterplot of the well test-derived effective permeabilities and the weighted power averages computed by using the calibrated parameters. The match is poor. This indicates the weighted power averages using isotropic average volume fail to reproduce the well test-derived effective permeabilities when flow is strongly channelized into a small number of channels within a low-net-gross fluvial reservoir, that is, when strong linear flow condition prevails.

To improve the quality of calibration, an anisotropic (elliptical) average volume oriented at the same direction of the channel distribution is chosen with a anisotropy ratio of 5 : 1 for a new calibration. The resulting optimal parameters are $Log(A_{opt}) = 0.1$ $\omega_{opt} = 0.6$. The scatterplot of the well test-derived effective permeabilities and weighted power averages using the new calibrated parameters is shown in Figure 3.41. A good correlation is obtained. This implies that the use of large anisotropy averaging volume may be suitable for low net-to-gross fluvial reservoir when the type of average volume is carefully determined according to the spatial distribution patterns of channels. The distance to channel boundaries may be interpreted from well test data alone [93]. Orientation of channels may be inferred from other information. This information may be of help in determining an appropriate type of averaging volume in calibration.

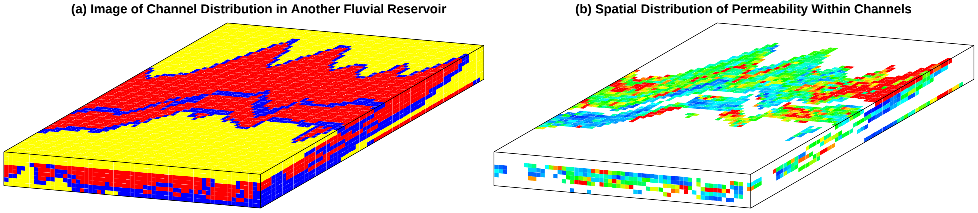
(a) Image of Channel Distribution in Another Fluvial Reservoir

(b) Spatial Distribution of Permeability Within Channels

Figure 3.39: Another 3D fluvial reservoir model constructed by a hierarchical object-based geostatistical method and the corresponding permeability distribution. In (a) channel is colored red, whereas shale is colored yellow. The bottom cell of every channel is colored blue. The permeability is color coded with blue being low permeability and red high permeability.

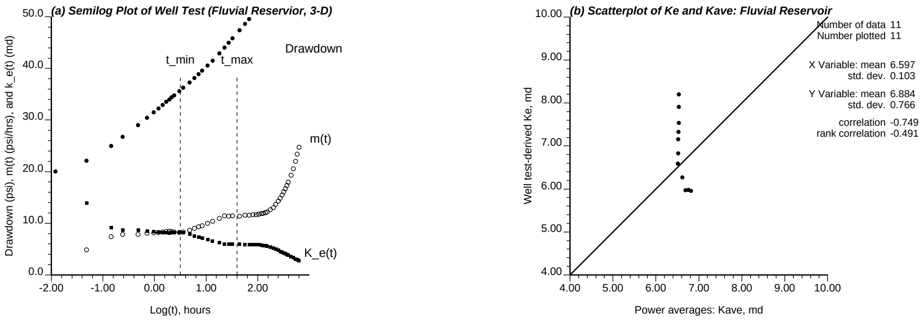
(a) Semilog Plot of Well Test (Fluvial Reservior, 3-D)

(b) Scatterplot of Ke and Kave: Fluvial Reservoir

Figure 3.40: Semilog plot of well test result and scatterplot of well test-derived effective permeabilities with weighted power averages for fluvial reservoir model shown in Figure 3.39.

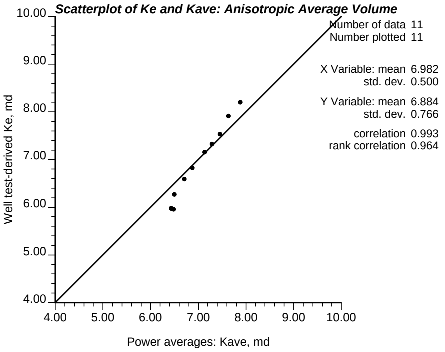
Scatterplot of Ke and Kave: Anisotropic Average Volume

Figure 3.41: The scatterplot of well test-derived effective permeabilities with weighted power averages using anisotropic averaging volume for fluvial reservoir model shown in Figure 3.39.

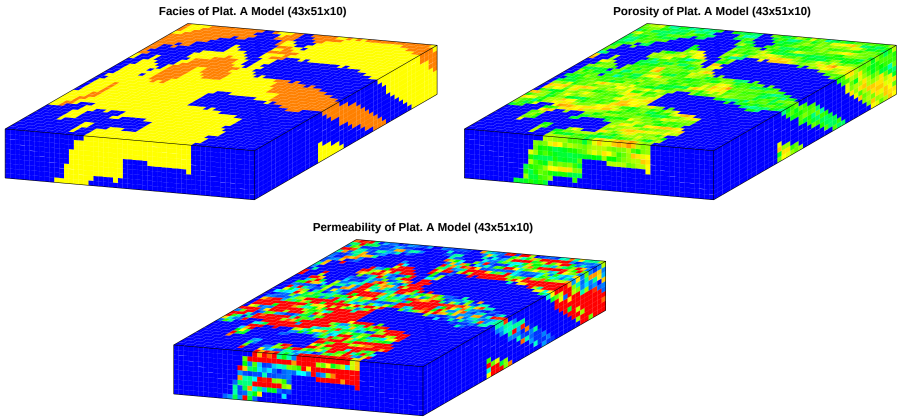

Figure 3.42: Facies and property models for platform A segment model.

3.7 Field-Scale Example

All permeability fields used in the previous sections are computer generated. In this section, documented is an application of the approach in two complex 3D segment reservoir models which are constructed based on real field data from a large Nigerian reservoir (VAA reservoir). The method of constructing these two segment models is described in the Appendix.

Figure 3.42 shows the property maps (facies, porosity and horizontal permeability) of segment model at platform A, consisting of 43×51×10 cells with uniform cell size of 200 ft × 196 ft × 20 ft. The permeability is isotropic in horizontal plane (i.e., $k_x = k_y$), and smaller vertical permeability $k_z = 0.7k_x$. Three lithofacies are identified in this model: impermeable shale ($k \approx 0$ md, $\phi < 0.20$), high permeable upper shoreface ($k \propto 1000 - 5000$ md, $\phi \propto 0.30 - 0.35$), and intermediate permeable lower shoreface ($k \propto 50 - 1000$ md, $\phi \propto 0.21 - 0.30$).

A vertical well located at the center of cell (22, 30) is used to perform a well test in this model with a constant flow rate $q = 2000$ STB/day. The well is completed and perforated over the entire thickness of the reservoir. Figure 3.43a shows the semilog plot of well test data. Other parameters used are $\mu = 0.3$ cp, $r_w = 0.33$ ft, $B = 1.4$, and $c_t = 5 \times 10^{-6}$ 1/psi. The optimal parameters calibrated from this data set are: $Log(A_{opt}) = -0.25$ and $\omega_{opt} = 0.4$. Again, a higher value of ω than geometric average is obtained for this 3D model. The scatterplot of the well test-derived effective permeability and the weighted power averages of permeability is given in Figure 3.43b. Good correlation is obtained.

The other segment model is at Platform C which contains 53×55×10 cells with uniform cell size of 168 ft × 166 ft × 20 ft. Figure 3.44 shows the property maps (facies, porosity and permeability) in this model. A well test is conducted at a vertical well located at the center of cell (34, 28), with a constant flow rate $q = 2000$ STB/day. Figure 3.45a shows the semilog plot of the well test results. Using the calibration approach, the optimal parameters for this model are: $Log(A_{opt}) = -0.2$ and $\omega_{opt} = 0.35$. The scatterplot of well test-derived effective permeability and the weighted power averages of permeability is given in Figure 3.45b: again excellent correlation is obtained.

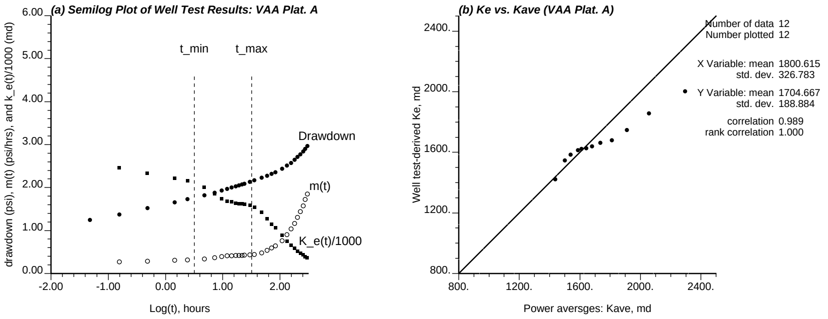

Figure 3.43: Semilog plot of well test result and scatterplot of well test-derived effective permeabilities with weighted power avegares for the platform A segment model shown in Figure 3.42.

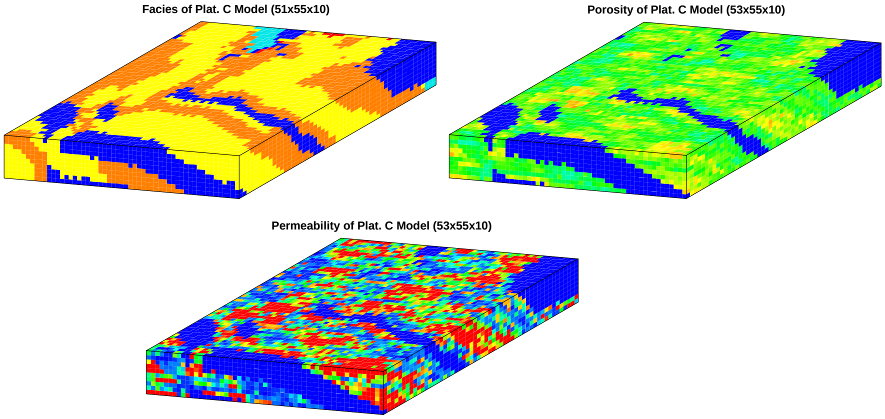

Figure 3.44: Facies and property models for platform C segment model.

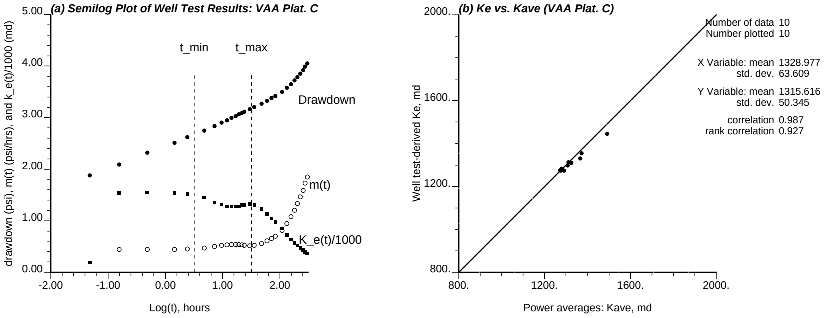

Figure 3.45: Semilog plot of well test result and scatterplot of well test-derived effective permeabilities with weighted power avegares for the platform C segment model shown in Figure 3.44.

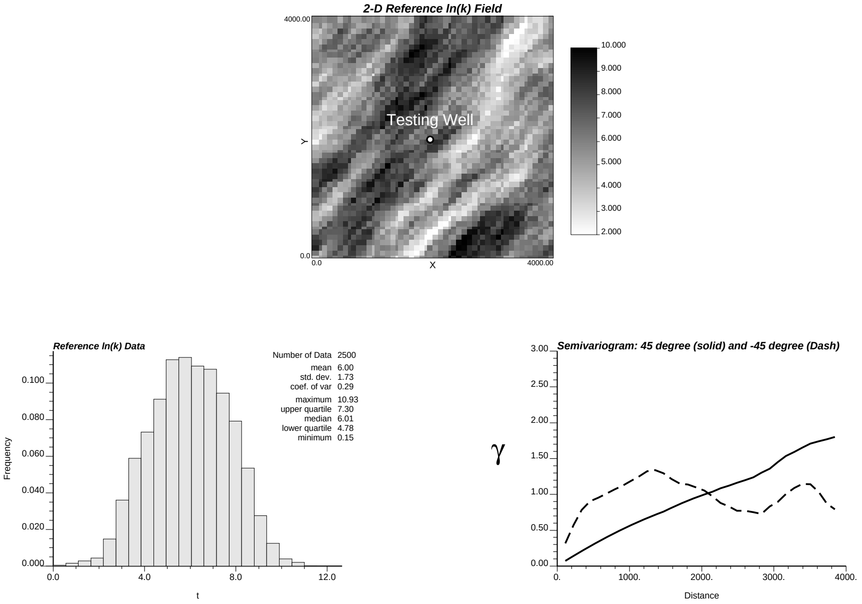

Figure 3.46: The reference $ln(k)$ field.

Results from the experiments in this section also indicate that porosity variations can be neglected in the calibration of well test-derived effective permeabilities.

3.8 Geostatistical Reservoir Models Honoring Well Test Data

Until now, the validation of calibration process is demonstrated for two parameters by assuming that the real permeability field is known. In this section, the entire process of Figure 3.1 is recounted to mimic a real practical case, however still using a synthetic field. The goal is to demonstrate application of the workflow of Figure 3.1, to construct geostatistical reservoir models that honor the well test data, and also to show the value of single well pressure transient data in reservoir characterization.

First, a reference permeability field is generated for which a synthetic well test data is obtained using a flow simulator. Effective permeabilities are computed using well test interpretation method. Optimal parameters $log(A)$ and ω are then obtained through the proposed calibration process using multiple realizations of permeability field with the same geostatistical features as the reference field. An annealing based technique is finally used to construct permeability models that honor the effective permeabilities, as well as the desired histogram and variogram.

Figure 3.46 shows the reference permeability field with 50×50 grid, the size of each grid is 80 ft *times* 80 ft. The permeability field for this field is generated by the sequential Gaussian simulation (`sgsim`) (GSLIB, [61]) with an anisotropic spherical type of variogram. The angle of anisotropy is at 45 degree. The output histogram and variogram of this model are also shown in the same figure.

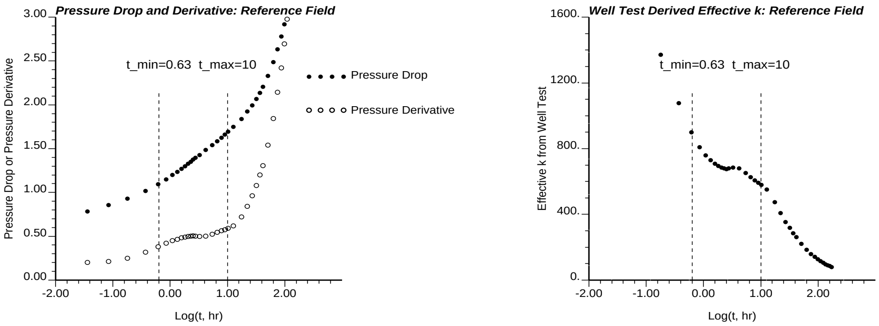

Figure 3.47: Pressure drawdown and effective permeabilities.

A well test is performed at the center of the field with a constant production rate of 50 STB/day. Other parameters used for generating well test data are: $\phi = 0.2$, $h = 10$ ft, $\mu = 0.3$ cp, $r_w = 0.33$ ft, $B = 1.4$, $c_t = 5 \times 10^{-5}$ psi. The corresponding pressure drawdown curve is shown in Figure 3.47. The time limits of infinite radial flow are determined to be at $t_{min} = 0.63$ hrs and $t_{max} = 10$ hrs. The effective permeabilities within the selected time limits are given in Figure 3.47b.

In order to calibrate the two parameters, multiple realizations of $ln(k)$ are generated using `sgsim` with the same variogram and histogram as the reference field, and conditioned to well data. Figure 3.48 shows four of the generated $ln(k)$ fields. The same well test is simulated in all generated realizations and effective permeabilities computed with the same interpretation method.

These effective permeabilities are then used to calibrate the two parameters A and ω. The resulting optimal parameters are $log(A) = 0.0$ and $\omega = 0.3$ (see Figure 3.49). With these parameters, the cross-plot of computed effective permeabilities and power-averaged permeabilities show good correlation as shown in Figure 3.49e. It is noted that an anisotropic average volume is used when calibrating the two parameters considering the anisotropic feature of permeability field. The calibration anisotropic average volume has the same principle directions as the variogram of permeability, but the anisotropic ratio of calibration volume (2) is smaller than the variogram anisotropic ratio (5). Figure 3.50 shows the reservoir volumes, as well as the weights used in computing power weighted averages of permeabilities at different times, based on the calibrated optimal parameters.

The next step is to construct reservoir permeability models that honor the power weighted averages. An annealing-based approach is used for such purpose with an additional component in the objective function as:

$$O_{wt} = \sum_{i=1}^{n_{wt}} \left[\overline{k}(i) - \overline{k}^*_{v(i)}(i) \right]^2$$

where $\overline{k}(i)$ is the well test derived effective permeability at time $t = t_i$, $i = 1, ..., n_{wt}$ $\overline{k}^*_{v(i)}(i)$ is the weighted ω-power average permeability:

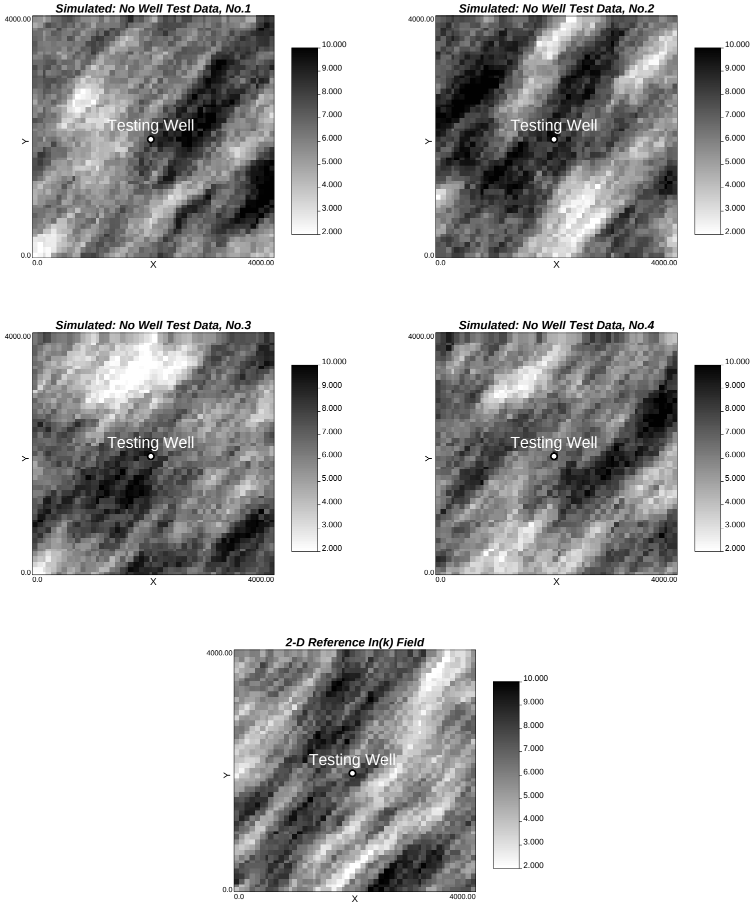
Simulated: No Well Test Data, No.1

Simulated: No Well Test Data, No.2

Simulated: No Well Test Data, No.3

Simulated: No Well Test Data, No.4

2-D Reference ln(k) Field

Figure 3.48: Four realizations of $ln(k)$ fields for calibration.

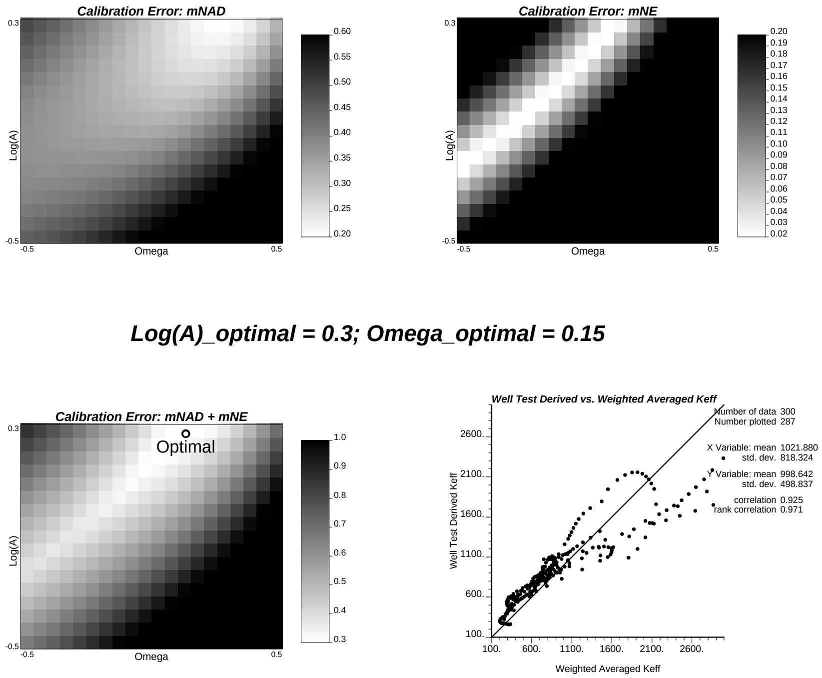

Figure 3.49: Calibration results.

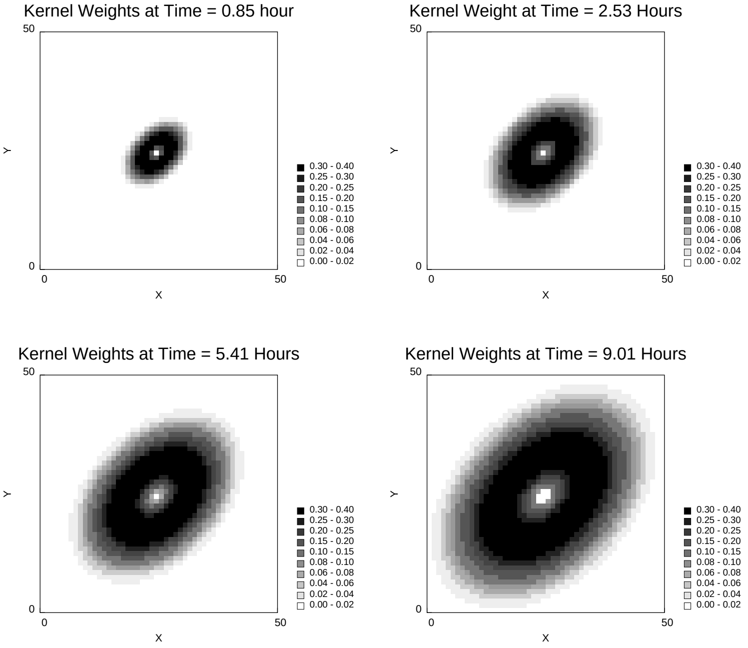

Figure 3.50: Kernel weights at different times.

$$\overline{k}^*_{v(i)}(i) = \left[\frac{1}{\sum_{i=1}^{N} \lambda(r_D, t_D)} \sum_{\mathbf{u}_i \in v(i)} \lambda(r_D, t_D) k(\mathbf{u}_i)^{\omega} \right]^{1/\omega}$$

where ω-power average permeability of the N permeability values $k(\mathbf{u}_i)$, $i = 1$, ..., N, at location $\mathbf{u}_i$ within the volume $V(i)$. A is a scaling parameter of dimensionless time to define the correct annular volume for averaging, $\lambda(r_D, t_D)$ is the kernel weighting function.

The program `swsasim` modified from original `sasim` (GSLIB, [61]) is used for generating multiple realizations of permeability that honor given histogram, variogram, and power weighted averages of permeabilities. Figure 3.51 shows four realizations of permeability fields by `sgsim` (only honor histogram and variogram) and `swsasim` (honor histogram, variogram and weighted power average permeabilities).

Finally, the reproduction of well test pressure transient data is checked by performing the same well test simulation in 20 realizations. Figure 3.52 shows the pressure drawdown and effective permeabilities: results at the left hand side are from the `sgsim` generated models where weighted power average permeabilities are not honored, while the results on the right are from the `swsasim` generated models that honor the weighted power averages. It can be seen that both pressure data and effective permeabilities are much better reproduced by integrating well test data. It should be noted, however, that it is impractical to exactly reproduce the pressure transient data by using the proposed approach since the pressure data are conditioned in the model indirectly. Rather, they are interpreted into effective permeabilities (the real features or spatial representation of pressure data), and the effective permeabilities are approximated by weighted power averages using two calibrated parameters.

Considering the facts that the pressure drawdown data are usually inaccurate in most cases, and there are more uncertainties in reservoir models, it is reasonable to argue that the exact reproduction of those well test derived pressure transient data is not necessary. On the other hand, it is suggested that particular user may check the final reproduction of the pressure responses to make sure that the results are satisfactory.

If the goal is to reproduce the pressure responses in an accurate degree so that it can not be achieved by this simple technique, it is suggested to use the inversion techniques discussed in the next chapter.

3.9 Discussion

Well test pressure transient data can be interpreted to yield time-dependent effective permeabilities by conventional well test analysis techniques. These time-dependent well test-derived effective permeabilities are controlled by permeability values within an annular volume that can be approximated by Oliver's analytical model [138].

A series of time-dependent weighted power averages of permeability can be used to approximate the well test-derived effective permeabilities. This requires two parameters: A to define the volume of averaging and ω to define type of averaging. The calibration of these parameters is straight forward in both 2D and 3D. Using the optimal parameters A and ω calibrated by the approach discussed, the weighted power averages of permeability give good approximations to the well test-derived permeabilities.

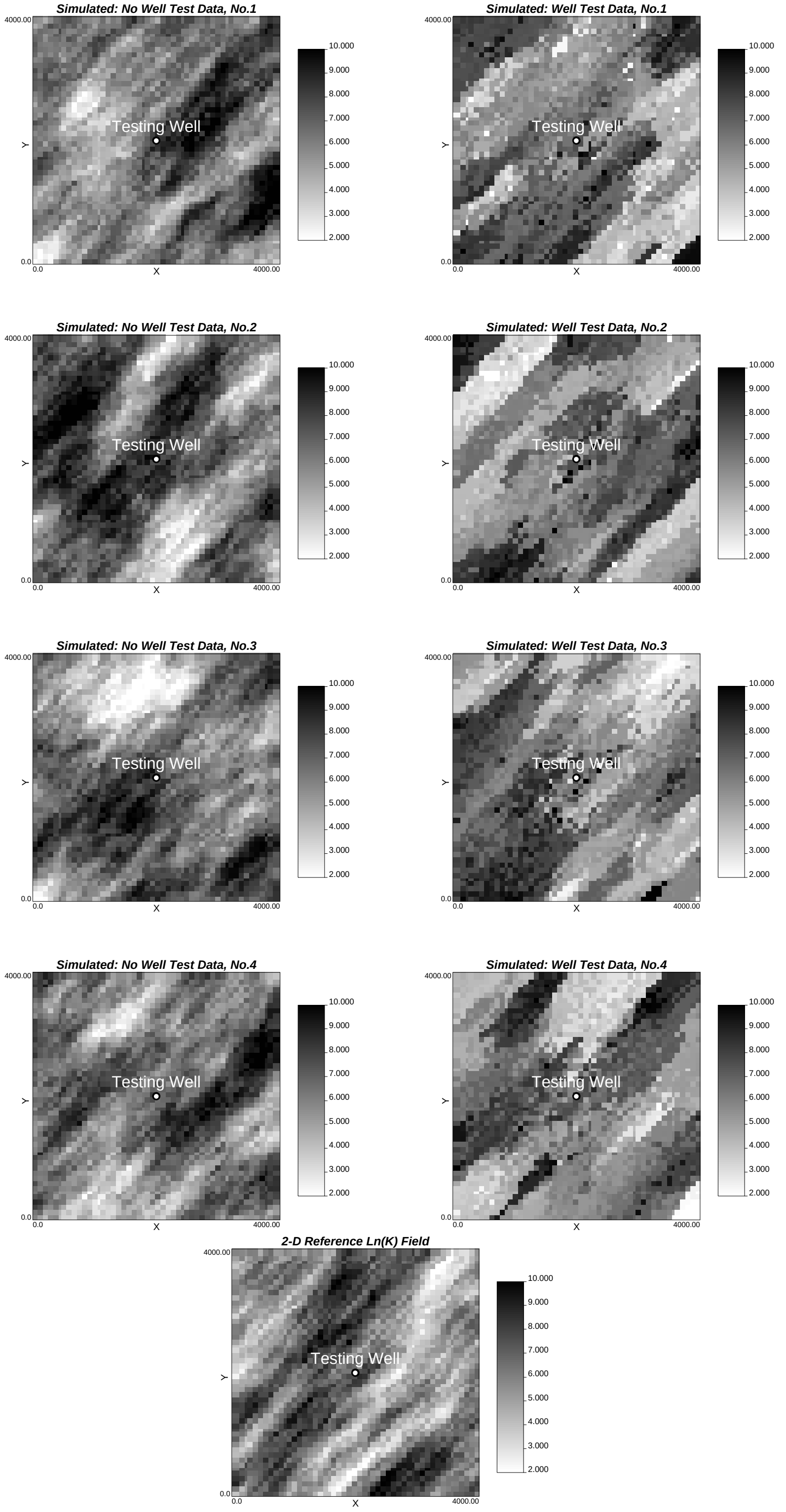

Simulated: No Well Test Data, No.1

Simulated: Well Test Data, No.1

Simulated: No Well Test Data, No.2

Simulated: Well Test Data, No.2

Simulated: No Well Test Data, No.3

Simulated: Well Test Data, No.3

Simulated: No Well Test Data, No.4

Simulated: Well Test Data, No.4

2-D Reference Ln(K) Field

Figure 3.51: Multiple realizations constructed.

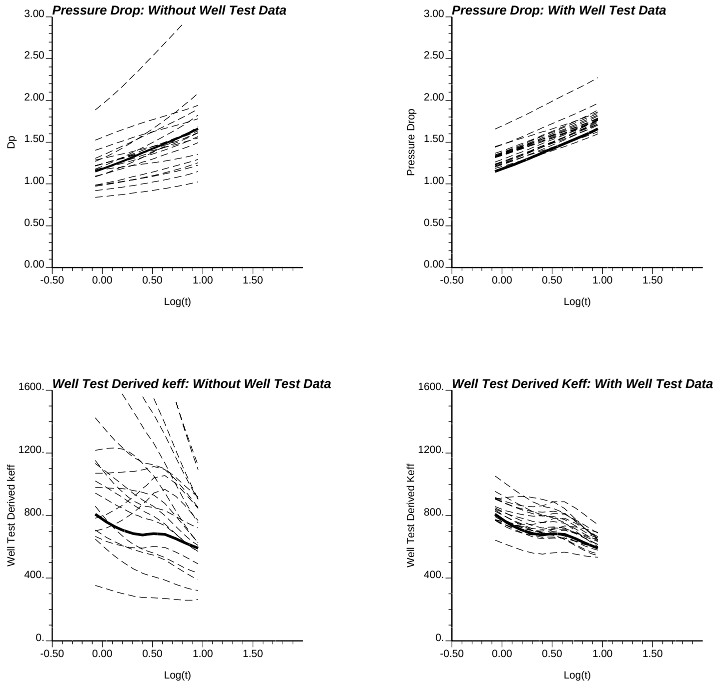

Figure 3.52: Pressure responses and effective permeabilities from before or after well test data are incorporated.

With this technique, well test (build-up or drawdown) data can be coded to spatial representations of detailed permeability distributions as long as radial analysis is valid. The results of this technique serve as input constraints in reservoir model-building.

The pressure transient data from a single well test can only provide constraints on radial variation of reservoir properties because pressure is measured at only a single point. Thus no direction information or multiple-point connectivity information can be retrieved. Instead, the directional information or constraints on the multiple-point spatial connectivity of reservoir properties should be interpreted from multiple-point pressure measurements, such as multiple-well tests. By integrating multiple-well pressure transient data, additional spatial constraints on the permeability distribution may be resolved, resulting in a better description of reservoir heterogeneity and less uncertainty in forecasting.

3.10 Hydraulic versus Geostatistical Anisotropy

There are two types of anisotropy frequently referred to in reservoir simulation: hydraulic anisotropy and geostatistical anisotropy. A porous medium is hydraulically anisotropic if the hydraulic behavior at any given location has directional dependence. Permeability at *any given point* within the medium is then a tensor with different values for the diagonal terms. Whereas geostatistical anisotropy refers to the *spatial variation features* of the permeability values within the medium, which is characterized by its variogram.

A medium can have any combination of these two types of anisotropy. The anisotropy discussed in this chapter is geostatistical anisotropy only, that is, permeability is direction

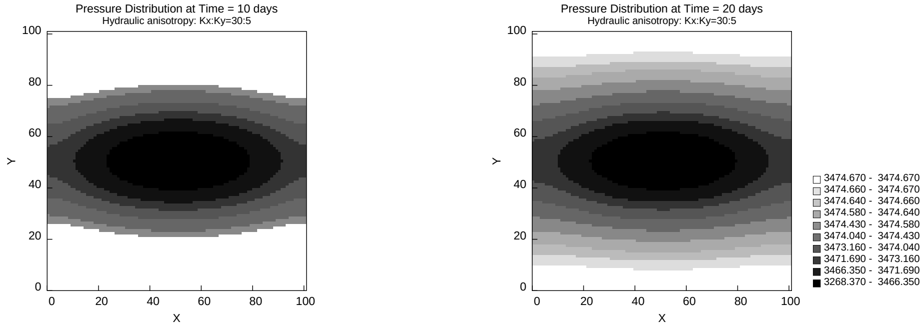

Figure 3.53: Pressure distributions at two different times in a hydraulically anisotropic permeability field, with $k_x/k_y = 30/5$.

independent at each location, but the variogram of the permeability values within the field is anisotropic in terms of correlation lengths in different directions.

The pressure diffusion in a hydraulically anisotropic permeability field should directly follow the hydraulic anisotropy feature. This can be seen from the pressure distributions in a homogeneous 2D hydraulically anisotropy field with $k_x = 30$ md and $k_y = 5$ md (see Figure 3.53). The "shapes" of pressure diffusion follow the square root of the "hydraulic anisotropy" as predicted by theory, i.e., a 30:5 k_x:k_y anisotropy leads to pressure contours that follow a 2.45:1 anisotropy.

The anisotropy in the variogram range leads to an apparent hydraulic anisotropy at a larger scale. However, the hydraulic anisotropy due to geostatistic anisotropy is much less than the anisotropy of the variogram, which was demonstrated earlier in the chapter. To further illustrate this, the effective permeabilities of the entire field are calculated in different directions for geostatistically anisotropic but hydraulically isotropic fields. The anisotropy of effective permeability can be used to reflect the apparent hydraulic anisotropy at a larger scale due to geostatistical anisotropy.

The effective permeabilities in six cases are computed with anisotropic variogram ranges increasing from 5 to 30. In each case, 100 permeability realizations are used, with log permeabilities being normally distributed in a 80 × 80 square domain. Each domain is discretized into 80 × 80 cells with cell size being 1 × 1.

Figure 3.54 shows the histograms of the anisotropy ratios of effective permeabilities for the six cases. The relationship between the anisotropy ratios of variograms and the anisotropy ratios of effective permeability or apparent hydraulic anisotropy can be seen in Figure 3.55. Mean values are used for the anisotropy ratios of effective permeability in this figure. Clearly, the anisotropy of effective permeability, that is the square of pressure diffusion anisotropy, is much less than the anisotropy of the variogram.

The square root of effective permeability anisotropy ratio is used for the calibration of average volume here. Inspecting Figures 3.16 and 3.17, the pressure diffusion anisotropy is found to be about 1.5 to 1.7 for the variogram anisotropy of 5 to 10, which is consistent with the results as shown on Figure 3.55.

Finally, it should be emphasized that it is not straightforward to generalize the relation between the anisotropy of variogram and the effective permeability, thus pressure diffusion, as shown in Figure 3.55 since it depends on (1) the distribution of permeability, (2) the

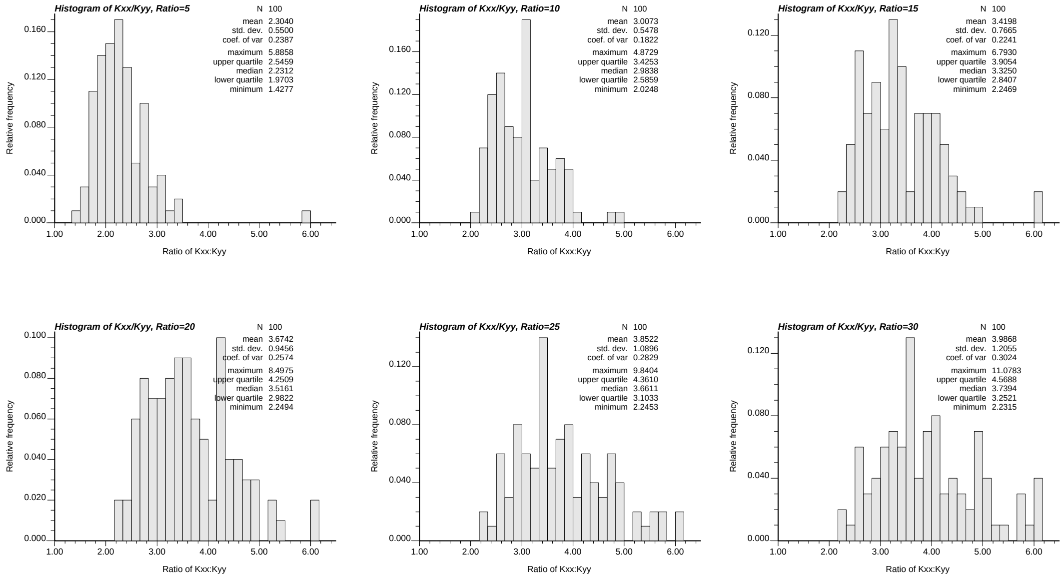

Figure 3.54: Histograms of anisotropy ratios of effective permeability from 100 realizations of geostatistically anisotropic fields.

shape of the variogram, (3) the presence of short scale variability - nugget effect, and (4) the block size over which the effective permeability is calculated.

In practice, given the variogram anisotropy of permeability field, the pressure diffusion anisotropy approximately may be established by repeated forward flow simulations using multiple permeability realizations with the same variation features as observed from field data.

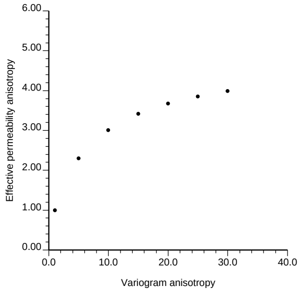

Figure 3.55: Relation between the anisotropy of effective permeability and the anisotropy of correlation lengths (variogram).

3.11 Exercise

3.11.1 Problem Setting

This is a synthetic reservoir, which we will characterize with the single-well single-phase inversion technique discussed in the chapter. For simplicity and applicability of the supplied programs, we restrict ourselves to 2D with a constant thickness of 20 ft. Areal extent of the reservoir is discretized by a 64×64 grid of the dimension 100 ft $\times$100 ft. Other reservoir and fluid properties are: ϕ 0.2, B 1.4, p_i 1502.008 psia, μ 0.3 cp, and c 5.5×10^{-5} 1/psia. Initial reservoir pressure is 1502.008 psia. The well is located in the (38,38) grid block. Wellbore radius is 0.33 ft. A reference ln(k) distribution is available (ref2d.dat). This is usually obtained from static (both hard and soft) data integration. The mean and variance of ln(k) are 0.73 and 0.6084, respectively. The reference ln(k) distribution is modeled by a two-structure variogram model with no nugget effect. The first structure is a spherical model with horizontal ranges 900 and 1400 ft and sill contribution of 0.5, and the other is a Gaussian model with horizontal ranges 1500 and 3200 ft and sill contribution of 0.5.

3.11.2 Steps Through the Single-Well Single-Phase Inversion Exercise

S1 Perform forward flow simulation to obtain synthetic well test data.

Forward flow simulation is performed to obtain synthetic well test data. This is not required when well test data from real well test or any other source are available. The program, `spsim`, is used to do the flow simulation. The parameter file for `spsim` is shown in Figure 3.56.

Here, `ref2d.dat` has the reference ln(k) distribution. A minimum time step of 0.01 and a maximum of 100 days are used. The simulation is performed for a total time of 1400 days. Maximum time step increment/decrement factor is 2.5, while there are nine time step controls. It is suggested that the duration of the well test data should be long enough to have the infinite-acting radial flow period. Any further well test data is not required as they are influenced by the boundary effects rather than the desired reservoir heterogeneity to be characterized.

N1 Infinite-acting radial flow period should not be masked by the initial wellbore effects or the late boundary effects. One way to get around this problem for synthetic data sets is to make the grid dimensions larger, so that the late effects are not pronounced in the well test data for a reasonable length of time. Users should examine the consequences for various grid dimensions, or change of fluid and reservoir properties.

S2 Determine the well test derived effective permeability and time limits for radial flow period. (Interpretation Stage)

`wtperm` is used to compute the slope and effective permeability. The parameter file for `wtperm` is shown below in Figure 3.57.

```
                  Parameters for SPSIM
                 *********************

START OF PARAMETERS:
../workdir/ref2d.dat       -file ln(k) field
2                          -columns ln(k) data
3                          -debugging level
../workdir/spsim2d.dbg     -file for debug output
../workdir/spsim2d.out     -file for output pressure solution
1                          -number of realizations
64  50.0  100.0            -X grid size: nx, xmn, xsiz
64  50.0  100.0            -Y grid size: ny, ymn, ysiz
1502.008                   -initial pressure (psia)
1.4  0.2  20  0.3  5.5e-5  -B, poro, thick,visco, comp
1  -15                     -number of wells, rate
38  38  0.33               -well location i,j, and radius (ft)
0.01  100  1400  2.5  9    -tsmin,tsmax,t_max,tfact,no. of time step control
5    0.01                  -time step control, nt, dt
5    0.05                  -time step control, nt, dt
5    0.1                   -time step control, nt, dt
5    0.5                   -time step control, nt, dt
5    1.0                   -time step control, nt, dt
5    5.0                   -time step control, nt, dt
5   25.0                   -time step control, nt, dt
5   50.0                   -time step control, nt, dt
10 100.0                   -time step control, nt, dt
```

Figure 3.56: Parameter file for **spsim**.

```
                 Parameters for WTPERM
                 *********************

START OF PARAMETERS:
..\workdir\spsim2d.out            -file with pressure data
1  2                              -columns for time and pressure
..\workdir\wtperm2d.out           -file for output pressure solution
1  55                             -number of realizations & time steps
 64  50.0  100.0                  -X grid size: nx, xmn, xsiz
 64  50.0  100.0                  -Y grid size: ny, ymn, ysiz
1502.008                          -initial pressure (psi)
15  1.4  0.2  20  0.3  5.5e-5     -flowrate,B,poro,thick,visco,comp
38  38  0.33                      -well location i,j, and radius (ft)
```

Figure 3.57: Parameter file for **wtperm**.

Any plotting tool can be used to draw the semilog plot of drawdown, slope and effective permeability versus logarithm of time in hours. Examining the semilog plots, the time limits are determined approximately. Usually, for a homogeneous reservoir this can be easily done. However, for realistic reservoirs, the idea is to first decide on the time limits from these graphs, then perform the calibration (which is the next step) and compute the correlation coefficient of well test derived effective permeability and the calibrated power-law averaged effective permeability. If a good correlation is obtained, then proceed with the next step. Otherwise come back to re-approximate the time limits.

N2 Time limits interpretation can be subjective. Users should examine the consequences of using different time limits for the same reservoir and fluid conditions.

N3 Users should also inspect the semilog plots for the presence of any obvious trends in the permeability heterogeneity. Corroboration of any initial interpretation with the later heterogeneity characterization should add to the confidence of the study.

S3 Calibrate the optimal parameter pair (ω and A) and obtain the calibrated power-law averaged permeability. (Calibration Stage)

The program, `swspcali`, is used to compute the optimal parameter pair (ω and A). The parameter file for `swspcali` is shown in Figure 3.58.

An isotropic permeability field and a circular annular region for the volume of averaging are considered here. $\log(t_{\min})$ and $\log(t_{\max})$ values of 2.32 and 3.8 are used. For calibration, $\log(A)$ is discretized into 25 steps from 0 to 1, while ω into also 25 intervals from -0.5 to 0.5. The geometric mean of 2.0698 md is obtained from the reference permeability distribution. Number of time steps used is 53, which is obtained from the response of `wtperm`.

Three output files are obtained: one for errors, one for permeabilities and, the other for kernel weights. The permeabilities computed are for the case of minimizing both normalized absolute deviation and normalized error. One can get the permeabilities for the simply absolute deviation or normalized error using “quick pick parameters” option. However, $\log(A)$ and ω values should be obtained first. Scatter plot of well test derived effective permeability and the calibrated permeability is plotted. A good correlation indicates probably the time limits are correct.

N4 Users should investigate using anisotropic annular regions. One might also be interested in exploring the effect of anisotropy on the calibrated optimal parameter pairs.

```
                    Parameters for SWSPCALI
                    ***********************

START OF PARAMETERS:
../workdir/ref2d.dat           -file with ln(k) data
2                              -column for ln(k) data
../workdir/wtperm2d.out        -file of effective permeability data
1  6                           -columns for time and keff
../workdir/swspcali2d.err      -file for output of errors
../workdir/swspcali2d.out      -file for output of keff and weighted averages
1                              -index for outputting weights
../workdir/kweight2d.out       -file for output of kernel weights
 64  50.0  100.0               -X grid size: nx, xmn, xsiz
 64  50.0  100.0               -Y grid size: ny, ymn, ysiz
1.0  1.0                       -correlation length in x and y directions
0.0                            -angle of anisotropic direction
38  38  0.33                   -well location i,j, and radius (ft)
2.32  3.8                      -log(time_min) and log(time_max)
0.0  1.0  25                   -log(A)_min, log(A)_max, nstep_A
-0.5  0.5  25                  -omega_min, omega_max, nstep_o
1  53  2.0698                  -nsim, nstep,geometric mean of k
2                              -interval of keff for calibration
15  1.4  0.3  0.2  20  5.5e-5  -rate,B,visco,poro,thick,comp
0                              -option for using quick pick parameters
0  0                           -quick pick for log(A) and omega
```

Figure 3.58: Parameter file for **swspcali**.

S4 Generate fine scale model with simulated annealing technique. (Model Building Phase)

So far, we have calibrated the optimal parameters and obtained the power-law averaged permeabilities. Now, fine scale permeability distributions can be obtained conditioned to calibrated permeabilities, reference histogram, variogram, and other conditioning secondary data. Integration of unaccounted soft data can also be done at this stage. The program, `swsasim`, is used for model generation. The parameter file for `swsasim` is shown in Figure 3.59.

For the present exercise, we have only reference histogram and variogram and the well test derived permeability. Unequal weights can be assigned to each of these data based on the information content and our conviction. Annealing schedule can be set automatic or manually. If set manually the parameters required are: initial temperature, reduction factor, maximum number of perturbations at any given temperature, target number of acceptable perturbations, the stopping number, and a low objective function value for convergence check. These values are set to 0.0, 0.05, 12, 3, 6 and 0.001 respectively. Number of lags for variogram calculation is fixed to be 15. For well test data, optimal $\log(A)$ and ω are derived earlier in the calibration phase to be 0.12

and -0.42 respectively. As earlier, circular annular region and isotropic permeability field are considered. The reservoir and fluid parameters will be same as before.

The response can be plotted by `pixelplt` or any other appropriate plotting program. A point to be noted, responses obtained using simulated annealing technique tend to have a higher nugget effect than desired. This is a limitation of the annealing technique. One way to improve the responses is to adjust the weights of different data giving a low weight to well test data, and also adjust the number of variogram lags.

N5 Users are encouraged to try different weights to various objective functions, or incorporating other secondary data if available to examine the variations in the generated realizations.

```
                  Parameters for SWSASIM
                  **********************

START OF PARAMETERS:
1  1  0  0  0  0  1          -components: hist,varg,ivar,corr,cpdf,csag,wtke
1  0.5  1  1  1  1  0.5      -weight:  hist,varg,ivar,corr,cpdf,csag,wtke
0                            -0=no transform, 1=log transform
2                            -number of realizations
64  50.0  100.0              -grid definition: nx,xmn,xsiz
64  50.0  100.0              -grid definition: ny,ymn,ysiz
 1  0.5  1.0                 -grid definition: nz,zmn,zsiz
46069                        -random number seed
3                            -debugging level
..\workdir\sasim2d.dbg       -file for debugging output
..\workdir\sasim2d.out       -file for simulation output
1                            -schedule (0=automatic,1=set below)
0.0  0.05  12  3  6  0.001   -schedule: t0,redfac,ka,k,num,Omin
30  0.1                      -max num of perturbations, reporting interval
400                          -max num without a change
0                            -conditioning data:(0=no, 1=yes)
******                       -file with data
1  2  0  3                   -columns: x,y,z,attribute
-1.0e21  1.0e21              -trimming limits
1                            -histogram:(0=no, 1=yes)
..\workdir\ref2d.dat         -file with histogram
2  0                         -column for value and weight
99                           -number of quantiles for obj. func.
1                            -number of indicator variograms
2.78                         -indicator thresholds
******                       -file with gridded secondary data
1                            -column number
0                            -vertical average (0=no, 1=yes)
0.60                         -correlation coefficient
******                       -file with paired data
2  1  0                      -columns for primary, secondary, wt
-0.5  100.0                  -minimum and maximum
1                            -number of primary thresholds
1                            -number of secondary thresholds
```

```
15                            -variograms: number of lags
1                             -standardize sill (0=no,1=yes)
2  0.0                        -nst, nugget effect
1  0.5  0.0  0.0  0.0         -it,cc,ang1,ang2,ang3
      900.0  1400.0  1.0      -a_hmax, a_hmin, a_vert
3  0.5  0.0  0.0  0.0         -it,cc,ang1,ang2,ang3
     1500.0  3200.0  1.0      -a_hmax, a_hmin, a_vert
0  12                         -itemp (0=global update, 1=local update),ntmp
2  2                          -ltail option for local ccdf
1  1                          -middle option for local ccdf
2  0.5                        -utail option for local ccdf
******                        -coarse grid field
20  100.0  200                -coarse grid definition: nxcs,xmncs,xsizcs
20  100.0  200                -nycs,ymncs,ysizcs
1  0.5  1.                    -nzcs,zmncs,zsizcs
1  1                          -omega power;id_csavg to conform k_avg at initial
..\workdir\wtperm2d.out       -well test effective permeability data file
1  6                          -columns for time and keff
0.12  -0.42                   -log(A) and omega_wt (optimal from calibration)
38  38  0.33                  -location of testing well and radius (ft)
1.0  1.0                      -correlation length for anisotropic annular
0.0                           -angle for anisotropic annular
2.32  3.8                     -min and max Log(t) in well test
15 1.4  0.3 0.2  20.  5.5e-5  -flowrate,fvf,visco,poro,thick,compress.
```

Figure 3.59: Parameter file for **swsasim**.

S5 Users should perform well test simulation using the generated realizations to compare the real well test pressure transient data.

S6 Suggested sensitivity analyses.

- It is often difficult to get a good variogram model. One logical sensitivity study can focus on variogram structures. With different variogram models, the entire process can be repeated and uncertainty due to variograms can be estimated.
- In the interpretation stage, one has to decide on the time limits. Different time limits can be used and the subsequent steps performed to evaluate uncertainty due to the time limits.
- Sensitivity to initial pressures, fluid properties, reservoir dimensions can be performed. It should be noted that reservoir dimensions can be quite important inasmuch as small domain can lead to boundary effects masking the infinite-acting flow period.
- Sensitivity to volume of averaging of different shapes, and also to anisotropic permeability field can be analyzed.

Chapter 4

Multiple Well - Single Phase

This chapter discusses integration of multiwell single-phase flow data. Data provided by permanent pressure gauges, simultaneous multiple well tests, or reservoirs under primary depletion are considered. A slightly different approach, from that discussed for single well single phase case, is applied for the integration. Spatial constraints are first established on large-scale permeability trends due to the production data. Detailed geostatistical models are then constructed subject to these spatial constraints.

Production data and reservoir petrophysical properties are nonlinearly related through flow equations. Establishing the constraints on permeability due to production data calls for the solution of a difficult inverse problem. A recently developed inversion technique, the sequential self-calibration (SSC) method, is adapted to multiple-well single-phase pressure transient data. This is a geostatistics-based iterative method, coupled with an optimization procedure that generates a series of coarse grid 2D permeability realizations, which reproduce the production data. Results with synthetic data indicate that the SSC method is flexible, computationally efficient, and robust. An annealing-based geostatistical technique is employed to construct fine scale reservoir models integrating the coarse scale permeability obtained from the SSC inversion.

4.1 Background

Highly nonlinear flow equations must be solved to establish the relationship between production data and reservoir properties. Consequently, accounting for dynamic engineering data in geostatistical reservoir modeling is a difficult inverse problem. Nevertheless, from the perspective of a reservoir engineer, historical production data are often the most important information available. These dynamic data provide a direct measurement of the actual reservoir response and are directly related to the recovery process and the response variables.

Ideally, all types of production data could be directly accounted for in the reservoir model at the required resolution simultaneously with other types of geological and geophysical data. The production data would then be explicitly reproduced in the reservoir model. This direct integration is not feasible because of the following reasons. The mathematical inversion of the flow equations is computationally intensive requiring many solutions to the flow equations. Consideration of multiphase production data further limits the size of the model. Furthermore, it is difficult to simultaneously match production data with other static geological and geophysical data.

The coarse grid models constructed by direct inversion techniques are usually inadequate for reliable production forecasting. In many practical situations, while keeping models as simple as possible, highly-resolved models of lithofacies, porosity and permeability are desired. This two-stage inversion is suitable for such problem.

Section 4.2 describes the sequential self-calibration (SSC) method in greater detail for application to single-phase production data from multiple wells. The application of SSC to a number of synthetic data sets, with the utility and robustness of the method, is documented in Section 4.3. Section 4.4 introduces an annealing-based geostatistical technique to construct fine-scale geostatistical models conditioned to the 2D coarse grid permeability models obtained by the SSC method.

4.2 The Sequential Self-Calibration (SSC) Method

The available production data include pressure $p_i(t)$ and flowrate $q_i(t)$ with time t at a number of wells $i = 1, ...n_w$. The goal is to find a set of permeability and porosity values for each numerical cell in a reservoir model that matches the observed pressure data under the given flowrate conditions. This match is established by solving the flow equations:

$$\nabla(\frac{kh}{\mu}\nabla p) + q = hc\phi\frac{\partial p}{\partial t} \tag{4.1}$$

where k is permeability, ϕ porosity, μ viscosity, h the thickness of the reservoir, and c formation compressibility. The closeness of the pressure match may be quantified by an objective function:

$$O = \sum_i \sum_t \left(p_i^{obs}(t) - p_i^{cal}(t)\right)^2 \tag{4.2}$$

where $p_i^{obs}(t)$ is the observed pressure data at well i at time t, and $p_i^{cal}(t)$ is the numerically calculated pressure at well i at time t.

The SSC method is an iterative geostatistics-based method coupled with an optimization procedure [22, 74]. Like most geostatistical approaches, the SSC method generates multiple equally-likely realizations of permeability honoring different types of static and dynamic field data. The realizations created by the SSC method honor a specified spatial variation structure as modeled from the field data. Dynamic pressure data at multiple wells are also honored in the sense that the solution of the flow equation in each of the generated realizations matches the measured pressure values at the same well locations.

The unique aspects of the SSC method are (1) the concept of *master points* that reduces the space of parameters, (2) a perturbation mechanism based on kriging that accounts for spatial correlation of parameters, and (3) fast computation of sensitivity coefficients. The combination of these features makes the SSC method flexibly, robust and computationally very efficient. As an overview, the method can be described by the following steps (see also Figure 4.1):

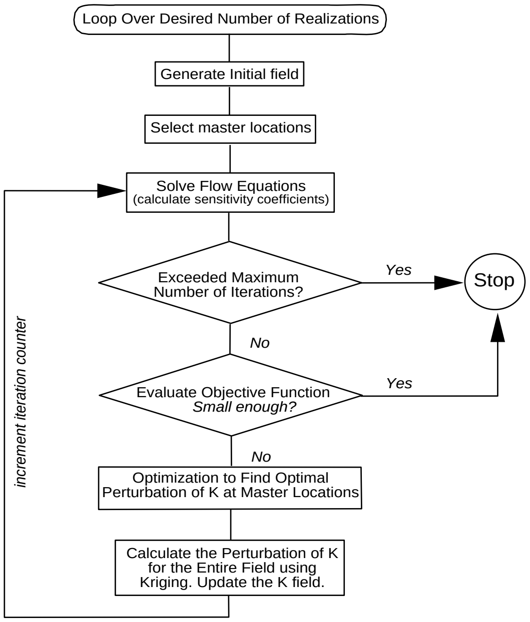

Figure 4.1: Flowchart of the Sequential Self-Calibration method.

Construction of initial realizations: Multiple, initial permeability realizations are created by conventional geostatistical techniques constrained to all static (hard and soft) data and the specified permeability histogram and variogram. Each realization is processed one at a time with the following steps.

Solving the flow equations: For the current model, the flow equations are solved using the specified boundary and production rate conditions. A block centered finite difference method with a direct matrix solver is used to solve the flow equations in this study. Other numerical methods can also be used for this purpose.

Mismatch calculation and convergence check: The difference in the observed and calculated pressure values at the available wells and at the given time is computed in some norm sense. If the difference is smaller than a preselected tolerance value, this permeability realization is considered to honor the dynamic pressure data and the procedure stops. Otherwise, the algorithm proceeds to the next step.

Selection of *master points* and solution of the optimization problem: Master points are selected randomly but with a criterion of having about one to three master points per correlation range of permeability variogram depending on the complexity of the problem. However, all the well locations with permeability data are included as the master points. In some cases, more master points are added in the vicinities of the well to better resolve some scale details. An optimization problem is then solved to find the optimal perturbations of permeability at the master point locations. The optimal perturbations minimize the difference between the observed and calculated pressures. The master point concept reduces the space of parameters to be optimized,

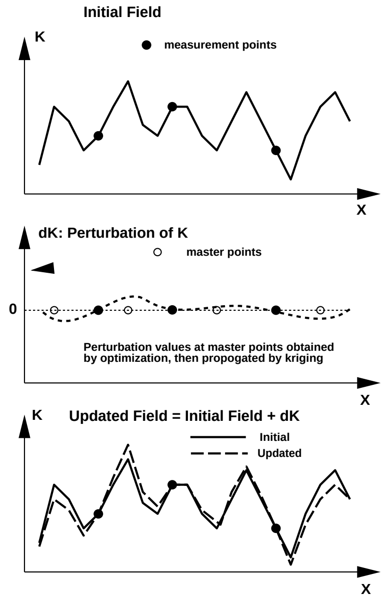

Figure 4.2: The schematical illustration of perturbation precess used in the SSC method using a 1D example.

which significantly improves the computational efficiency of the method. To achieve better results, the locations of master points are changed after each specified number of iterations so that the optimization process can search broader range of parameter space without increasing the computer time considerably.

Propagation of the optimal perturbations: The optimal perturbations for the master points determined in the previous step are propagated through the entire field by kriging. The permeability field is updated by adding the smooth perturbation field to the previous permeability field (see Figure 4.2). The variogram, used to generate initial models, is used to propagate the permeability perturbations at master points. This preserves the original spatial variation patterns in the permeability field.

Outer iteration: The algorithm loops back to the step **"Solving the flow equations"**. The cycle is repeated until the convergence is achieved. Typically, fewer than 20 iterations are required.

Sensitivity coefficients (derivatives of pressure with respect to the perturbation of permeability values) at all master point locations at each time step are needed when solving the optimization problem using gradient-based methods. The efficient calculation of sensitivity coefficients has received significant attention in the literature [39, 47, 120, 141]. An efficient method of obtaining the required sensitivity coefficients is applied here as part of the flow solution.

Discretization of the flow equation (4.1) using an implicit scheme leads to the following equation in matrix notation:

$$[A]\{p\}^{t+1} = [B]\{p\}^{t} + \{f\}^{t} \tag{4.3}$$

where $[A]$ is the transmissibility matrix which accounts for spatial and time discretizations, as well as boundary conditions, $[B] = [hc\phi]/\triangle t_{t+1}$, and $\{f\}^t$ is the right hand side matrix that accounts for the load vector (production or injection) and flow boundary conditions. The solution of pressure at time $t+1$ is obtained by inverting matrix $[A]$, that is,

$$\{p\}^{t+1} = [A]^{-1}[B]\{p\}^t + [A]^{-1}\{f\}^t \tag{4.4}$$

The sensitivity coefficients at time step $t+1$ are calculated right after the pressure at time $t+1$ is obtained. The perturbation of parameter k_m can be written as:

$$[A]\frac{\partial\{p\}^{t+1}}{\partial \triangle k_m} + \frac{\partial[A]}{\partial \triangle k_m}\{p\}^{t+1} = \frac{\partial[B]}{\partial \triangle k_m}\{p\}^t + [B]\frac{\partial\{p\}^t}{\partial \triangle k_m} + \frac{\partial\{f\}^t}{\partial \triangle k_m}, \qquad m = 1, \ldots, n_m \tag{4.5}$$

where n_m is the total number of master points, thus,

$$[A]\frac{\partial\{p\}^{t+1}}{\partial \triangle k_m} = \frac{\partial[B]}{\partial \triangle k_m}\{p\}^t + [B]\frac{\partial\{p\}^t}{\partial \triangle k_m} + \frac{\partial\{f\}^t}{\partial \triangle k_m} - \frac{\partial[A]}{\partial \triangle k_m}\{p\}^{t+1}, \qquad m = 1, \ldots, n_m \tag{4.6}$$

Equation (4.6) has the same form as Equation (4.3) and the matrix $[A]$ has just been inverted when solving for the pressure $\{p\}^{t+1}$. The sensitivity coefficients can be obtained at the same time step $t+1$ by simple matrix operations, that is,

$$\begin{aligned} s_{m,t+1} &= \frac{\partial\{p\}^{t+1}}{\partial \triangle k_m} \\ &= [A]^{-1}[B]\frac{\partial\{p\}^t}{\partial \triangle k_m} + [A]^{-1}\frac{\partial[B]}{\partial \triangle k_m}\{p\}^t + [A]^{-1}\frac{\partial\{f\}^t}{\partial \triangle k_m} - [A]^{-1}\frac{\partial[A]}{\partial \triangle k_m}\{p\}^{t+1}, \end{aligned}$$

$$m = 1, \ldots, n_m \tag{4.7}$$

The elements of matrices, $\frac{\partial[A]}{\partial\triangle k_m}$, $\frac{\partial[B]}{\partial\triangle k_m}$, and $\frac{\partial\{f\}^t}{\partial\triangle k_m}$ can be directly computed from the expressions of elements in matrices $[A]$, $[B]$ and $\{f\}$ with $\frac{\partial\{p\}^0}{\partial\triangle k_m} = 0$. The efficient calculation of sensitivity coefficients has received significant attention in the literature. Other methods can be found in the literature [39, 47, 120, 141].

A modified gradient projection method is then used to obtain the optimal perturbation values at the selected master locations by minimizing the objective function. The objective function given in Equation (4.2) can be written in the following matrix form:

$$O = O(\{p^{cal}\}) = \sum_{t=1}^{n_t}(\{p^{cal}\}_t - \{p^{obs}\}_t)^T[W_p]_t(\{p^{cal}\}_t - \{p^{obs}\}_t) \tag{4.8}$$

where $\{P^{cal}\}_t = \{p^{cal}_{t,1}, p^{cal}_{t,2}, ..., p^{cal}_{t,n_w}\}^T$ and $\{P^{obs}\}_t = \{p^{obs}_{t,1}, p^{obs}_{t,2}, ..., p^{obs}_{t,n_w}\}^T$ are the numerically calculated and observed pressures at well $i = 1, ..., n_w$ and time $t = t_1, ..., t_n$. $[W]_t$ is the inverse covariance matrix of observation errors at time t. If pressure measurement errors at different wells are independent, $[W]_t$ is a diagonal matrix with the form of

$$[W]_t = \begin{bmatrix} w_{1,t} & & \\ & \ddots & \\ & & w_{n_w,t} \end{bmatrix} \tag{4.9}$$

Objective function (4.8), a non-linear function of the model parameters, needs to be computed (i.e., the perturbations of permeability at master locations, $\{M\} = \{\Delta k_1, \Delta k_2, ..., \Delta k_{n_m}\}^T$). Linearization of this objective function is attained by approximating the pressure data by retaining its first order Taylor expansion, i.e.,

$$\{P^{cal}\}_t^1 \approx \{P^{cal}\}_t^0 + \frac{\partial\{P\}_t}{\partial\{M\}}\{M\} \tag{4.10}$$

where $\{S\}_t = \partial\{P\}_t/\partial\{M\} = \{s_{1,t}, s_{2,t}, ..., s_{n_m,t}\}$ is the sensitivity vector at time t with respect to the permeability perturbation at location m computed, with $s_{m,t} = \partial\{P\}_t/\partial\{\Delta k_m\}$. $\{P^{cal}\}_t^0$ and $\{P^{cal}\}_t^1$ are pressure values at time t before and after introducing a perturbation matrix $\{M\}$. Using this linear approximation, after some manipulation, the objective function (4.8) can be rewritten as following:

$$O(\{p^{cal}\}^1) = O(\{p^{cal}\}^0) + \sum_{t=1}^{n_t}\{D\}_t^T\{M\} + \sum_{t=1}^{n_t}\{M\}^T[C]_t\{M\} \tag{4.11}$$

where the matrices $\{D\}_t$ and $\{C\}_t$ are expressed as follows:

$$\{D\}_t = 2\left(\{p^{cal}\}_t - \{p^{obs}\}_t\right)^T [W]_t\{S\}_t \tag{4.12}$$

$$\{C\}_t = (\{S\}_t)^T [W]_t\{S\}_t \tag{4.13}$$

The constraints used for minimizing the objective function (4.11) are simply the possible minimum and maximum values of perturbations, i.e.,

$$\{\Delta k_{\min}\} \leq \{M\} \leq \{\Delta k_{\max}\} \tag{4.14}$$

that is,

$$\begin{aligned} [I]\{M\} &\leq \{\Delta k_{\max}\} \\ -[I]\{M\} &\leq \{\Delta k_{\min}\} \end{aligned} \tag{4.15}$$

where $[I]$ is a $n_m \times n_m$ identity matrix, $\{\Delta k_{\min}\} = \min\{k^0, k_{krig} - \alpha\sigma_{krig}\}$ and $\{\Delta k_{\max}\} = \max\{k^0, k_{krig} + \alpha\sigma_{krig}\}$. $\{k^0\}$ is the vector of permeability values at master points in the initial field, $\{k_{krig}\}$ and $\{\sigma_{krig}\}$ are kriging estimations and the corresponding kriging standard deviations at the master points based on available measured permeability data. If there is no prior k measurements, $\{k_{krig}\}$ and $\{\sigma_{krig}\}$ can be selected as the mean and standard deviation of the desired permeability histogram. α is a constant value that specifies the interval size of the constraints.

The above formulation is a standard quadratic optimization problem. In the current SSC code, this optimization problem is solved using a modified gradient projection method to take advantage of the simple expression of constraints expressed in equation (4.15). At each iteration of the optimization process, the search direction is obtained by projecting the gradient of the objective function on the null space of the gradients of the binding constraints [73].

It should be noted that the application of the SSC method requires information on the distribution of permeability at the scale of the numerical grid (histogram and variogram). Also it assumes that the permeability variation in entire model is governed by a single histogram and a single variogram model, which may limit its application when the permeability variations in a reservoir are due to the mixture of multiple populations (e.g., controlled by multiple lithofacies or channel objects), or when there are discontinuous features such as faults, channels, or facies boundaries. Furthermore, there is no direct control on the reproduction of the variogram in the updated realizations. A posteriori check is thus needed to ensure that the appropriate inverse results are obtained. Nevertheless, promising results have been obtained in groundwater hydrology using the SSC method with different heterogeneity features including the identification of non-multiGaussian features and high permeability flow channels [187, 188, 195, 204].

4.3 Application of the SSC Method

The SSC method can retrieve important spatial features of permeability from multiple well production data. This is demonstrated below. A reference permeability model is first constructed. The dynamic pressure responses, at a number of wells due to changing flow rates, are then obtained by flow simulation. Based on the dynamic flowrate and pressure data, and information on the spatial variation structure of permeability, the SSC method is used to invert for permeability fields that match the production data. The inverted permeability fields are compared with the reference field to assess the capability of the SSC method.

A 2D, 4000 ft square, domain of interest is discretized into 25 × 25 grid cells 160 ft × 160 ft. There is a high permeability (500 md) band connecting the lower-left corner and upper-right corner. The permeability in other areas is constant at 10 md (see Figure 4.3). There are four wells: W1 at the center of cell (5,21), W2 at (21,21), W3 at (5,5), and W4 at (21,5). The four boundaries are no-flow boundaries, porosity is assumed constant at 0.2, reservoir thickness is 100 ft, viscosity 0.2 cp, formation compressibility 10^{-6} 1/psi, and well radius 0.3 ft.

The imposed production rates and the corresponding pressure responses at the different wells were solved by *Eclipse* [101] and are shown in Figure 4.4. The reason for the different shut-in times is to create as much between-well interference as possible. This reveals more information on spatial variations of permeability by the available production data. Clearly, the hydraulic connection between wells W2 and W3 is stronger than that between other well pairs.

The SSC method is used to estimate the spatial distribution of permeability within the domain using the same discretization based on the production and pressure data at the four wells. Initially, a constant permeability with $k = 2$ md is assumed at all cells. An anisotropic variogram with very long correlation length in the 45 degree direction is assumed to be accessible from other information. The sensitivity of the inverted results on the selection of the anisotropy and initial k model will be studied later.

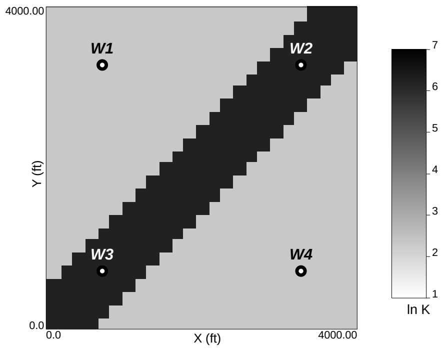

Figure 4.3: Reference deterministic permeability field. $ln(k)$ is the natural logarithm of permeability.

The pressure responses in the updated permeability field converge to the measured pressure data after 20 iterations (5 minutes in a SGI workstation). Figure 4.5 shows the resulting updated permeability field. The spatially connected high permeability band connecting wells W2 and W3 is seen clearly. Figure 4.6 shows the pressure values at the four wells computed from the initial uniform permeability field and from the final updated permeability field together with the results from the reference field. These responses in the initial field deviate dramatically from the true values, due to the poor initial model. However, the permeability field updated by the SSC method accurately reproduces the observed pressure data at all wells.

The information extracted from production data can be evaluated by comparing the true and estimated permeability values at the same cells. Figure 4.7 shows the distributions of estimated permeability values in high and low permeability regions, respectively. As no prior information on the permeability values was available before accounting the production data, the information obtained on the permeability distribution is quite significant. More importantly, the spatial distribution patterns of permeability are revealed (see Figure 4.5), which cannot be represented by the histograms on Figure 4.7.

It is difficult to obtain the correct variogram parameters, i.e., anisotropy angle and correlation length. Influence of these variogram parameters on inverse results is investigated. Sensitivity of the initial permeability values and the number of master points on the inversion results is also explored. Figure 4.8 shows the inverted permeability fields using different variogram parameters and different initial permeability values. The high permeability band is always obtained, indicating the robustness of the SSC method.

Production data were computed from coarse grid models in this example. SSC method was used to invert the permeability fields on the same coarse grid. This does not give reasonable flow responses and is rightly avoided in practice. The coarse grid models may be too coarse to provide realistic reference production data. A more realistic approach would be to create synthetic production data by solving the flow equation on a fine grid model. However, it is practically too expensive to directly invert permeability on the same fine scale, used to create production data. Therefore, the idea is to use a coarser model for the production data inversion. Then the coarse model inversion responses serve as constraints

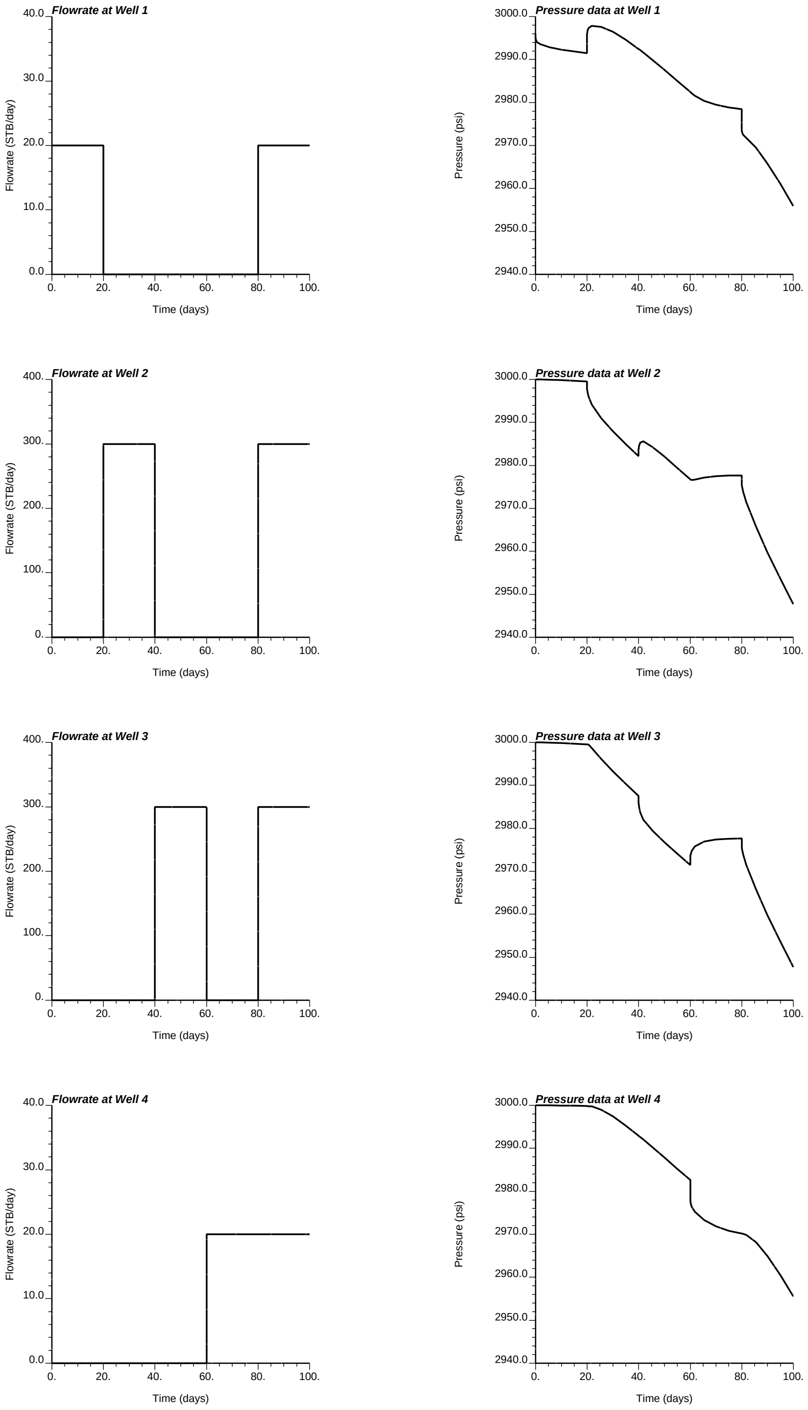

Figure 4.4: The production data (production rates and pressures) obtained from the reference field.

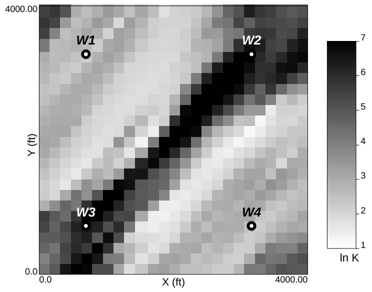

Figure 4.5: Final SSC-derived permeability field honoring pressure data from reference permeability field (see Figure 4.3).

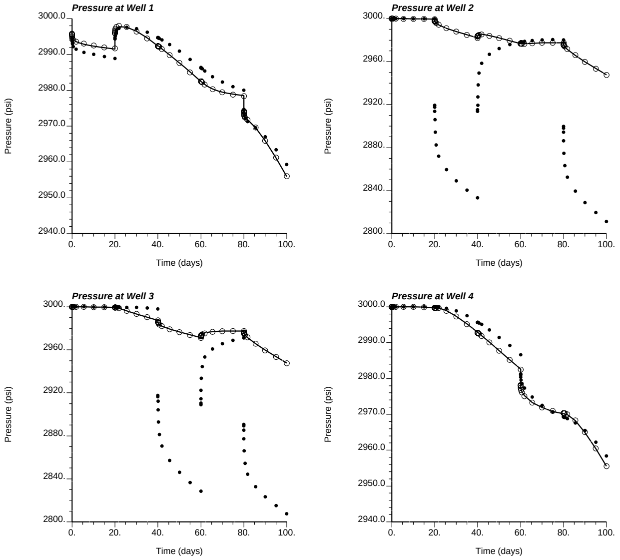

Figure 4.6: The pressure responses computed from initial (bullets) and updated (open circles) permeability fields together with the true data (solid lines).

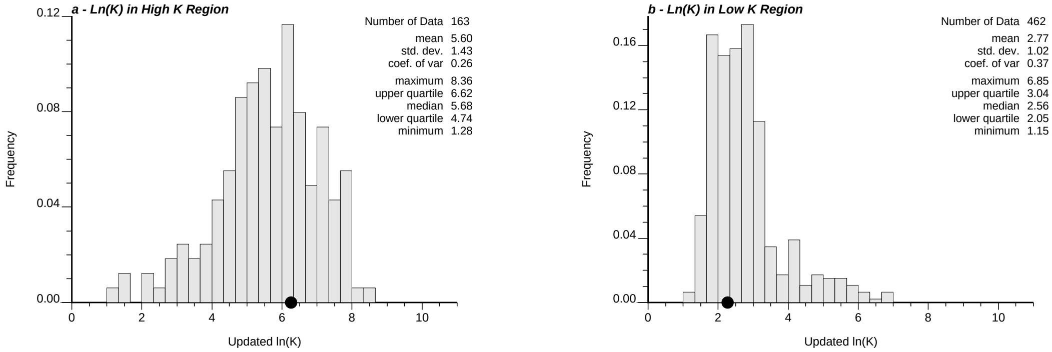

Figure 4.7: The histograms of updated permeability values in (a) high and (b) low permeability regions of the reference field. The bullets represent the true values in the reference field.

in constructing fine scale models.

4.3.1 Inversion of Pressure Data on Coarse Model

In the previous example, the production data were computed from a coarse grid reference model and the SSC method was used to invert permeability fields on the same coarse grid. This would not usually be the situation in field applications since simulation is usually done on a coarse scale. A more realistic test is to have the synthetic production data generated from simulation using a fine grid reference model. Then the inversion technique is used to create coarse grid models, which are subsequently used as spatial constraints for the construction of high resolution reservoir models (i.e., the two-stage approach, see Figure 4.9). An outstanding issue is to check that the matching of production data at the coarse grid model is preserved at the final fine grid model.

In the example, a 4000 ft × 4000 ft 2D square domain was discretized into 100 × 100 fine grid with cell size of 40 ft × 40 ft. A reference permeability model (see Figure 4.10a) at this fine scale was generated using sequential Gaussian simulation, `sgsim` (GSLIB, [61]). The mean and variance of $ln(k)$ were 3.0 and 3.0, respectively. The variogram model used to generate this reference field was anisotropic spherical, with correlation ranges of 1700 ft and 350 ft in the two principal directions. A coarse grid model (20 × 20) scaled up by geometric averaging from the reference field is shown in Figure 4.10b. This scaled-up coarse grid model is later used for visual comparison with the inverse coarse grid results.

Three wells (W1, W2, and W3) located at the center of fine scale cells (58, 88), (13, 43) and (88, 33) producing oil with varying production rates, analogous to the first example, and the corresponding pressure responses are shown in Figure 4.11. Wells W2 and W3 were connected by relatively high permeabilities, whereas well W1 was located in a low permeability region. Other parameters used in solving the flow equation for pressure on the fine (100 × 100) were the same as in the previous section.

Applying the SSC method, the coarse grid (20 × 20) permeability realizations are generated for which flow simulation matches the production data. Figure 4.12 illustrates three

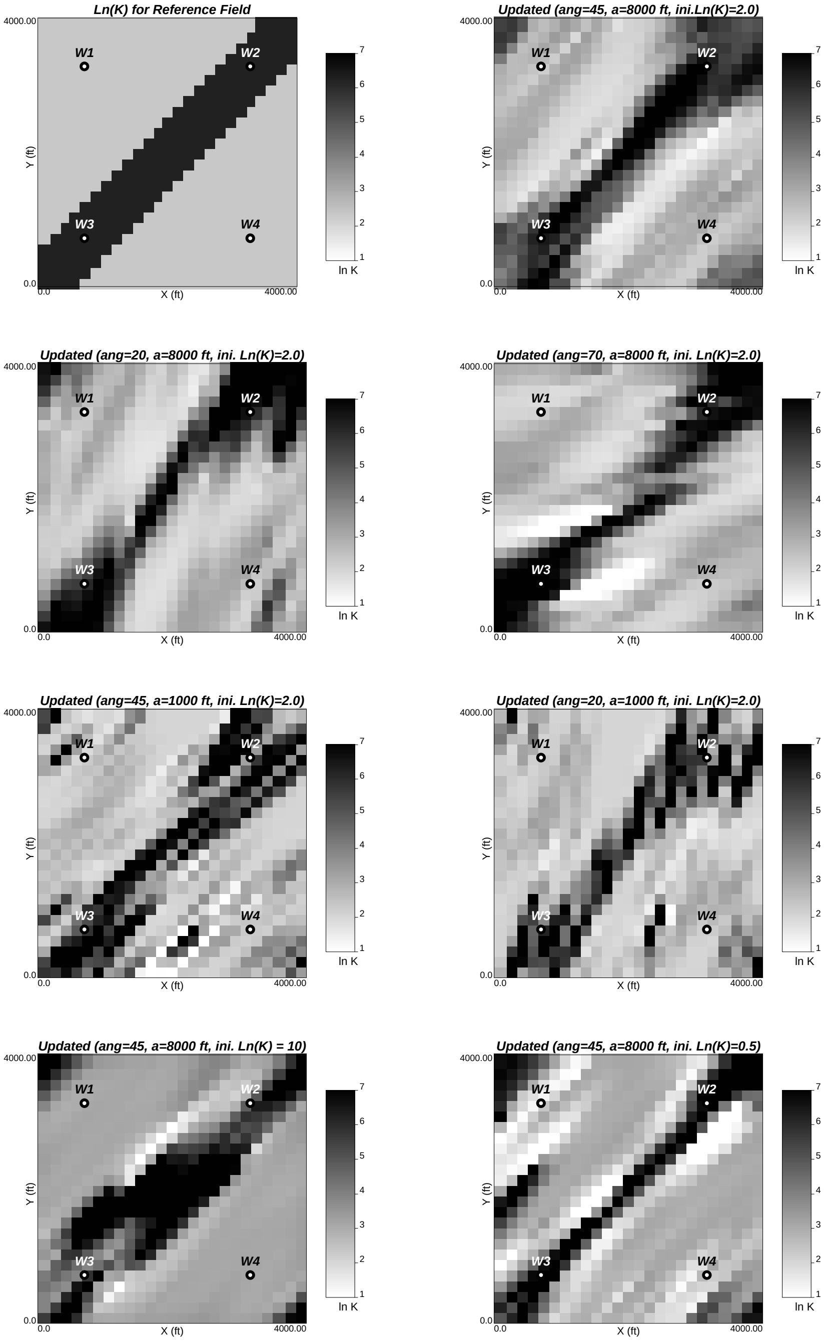

Figure 4.8: Inverse permeability fields from the SSC method by using different variogram parameters and different initial values.

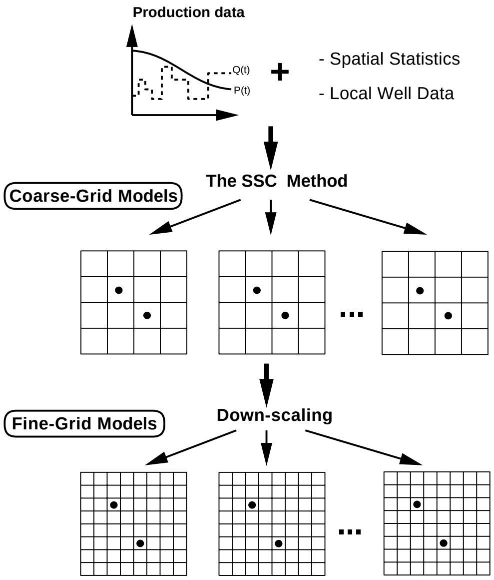

Figure 4.9: The schematic representation of the two-stage inversion technique.

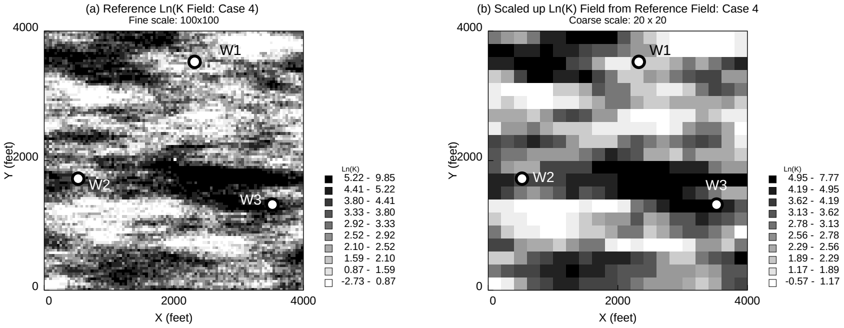

Figure 4.10: (a) The reference permeability field at fine scale, and (b) and the scaled up coarse grid permeability model: the second example.

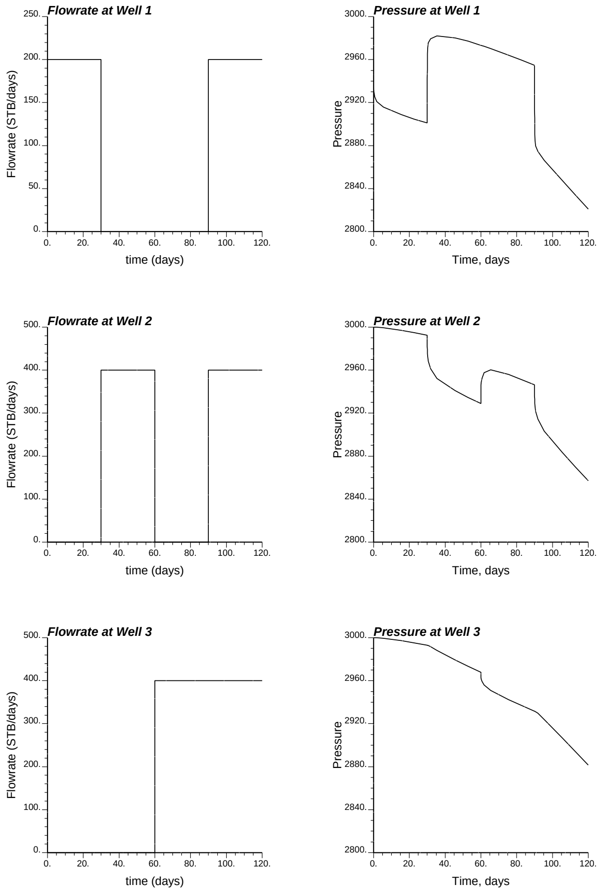

Figure 4.11: The production data (rates and pressures) obtained from the reference field at fine scale: the second example.

initial coarse scale permeability realizations generated using `sgsim`, and the corresponding three updated realizations by the SSC method. The statistics of the reference coarse grid model (Figure 4.10b) are used for generating these realizations (i.e., mean and variance of $ln(k)$ are 3.0 and 2.03, respectively; correlation lengths are 1800 ft and 400 ft in $X-$ and $Y-$ directions, respectively). Large differences are apparent among the initial realizations all of which deviate significantly from the reference coarse grid model. However, the spatial variation patterns in the updated realizations are much closer to the reference field, yet the difference from realization to realization is much smaller compared to the initial realizations. Figure 4.13 shows the pressure responses computed from a typical initial realization and its corresponding updated permeability realization compared with the true pressure data. The true pressure response is reproduced with high accuracy by the updated field, whereas the initial field's pressure responses deviate significantly from the true data.

Three hundred coarse-grid realizations were generated using the SSC method, from which the ensemble mean and standard deviation fields were computed and compared with the 300 initial fields (Figure 4.14). Figure 4.14 shows the reduced standard deviation (i.e., uncertainty) from the updated fields, particularly in the areas around the wells. Even away from the wells, the updated fields have lower standard deviations.

4.4 Construction of Fine Scale Permeability Models

A series of equiprobable realizations of coarse grid permeability fields can be generated using the SSC method. All of these realizations share the same histogram, variogram and production data. However in practice, more detailed geostatistical models are required for flow simulation predictions of reservoir performance. In this section, the promise of the two-stage approach to integrate production data is demonstrated using the SSC results of the first stage. Construction of fine scale models that honor the coarse grid realizations is a problem of downscaling.

Simulated annealing is one method that can construct fine scale permeability models based on the coarse grid realizations, as well as honor information on the histogram and variogram of fine scale permeability [55]. The first approach was to use annealing technique with an additional component to the objective function to represent the difference between the coarse grid permeability values and the power averages of fine scale permeabilities within the same coarse block, i.e.,

$$O_{mw} = \sum_{i=1}^{n_{cg}} \left[\overline{k}_v(\mathbf{u}_i) - \overline{k}^*_v(\mathbf{u}_i) \right]^2 \tag{4.16}$$

where n_{cg} is the number of blocks on coarse grid model, $\overline{k}_v(\mathbf{u}_i)$ is the inverse permeability value at coarse block $\mathbf{u}_i$, and $\overline{k}^*_v(\mathbf{u}_i)$ is the ω power average of fine grid permeability values within the coarse block $\mathbf{u}_i$, which is given as:

$$\overline{k}^*_v(\mathbf{u}_i) = \left[\frac{1}{N} \sum_{\mathbf{u}_i \in V} k(\mathbf{u}_i)^{\omega} \right]^{1/\omega}$$

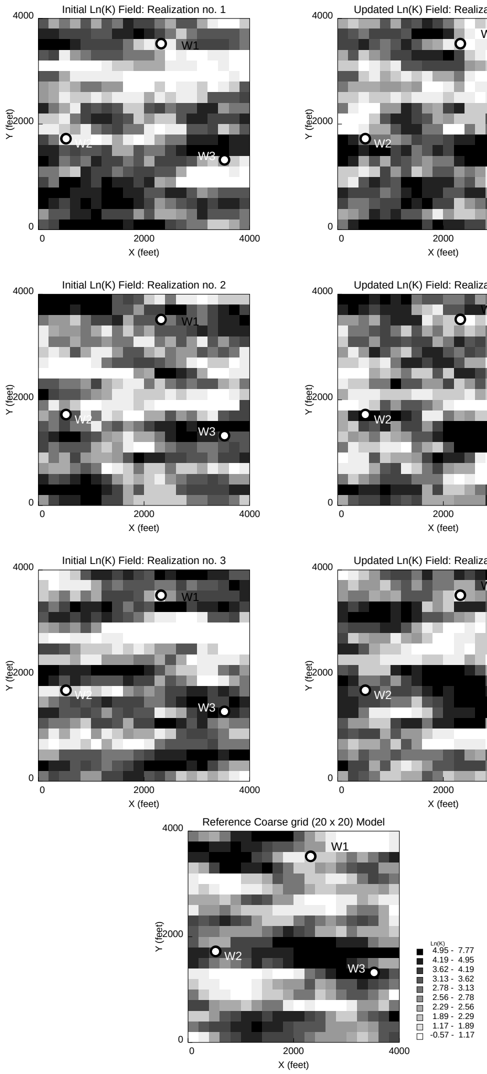

Figure 4.12: Three initial permeability realizations and the corresponding updated fields from the SSC method.

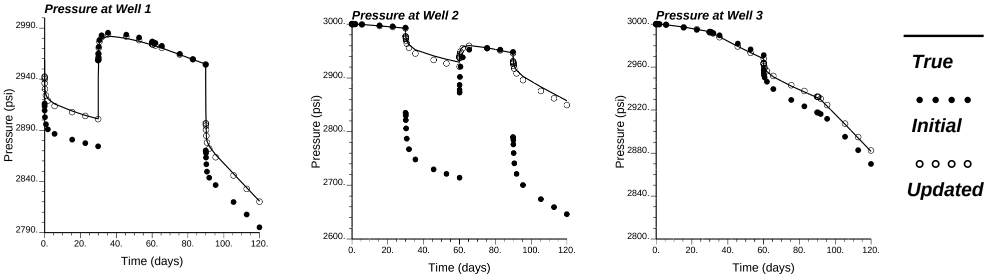

Figure 4.13: The pressure responses computed from the typical initial and updated permeability fields together with the true data in a typical realization: the second example.

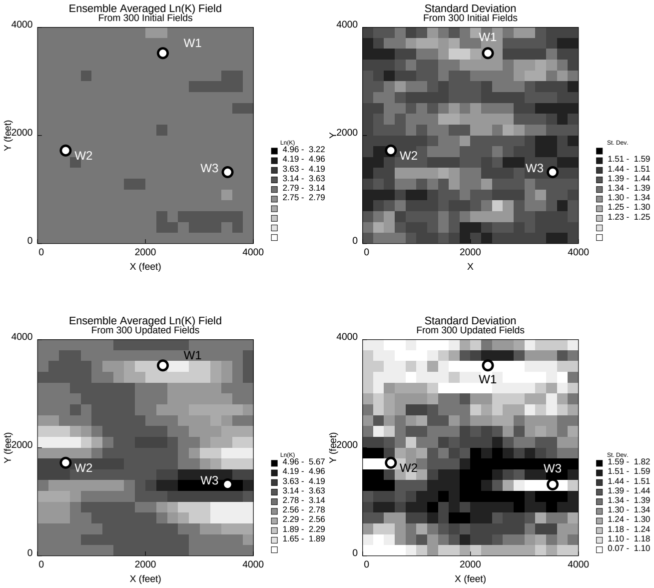

Figure 4.14: The ensemble averaged permeability field and the corresponding standard deviations from 300 initial and updated realizations: the second example.

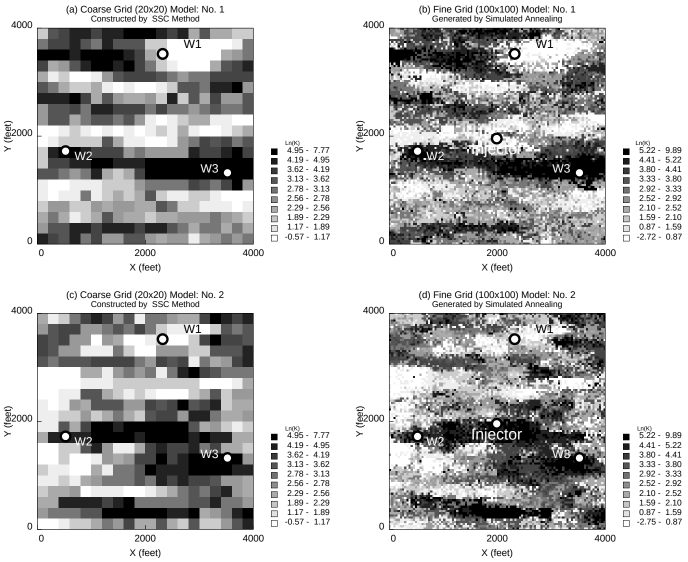

Figure 4.15: Two realizations of fine grid models, constructed by the simulated annealing method, that honor the coarse grid models generated by the SSC method shown on the left-hand side.

where N is the number of fine grid within a coarse block V. Different fine grid permeability models can be constructed, each of which matches the corresponding coarse grid permeability realization.

Figure 4.15 depicts two realizations of fine grid (100 × 100) permeability generated by this annealing technique and compared with the corresponding coarse grid (20 × 20) images from the SSC inversion in the second example. The histogram and variogram used to construct the fine grid models were taken from the fine grid reference model and geometric averaging ($\omega \rightarrow 0$) was used. Other types of data, e.g. seismic data, could also be honored at this stage.

In order to check if the fine grid permeability models still reproduce the dynamic production data, the pressure responses at the wells were solved on the fine grid models of Figure 4.15. Figure 4.16 shows the results (open circles) compared to the true responses from the reference field (solid lines) and the responses from the coarse grid model (bullets). The pressure responses are closely reproduced in the annealing-based fine grid permeability models. This indicates the promise of the two stage geological coding approach to integrate production data.

An alternative and more sophisticated approach for constructing fine grid models using the coarse grid spatial representations is to compute local conditional distributions of coarse grid permeability at each coarse grid block, then use simulated annealing to construct fine grid models integrating these probability constraints of the coarse grid values [61]. Nevertheless, the simpler approach presented above may see more extensive use in practice.

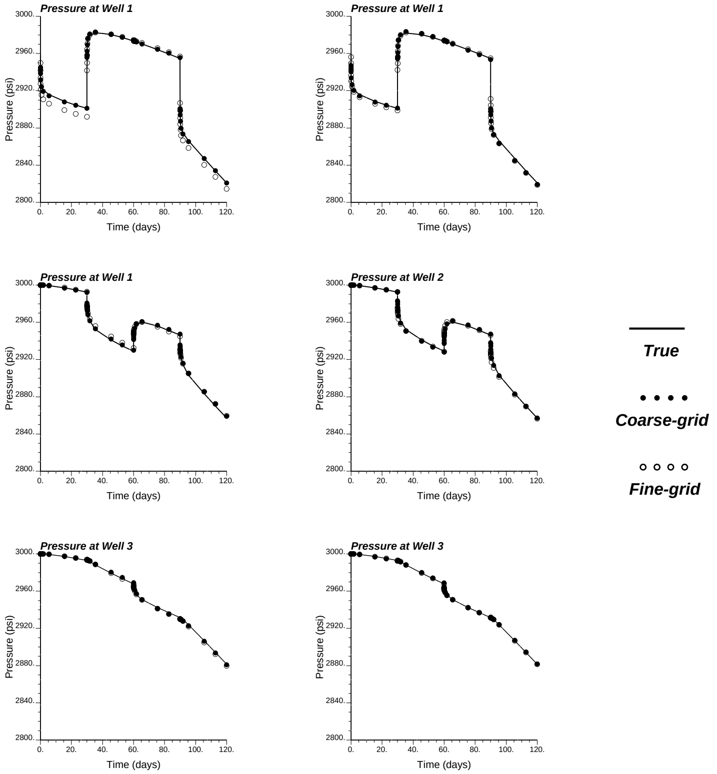

Figure 4.16: The comparison of pressure responses computed from fine and coarse grid models shown on the top of Figure 4.15 to the true results.

4.5 Performance Prediction Improvement by Dynamic Integration

The importance of integrating production data is exhibited by predicting the reservoir performance in Example 2 using two sets of fine scale (100 × 100) geostatistical models: one generated by `sgsim` not accounting for the production data, the other generated by simulated annealing accounting for the coarse-scale spatial representations derived from the production data as discussed previously. Two realizations of the second model are shown in Figures 4.15b,d. At 120 days, a water injection well located at the center of cell (50, 49) begins injecting water at constant rate of 20000 STB/day (see Figure 4.15). The three wells (W1, W2, and W3) are producing with constant pressure of 1000 psi. Although this example is for a multiphase situation, it was considered suitable in this context as permeability inversion was performed with the single-phase inversion formulation.

The comparisons of predicted total produced oil and water cuts in three wells (W1, W2 and W3) from 30 realizations of both models are shown in Figures 4.17 and 4.18, respectively. The true results computed from the reference fine-scale model are plotted as the thick, light curves. It is evident that the reservoir models, not conditioned to the production data overestimate oil production rates, severely overestimate water cuts at W1 but underestimate water cuts at W2 and W3 with large uncertainty. When the production data are integrated, the predicted performance is much closer to the true results with significantly less uncertainty. The low permeability barrier in the reference find grid model between the injection well and W1 is not well captured in the inverse coarse grid models. Also the variogram distance between the injection well and W1 is larger than other well pairs, thus there are more permeability variations between these two wells. These may explain why the predictions in W1 are so much away from the true results compared to the results at W2 and W3.

Figure 4.19 shows the histograms of total oil production rates of the entire field (Figures 4.19a,b), as well as the water cuts at individual wells (Figures 4.19c-h) from 200 unconditioned and conditioned models when the injected water is at pore volume injected (PVI) of 1.0. The true values from the reference field are shown in the same figure by bullets. The accuracy and uncertainty of forecasting are large using the models in which production data are not integrated, whereas integrating production data shows significant improvement in forecasting results in terms of accuracy and uncertainty.

4.6 Application to Facies Modeling

Integration of well production data in numerical geological modeling improves the reliability of reservoir forecasting. A methodology to derive facies proportion maps from multiple-well, single-phase, production data is presented here. SSC method is used to generate a series of coarse scale permeability maps from the production data. These permeability maps are then converted into facies proportion maps according to a calibration relationship between facies proportion and effective block permeability.

The facies proportion maps can be used with well petrophysical data, conceptual and descriptive geologic models, and geophysical data to create fine scale geostatistical reservoir

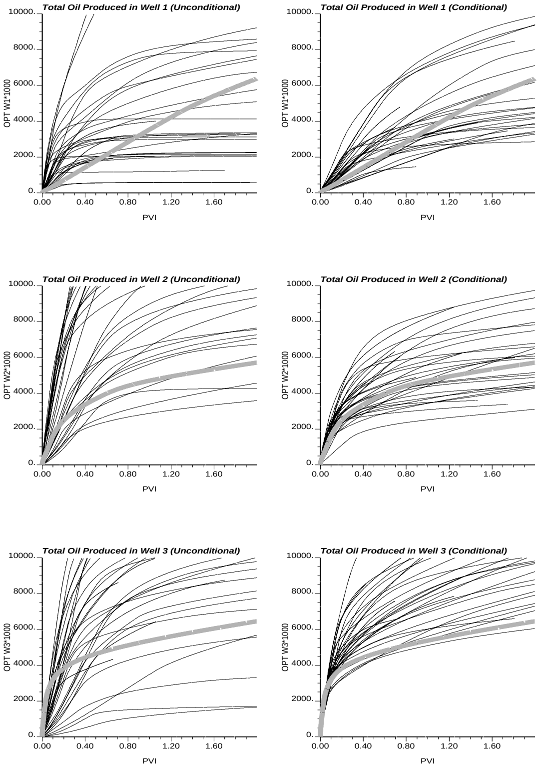

Figure 4.17: The total oil production rates at the producing wells from 30 unconditioned (left) and conditioned (right) realizations. The thick light curves are results from the reference true field.

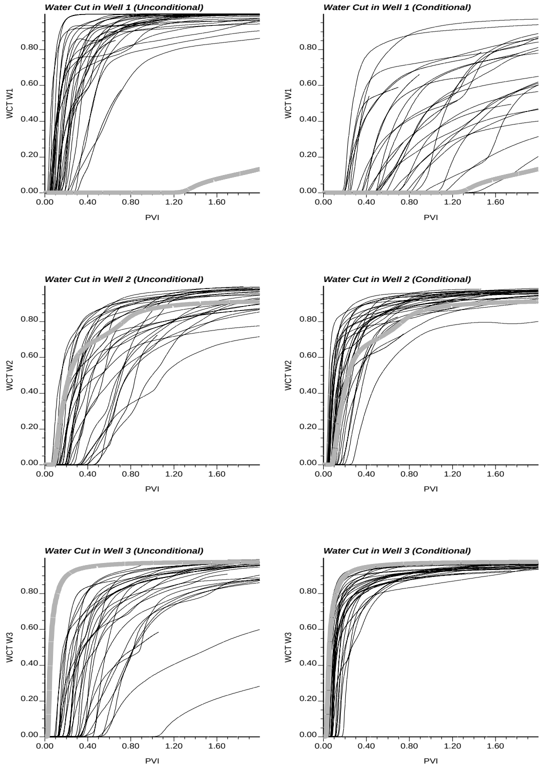

Figure 4.18: The water cuts at the producing wells from 30 unconditioned (left) and conditioned (right) realizations. The thick light curves are results from the reference true field.

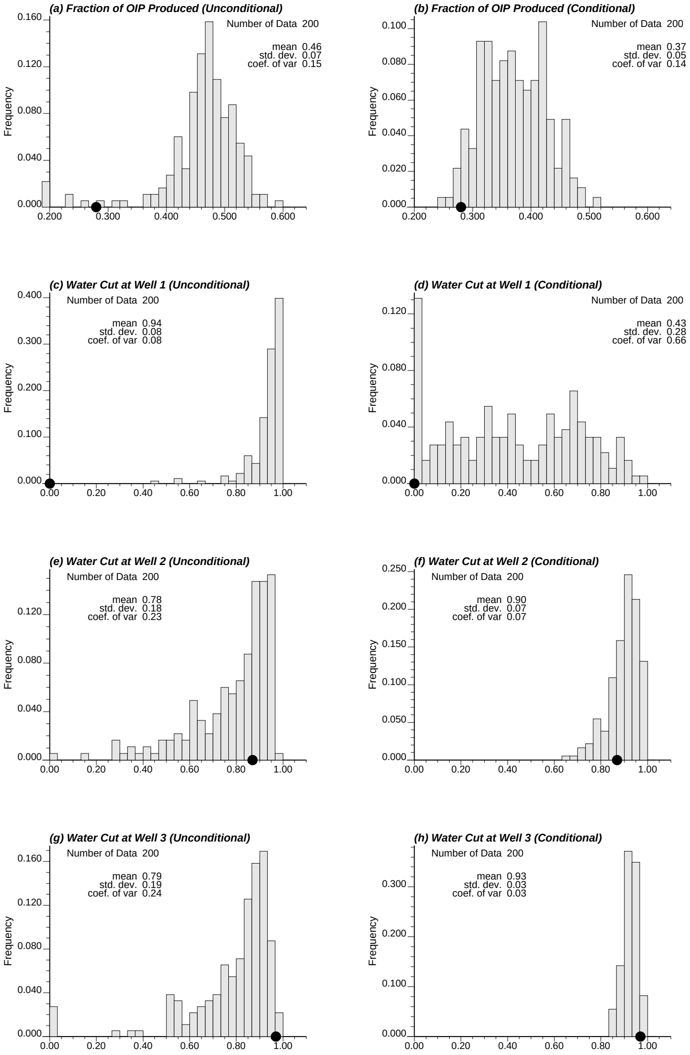

Figure 4.19: The histograms of total oil produced (a, b) and water cuts at three wells (c-h) from 200 unconditioned (left) and conditioned (right) realizations when the injected water is at $PVI = 1.0$. Bullets are the true results from the reference field.

models for reservoir management. The production data are thus honored indirectly in the final reservoir models, which reduces the need for extensive history matching.

Single-phase production data are used to infer reservoir facies proportions from the interpreted permeabilities. These single-phase production data are observed in primary depletion or before water breakthrough. Data considered are flowrate $q_i(t)$ and pressure $p_i(t)$ as a function of time, t, at any arbitrary number of well locations, $i = 1, \ \dots, n_i$. It should be noted that multiphase flow production data may be more important in many situations and can be addressed by a similar technique.

Application of SSC inversion provides multiple coarse-scale maps of permeability that reproduce the available rate $q_i(t)$ and pressure $p_i(t)$ data. Figure 4.20 gives a schematic illustration of the concept, that is, the temporal pressure and rate information at the well locations are inverted to a spatial description throughout the reservoir.

The permeability maps provide constraints on the distribution of facies derived by integrating other geological and geophysical data. The production data derived facies proportion constraints are limited to two "lumped" petrophysical facies: one low permeability facies and one high permeability facies. Considering more than two facies leads to ambiguous results.

A calibration approach is necessary to relate coarse-scale permeability to facies proportions. Fine scale facies models are first constructed with spatially variable proportions of high and low facies. The effective permeability is calculated by flow simulation for coarse-scale blocks. Then, a cross plot between facies proportion and effective permeability is constructed. For a given coarse-scale permeability value, the conditional distribution of associated facies proportions can be extracted. The higher the permeability, the greater is the proportion of high-permeability facies. Figure 4.21 gives a schematic illustration of a calibration cross plot and the facies proportion distribution for a coarse-grid block permeability of 100 md.

The facies proportion maps are constructed by merging the coarse scale permeability maps obtained from the SSC inversion and the calibration relationship. There are L permeability values $(k_i, i = 1, \dots L)$ for each coarse block from as many realizations derived from the SSC inverse method. For each of these permeability values, all possible facies proportions are retained that fall within a narrow window, $[k_i - \Delta k, k_i + \Delta k]$, from the calibrated relationship of facies proportion $(P_i^j, j = 1, \dots, N_i)$ and effective permeability. All facies proportion values are then combined into a histogram of possible facies proportions at each location. The local distributions of facies proportions may be summarized by local mean and variance values.

There are two sources of uncertainty in the facies proportion maps. First, the effective permeability inferred from the production data is non-unique. It is not possible to uniquely determine the permeability everywhere using limited production data. However, useful spatial trends and information around the well locations can be extracted. Second, as illustrated on Figure 4.21, the calibration of facies proportion to effective permeability is also non-unique. Both of these sources can be quantified allowing to create a map of the expected facies proportion and the associated uncertainty in facies proportion.

The coarse-scale facies information derived from production data could be used as a production-data based check on a conventional or geostatistically derived facies model developed from core, seismic and well log data. It is, however, better to use the facies propor-

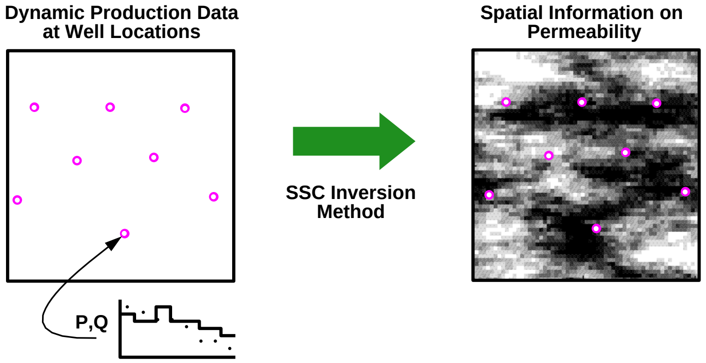

Figure 4.20: A schematic illustration of the concept behind the SSC inversion method: the dynamic data at the well locations (the pressure and rate is illustrated at one well only) is converted to information on the spatial distribution of permeability. The gray scale illustrates areas of high and low permeability.

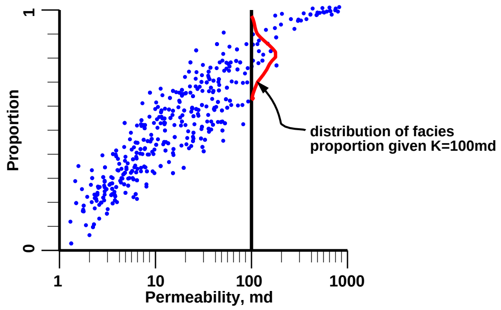

Figure 4.21: A schematic illustration of the calibration between permeability and facies proportion. The conditional distribution of facies proportion given $k = 100$ is shown.

tion maps as an input data to build high resolution 3D facies models. These models can be constructed by a variety of geostatistical techniques.

Applications of the methodology are demonstrated in the following sections using synthetic data sets. The sensitivity of results on the distributions of facies permeability is also investigated.

4.7 A Fluvial Reservoir Example

A fluvial reservoir, dominated by the distribution of high permeability channel sand within a background of low permeability floodplain shales, is considered. The reference facies model was constructed by `fluvsim` [63]. An isometric view of the reference model is shown on Figure 4.22. The permeability of the fluvial channel sand and floodplain shale are constant 1000 md and 1 md, respectively. Historical production data were simulated using three well locations shown on the 3D fine-scale model (W1, W2, W3 on Figure 4.22). The rate and pressure data (see Figure 4.23) are used to infer the proportion of channel sand facies.

A 2D map of the reference sand proportion and the upscaled permeability are shown on Figure 4.24. The global proportion of channel sand in the model is 0.50. The cross plot of

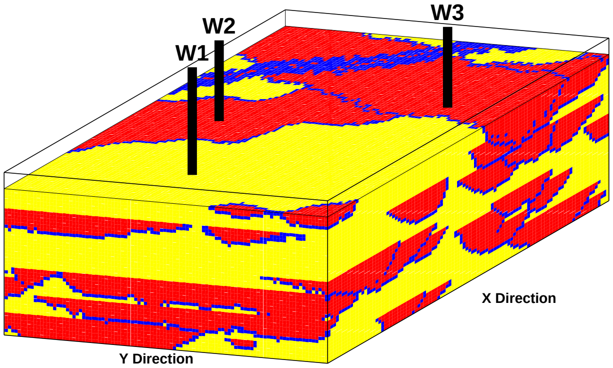

Figure 4.22: An isometric view of the reference fluvial model. The high permeability fluvial channel facies (darker color) are embedded within low permeability floodplain shales.

the sand proportion versus coarse-scale permeability (see Figure 4.25) is used for calibration only.

Based on the simulated production data and the histogram and variogram of the coarse scale permeability values, the SSC method was used to construct multiple realizations of coarse scale permeability. Figure 4.26 shows the first four realizations in which the production data are matched. The pressure match for one realization is given in Figure 4.23. Two hundred realizations of coarse scale permeability were constructed. To summarize the results, the ensemble averaged permeability field and the corresponding variance field are shown on Figure 4.27.

The sand proportion for each coarse block can then be computed using the procedure described in Section 4.6. The relationship between permeability and facies proportion (Figure 4.25) has little spread. Therefore, the sand proportion maps look very similar to the permeability maps. After conversion, Figure 4.28 shows the ensemble mean proportion and a cross plot of the true proportion and estimated proportion. The regions of low and high sand proportion have been identified, although there are regions of indeterminate sand proportion.

In order to show the value of more production data, the entire procedure was repeated using the production data from 20 wells instead of the original 3 wells. An SSC inversion realization, the cross plot between the true sand proportion and the estimated sand proportion, and the final ensemble mean and variance of the sand proportion are shown in Figure 4.29. Higher correlation coefficient clearly indicates the added value of using more production data: more accuracy with less uncertainty.

4.8 Another Example - Carbonate Reservoir

The facies in this example have less spatial structure and less certain distributions of permeability. The 2D reference distributions of facies and permeability are shown on Figure 4.30. The “patchy” spatial distribution of facies is more representative of a reservoir with a strong

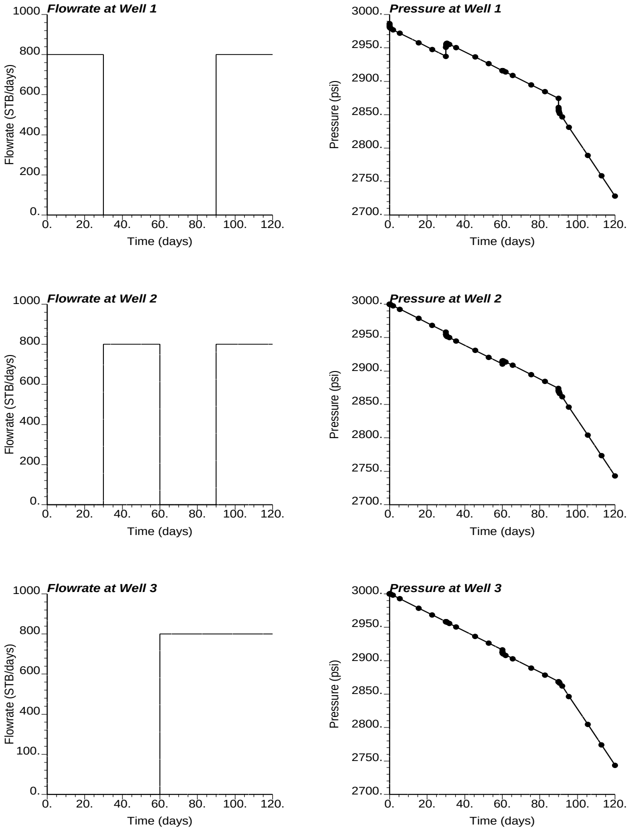

Figure 4.23: Production rates and pressure responses at the three wells. The pressure match for one permeability realization generated by the SSC method is also shown by bullets on the right-hand side figures.

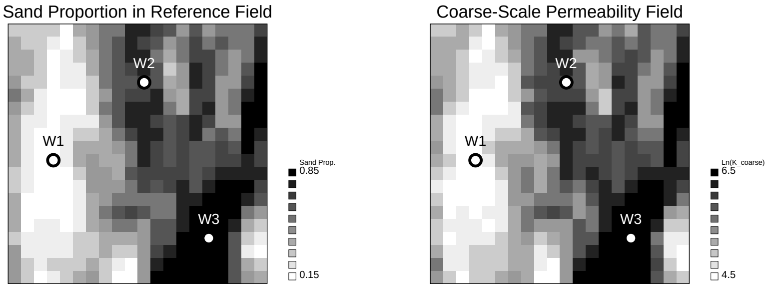

Figure 4.24: Proportion of sand from the reference model and the upscaled coarse-scale permeability field (used for calibration only - historical production data taken from fine-scale model).

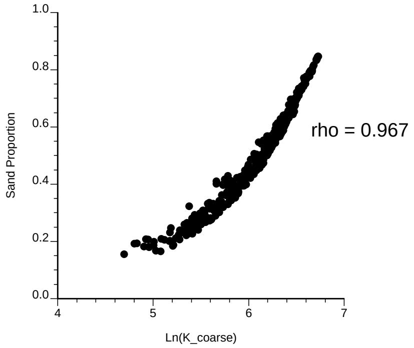

Figure 4.25: Cross plot of sand proportion and upscaled permeability.

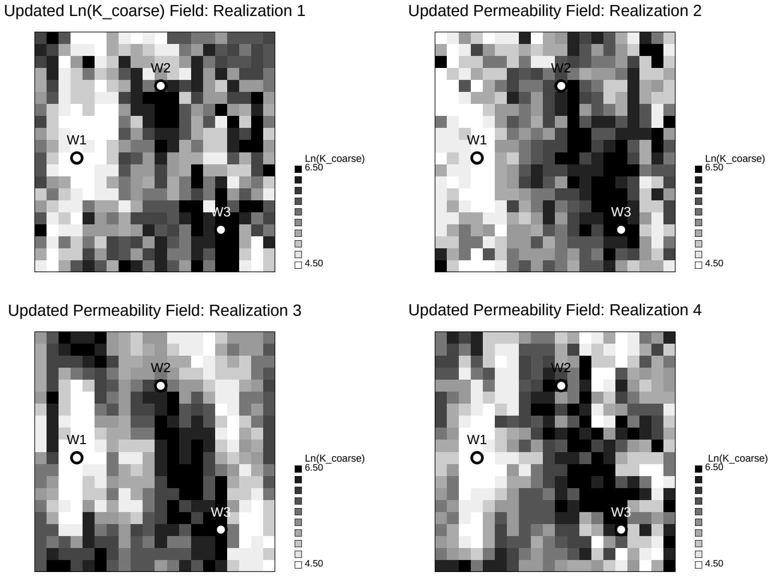

Figure 4.26: Four coarse-scale realizations of permeability that match production data at three well locations.

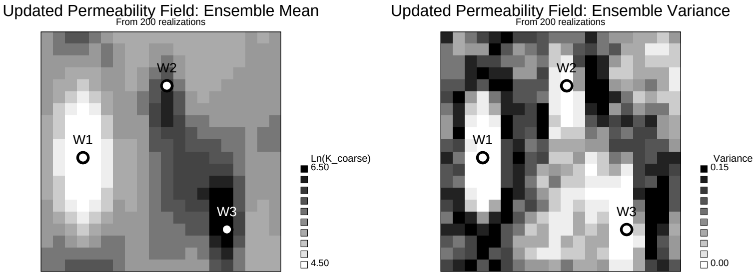

Figure 4.27: The ensemble average mean and variance of the coarse-scale permeability computed from 200 realizations.

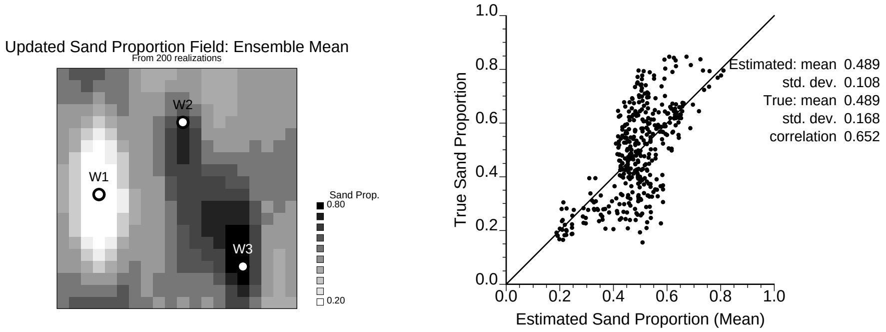

Figure 4.28: The ensemble average mean facies proportion and a cross plot between the true sand proportion (from 3D fluvial model) and estimated sand proportion (average of 200 realizations).

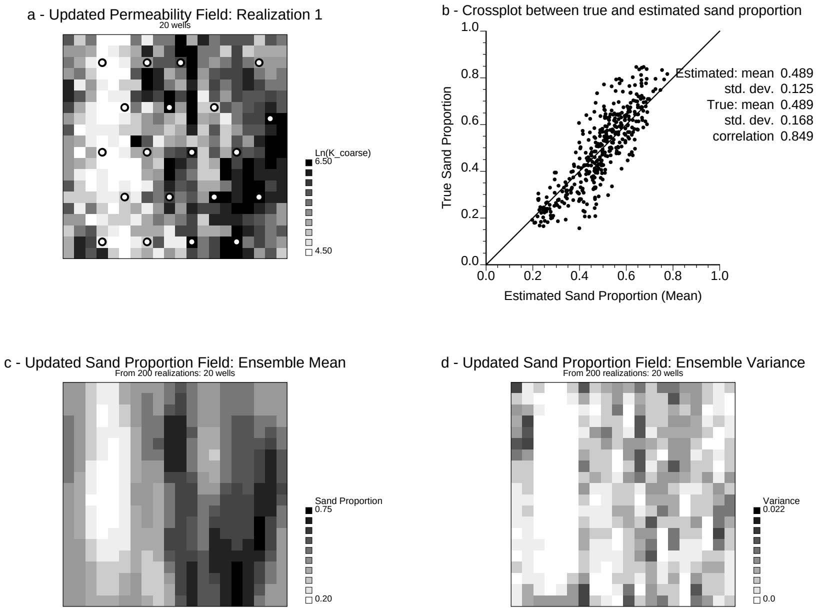

Figure 4.29: The results when production data for 20 wells are used. (a) One realization of the SSC inversion, (b) the cross plot between the true sand proportion and the estimated sand proportion, (c) and (d) the final ensemble mean and variance of the sand proportion, respectively.

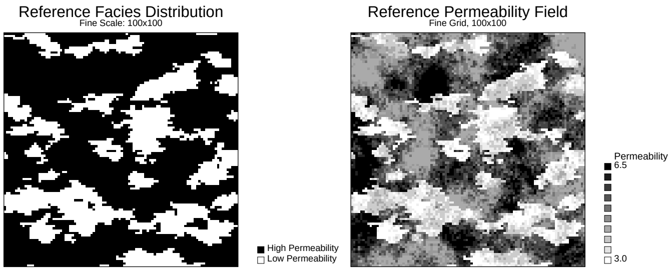

Figure 4.30: Reference facies and fine-scale permeability distributions for the second example.

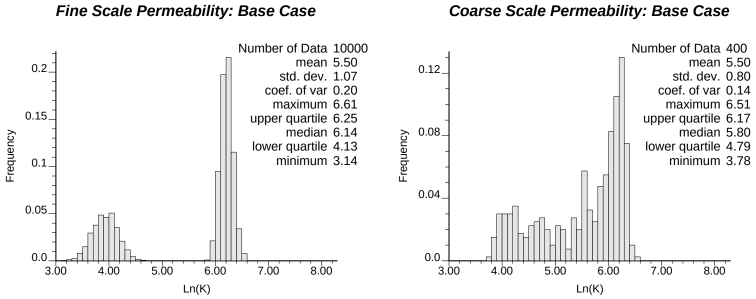

Figure 4.31: Histogram of fine-scale and coarse-scale permeability calculated from reference image.

diagenetic overprint, such as a carbonate reservoir. High permeability facies proportion is 70%.

The base case histograms of permeability in the "high" and "low" permeability facies are shown on Figure 4.31. The coarse grid histogram of permeability does not show a bimodal character. Although the high permeability and low permeability modes disappear, there is still valuable information on the facies proportions. Figure 4.32 shows the reference coarse-scale facies proportion map and permeability map together with cross plot between the two - for calibration. This calibration cross plot indicates the dependence of coarse-scale permeability on the facies.

The procedure, described in Section 4.6, was followed to generate facies proportion maps. The intermediate coarse scale permeability maps were generated using 3 wells and 20 wells of production data. They were converted to facies proportions using the calibration relationship. The facies maps were checked for correspondence with the truth, which is known in this synthetic example. Figure 4.33 summarizes the results by cross plotting the true proportion and estimated mean proportion using 3 wells and 20 wells of production data. The correlation between the true and estimated mean proportion is not as good as the first example, mainly because the facies have a smaller range of correlation. However, as expected, there is some improvement when there are 20 wells.

The quality of the areal facies proportion maps depends on the histograms of permeability in the high and low permeability facies. As a sensitivity case, the inversion/calibration

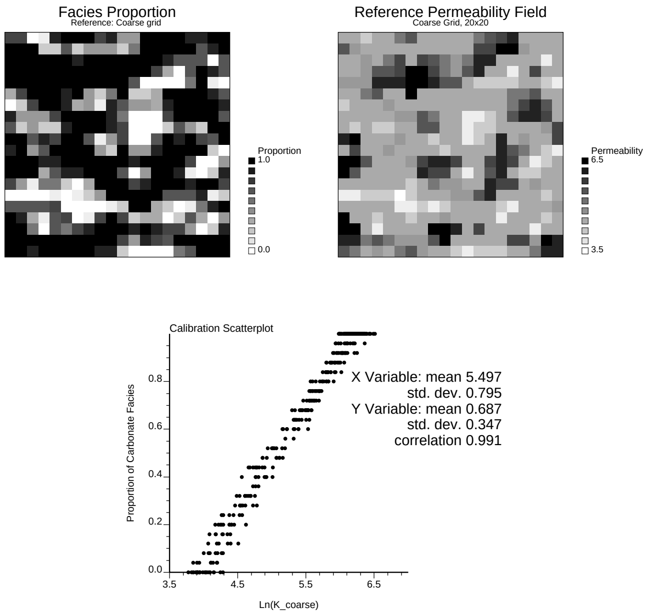

Figure 4.32: Reference coarse-scale facies proportion map and permeability map together with cross plot between the two - for calibration.

was repeated with distributions of permeability that overlap (see Figure 4.34). The calibration cross plot now has more uncertainty (see Figure 4.35). Repeating the procedure (permeability ⟶ proportion maps ⟶ summarize), leads to the results on Figure 4.36. As expected, the results are systematically poorer than the results from the base case (Figure 4.33). In the extreme case, with completely overlapping permeability distributions, there would be no possible facies resolution from the production data alone. This example also reveals, for a reservoir having significant facies variations at a finer scale, the facies-specific permeabilities are averaged out at the coarse-scale obtained from the production data. The estimation of individual facies proportions then is subject to increased error.

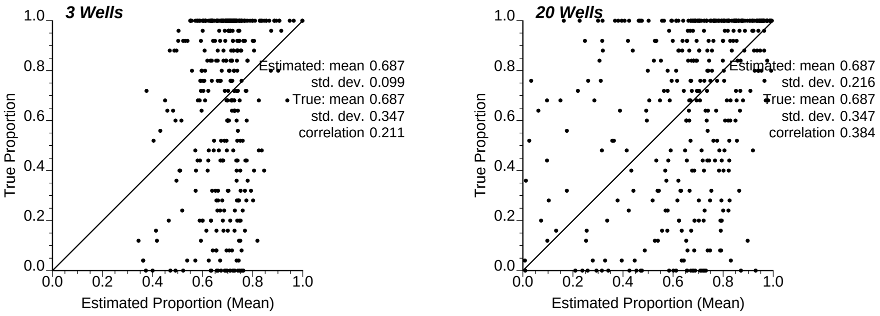

Figure 4.33: Cross plot of true proportion and estimated mean proportion using 3 wells and 20 wells of production data (same well conditions as first example).

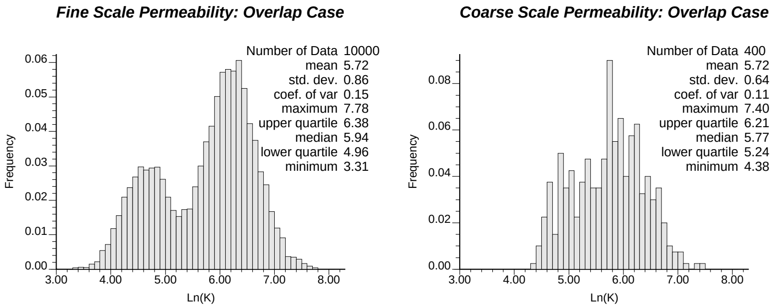

Figure 4.34: Histograms of fine-scale and coarse-scale permeability calculated considering facies that overlap.

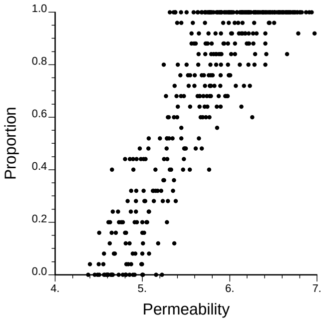

Figure 4.35: Calibration cross plot using the "overlap" distributions of permeability. The calibration has greater variability than the base case (Figure 4.32).

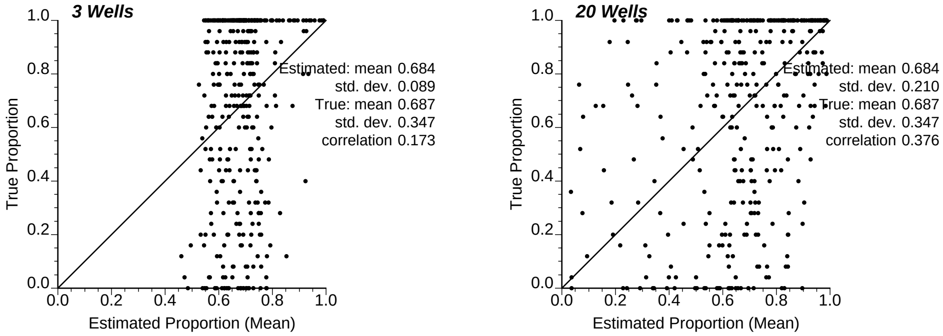

Figure 4.36: Cross plot of true proportion and estimated mean proportion using 3 wells and 20 wells of production data using the "overlap" distributions of permeability.

4.9 Uses for Facies Proportion Maps

The facies proportion maps are directly useful for mapping areas with greater and lesser *pay* facies. The resulting maps can be used to guide the location of new wells or to assess areal sweep efficiency.

The facies proportion maps, obtained by this technique, can also be used as constraints for creating more detailed geostatistical facies models. There are two primary reasons to create more detailed geostatistical facies / porosity / permeability models that account for the production data-derived facies maps. First, there is additional information from seismic data and detailed well logs and cores that must be accounted for. Second, more refined reservoir management is possible using reservoir simulation that needs 3D input and local refinement around wells for reliable predictions. A number of methods can be used to build more detailed models using coarse-scale information:

1. *Multiple Truncations of a Gaussian Field* [61, 113, 133, 197] or “truncated Gaussian simulation” permits the simulation of a categorical variable with an underlying trend. In practice, the areal and vertical proportion curves used in truncated Gaussian simulation are established from seismic data or mapping geologic trends. The proportion maps from production data can be used directly.

2. *Sequential Indicator Simulation* [3, 61, 75, 109, 111] can directly use production-data derived proportion maps as prior mean values.

3. *Object based modeling* techniques [63, 72, 84, 176, 180, 181] consider the production-data derived proportion maps as so-called “intensity functions” to increase the likelihood of specific facies where the proportion is high.

Most commonly applied facies modeling techniques permit the use of locally varying proportions. This flexibility was added primarily to use seismic data and geological trends. However, the same flexibility can be adapted to production data-derived proportions.

4.10 Discussion

An outstanding challenge in reservoir characterization is understanding the constraints on the spatial distribution of facies provided by well production data. The methodology presented in this chapter provides a tool to guide facies mapping using single phase multiple-well production data. These data are available in primary depletion and before water breakthrough, that is, early in the life of a reservoir. A number of important reservoir management decisions have to be made during these early stages. The methodology, discussed here, should be very useful. The use of multiphase production data remains an important and active area of research.

Examples were presented to demonstrate the efficacy of the proposed methodology. The SSC method establishes multiple realizations of coarse-scale permeability that can be translated into constraints on the proportion of facies with the aid of a calibration. Comparison of the results with 3 wells and 20 wells illustrated the value of more production data and the ability of the method to converge toward the true facies distribution.

These examples also illustrated some of the limitations of the approach. First, it is limited to considering two petrophysical facies groups - a low and high permeability facies. Second, the calibration depends on the overlap of the permeability histograms between the coarse-scale permeability and lumped facies. The examples also provided some rules-of-thumb for the conditions to expect reasonably good estimates of the coarse-scale facies proportion, that is, for a high correlation and low standard deviation between the true proportion and the estimated proportion. The estimates should be reasonably good when both the core-measured permeability histograms have little overlap and the areal extent of reservoir facies is on the scale of the coarse-scale representation. These conditions were present in the fluvial example. Such conditions will be true for many siliciclastic environments for which there are large-scale pay and non-pay facies. In addition to fluvial channel systems, some examples are lower shoreface, deep water channel-levee, and deep water fan-lobe complexes. Finally, it was also shown how the *lumped* facies proportions can be used to guide subsequent geostatistical modeling of a greater number of lithofacies.

4.11 Exercise

4.11.1 Problem Setting

We will use the same reservoir data as that used in Chapter 3 for single-well single-phase inversion. Only number and locations of the wells are different. Again, for simplicity and applicability of the supplied programs, we restrict ourselves to 2D with a constant thickness of 20 ft. Areal extent of the reservoir is discretized by a 64 × 64 grid of the dimension 100 ft ×100 ft. Other reservoir and fluid properties are: ϕ 0.2, B 1.4, p_i 1502.008 psia, μ 0.3 cp, and c 5.5×10^{-5} 1/psia. Initial reservoir pressure is 1502.008 psia. A reference $\ln(k)$ distribution is available (ref2d.dat). This is usually obtained from static (both hard and soft) data integration. The mean and variance of $\ln(k)$ are 0.73 and 0.6084, respectively. The reference $\ln(k)$ distribution is modeled by a two-structure variogram model with no nugget effect. The first structure is a spherical model with horizontal ranges 900 and 1400 ft and sill contribution of 0.5, and the other is a Gaussian model with horizontal ranges 1500 and 3200 ft and sill contribution of 0.5. There are 5 wells, located at the center of the grid blocks: (10,50), (32,40), (40,40), (39,30) and (50,8). Each of these wells has the same wellbore radius of 0.33 ft. The wells are producing with constant flow rates of 10, 15, 15, 15 and 7.5 (STB/DAY) respectively. No flow boundary is considered.

4.11.2 Steps Through the Multiple-Well Single-Phase Inversion Exercise

S1 Perform forward flow simulation to obtain synthetic well test data.

This step is required only when well test data are not available from any other source. Program supplied here, `spsim`, has the limitation of having same flow rates for all wells. The parameter file for `spsim` is the same as shown in Section 3.11. Thus, it is not repeated here. However irrespective of the provenance, all data required for the inversion process should be arranged in the format shown below.

Reservoir and well data are given in `wellpara.dat`, which is shown below in Figure 4.37. First line in Figure 4.37 has 5 records. These are number of wells: 5, ϕ 0.2, thickness 20 ft, μ 0.3 cp, and c 5.5×10^{-5} 1/psia. The subsequent 5 lines give i, j locations and wellbore radius of each well.

```
5    0.2     20.0    0.3     5.5e-5
10    50    0.33
32    40    0.33
40    40    0.33
39    30    0.33
50     8    0.33
```

Figure 4.37: Data file for reservoir and well parameters.

Boundary condition options and boundary flow rates are provided in data file `boundary.dat`. This is shown in Figure 4.38. First line in Figure 4.38 has 64 records of value 0 indicating no flow condition for each cell in the top boundary. Next 64 lines have 2 records of value 0 indicating no flow condition for each cell in the left and right boundaries. Again, next line has 64 records of value 0 for no flow condition for each cell in the bottom boundary. In a similar format except for using floating point numbers, subsequent 66 lines give the flow rates at each of these cells.

```
0 0 0 0 0 ... 0 0 0 0 0
0 0
0 0
 .
 .
 .
0 0
0 0 0 0 0 ... 0 0 0 0 0
0. 0. 0. 0. 0. ... 0. 0. 0. 0. 0.
  0.   0.
  0.   0.
      .
      .
      .
  0.   0.
0. 0. 0. 0. 0. ... 0. 0. 0. 0. 0.
```

Figure 4.38: Data file for boundary conditions and flow rates.

From some source or real well test, data must be available for the dynamic data integration. Flow rate data are given here in data file `flowrate.dat` Format of this data file is excerpted here in Figure 4.39. The only record in the first line is the number of time steps. For each time step, 6 records must be there in the subsequent lines. These records are time in days, and flow rates of the five wells in the correct order.

```
          50
     .010    -10.00    -15.00    -15.00    -15.00     -7.50
     .020    -10.00    -15.00    -15.00    -15.00     -7.50
     .030    -10.00    -15.00    -15.00    -15.00     -7.50
     .040    -10.00    -15.00    -15.00    -15.00     -7.50
          ...        ...        ...        ...
 1033.050    -10.00    -15.00    -15.00    -15.00     -7.50
 1133.050    -10.00    -15.00    -15.00    -15.00     -7.50
 1233.050    -10.00    -15.00    -15.00    -15.00     -7.50
 1333.050    -10.00    -15.00    -15.00    -15.00     -7.50
```

Figure 4.39: Data file for flow rates.

Well pressure data are in the data file `wellpress.dat`. The format of this file is shown below in Figure 4.40. The two records in the first line are number of wells and number of time steps. Following lines have 11 records: time in days, and pressure (psia) and weight data for five wells.

```
   5    50
    .01  1484.607  1  1468.533  1  1472.980  1  1473.825  1  1482.919  1
    .02  1484.264  1  1468.009  1  1472.468  1  1473.312  1  1482.641  1
    .03  1483.974  1  1467.538  1  1472.015  1  1472.857  1  1482.406  1
    .04  1483.705  1  1467.090  1  1471.589  1  1472.429  1  1482.183  1
       ...        ...        ...        ...        ...        ...
1033.05  1406.792  1  1344.673  1  1355.659  1  1357.363  1  1409.159  1
1133.05  1400.716  1  1338.334  1  1349.251  1  1351.055  1  1403.410  1
1233.05  1394.670  1  1332.070  1  1342.921  1  1344.824  1  1397.675  1
1333.05  1388.655  1  1325.869  1  1336.659  1  1338.658  1  1391.954  1
```

Figure 4.40: Data file for well pressures.

Initial pressure data is provided in data file `pinit.dat`. Format of this data file is shown here in Figure 4.41. First line gives the title of the file. Second line has only record indicating the number of columns available in the file. Next few lines (as many as the number of columns indicated before) have the column headers. Subsequent 64×64 lines give the initial pressure for each cell in the data grid.

```
Initial Pressure file
1
Initial Pressure (PSIA)
 1502.008
 1502.008
 1502.008
    .
    .
    .
 1502.008
 1502.008
```

Figure 4.41: Data file for initial grid pressures.

S2 Integrate well test data with other static data.

The `ssc` program is used for the integration of multiple-well single-phase dynamic data inversion. Parameter file, `ssc.par`, for the `ssc` is shown below in Figure 4.42.

Here, the number of "master points" used is 25 (=5 × 5). Maximum number of outer iterations to update the master points is 3. A factor of 3.0 is used for defining constraint interval for optimization. Maximum number of outer iteration, relaxation parameter and minimum tolerance are 15, 0.3 and 0.01 respectively. Optimization parameters are 50, 5.0×10^{-4}, 5.0×10^{-4}, 5.0×10^{-3} and 40. These are minimum number of iterations, tolerances for checks of norm 1, norm 2 and difference in objective functions in two consecutive iterations, and number of times the differences of two consecutive objective functions becomes less than the tolerance specified, respectively. A search radius of 2000 ft is used for kriging. Minimum and maximum number of samples for kriging are 1 and 24. Type of kriging used is "ordinary kriging" indicated by 0. The other option available is "simple kriging" indicated by 1. The variogram model from the reference distribution is used. Besides the data file mentioned earlier, the `ssc` program needs a seed file (here, `seed.dat`) with $\ln(k)$ data.

N1 Users should determine histograms, variograms of the generated realizations and check how good are the histogram, variogram reproduction. Adjustments should be done by tuning different parameters in order to get better reproductions.

N2 One might be interested in exploring the cases for increased maximum number of outer iterations, or finer tolerances.

N3 The objective function values, the pressure match responses should be inspected to check whether a good optimization is obtained.

```
                  Parameters for SSC
                  *******************

START OF PARAMETERS:
******                       -file with local well conditioning ln(k) data
1  2  3  4                   -columns for X, Y coordinates, perm. & error
0  5                         -num of ln(k) data, num of wells with flow data
1                            -index for identifying desired histogram
..\workdir\ref2D.dat         -file with ln(k) histogram (scale of SSC model)
2  0                         -columns for permeability and weight
0.73   0.6084                -mean and variance of ln(k) distribution
..\workdir\wellpara.dat      -file with reservoir and well data
..\workdir\flowrate.dat      -file with input flow rate and time step data
..\workdir\wellpress.dat     -file with input pressure data
..\workdir\boundary.dat      -file with boundary conditions
..\workdir\pinit.dat         -file with initial pressure for the entire field
..\workdir\seed.dat          -file with input realizations
1  1  1                      -number of total, start and end realizations
-999.0  1.0e21               -trimming limits for missing values
3                            -debugging level
..\workdir\ssc2d.dbg         -file for debug output
..\workdir\ssc2d.out         -file for output ln(k) realizations
..\workdir\obj2d.out         -file for output obj func after each iter
..\workdir\prematch2d.out    -file for output matching of pressure responses
64  50.0  100.0              -X grid size: nx, xmn, xsiz
64  50.0  100.0              -Y grid size: ny, ymn, ysiz
38774                        -random number seed
5  5                         -num of master points in X and Y
3                            -num of outer iter to update master points
3.0                          -factor for constraint interval for optim.
15  0.3  0.01                -max num of outer iter, dumping para & min tol
50  5.e-4  5.e-4  5.e-3  40  -optimization parameters
2000.                        -search radius for kriging
1  24                        -min and max num. of samples for kriging
0                            -type of kriging
2  0.0                       -nst, nugget effect
1  0.5  0.0  900.0  1400.0   -type, sill, azm, max range, min range
1  0.5  0.0  1500.0  3200.0  -type, sill, azm, max range, min range
```

Figure 4.42: Parameter file for `ssc`.

S3 Generate fine scale models with simulated annealing technique.

One can downscale coarse grid inverted permeability distributions to higher resolution fine scale models with the program, `sasim`. Detailed information about the parameter file and the code is given in the Appendix A. The format of the parameter files is almost same as that in GSLIB [61]. Interested readers can perform the downscaling; programs and parameter files are supplied here.

S4 Suggested sensitivity analyses.

- Sensitivity to number of master points, search radius for kriging, number of samples used for kriging can be performed.
- Sensitivity to initial seed of $\ln(k)$ distributions can be interesting.
- It is often difficult to get a good variogram model. One logical sensitivity study can focus on variogram structures. With different variogram models, the inversion process can be repeated and uncertainty due to variograms can be estimated.
- Sensitivity to initial pressures, fluid properties, reservoir dimensions can be performed.

Chapter 5

Multiple Well - Multiple Phase

Computational effort for multiphase flow simulation and sensitivity computation is orders of magnitude higher than that for single phase flow. Thus, the inverse problem requires efficient algorithm for sensitivity coefficients of reservoir response with respect to the change in reservoir petrophysical properties. A streamline-based method is applied for fast calculation of such sensitivity coefficients. The method decomposes the multiple-dimensional full flow problem into multiple 1D problems along streamlines. The sensitivity of fractional flow rate at the production well is directly related to the sensitivity of time-of-flight along each individual streamline and the sensitivity of pressure at cells along the streamline. The time-of-flight sensitivity of streamline can be obtained analytically assuming unchanged streamline geometry due to the perturbation of reservoir property. The sensitivity of pressure is obtained as part of a computationally fast single phase flow simulation. The complete set of sensitivity coefficients are obtained simultaneously with one single phase flow simulation, and the perturbations at all master locations are jointly considered. Implementation of this method in a geostatistics-based inversion technique, called the sequential self-calibration (SSC) method, ensues generating multiple permeability models. Results indicate improved efficiency of this method, yet more accurate than the traditional perturbation method.

5.1 Background

In the previous chapter, the sequential self-calibration (SSC) method was adapted to solve the single phase inversion problem. In this chapter, the SSC method is extended for inverting fractional flow rate data, such as watercut or GOR at production wells, in addition to pressure data. The objective function for the minimization problem is:

$$O = \sum_i \sum_t W_p(i,t) \left[p_i^{obs}(t) - p_i^{cal}(t) \right]^2 + \sum_j \sum_t W_f(j,t) \left[f_j^{obs}(t) - f_j^{cal}(t) \right]^2 \tag{5.1}$$

where $p_i^{obs}(t)$ and $p_i^{cal}(t)$ are the observed and simulated pressure at well i at time t. $f_j^{obs}(t)$ and $f_j^{cal}(t)$ are the observed and simulated fractional flow rate at well i at time t. $W_p(i,t)$ and $W_f(j,t)$ are weights assigned to pressure and fractional flow rate data at different wells and at different time.

For the optimal permeability perturbations at master locations minimizing the objective function (5.1), sensitivity coefficients of pressure and fractional flow rate at the wells with respect to the permeability perturbations are required for all master points at all time steps. These sensitivity coefficients are:

$$s_{p,m,t}(i) = \frac{\partial p_i(t)}{\partial \triangle k_m}, \quad \forall i, t, k_m \tag{5.2}$$

and

$$s_{f,m,t}(j) = \frac{\partial f_j(t)}{\partial \triangle k_m}, \quad \forall j, t, k_m \tag{5.3}$$

with $m = 1, \ldots, n_m$ being the index of master points. Chapter 4 discussed a method for computing sensitivity of pressure at **all** locations ($s_{p,m,t}(x), x \in$ all cells). So the focus, in this chapter, is on the calculation of the sensitivity coefficient of fractional flow rate, $s_{f,m,t}(j)$.

In matrix notation, discretization of the flow equation with an implicit scheme leads to the following equation:

$$[A]\{p\}^{t+1} = [B]\{p\}^t + \{f\}^t \tag{5.4}$$

where $[A]$ is the transmissibility matrix which accounts for spatial and temporal discretizations, as well as boundary conditions, $[B] = [hc\phi]/\triangle t_{t+1}$, and $\{f\}^t$ is the right hand side matrix that accounts for the load vector (production and injection) and flow boundary conditions. The solution of pressure at time $t+1$ is obtained by inverting matrix $[A]$, that is,

$$\{p\}^{t+1} = [A]^{-1}[B]\{p\}^t + [A]^{-1}\{f\}^t \tag{5.5}$$

The sensitivity coefficients at time step $t+1$ can be calculated right after the pressure at time $t+1$ is obtained. The perturbation equation of parameter k_m can be written as:

$$[A]\frac{\partial\{p\}^{t+1}}{\partial \triangle k_m} + \frac{\partial[A]}{\partial \triangle k_m}\{p\}^{t+1} = \frac{\partial[B]}{\partial \triangle k_m}\{p\}^t + [B]\frac{\partial\{p\}^t}{\partial \triangle k_m} + \frac{\partial\{f\}^t}{\partial \triangle k_m}, \qquad m = 1, \ldots, n_m \tag{5.6}$$

where n_m is the total number of master points, thus,

$$[A]\frac{\partial\{p\}^{t+1}}{\partial \triangle k_m} = \frac{\partial[B]}{\partial \triangle k_m}\{p\}^t + [B]\frac{\partial\{p\}^t}{\partial \triangle k_m} + \frac{\partial\{f\}^t}{\partial \triangle k_m} - \frac{\partial[A]}{\partial \triangle k_m}\{p\}^{t+1}, \qquad m = 1, \ldots, n_m \tag{5.7}$$

Equation 5.7 has the same form as Equation 5.4 and the matrix $[A]$ is inverted when solving for the pressure $\{p\}^{t+1}$. The sensitivity coefficients can be obtained at the same time step $t+1$ by simple matrix operations, that is,

$$\begin{aligned} s_{p,m,t+1} &= \frac{\partial\{p\}^{t+1}}{\partial \triangle k_m} \\ &= [A]^{-1}[B]\frac{\partial\{p\}^t}{\partial \triangle k_m} + [A]^{-1}\frac{\partial[B]}{\partial \triangle k_m}\{p\}^t + [A]^{-1}\frac{\partial\{f\}^t}{\partial \triangle k_m} - [A]^{-1}\frac{\partial[A]}{\partial \triangle k_m}\{p\}^{t+1}, \\ & \qquad m = 1, \ldots, n_m \end{aligned} \tag{5.8}$$

The elements of matrices, $\frac{\partial[A]}{\partial\triangle k_m}$, $\frac{\partial[B]}{\partial\triangle k_m}$, and $\frac{\partial\{f\}^t}{\partial\triangle k_m}$ can be directly computed from the expressions of elements in matrices $[A]$, $[B]$ and $\{f\}$ with $\frac{\partial\{p\}^0}{\partial\triangle k_m} = 0$.

The underlying bases of the inversion method are (1) the analytical 1D solutions of fractional flow along each streamline [9, 11, 18, 173, 174], (2) the ability to compute sensitivity coefficients of pressure over the entire field from single phase flow solutions, and (3) the assumption that streamline geometry remains unchanged with perturbed permeabilities. The sensitivity coefficients of fractional flow are obtained extremely fast by simple book-keeping of the streamlines in space. The permeability perturbations are jointly considered rather than one at a time as in the perturbation method. This method is implemented within the SSC algorithm for generating geostatistical permeability realizations that simultaneously honor transient pressure and fractional flow rate data. Streamlines are updated in each outer iteration of the SSC inversion (see Figure 4.1). The assumption of streamline geometry remaining unchanged during the perturbation is justified by comparing the SSC inverse results based on both the perturbation method and the analytical method.

5.2 Perturbation Method

A series of measurements of reservoir response $\mathbf{d}^{obs}(\mathbf{u}, t)$ (pressure or fractional flow rate at wells) is observed at location $\mathbf{u} \in A$ and time t. A is the entire space. The reservoir data are nonlinear functions of the parameter vector $\mathbf{a}$ (porosity or permeability): $\mathbf{d} = g(\mathbf{a})$. In this case, the function g represents the multiphase flow equations. The inverse problem consists of finding the optimal parameter $\mathbf{a}$ so that the solution $\mathbf{d}^{cal}(\mathbf{u}, t) = g(\mathbf{a})$ matches the observed data $\mathbf{d}^{obs}(\mathbf{u}, t)$. Thus, the mismatch $(\mathbf{d}^{obs} - \mathbf{d}^{cal})^2$ is minimized. For a gradient-based method (e.g., steepest descent, Gauss-Newton or conjugate gradient method), to find the optimal parameter set $\mathbf{a}$, the sensitivity coefficients of $\mathbf{d}$ with respect to the parameters in $\mathbf{a}$ are required.

The simplest way of computing such sensitivity coefficients is the so-called substitution or perturbation method. The first order approximation of the sensitivity coefficient is computed in this method using a finite difference procedure. The SSC method is adapted to the perturbation method to find the optimal permeability fields that match the fractional flow data $f_j(t)$. An initial permeability field, $\mathbf{a}_0 = \mathbf{k}_0 = \{k_0(\mathbf{u}_i), i = 1, \ldots, N\}$, is selected. N is the number of cells in the model. The flow equations are solved for fractional flow rate, $f_j(0)$, at all wells and at all time steps using the initial permeability field.

For all master point locations $m = 1, \ldots, n_m$ ($\ll N$ usually), a small perturbation $\triangle k_m$ is introduced individually to the initial permeability at master location $\mathbf{u}_m$. The field $\triangle\mathbf{k}_m = \{\triangle k(\mathbf{u}_i), i = 1, \ldots, N\}$ due to the perturbation $\triangle k_m = \triangle k(\mathbf{u}_m)$, at location $\mathbf{u}_m$ is calculated by kriging. This kriged perturbation field is then added to the initial permeability field to obtain the perturbed permeability field $\mathbf{k}' = \mathbf{k}_0 + \triangle\mathbf{k}_m$. The flow equations are solved using this perturbed field $\mathbf{k}'$ to obtain the new fractional flow rate solution, $f'_j(t)$ induced by the perturbation at master point $\mathbf{u}_m$. The sensitivity coefficient of fractional flow rate with respect to the permeability change at master location m can then be computed as:

$$s_{f,m,t}(j) = \frac{f'_j(t) - f_j(0)}{\triangle k_m} \tag{5.9}$$

Thus, for each outer-iteration of the SSC method (see Figure 4.1), a total of $n_m + 1$ flow simulation runs are needed to obtain all sensitivity coefficients required, which is very computationally intensive. In addition, the values of $s_{f,m,t}(j)$, computed with this substitution method, are sensitive to the perturbation magnitude, $\triangle k_m$, particularly when the function f is nonlinear. More importantly, the substitution method computes sensitivity coefficients of each parameter independently. Thus, it does not account for joint perturbations at all n_m master locations. The spatial relationship of different master locations is not accounted for. This is crucial for optimization, which will be elaborated later. However, many improvements have been proposed to speed up the computation of sensitivity coefficients of fractional flow rate [39, 118]. These improved methods remain computationally intensive and none accounts for joint perturbations.

5.3 Streamline-Based Analytical Method

The sensitivity coefficients are calculated based on the streamline algorithm and the analytical relationship between fractional flow rate and the time-of-flight of streamline [9, 175]. The key assumption is that the streamline geometry is insensitive to the relatively small perturbations of the permeability field. This assumption is appropriate if the perturbations are kept small and all streamlines are updated after each outer loop of the SSC inversion. The complete set of sensitivity coefficients at all master points are obtained simultaneously. The spatial correlation of perturbation at multiple master locations is accounted for by using kriging weights computed for all master locations to propagate the perturbations from the master locations to the entire field.

In the streamline-based method, the fractional flow for a given producing well j at time t is expressed as [9]:

$$f_j(t) = \frac{\sum_{s=1}^{n_j^{sl}} q_s^{sl} f_s^{sl}(t)}{\sum_{s=1}^{n_j^{sl}} q_s^{sl}} \tag{5.10}$$

where q_s^{sl} is the flow rate associated with streamline s, and $f_s^{sl}(t_f)$ is the fractional flow of streamline s at time t. n_j^{sl} is the total number of streamlines arriving to well w_f. The derivative of $f_j(t)$ with respect to the permeability perturbation at master point j is then:

$$s_{f,m}(j,t) = \frac{\partial f_j(t)}{\partial \triangle k_m} = \frac{1}{\sum_{s=1}^{n_j^{sl}} q_s^{sl}} \sum_{s=1}^{n_j^{sl}} q_s^{sl} \frac{\partial f_s^{sl}(t)}{\partial \triangle k_m} \tag{5.11}$$

Depending on the flow regime, the fractional flow rate $f_s^{sl}(t)$ of streamline s can be expressed as a function of time-of-flight τ_s, that is, $f_s^{sl}(t) \sim (\frac{\tau_s}{t})$. Examples of the function $f_s^{sl}(t)$ for tracer flow and immiscible two-phase displacement are shown in Figure 5.1. These functions can either be obtained analytically or numerically [9]. Thus, for $\frac{\partial f_s^{sl}(t)}{\partial \triangle k_m}$, it is only required to compute $\frac{\partial \tau_s}{\partial \triangle k_m}$.

For simplification, a non-diffusive tracer flow (unit mobility ratio and matched fluid density) is considered. In such case, the fractional flow rate is (see Figure 5.1a):

$$f_s^{sl}(t) = \begin{cases} 1, & if\ \tau_s \le t \\ 0, & if\ \tau_s > t \end{cases} \tag{5.12}$$

(a) Tracer Flow

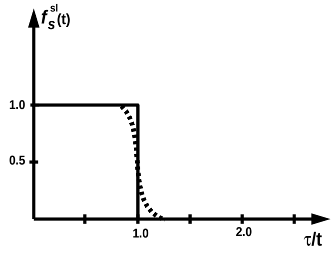

(b) Immiscible Two-Phase Displacement

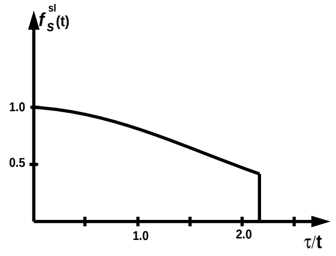

Figure 5.1: (a) Analytical 1D solution of tracer flow and its approximation using a Gaussian cumulative function (dashed line), and (b) analytical 1D solution of immiscible two-phase displacement.

Since Equation (5.12) is not differentiable at $\tau_s/t = 1$, a Gaussian cumulative function $F(\tau_s/t)$ with small variance is used to approximate the 1D tracer solution (Figure 5.1a):

$$f_s^{sl}(t) \approx 1 - F(\frac{\tau_s}{t}) \tag{5.13}$$

hence,

$$\frac{\partial f_s^{sl}(t)}{\partial \triangle k_m} = -\frac{1}{t} G(\frac{\tau_s}{t}) \frac{\partial \tau_s}{\partial \triangle k_m} \tag{5.14}$$

where

$$G(\frac{\tau_s}{t}) = \frac{1}{\sqrt{2\pi}\sigma} e^{-\frac{(\tau_s - t)^2}{2t^2\sigma^2}}$$

is a Gaussian distribution function with mean 1 and variance σ^2. The variance σ^2 should be small so that the approximation is close. The influence of that variance on the sensitivity coefficients is investigated later.

In the case of two-phase immiscible displacement as shown in Figure 5.1b, the derivatives of fractional flow with respect to the time-of-flight can be directly computed from Buckley-Leverett solution.

The time-of-flight of streamline s is a function of total flow velocity itself is a function of permeability and total pressure along the streamline:

$$\tau_s = \int_0^s \frac{1}{v_s} ds. \tag{5.15}$$

In a discretized numerical model (see Figure 5.2), the time-of-flight of streamline s from injector to producer is the sum of the time-of-flight in each cell that streamline s passes

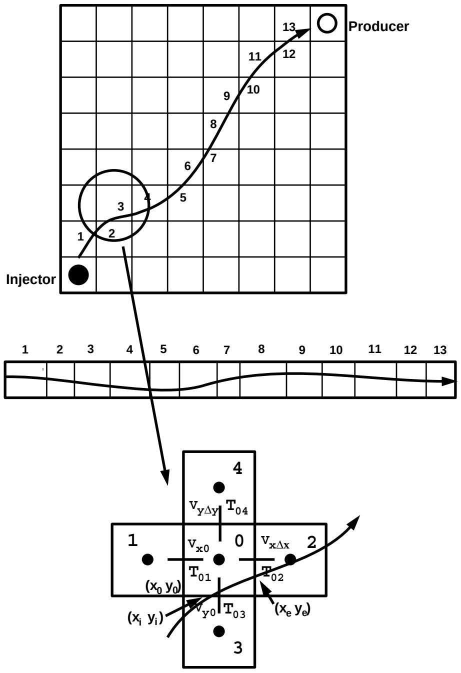

Figure 5.2: Schematic illustration of tracking a streamline through a discretized numerical model.

through, that is,

$$\tau_s = \sum_{c=1}^{n_{s,c}} \triangle\tau_{s,c} \tag{5.16}$$

$n_{s,c}$ being the number of cells crossed by streamline s from injector to producer, and $\triangle\tau_{s,c}$ is the associated time-of-flight for streamline s to pass through cell c.

In Figure 5.2, for example, the total number of cells crossed by the streamline from injector to producer is 13 ($= n_{s,c}$). Based on the semi-analytical solution [46, 149], that is, assuming linear variation of velocity in all directions within a numerical cell, the cell (or differential) time-of-flights are:

- if the streamline exits the cell c in the X-direction,

$$\triangle\,\tau_{s,c} = \triangle\tau_{s,c,x} = \frac{1}{J_x}\ln\left\{\frac{v_{x,0} + J_x(x_e - x_0)}{v_{x,0} + J_x(x_i - x_0)}\right\} \tag{5.17}$$

- if the streamline exits the cell c in the Y-direction,

$$\triangle\,\tau_{s,c} = \triangle\tau_{s,c,y} = \frac{1}{J_y}\ln\left\{\frac{v_{y0} + J_y(y_e - y_0)}{v_{y0} + J_y(y_i - y_0)}\right\} \tag{5.18}$$

where

$$J_x = \frac{v_{x,\triangle x} - v_{x,0}}{\triangle x}$$

$$J_y = \frac{v_{y,\triangle y} - v_{y,0}}{\triangle y}$$

$$\begin{aligned}
v_{x,0} &= -T_{01}\frac{p_0 - p_1}{\triangle x \phi \mu}, \qquad & T_{01} &= \frac{2k_0k_1}{k_0 + k_1} \\
v_{x,\triangle x} &= -T_{02}\frac{p_2 - p_0}{\triangle x \phi \mu}, \qquad & T_{02} &= \frac{2k_0k_2}{k_0 + k_2} \\
v_{y,0} &= -T_{03}\frac{p_0 - p_3}{\triangle y \phi \mu}, \qquad & T_{03} &= \frac{2k_0k_3}{k_0 + k_3} \\
v_{y,\triangle y} &= -T_{04}\frac{p_4 - p_0}{\triangle y \phi \mu}, \qquad & T_{04} &= \frac{2k_0k_4}{k_0 + k_4}
\end{aligned} \tag{5.19}$$

where $\triangle x$ and $\triangle y$ are the cell size in X and Y directions, ϕ the porosity, T_{01} to T_{04} the transmissibilities for the four interfaces of the cell intersected by the streamline (cell 0 in Figure 5.2), p_0 to p_4 and $k_0$to k_4 the pressure and permeability values at the current (0) and the surrounding (1 to 4) cells, respectively (see Figure 5.2). $(x_i,\, y_i)$ and $(x_e,\, y_e)$ are the inlet and exit coordinates of the streamline in current cell 0, and $(x_0,\, y_0)$ is the coordinate of the lower-left corner of current cell 0.

From Equations (5.16) to (5.19), the derivatives of time-of-flights with respect to permeabilities are derived to be:

$$\frac{\partial \tau_s}{\partial \triangle k_j} = \sum_{c=1}^{n_{s,c}} \left\{ \sum_{g=1}^{4} \frac{\partial \triangle \tau_{s,c}}{\partial T_{0g}} \frac{\partial T_{0g}}{\partial \triangle k_j} + \sum_{l=0}^{4} \frac{\partial \triangle \tau_{s,c}}{\partial p_l} \frac{\partial p_l}{\partial \triangle k_j} \right\} \tag{5.20}$$

$\frac{\partial \triangle \tau_{s,c}}{\partial T_{0g}}$ and $\frac{\partial \triangle \tau_{s,c}}{\partial p_l}$ can be computed from Equations (5.17) and (5.18). $\frac{\partial p_l}{\partial \triangle k_j}$ are the sensitivity coefficients of pressure with respect to permeability change, Their computation is discussed in the previous chapter [191]. Finally [73].

$$\frac{\partial T_{0g}}{\partial \triangle k_j} = \frac{T_{0g}^2}{2} \left\{ \frac{\lambda_j^0}{k_0^2} + \frac{\lambda_j^g}{k_g^2} \right\} \tag{5.21}$$

λ_j^0 and λ_j^g are the kriging weights attributed to master point j, cells 0 and g $(g = 1, \ldots, 4)$. Since the kriging weights are computed accounting for all master points [112], the resulting sensitivity coefficients account for the spatial distribution of all master points. The permeability perturbations at all master locations are now considered jointly rather that one at a time. The complete set of sensitivity coefficients at all master points are obtained simultaneously. In addition, there is no need to choose a specific value of $\triangle k_j$ before computing sensitivity coefficients.

5.4 Derivation of Time-of-Flight and Derivatives

The derivations of the time-of-flights and their derivatives or the sensitivity coefficients are laid out in this section. Essentially, this calculation reduces to a simple book-keeping of the streamlines in the simulation model. This is both mathematically simple and computationally efficient. Extension of this method to other types of flow, such as immiscible two-phase flow and 3D flow, should be straightforward.

From Equations (5.17) to (5.19), the cell time-of-flights, derived, are:

$$\triangle \tau_{s,c,x} = \frac{- \triangle x^2 \phi}{A_x} \ln \left\{ \frac{\triangle x T_{01}(p_0 - p_1) + A_x(x_e - x_0)}{\triangle x T_{01}(p_0 - p_1) + A_x(x_i - x_0)} \right\} \tag{5.22}$$

$$\triangle \tau_{s,c,y} = \frac{- \triangle y^2 \phi}{A_y} \ln \left\{ \frac{\triangle y T_{01}(p_0 - p_3) + A_y(y_e - y_0)}{\triangle y T_{01}(p_0 - p_3) + A_y(y_i - y_0)} \right\} \tag{5.23}$$

where $A_x = T_{01}(p_1 - p_0) + T_{02}(p_2 - p_0)$, and $A_y = T_{03}(p_3 - p_0) + T_{04}(p_4 - p_0)$.

The derivatives, required in Equation (5.20) in the x-direction, are stated below (refer to Figure 5.2). Taking partial derivatives of Equation 5.22 with respect to T_{01}, T_{02}, T_{03}, T_{04}, p_0, p_1, p_2, p_3 and p_4, respectively, Equations (5.24) to (5.30) are obtained.

$$\frac{\partial \triangle \tau_{s,c,x}}{\partial T_{01}} = \frac{- \triangle x^2 \phi (p_0 - p_1)}{A_x^2} \left\{ \ln \frac{D_x}{C_x} + A_x \frac{\left[\triangle x - (x_e - x_0)\right] C_x - \left[\triangle x - (x_i - x_0)\right] D_x}{C_x D_x} \right\} \tag{5.24}$$

$$\frac{\partial \triangle \tau_{s,c,x}}{\partial T_{02}} = \frac{- \triangle x^2 \phi (p_0 - p_2)}{A_x^2} \left\{ \ln \frac{D_x}{C_x} + A_x \frac{-(x_e - x_0) C_x + (x_i - x_0) D_x}{C_x D_x} \right\} \tag{5.25}$$

$$\frac{\partial \triangle \tau_{s,c,x}}{\partial T_{03}} = \frac{\partial \triangle \tau_{i,s,x}}{\partial T_{04}} = 0 \tag{5.26}$$

$$\begin{aligned} \frac{\partial \triangle \tau_{s,c,x}}{\partial p_0} = \frac{- \triangle x^2 \phi}{A_x^2} \Bigg\{ & -(T_{01} + T_{02}) \ln \left(\frac{D_x}{C_x} \right) + \\ & A_x \frac{\left[\triangle x T_{01} - (T_{01} + T_{02})(x_e - x_0)\right] C_x - \left[\triangle x T_{01} - (T_{01} + T_{02})(x_i - x_0)\right] D_x}{C_x D_x} \Bigg\} \end{aligned} \tag{5.27}$$

$$\begin{aligned} \frac{\partial \triangle \tau_{s,c,x}}{\partial p_1} = \frac{- \triangle x^2 \phi}{A_x^2} \Bigg\{ & T_{01} \ln \left(\frac{D_x}{C_x} \right) + \\ & A_x \frac{\left[- \triangle x T_{01} + T_{01}(x_e - x_0)\right] C_x - \left[\triangle x T_{01} + T_{01}(x_i - x_0)\right] D_x}{C_x D_x} \Bigg\} \end{aligned} \tag{5.28}$$

$$\frac{\partial \triangle \tau_{s,c,x}}{\partial p_2} = \frac{- \triangle x^2 \phi}{A_x^2} \left\{ T_{02} \ln \left(\frac{D_x}{C_x} \right) + A_x \frac{T_{02}(x_e - x_0) C_x - T_{02}(x_i - x_0) D_x}{C_x D_x} \right\} \tag{5.29}$$

$$\frac{\partial \triangle \tau_{s,c,x}}{\partial p_3} = \frac{\partial \triangle \tau_{i,s,x}}{\partial p_4} = 0 \tag{5.30}$$

where $C_x = \triangle x T_{01}(p_0 - p_1) + A_x(x_i - x_0)$ and $D_x = \triangle x T_{01}(p_0 - p_1) + A_x(x_e - x_0)$.

Similarly, in the y-direction, taking partial derivatives of Equation 5.23 with respect to T_{03}, T_{04}, T_{01}, T_{02}, p_0, p_3, p_4, p_1 and p_2, respectively, Equations (5.31) to (5.37) are obtained.

$$\frac{\partial \triangle \tau_{s,c,y}}{\partial T_{03}} = \frac{- \triangle y^2 \phi (p_0 - p_3)}{A_y^2} \left\{ \ln \frac{D_y}{C_y} + A_y \frac{\left[\triangle y - (y_e - y_0)\right] C_y - \left[\triangle y - (y_i - y_0)\right] D_y}{C_y D_y} \right\} \tag{5.31}$$

$$\frac{\partial \triangle \tau_{s,c,y}}{\partial T_{04}} = \frac{-\triangle y^2 \phi (p_0 - p_4)}{A_y^2} \left\{ \ln \frac{D_y}{C_y} + A_x \frac{-(y_e - y_0)C_y + (y_i - y_0)D_y}{C_y D_y} \right\} \tag{5.32}$$

$$\frac{\partial \triangle \tau_{s,c,y}}{\partial T_{01}} = \frac{\partial \triangle \tau_{s,c,y}}{\partial T_{02}} = 0 \tag{5.33}$$

$$\frac{\partial \triangle \tau_{s,c,y}}{\partial p_0} = \frac{-\triangle y^2 \phi}{A_y^2} \left\{ -(T_{03} + T_{04}) \ln \left(\frac{D_y}{C_y} \right) + \right.$$

$$\left. A_y \frac{[\triangle y T_{03} - (T_{03} + T_{04})(y_e - y_0)]\, C_y - [\triangle y T_{03} - (T_{03} + T_{04})(y_i - y_0)]\, D_y}{C_y D_y} \right\} \tag{5.34}$$

$$\frac{\partial \triangle \tau_{s,c,y}}{\partial p_3} = \frac{-\triangle y^2 \phi}{A_y^2} \left\{ T_{03} \ln \left(\frac{D_y}{C_y} \right) + \right.$$

$$\left. A_y \frac{[-\triangle y T_{03} + T_{03}(y_e - y_0)]\, C_y - [\triangle y T_{03} + T_{03}(y_i - y_0)]\, D_y}{C_y D_y} \right\} \tag{5.35}$$

$$\frac{\partial \triangle \tau_{s,c,y}}{\partial p_4} = \frac{-\triangle y^2 \phi}{A_y^2} \left\{ T_{04} \ln \left(\frac{D_y}{C_y} \right) + A_y \frac{T_{04}(y_e - y_0)C_y - T_{04}(y_i - y_0)D_y}{C_y D_y} \right\} \tag{5.36}$$

$$\frac{\partial \triangle \tau_{s,c,y}}{\partial p_1} = \frac{\partial \triangle \tau_{s,c,y}}{\partial p_2} = 0 \tag{5.37}$$

where $C_y = \triangle y T_{03}(p_0 - p_3) + A_y(y_i - y_0)$ and $D_y = \triangle y T_{03}(p_0 - p_3) + A_y(y_e - y_0)$.

This elegant account of the streamline derivatives is an essential feature of the streamline-based analytical technique. For increasiingly large grid sizes, this method with simple book-keeping of streamlines proves to be far more efficient than the perturbation methods. The derivatives here have been derived for 2D grids, which can easily be extended to 3D grids.

A simplification to the computation of the time-of-flights derivatives can be implemented. One can assume that the contribution of the second term of the derivation shown in Equation 5.20 is negligible. So the derivatives of time-of-flights with respect to permeabilities will now be:

$$\frac{\partial \tau_s}{\partial \triangle k_j} = \sum_{c=1}^{n_{s,c}} \left\{ \sum_{g=1}^{4} \frac{\partial \triangle \tau_{s,c}}{\partial T_{0g}} \frac{\partial T_{0g}}{\partial \triangle k_j} \right\} \tag{5.38}$$

with the notations having earlier implications. Further simplification, which precludes a few computational steps, can be implemented if one considers $\frac{\partial \triangle \tau_{s,c}}{\partial k_c} \frac{\partial k_c}{\partial \triangle k_j}$ instead of $\frac{\partial \triangle \tau_{s,c}}{\partial T_{0g}} \frac{\partial T_{0g}}{\partial \triangle k_j}$, where k_c is the permeability at cell c. This reduces the necessary derivative equation to:

$$\frac{\partial \tau_s}{\partial \triangle k_j} = \sum_{c=1}^{n_{s,c}} \frac{\partial \triangle \tau_{s,c}}{\partial \triangle k_j} = \sum_{c=1}^{n_{s,c}} \frac{\partial \triangle \tau_{s,c}}{\partial k_c} \frac{\partial k_c}{\partial \triangle k_j}. \tag{5.39}$$

The partial derivatives in Equation 5.39 can be derived from the basic equations. Combining Equations 5.15, 5.16 and Darcy's law one can obtain:

$$\triangle \tau_{s,c} = \int_{s_{in}}^{s_{out}} \frac{1}{v_{s,c}} dr = \int_{s_{in}}^{s_{out}} \frac{\phi_c \mu}{k_c |J|} dr \tag{5.40}$$

where ϕ, μ and k_c are porosity, viscosity and permeability at cell c, and $|J|$ is the absolute value of the pressure gradient. Assuming independence of the time-of-flights to the pressure gradient, the partial derivatives can be approximated to be:

$$\frac{\partial \triangle \tau_{s,c}}{\partial k_c} = -\frac{\triangle \tau_{s,c}}{k_c}. \tag{5.41}$$

Applying the above to Equation 5.39, the derivative equation will be reduced to:

$$\frac{\partial \tau_s}{\partial \triangle k_j} = \sum_{c=1}^{n_{s,c}} \frac{\partial \triangle \tau_{s,c}}{\partial k_c} \frac{\partial k_c}{\partial \triangle k_j} = -\sum_{c=1}^{n_{s,c}} \frac{\triangle \tau_{s,c}}{k_c} \omega_{j,c} \tag{5.42}$$

where $\omega_{j,c}$ is the kriging weight of master point j to cell c, which accounts for the correlation of permeability at the two locations. Studies indicate faster convergence using this simplified approach with little loss of accuracy.

5.5 Implementation Issues with Synthetic Examples

Some implementation issues regarding the number of master points and computational efficiency are discussed here. This section also compares the accuracy and efficiency of the streamline-based perturbation method and the analytical method for computing sensitivity coefficients for the SSC inversion.

5.5.1 Single master point

The sensitivity coefficients, computed by the streamline-based analytical method and perturbation method with only one master point, are compared first. The perturbation method does not account for the spatial distribution of all master points, whereas the analytical method does. Therefore, the sensitivity coefficients computed by the two methods are comparable only when there is single master point. Figure 5.3 provides this comparison. Figure 5.3a is the 2D $ln(k)$ field with constant permeability $ln(k) = 2$ md. There are four producers at the four corners and one water injector at the center of the field. Injection rate is 3000 STB/day. Tracer flow conditions, that is, unit mobility ratio and matched fluid density are assumed. The production rates are held constant for each producer at 500 STB/day for wells 1 and 4, 1000 STB/day for wells 2 and 3. Other reservoir parameters are: thickness $h = 100$ ft, porosity $\phi = 0.2$, viscosity $\mu = 0.3$ cp, and compressibility $c = 10^{-5}$ 1/psi. The streamline geometry for this base field is also given in Figure 5.3a. The fractional flow rate at well 1, $f_j^0(t)$, is shown in Figure 5.3b.

A single master point is selected close to well 1 with a perturbation of $\triangle(\ln(k))_1 = 0.2$. This perturbation is then propagated through the entire field by kriging to obtain a perturbation field (Figure 5.3c) resulting in the updated field shown in Figure 5.3d. An anisotropic

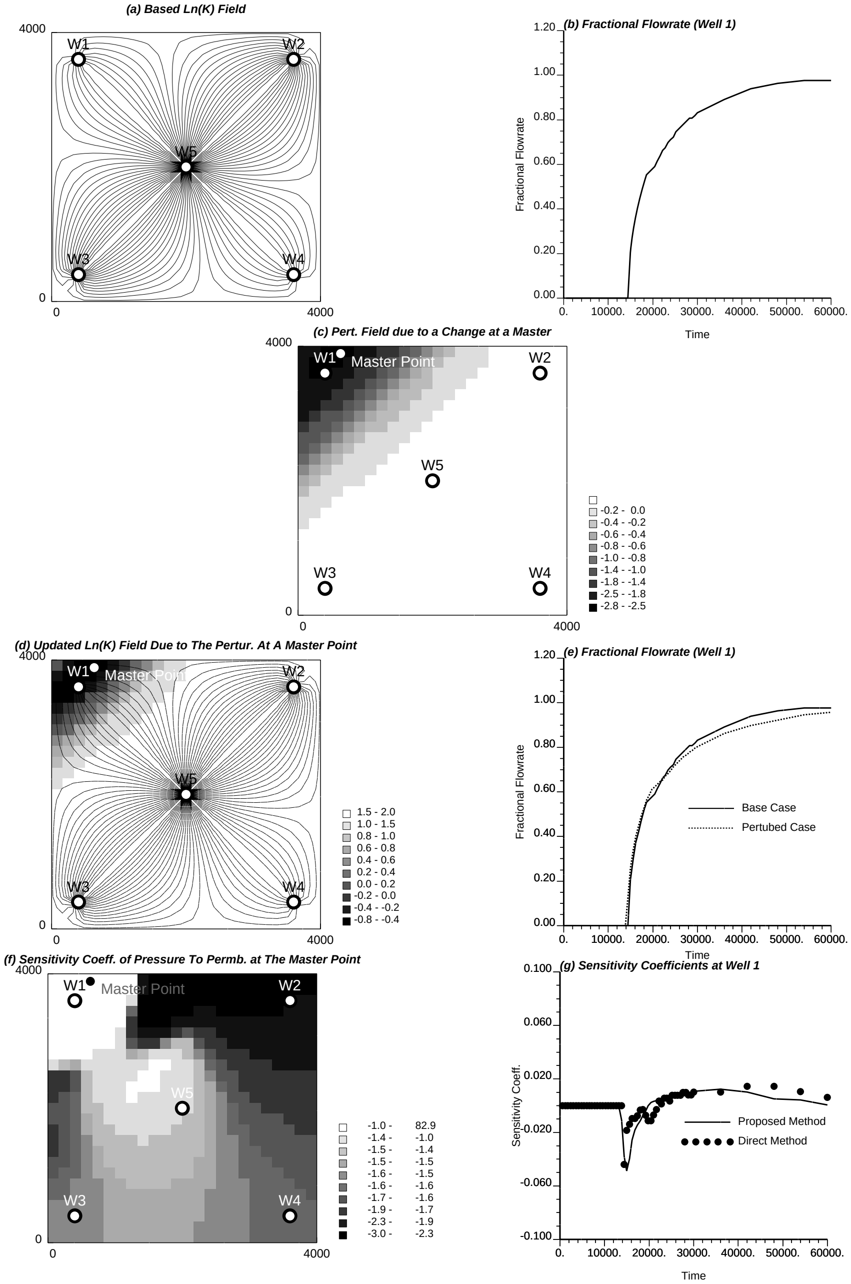

Figure 5.3: Comparison of sensitivity coefficients computed by the two methods for the case of a single master point.

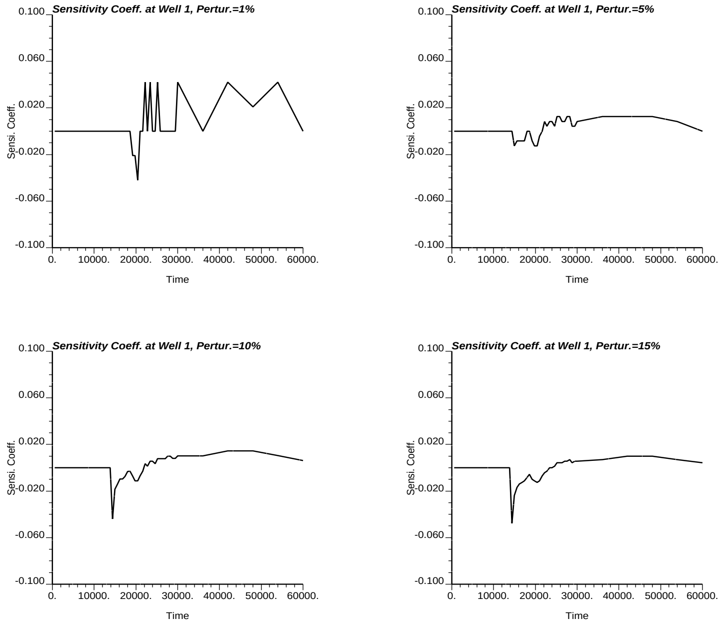

Figure 5.4: Sensitivity coefficients computed by the perturbation method using different perturbation values at the master point.

variogram with major range in direction 45° is used for this propagation. The flow equation is solved again based on the perturbed permeability field to obtain the perturbed fractional flow rate $f_j^1(t)$ at well 1 due to the original perturbation at the master point (see Figure 5.3e). The new streamline geometry for the perturbed permeability field is also shown in Figure 5.3d. There is very little change in streamline geometry.

Using the perturbation method, the sensitivity coefficients are computed as:

$$s_{f,1,t}(j) = \frac{f_j^1(t) - f_j^0(t)}{\triangle k_1}$$

The corresponding values are shown in Figure 5.3g. The sensitivity coefficients of pressure for the entire field with respect to the permeability perturbation at the master point required by the proposed method are shown in Figure 5.3f. These are computed as part of single phase flow simulation [191]. The results obtained by the method illustrated are also in Figure 5.3g. The results from the two methods are similar which indicates the accuracy of the proposed method.

The sensitivity coefficients computed by the perturbation method are sensitive to the value of perturbation $\triangle k_1$ used in the calculation. Figure 5.4 shows the sensitivity coefficients at well 1 using different permeability perturbations at the master point. A 15 % perturbation of the initial value provides reasonably stable results. The appropriate $\triangle k_1$ changes for different master points and different wells because of their relative configuration. The accuracy of the calculation of sensitivity coefficients using the perturbation method will vary for different master points and different wells although using the same $\triangle k_1$ value.

Here, a Gaussian cumulative function, with a mean of 1 and a small variance, is used to approximate the analytical 1D tracer flow solution (see Figure 5.1a). The influence of that

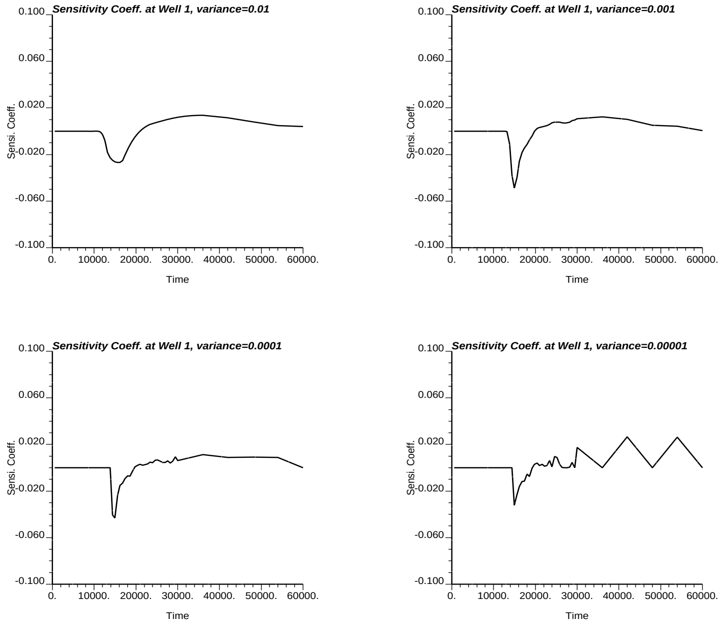

Figure 5.5: Sensitivity coefficients computed by the proposed method using different variance values to approximate the 1D analytical solution.

variance on the sensitivity coefficient results is shown in Figure 5.5 using the field shown in Figure 5.3. The larger the variance value, the smoother are the sensitivity coefficient results. Therefore, the variance should be small enough (say 0.01). The accuracy of the sensitivity coefficients calculated at different master points and for different wells does not change if the same variance value is used.

Experience shows that the positive or negative signs of the sensitivity coefficients guide the direction of perturbation in the optimization. Thus, the signs of the coefficients are more important than the amplitudes in the inversion process.

5.5.2 Multiple Master Points

For multiple master points, the sensitivity coefficients calculated by the two methods are not directly comparable. Since the analytical method accounts for the spatial correlation of perturbations at the multiple master points, whereas the perturbation method does not. Nevertheless, their accuracy can be judged indirectly by comparing the final inversion results and corresponding objective functions.

Figure 5.6 shows a reference deterministic field (25×25 nodes over a 2D grid with cell size of 160 ft ×160 ft) and the corresponding fractional flow data at 4 wells. Starting from the homogeneous permeability field with $k = 7$ md (Figure 5.7b), the SSC method is used to match the fractional flow data. Sixteen master points, randomly selected and updated after 3 outer iterations, and an anisotropic variogram with long correlation length at 45° were used for the inversion. The final permeability fields obtained after 20 iterations are shown in Figures 5.7c,d using both methods. Decreases in the objective function using the two methods are shown in Figure 5.7e. It appears that the SSC inversion results using

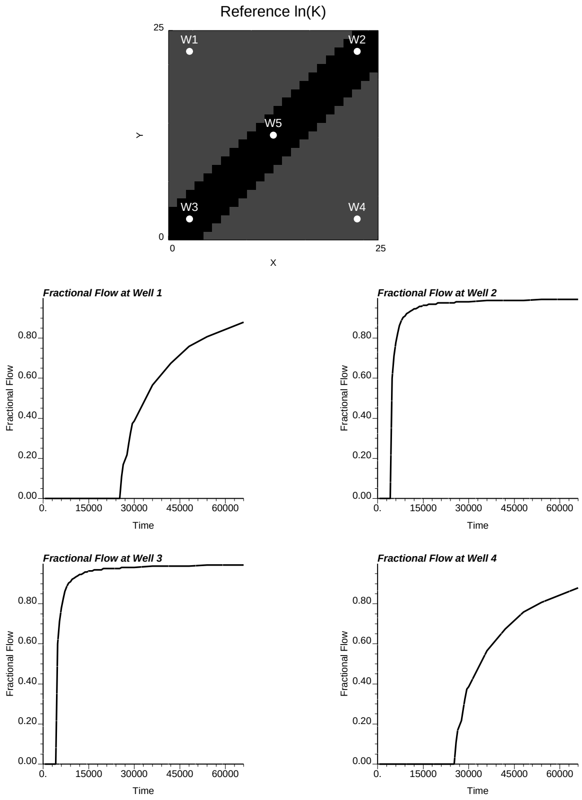

Figure 5.6: A synthetic deterministic reference field and the fractional flow rate data from four wells.

either method reproduce well the high permeability band of the reference field with a final objective function close to zero. However, a visually better inversion result is obtained with slightly lower objective function when using the the streamline-based analytical method.

Figure 5.8 shows another 2D stochastic reference field (50×50 grid with cell size 80 ft ×80 ft) and the corresponding fractional flow data at 4 wells. The injection rate at the central well is 1600 STB/day, and the production rate for the 4 producing wells is 400 STB/day/well. Figure 5.9 shows three initial permeability fields, the resulting fields updated by SSC using the two different methods for computing sensitivity coefficients and the decreases of the objective function with number of iterations. The same 25 randomly selected master points are used for all realizations. The analytical method provides more accurate inverse permeability fields with lower objective functions for all three realizations. Also, the objective function shows monotonic decrease for the analytical method.

The comparison of individual realizations as shown in Figure 5.9 is difficult and subjective. A better comparison of the inverse results from the two methods is given by the ensemble results calculated from 200 realizations, (see Figure 5.10). In comparison with the reference field given at the bottom of the figure, the inverse results using the streamline-based method are superior in that the results are more accurate (better representation of the reference spatial variation patterns) and have less uncertainty (smaller standard deviation).

Thus, compared to the perturbation method, the inversion responses using the streamline-based analytical method in the SSC inversion have the following characteristics. The objec-

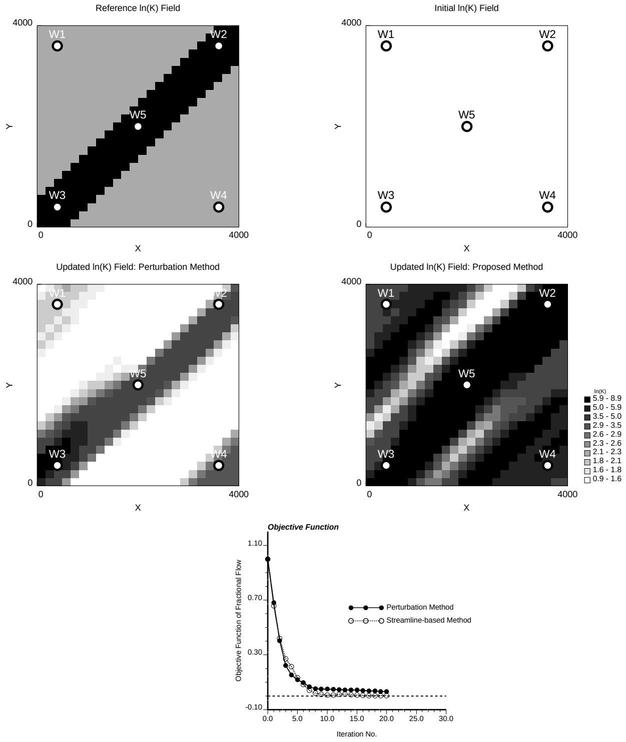

Figure 5.7: Inversion responses from SSC using two methods for computing sensitivity coefficients.

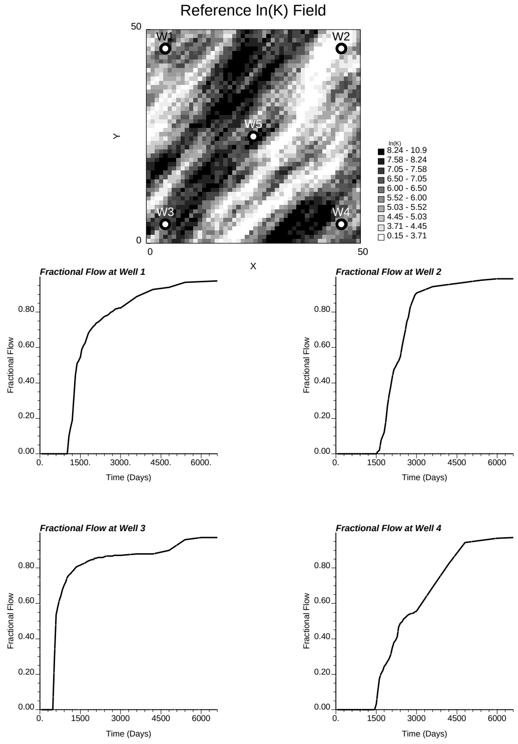

Figure 5.8: A synthetic stochastic reference field and the fractional flow rate data from the four corner wells.

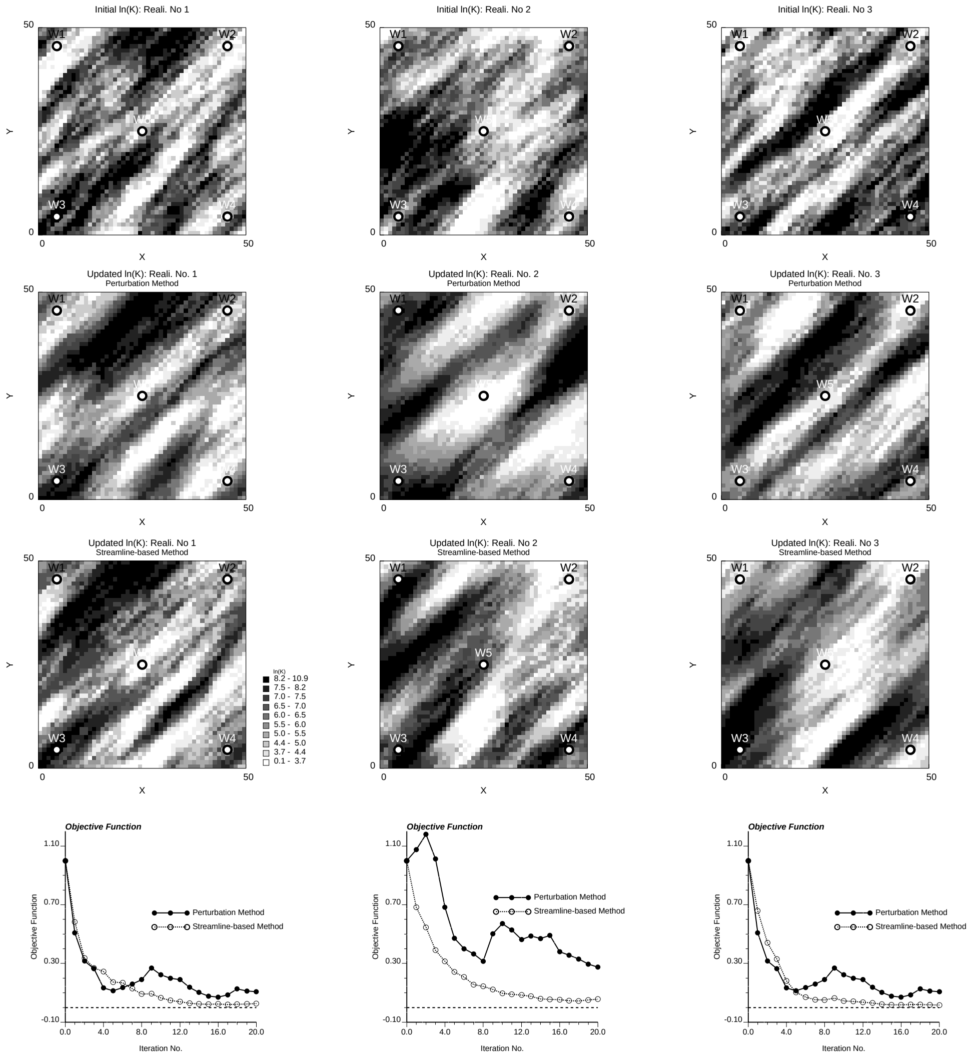

Figure 5.9: Three realizations of initial and inverse results from the SSC method using different methods for computing sensitivity coefficients, and the variations of objective functions after each iteration.

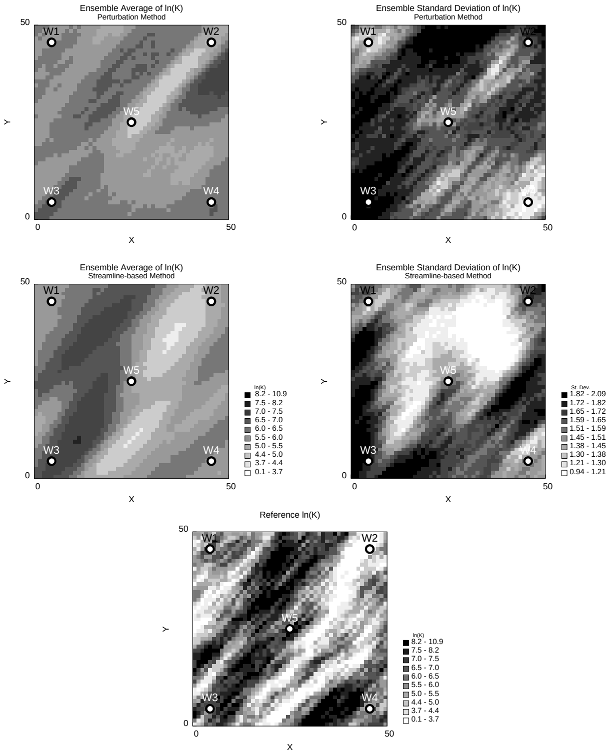

Figure 5.10: Ensemble fields (mean and standard deviation) from 200 inverse realizations using the two methods for computing sensitivity coefficients.

tive function behavior is better revealing a monotonic decrease for almost all realizations. A lower objective function value can be achieved in the minimization problem. Reference spatial patterns are better reproduced with less uncertainty.

The improved accuracy of this method may be attributed to the following reasons. This method jointly accounts for the perturbations of multiple master locations through the kriging weights. The magnitude of the specific perturbation values does not affect the responses much. The absolute values of the sensitivity coefficients are not as important to the inversion as their signs for the SSC inversion. The assumption that the streamline geometry is relatively insensitive to the permeability perturbation within a single inner iteration of the SSC does not limit the application of the proposed method due to the updating of streamlines after each outer loop of SSC inversion. This is a reasonable assumption as long as the permeability perturbation is small, which is the case within each inner iteration.

5.5.3 CPU Time Comparison

The CPU time for computing sensitivity coefficients of fractional flow using the two methods depends mainly on the size of the simulation model (number of cells), number of master points, and total number of streamlines used. Other minor factors include the number of producers and the number of time steps in the simulation. Model size is, however, the dominant factor due to the flow simulation.

Figure 5.11 shows CPU time (SGI workstation) of 10 SSC iterations versus the number of cells in the model with 25 master points and 1000 streamlines. For a small model, the perturbation method is slightly faster than the streamline-based analytical method because solving a few flow equations using the streamline method is quicker than the proposed bookkeeping of streamlines. As the model becomes larger, the CPU time increases dramatically using the perturbation method because the flow equations must be solved many more times. Total number of flow simulation is the product of the iteration number and the sum of number of master points and 1, for the perturbation method. Whereas the CPU time for the proposed method increases much more slowly than the perturbation method. In this case, the total number of flow simulations is the number of iterations. With a 100 × 100 grid model, the CPU time using the perturbation method is more than 5 times that using the analytical method.

Other non-SSC based methods for inverting production data that require flow simulations at every iteration for every cell or zone (i.e., full matrix) without using streamline-based simulator could be orders of magnitude slower than the SSC-based streamline methods [87, 118, 144]. The CPU time of one such inversion is also given in Figure 5.11 for comparison. It is orders of magnitude slower than this method here. In fact, the full matrix-based perturbation method used can not run model with cells number larger than 30 × 30 for this particular code due to its extreme memory demanding.

5.6 Application to a Realistic Reservoir

This section applies the inversion technique to a realistic reservoir example. Sensitivity of the technique to initial models and variograms, and the value of additional well data are also demonstrated. Figure 5.12 shows a 2D reference field (50×50 grid with cell size

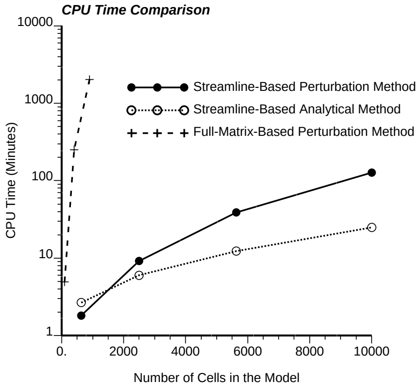

Figure 5.11: Comparison of CPU times for 10 SSC iterations using the two methods of computing sensitivity coefficients. The CPU time for one full matrix (non-SSC) based perturbation method is also shown.

80 ft ×80 ft) and the corresponding fractional flow data at 4 wells. The injection rate at the central well is 1600 STB/day and the production rate for the 4 producing wells is 400 STB/day/well. This synthetic field was generated by sequential Gaussian simulation `sgsim` [61] with an assumed variogram. Other reservoir parameters are the same as in the earlier example. A high permeability zone and a low permeability zone exist in the middle of the field. There is relatively higher interconnectivity between the injection well and well 3 than that between the injection well and other wells (2 and 4).

Pressure data at the five wells and the fractional flow rates at the four production wells up to 1800 days are used for inverting to permeability models. Figure 5.13 shows three initial permeability fields computed using the same variogram that was used to generate the reference model and the histogram from the exhaustive data, the resulting fields updated by SSC for pressure data only at the five wells, fractional flow rate data only at the four production wells, and both pressure and fractional flow rate data. The reference field is shown at the bottom of the figure for comparison. The relative decreases of both components of the objective function with number of iterations for the three realizations are given in Figure 5.14. The same 25 randomly selected master points are used for all realizations. The variogram determined from the exhaustive reference field is used for propagating the perturbations from the master locations throughout the entire field. The reference histogram is explicitly honored in all updated realizations. Twenty SSC iterations are used for obtaining the final permeability models in all realizations. The CPU time for generating one realization is about 10 minutes (SGI workstation) for the case of matching both pressure and fractional flow rate data. Less CPU time is required when only pressure or fractional flow rate data alone are matched. As shown in [192], the CPU time increases approximately linearly with number of grid cells.

Figure 5.13 provides comparisons of inverted permeability models derived from matching of production data for three different initial permeability models. The initial models were initialized with only the correct variogram and histogram. The figures show increasing improvement in predicting the high and low permeability regions between wells as compared to the reference model as pressure, fractional flow, and both pressure and fractional flow

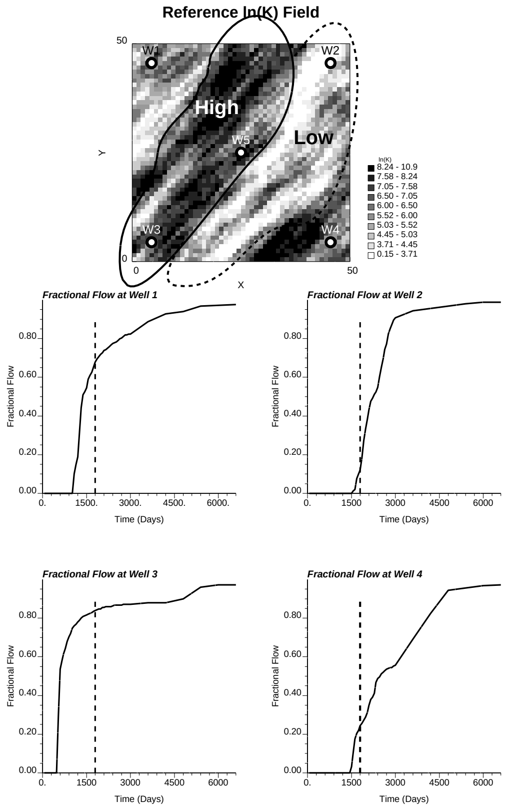

Figure 5.12: Synthetic reference field (`sgsim`-generated) and the fractional flow rate data from the four corner production wells. Production data inverted up to 1800 days.

are inverted in turn.

Figure 5.14 shows that the component of fractional flow in the objective function is not well constrained when only pressure data are used to invert the permeability field. Similarly, when only fractional flow rate data are used, the resulting permeability field may produce relatively large deviations in the pressure responses from the true field. Only when both pressure and fractional flow rate data are used, do the resulting permeability models reproduce both pressure and fractional flow rate data jointly with both components of the objective function monotonically decreasing to close zero.

The comparisons of simulated and observed pressure and fractional flow rate data for the first initial model are given in Figure 5.15. Both pressure and fractional flow rate data deviate significantly from the true results for the initial field. The pressure data are exactly matched when only pressure data are used in the inversion, but fractional flow rate data remain significantly deviated from the true data. When only fractional flow rate data are used in the inversion, the model reproduces the fractional flow data accurately but with large deviation for the pressure data. Both pressure and fractional flow rate data are accurately matched when both data sets are used to constrain the model in the inversion.

To compare the inversion results from the different data sets, the ensemble statistics from 200 different initial field realizations were computed (see Figure 5.16). For the initial fields, no additional spatial information is retained except the mean (6.0) and variance (3.0). Some large scale spatial patterns of the permeability can be identified from inversion of the

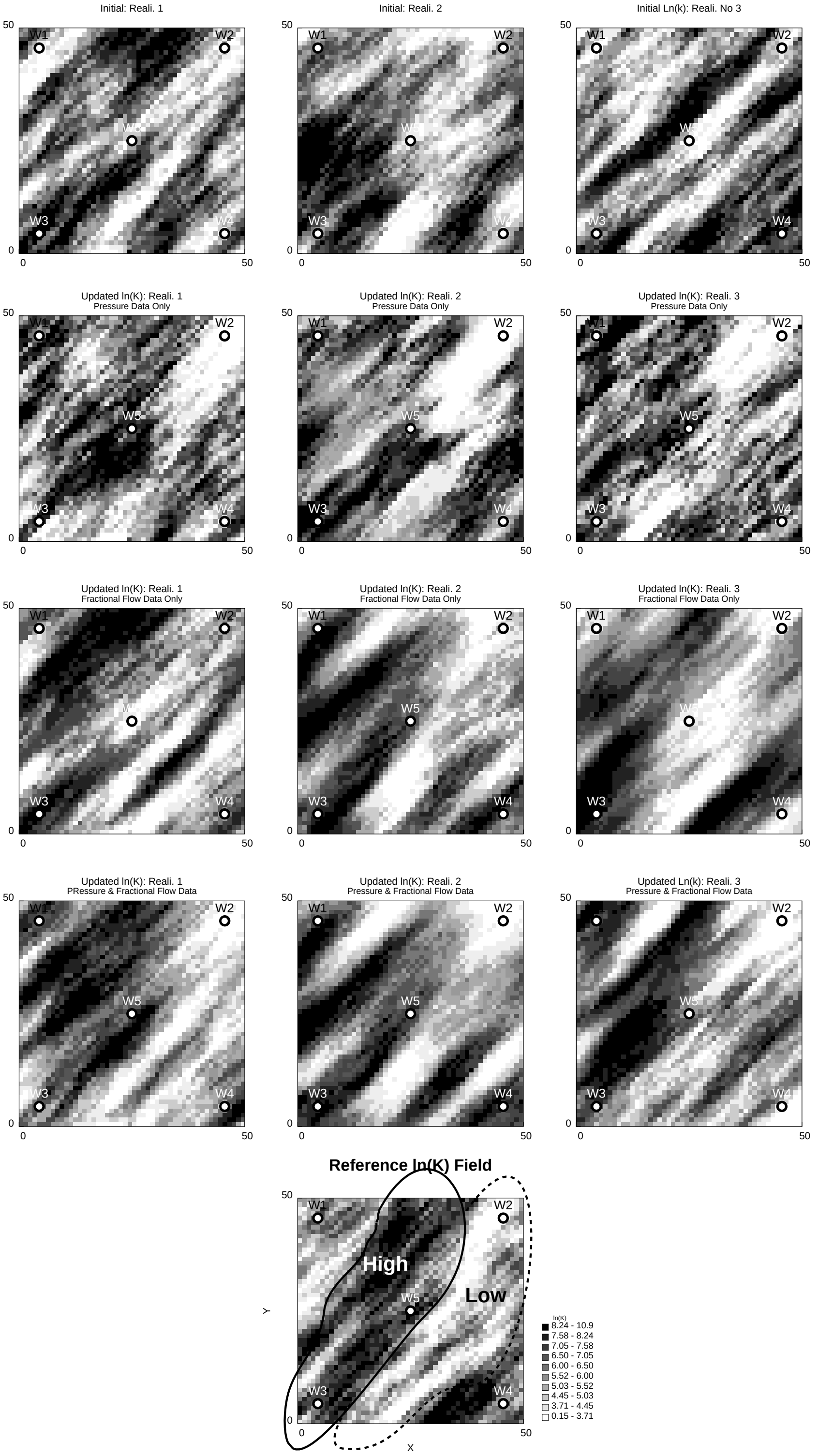

Figure 5.13: SSC-inverted permeability models derived from three different initial models: inverted pressure data only, inverted fractional flow data only, and jointly inverted pressure and fractional flow data.

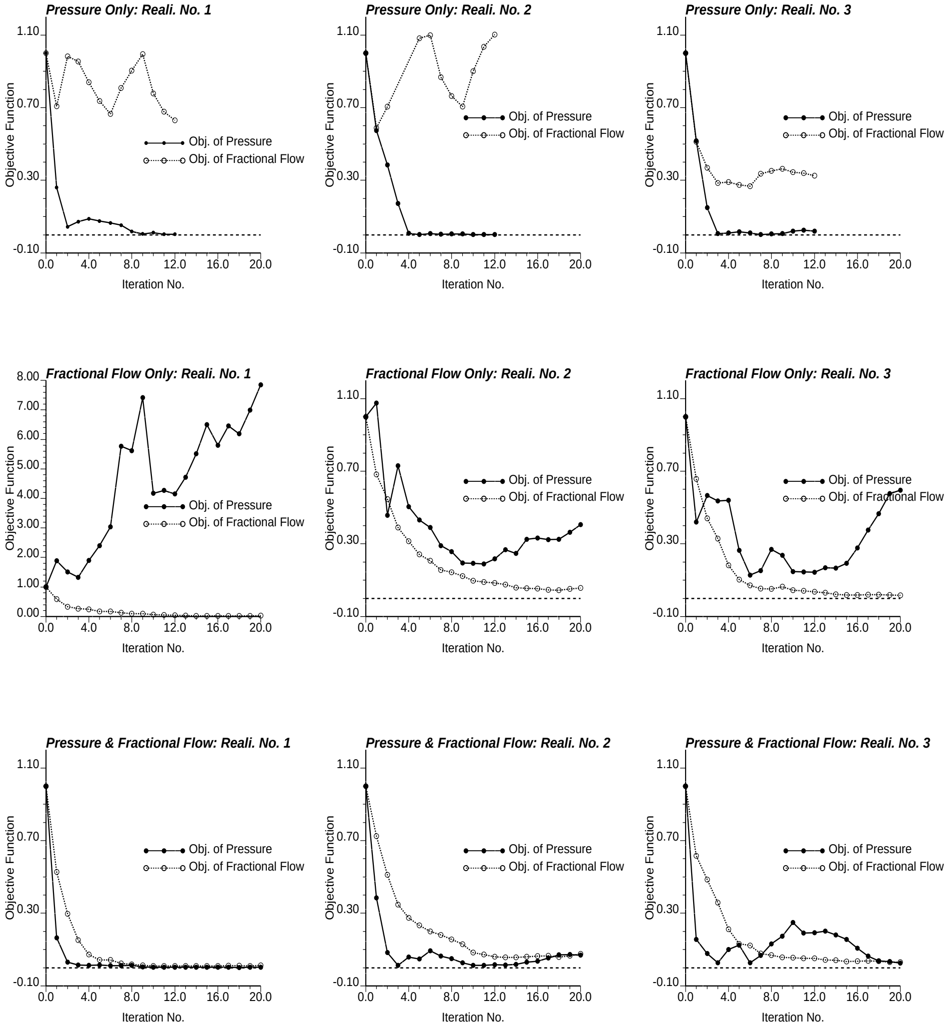

Figure 5.14: Decrease of relative objective function values for the three initial models : inverted pressure data only, inverted fractional flow data only, and jointly inverted pressure and fractional flow data.

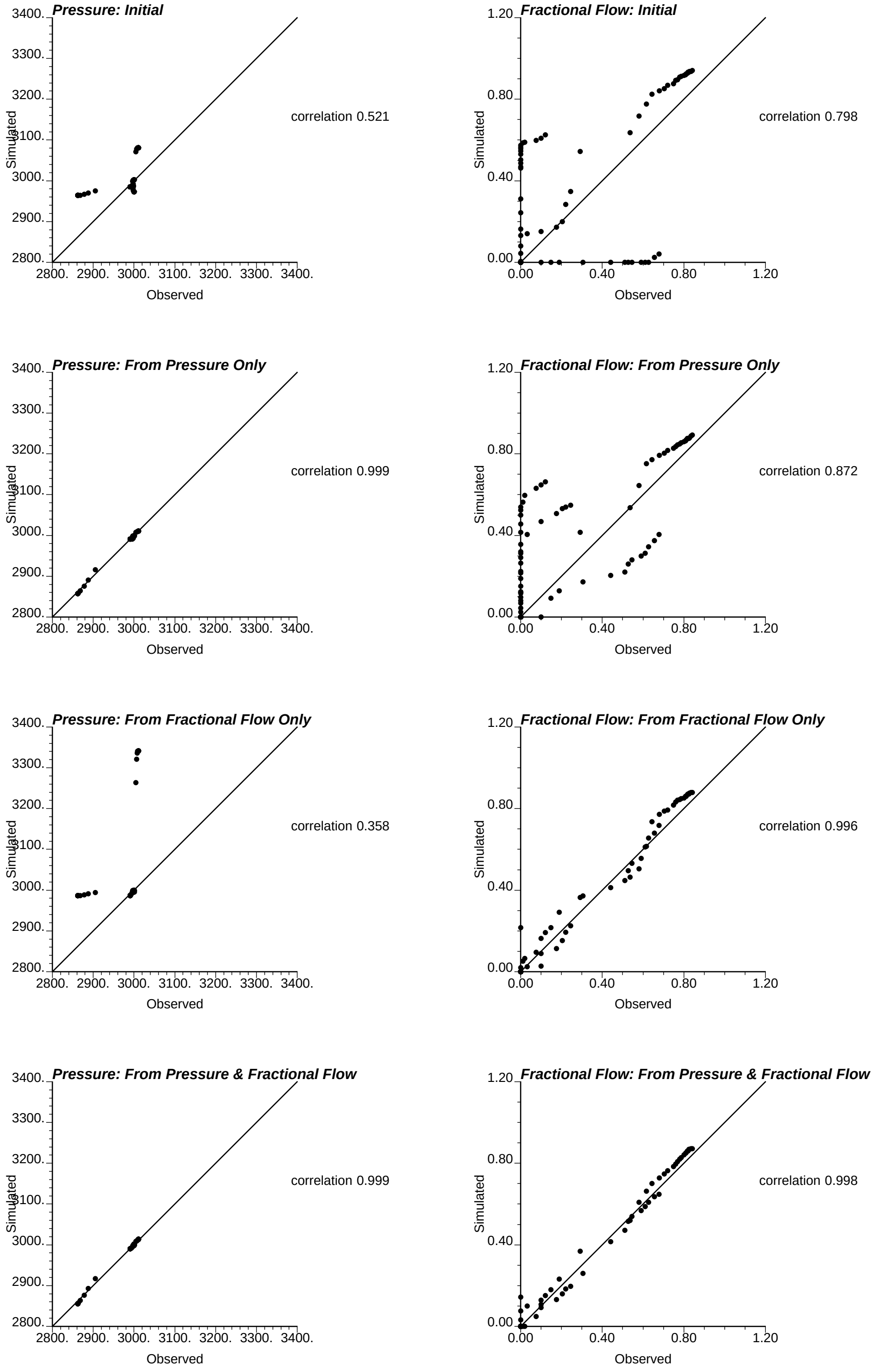

Figure 5.15: Simulated versus observed (reference) pressure and fractional flow data for one initial permeability model: initial model, inverted pressure data only, inverted fractional flow data only, and jointly inverted pressure and fractional flow data.

pressure data alone with reduced uncertainty in the areas immediate to the well locations. More spatial variation patterns are identified from the fractional flow rate data with lower uncertainty in the interwell areas. The best results are those inverted jointly from both pressure and fractional flow rate data. They more accurately reproduce most of the high and low permeability features in the reference field with much less uncertainty compared to the results using only pressure or fractional flow rate data alone.

5.6.1 Sensitivity to Initial Models and Variograms

The robustness of the inverse algorithm to different input models was tested with the initial models having completely different features from the reference field. SSC was used to update them to match the pressure and fractional flow rate data. The sensitivity of the inversion responses to two different variograms was also investigated.

Figure 5.17 shows three models updated from uniform permeability fields and two purely random permeability fields. The relative decreases of both components of the objective function are also given at the bottom row of this figure. The three final updated models (after 20 SSC iterations, using the reference field variogram) reproduce the spatial variation patterns of the reference field very well as shown in the figure. The model updated from the uniform initial model displays smoother variations than the true field, while the models updated from the purely random initial fields have more small scale fuzzy features, although their large scale patterns are correct. All updated models accurately match both the pressure and fractional flow rate data with objective functions close to zero.

Figure 5.18 shows the inverse results updated from an uniform initial field with quite different anisotropic variograms. The major correlation of one variogram is in the vertical direction, while of the other in the horizontal direction. Although the final results have a different appearance than the reference field, due to the variogram structure, they both still correctly identify the relative locations of high and low permeability regions, as well as the spatial inter-connections between well pairs. Both pressure and fractional flow rate data are matched in both models with excellent convergence.

5.6.2 Value of Additional Well Data

For the same reference model, production data from a nine-well pattern was utilized for the inversion of the permeability. Pressure data from the nine wells and fractional flow rate data up to 1800 days from the eight production wells are used. Two inverted permeability fields, the ensemble fields of mean and standard deviation from 200 initial field realizations are shown in Figure 5.19. These models more accurately reproduce the reference permeability model with less uncertainty as compared to the results with data from 5 wells (Figure 5.13). Additional well data, as expected, yield more constrained inversion responses.

5.7 Reservoir Performance Predictions

The ability of the streamline-based methods to match historical temporal production data at wells was demonstrated previously. For a greater control and better reservoir management,

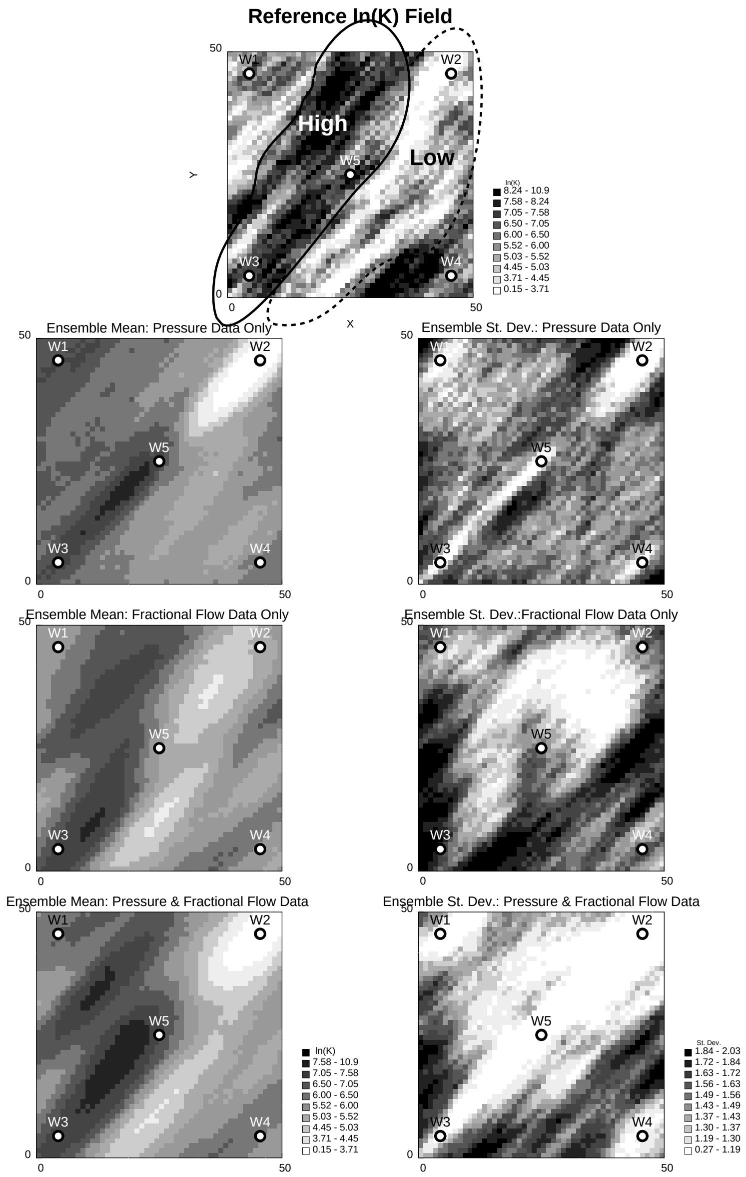

Reference ln(K) Field

Ensemble Mean: Pressure Data Only

Ensemble St. Dev.: Pressure Data Only

Ensemble Mean: Fractional Flow Data Only

Ensemble St. Dev.:Fractional Flow Data Only

Ensemble Mean: Pressure & Fractional Flow Data

Ensemble St. Dev.: Pressure & Fractional Flow Data

Figure 5.16: Ensemble means and standard deviations from inversions of 200 initial permeability realizations: inverted pressure data only, inverted fractional flow data only, and jointly inverted pressure and fractional flow data.

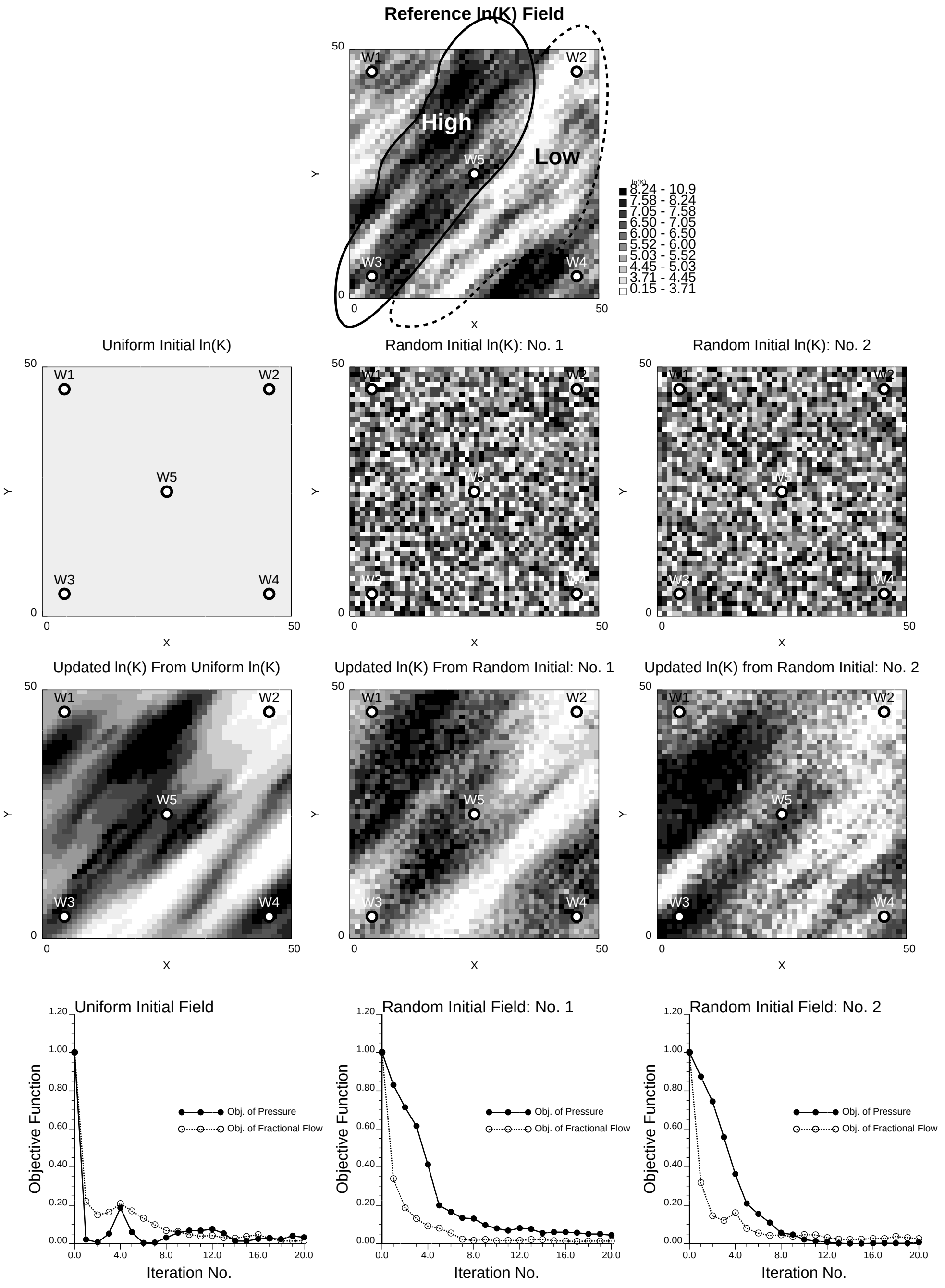

Figure 5.17: Inversion responses from very different initial models and their associated objective functions: uniform model and two random models that honor the permeability histogram. The SSC utilizes the variogram from the reference model.

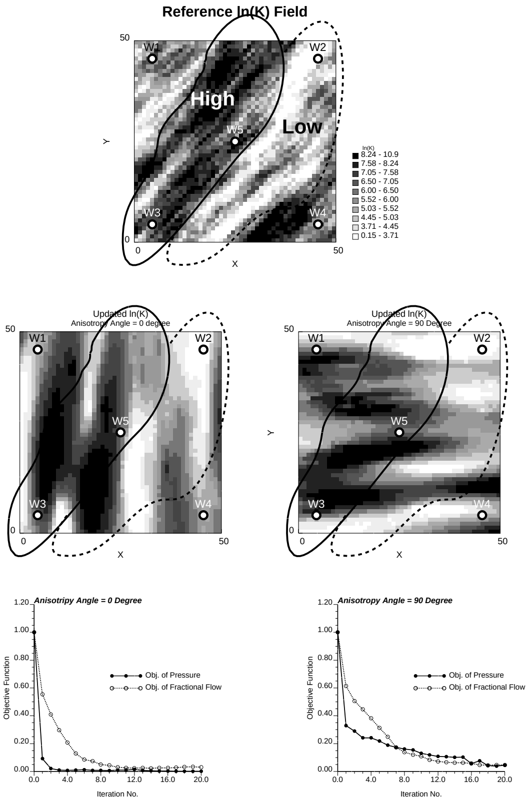

Figure 5.18: Inversion responses from two very different anisotropic variogram models and their associated objective functions.

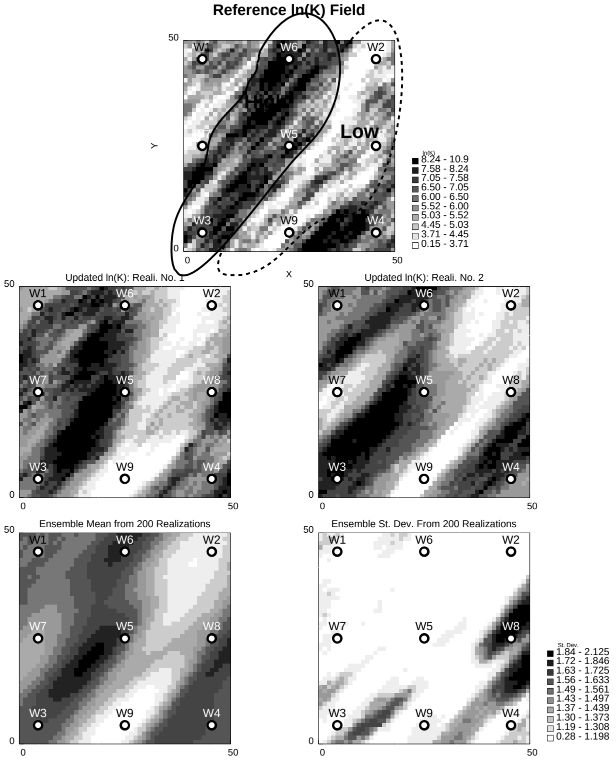

Figure 5.19: The reference field, two realizations of inversion responses, the ensemble mean and standard deviation from 200 initial field realizations when production data from 9 wells are used for the SSC inversion.

some insight into the future reservoir behavior is essential. This section illustrates the predictive capability of the inverted permeability models.

First, results from the synthetic model used in Section 5.6 were used to predict the fractional flow at the 4 production wells to 6600 days with the same well conditions. The same injection and production rates are used as before to match the models. Using the initial fields where neither pressure data nor fractional flow rate data are matched, the production from 30 initial field realizations are shown in Figure 5.20. These predictions have large deviations from the true results and large uncertainty.

When the pressure data at the five wells are matched, the predictions in the 4 production wells from 30 realizations are given in Figure 5.21. Clear improvement is evident compared to the initial fields. However, these predictions still exhibit large uncertainty. This indicates that matching single phase pressure data for this reservoir model may not be sufficient for reliable prediction of multiphase flow. More information is required.

Predictions are shown in Figure 5.22 for the permeability models obtained from matching the fractional flow rate data to 1800 days at the 4 wells. It is clear that the predictions of fractional flow at the 4 wells are dramatically improved over those of pressure data matching. As more historical fractional flow data are available, the match improves. For example, well 3 with about 1300 days of historical fractional flow production is matched much better than well 2, which has only about 150 days of historical fractional flow production matched. There is still some spread from the 30 models around the breakthrough times and fractional flow production up to 1800 days. This indicates the quality of the matches achievable for the fractional flow data.

The best predictions of reservoir performance are obtained by using reservoir models for which both pressure and early time fractional flow rate data at the same wells are used in the inversion (Figure 5.23). Results in this example suggest that there is interaction between the pressure and fractional flow rate data. Incorporating pressure data, when matching fractional flow rate data, results in a better match of fractional flow rate than using only fractional flow rate data.

Whether reservoir models matching production data at one set of wells are good predictors of reservoir performance at other wells where production data was not matched, was also investigated. Again, using results from synthetic example in Section 5.6, prediction was made for the fractional flow rate at wells 6 to 9. Permeability realizations generated by matching pressure and fractional flow rate data only at wells 1 to 5 (Figure 5.19) were used. Figures 5.24 and 5.25 show the histograms of the first water breakthrough times and times of 80% watercut predicted at wells 6 to 9 from 200 initial model realizations. Predictions, from the initial realizations with no production data matched, have large uncertainty. When the pressure data at wells 1 to 5 and the fractional flow rate to 1800 days at wells 1 to 4 are inverted, the resulting predictions at wells 6 to 9 are improved. However, the improvement is not as good as that when the early time production data, at the same wells being predicted, were matched. This implies that the predictive improvement for a set of wells with the models, inverting the production data at another set of wells, is limited. The coarse permeability model, generated from production data, must be integrated with the other reservoir static geologic and petrophysical data for additional improvement.

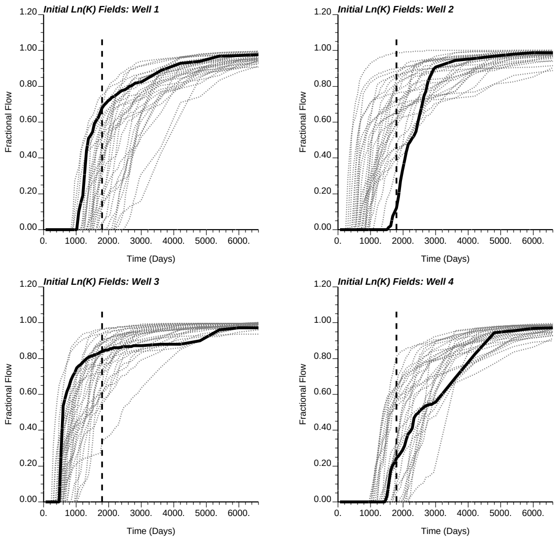

Figure 5.20: Predictions of fractional flow rates at the four production wells from 30 realizations of initial permeability fields. Thick lines are results from the reference field. Dashed line is at 1800 days.

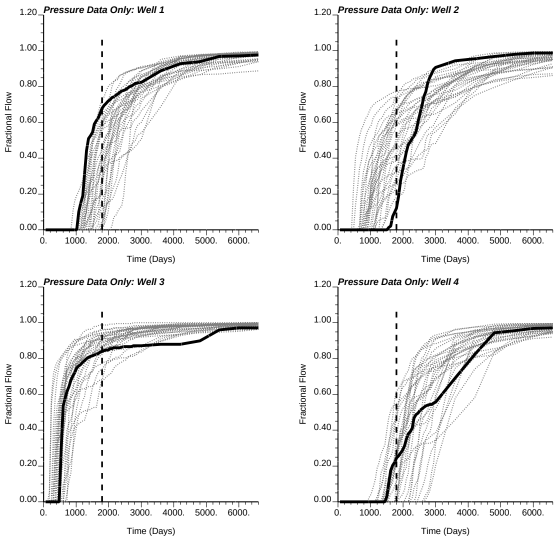

Figure 5.21: Predictions of fractional flow rates at the four production wells from 1800 days to 6600 days for 30 initial field realizations of permeability inverted from pressure data to 1800 days (dashed line). Thick lines are results from the reference field.

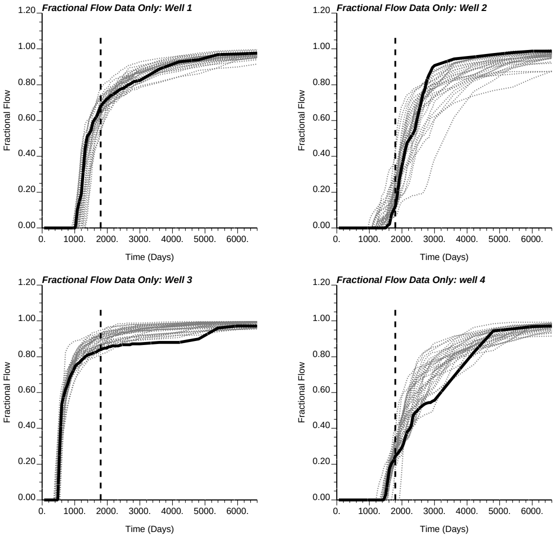

Figure 5.22: Predictions of fractional flow rates at the four production wells from 30 initial field realizations of permeability inverted from fractional flow rate data to 1800 days (dashed line)alone. Thick lines are results from the reference field.

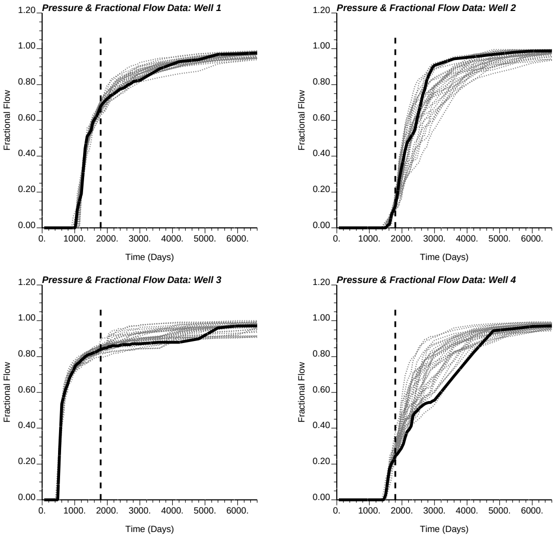

Figure 5.23: Predictions of fractional flow rates at the four production wells from 30 initial field realizations of permeability inverted from pressure and fractional flow rate data to 1800 days (dashed line).Thick lines are results from the reference field.

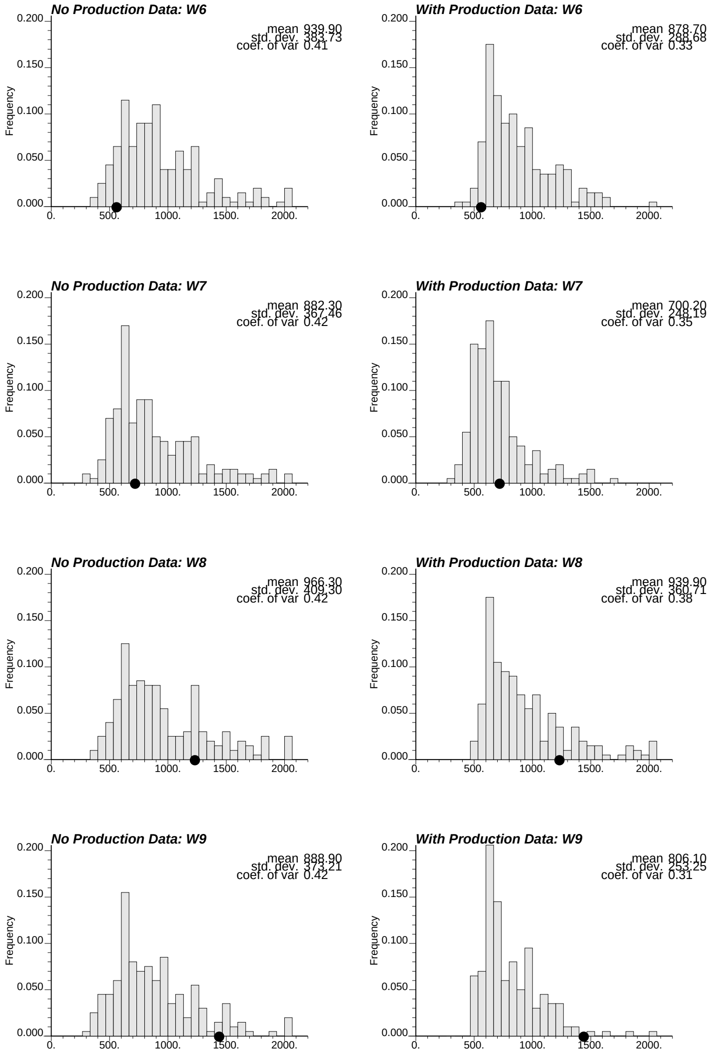

Figure 5.24: Histograms of water breakthrough time predicted at wells 6 to 9 using initial permeability fields (left) and updated permeability fields that honor pressure and fractional flow rate data at wells 1 to 5 (right). The bullets are the times from the reference field.

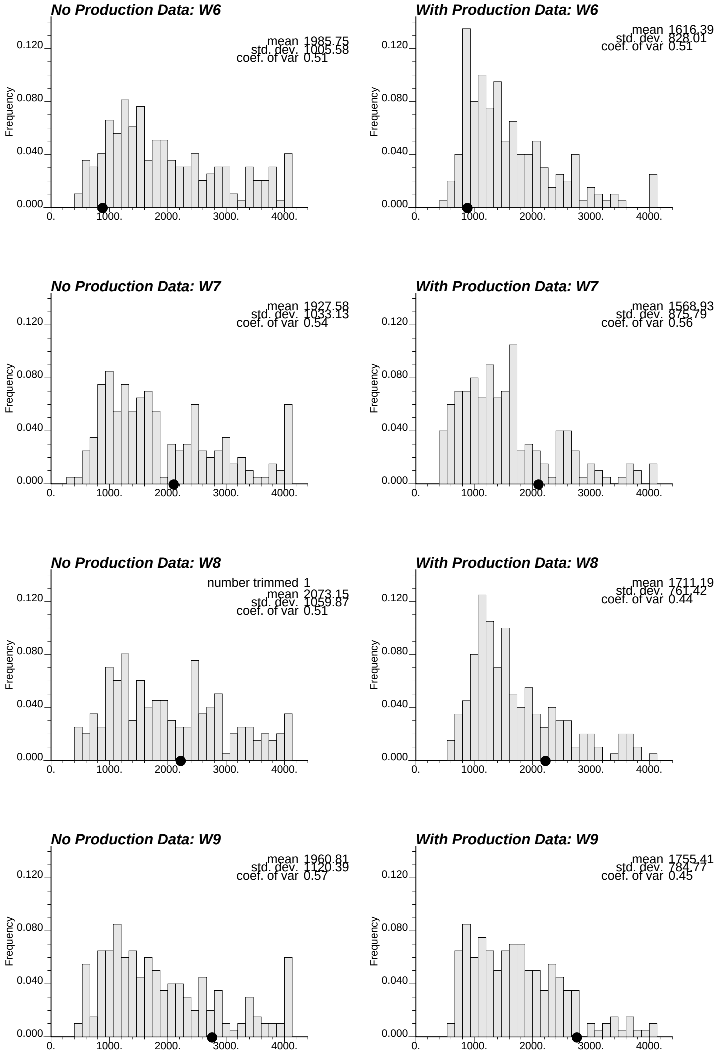

Figure 5.25: Histograms of time for 80% watercut predicted at wells 6 to 9 using initial permeability fields (left) and updated permeability fields that honor pressure and fractional flow rate data at wells 1 to 5 (right). The bullets are the times from the reference field.

5.8 Discussion

An inversion methodology has been discussed in this chapter for computing sensitivity coefficients of fractional flow with respect to permeability based on the streamline method. This method is implemented within the SSC framework for inverting permeability models from fractional flow rate data. Furthermore, the method is tested by comparing the sensitivity coefficient results using the perturbation method in presence of only one single master point. For multiple master points, this streamline-based analytical method is more accurate than the perturbation method. The SSC inversion with the streamline-based analytical method provides more accurate inverse permeability field than with the perturbation method. It was also shown that this method is computationally more efficient than the perturbation method for large models.

Essentially, the streamline-based method of sensitivity coefficient has the following features. The fractional flow is the sum of of fractional flow rate of all contributing streamlines (Equation 5.10). The sensitivity coefficient of fractional flow for each streamline is a function of sensitivity of time-of-flight and a derivative of the 1D solution (Equation 5.14). The sensitivity coefficient of time-of-flight is separated into a pressure part and a permeability part along the streamline (Equation 5.20). The pressure part comes from a single phase flow solution [191]. The permeability part comes from the algorithm (kriging) used to propagate the permeability perturbation (Equation 5.21). The derivatives of time-of-flight with respect to transmissibility and pressure are obtained from the analytical expression of time-of-flight (Section 5.4).

Computation of the sensitivity coefficients with respect to permeability perturbation is reduced to solving a single phase flow equation only **once** and then keeping track of the streamlines from injectors to producers. The complete set of sensitivity coefficients at all master locations are obtained simultaneously, thus the spatial correlation of perturbations at multiple master locations is accounted for. It is fast and more accurate than the perturbation method.

The main assumption for this method is that the streamline geometry is unchanged after any one single perturbation of the permeability field. The impact of this assumption is limited by keeping the permeability perturbation small in each iteration, and by re-solving the flow equation and updating the streamline geometry after each outer loop in the SSC inversion.

The method requires to calculate the sensitivity coefficients of single phase pressure to permeability changes of all cells intersected by the streamlines and their immediate neighbors (essentially all cells of the model). Advantage can be taken of the computation of sensitivity coefficients of pressure for a single phase flow simulation [191].

Only tracer flow representation with an unit mobility ratio and matched fluid density displacement was implemented here. The exact 1D analytical solution along the streamline for such flow is available and the pressure field does not change during the course of injection. For other types of flow with different mobility ratio and different fluid density, or when there are changes in well configuration and injection (or production) conditions, the pressure field must be periodically updated and thus also the streamline geometry within any one flow simulation [9, 10]. In such cases, it is required to retain all information about the locations (geometry) of all streamlines and their associated time-of-flight, as well as the associated pressure fields. When the analytical 1D solution along the streamline is not available, other method (such as the semi-analytical or numerical method) can be used to compute the 1D fractional flow rate solution. In case the 1D solutions are discontinuous, these solutions require smoothing to render them differentiable.

Finally, only the derivations of the sensitivity coefficients of fractional flow to permeability were presented here. When inverting for porosity, the method can be extended to compute sensitivity coefficients of fractional flow rate to porosity. Also, the method could be extended to computing sensitivity coefficients of saturations to honor saturation data from wells or from 4D seismic data.

5.9 Inversion of Saturation Distribution Data

So far in this chapter permeability inversion is considered using only pressure and fractional flow data. Saturation data derived from the interpretation of 4D seismic (i.e. time-lapse seismic) survey can also be included in the inversion algorithm. This notion is comparatively recent than those discussed in the chapter. In this section, the streamline-based SSC method is extended to invert permeability models from saturation distribution data.

With all the production data mentioned above, the objective function in SSC method can be written as:

$$O = \sum_i \sum_t W_p(i,t) \left[p_i^{obs}(t) - p_i^{cal}(t)\right]^2 + \sum_j \sum_t W_f(j,t) \left[f_j^{obs}(t) - f_j^{cal}(t)\right]^2 + \sum_c \sum_t W_s(c,t) \left[S_c^{obs}(t) - S_c^{cal}(t)\right]^2 \tag{5.43}$$

where $p_i^{obs}(t)$, $p_i^{cal}(t)$, $f_j^{obs}(t)$, $f_j^{cal}(t)$, $W_p(i,t)$ and $W_f(j,t)$ have the same implications as in Equation 5.1. $S_c^{obs}(t)$ and $S_c^{cal}(t)$ are the observed and simulated saturation of the injected phase at cell c at time t, and $W_s(c,t)$ is the weight assigned to saturation data at different wells and at different time.

For a streamline-based flow simulator, the saturation of injected fluid at a given cell c at a given time t can be computed as ([9, 11]):

$$S_c(t) = \sum_{l=1}^{nsl_c} w_l^c \overline{S}_l^{sl_c}(t) \tag{5.44}$$

where nsl_c is the total number of streamlines passing cell c. $\overline{S}_l^{sl_c}(t) = \overline{S}_p^{sl_c}(\overline{\tau}_l^c/t)$ is the averaged saturation of streamline l, and $\overline{\tau}_l^c = \frac{\tau_l^{c_{in}} + \tau_l^{c_{out}}}{2}$ is the averaged time-of-flight of streamline l when passing through the cell c. The weight is usually computed as:

$$w_l^c = \frac{\triangle \tau_l^c}{\sum_{n=1}^{nsl_c} \triangle \tau_n^c} \tag{5.45}$$

The sensitivity of saturation required for the inversion can be computed quickly with the streamline-based method. More specifically, the sensitivity coefficient at cell c with respect to the permeability at master point j is:

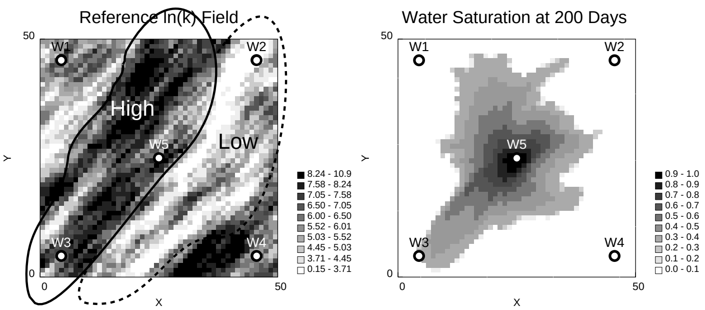

Figure 5.26: The reference ln(k) field and saturation data at t = 200 days.

$$\begin{aligned}\frac{\partial S_c(t)}{\partial k_j} &= \sum_{l=1}^{nsl_c} w_L^c \frac{\partial S_l^{sl}(\overline{\tau}_l^c/t)}{\partial k_j} = \sum_{l=1}^{nsl_c} w_L^c \frac{\partial S_l^{sl}(\overline{\tau}_l^c/t)}{\partial \tau_l^c}\frac{\partial \tau_l^c}{\partial k_j} \\ &= \sum_{l=1}^{nsl_c} w_L^c \frac{\partial S_l^{sl}(\overline{\tau}_l^c/t)}{\partial \tau_l^c} \sum_{i=1}^{n_i} \frac{\partial \tau_l^{c,i}}{\partial k_i}\omega_{j,i} \qquad (5.46)\end{aligned}$$

where n_i is the number of cells that streamline l passes before entering cell c. Here, the weights are assumed to be unchanged in sensitivity computation. $\frac{\partial S_l^{sl}(\overline{\tau}_l^c/t)}{\partial \tau_l^c}$ can be computed from analytical solution of Buckley-Leverett equation for the case of immiscible two-phase displacement. For matching 4D seismic derived map of saturation changes at different times, the same mathod can be used to compute the sensitivity coefficients of saturation changes at any given time.

Next, the efficiency of incorporating multiphase production data (including fractional flow rate and saturation distribution at given time) is demonstrated by using streamline-based SSC method. The same reference field as in the previous section is used (see Figure 5.26). A nine well pattern is used to produce the oil from the reservoir with an injection well at the center. All the production wells are producing at a constant rate of 400 RTB/day, and the injection rate is 3200 RTB/day. The injected water and original oil in place has mobility ratio of 5. The relative permeability curves for oil and water are of power-2 type with residual oil and irreducible water saturations of zero. The water saturation at time of 200 days is shown in Figure 5.26.

It is important to note that mobility changes were accounted for during water flooding by updating pressure field several times in the simulation process. The sensitivity coefficients of fractional flow rate and saturation also account for such mobility change.

Figure 5.27 shows three initial realizations of (absolute) permeability fields and the corresponding models updated by SSC method by matching the fractional flow rate data at the 8 production wells and the saturation distribution data at 200 days. The same relative permeability curves were used during the inversion (i.e., it was assumed that there is no uncertainty in relative permeabilities). Clearly evident in this figure is the much closer spatial variation features to the reference field in the updated models than in the initial fields.

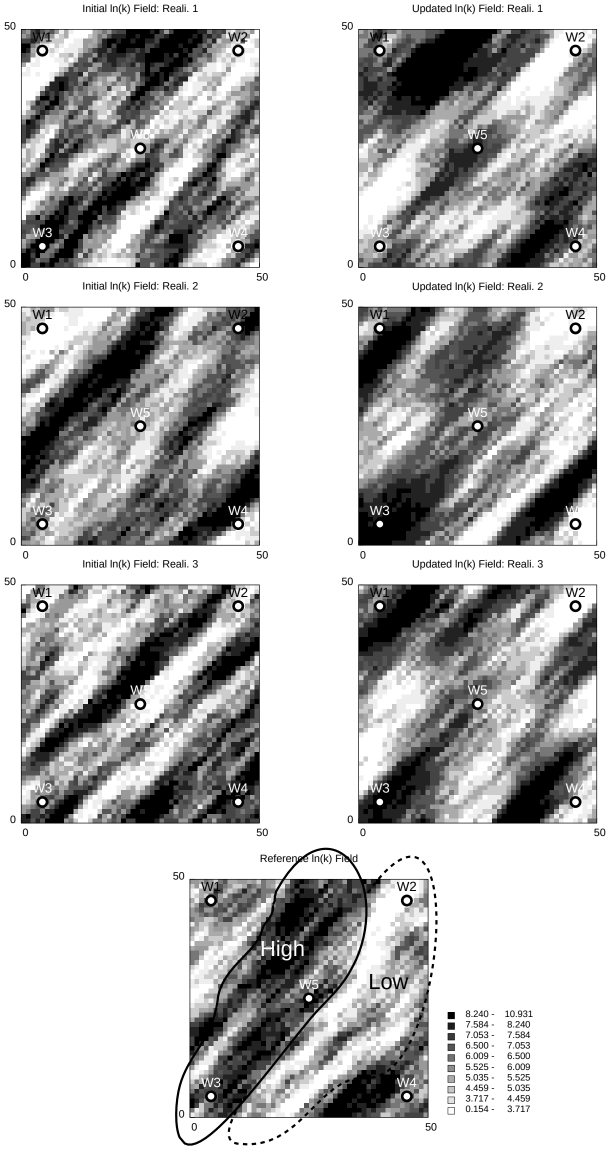

Figure 5.27: Three initial and updated permeability fields.

The saturation fields at 200 days in the initial and updated models are shown in Figure 5.28. It appears that the saturation fields at the initial models are largely deviated from the reference field, whereas the results from the updated models are much closer to the reference result, indicating a good matching. The ensemble averages (representing the large scale smooth spatial patterns) and standard deviations (representing the uncertainty) from 100 updated models are given in Figure 5.29. It is apparent that most large scale spatial features of the reference field in the averaged field, and the uncertainties between well regions are reduced dramatically.

5.10 Exercise

5.10.1 Problem Setting

For the present problem, only two phases are considered. Again, for simplicity and applicability of the supplied programs, we restrict ourselves to 2D with a uniform thickness of 100 ft. Areal extent of the reservoir is discretized by a 64 × 64 grid of the dimension 100 ft ×100 ft. Other reservoir and fluid properties are: ϕ 0.2, B 1.4, μ 0.3 cp, and c 5.5×10^{-5} 1/psia. Initial reservoir pressure is 3011.812 psia. A reference $\ln(k)$ distribution is available (ref2d.dat). This is usually obtained from static (both hard and soft) data integration. The mean and variance of $\ln(k)$ are 0.73 and 0.6084, respectively. The reference $\ln(k)$ distribution is modeled by a two-structure variogram model with no nugget effect. The first structure is a spherical model with horizontal ranges 900 and 1400 ft and sill contribution of 0.5, and the other is a Gaussian model with horizontal ranges 1500 and 3200 ft and sill contribution of 0.5. There are 5 wells, located at the center of the grid blocks: (10,50), (32,40), (40,40), (39,30) and (50,8). Each of these wells has the same wellbore radius of 0.33 ft. The wells in (10,50) and (50,8) are injectors injecting water at a constant rate of 400 and 500 (STB/DAY), respectively. While the other three are producing with constant flow rates of 200, 300 and 400 (STB/DAY), respectively. No flow boundary is considered.

5.10.2 Steps Through the Multiple-Well Multi-Phase Inversion Exercise

S1 Perform forward flow simulation to obtain synthetic well test data.

This step is required only when well test data are not available from any other source. A streamline-based reservoir simulator, `mpsim`, is supplied here. The parameter files for `mpsim` is shown in Figure 5.30.

A number of data files are required for the program as shown in the Figure 5.30. The reference logarithm permeability distribution is in file `ref2D.dat`. The boundary data and initial pressure data for each grid cell are given in `boundary.dat` and `pinit.dat`, respectively. Well flow rates and locations are in `wellff.dat`. While `timestep.dat` contains the time step data for fractional flow calculation. Other data specified in the above parameter file are realization numbers for the data to be used for the inversion, debugging level, grid specifications, rock and fluid properties, number of wells and producers, and number of streamlines to be used for fractional flow computation. The output of the simulator, `mpsim.out`, presently solves for only the watercut values at the producers. Formats of some of the data files are given below.

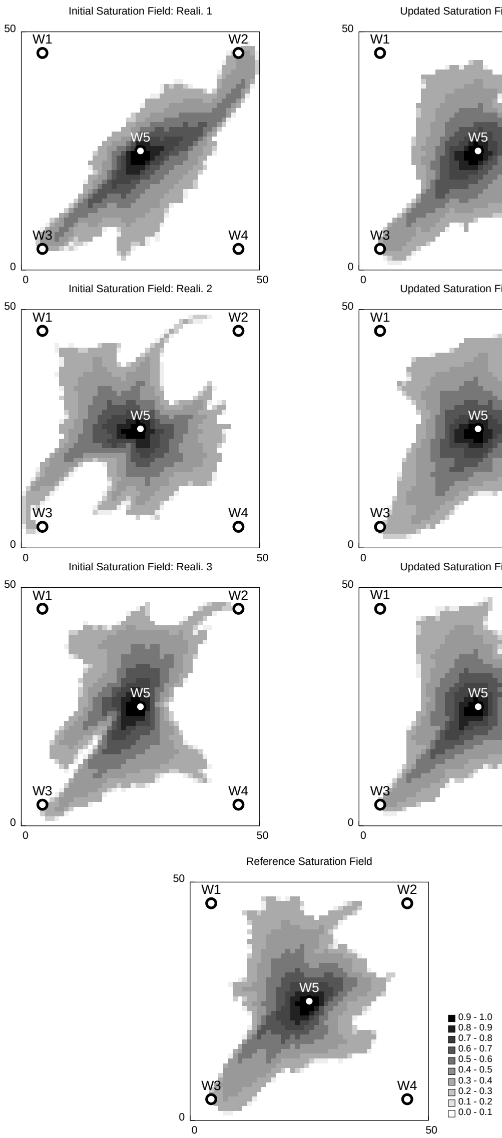

Figure 5.28: Saturation fields before and after inversion.

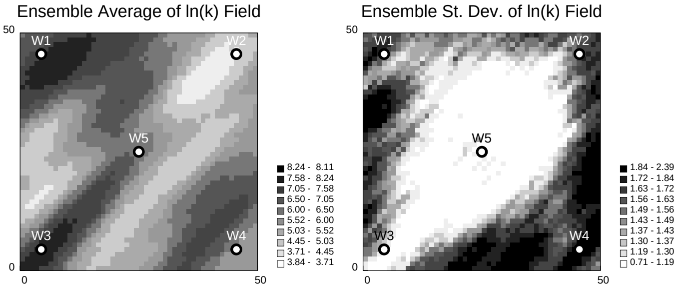

Figure 5.29: Ensemble $ln(k)$ fields from 200 realizations.

Boundary condition options and boundary flow rates are provided in data file `boundary.dat`. This is shown below in Figure 5.31. The first line has $64 (= ny)$ records of value 0 indicating no flow condition for each cell in the top boundary. Next $64 (= nx)$lines have 2 records of value 0 indicating no flow condition for each cell in the left and right boundaries. Again, next line has 64 records of value 0 for no flow condition for each cell in the bottom boundary. In a similar format except for using floating point numbers, subsequent 66 lines give the flow rates at each of the boundary cells.

```
                  Parameters for MPSIM
                  **********************

START OF PARAMETERS:
../workdir/ref2D.dat    -file with ln(k) data: first column
../workdir/boundary.dat -file with boundary conditions
../workdir/pinit.dat    -file with initial pressure for the entire field
1  1  1                 -total, start and end realization numbers
3                       -debugging level
../workdir/mpsim.dbg    -file for debug output
../workdir/mpsim.out    -file for output of watercuts at the producers
64  50.0  100.0         -X grid size: nx, xmn, xsiz
64  50.0  100.0         -Y grid size: ny, ymn, ysiz
0.2  100  0.3  5.5e-5   -porosity, thickness, viscosity and compressibility
5  3                    -no of wells, no of producers
../workdir/wellff.dat   -file with well locations and flow rates
../workdir/timestep.dat -file with time steps for factional flow data
1000                    -number of streamlines
```

Figure 5.30: Parameter file for the program, `mpsim`.

```
0 0 0 0 0 ... 0 0 0 0 0 0 0
 .
 .
 .
0 0
0 0 0 0 0 ... 0 0 0 0 0
0. 0. 0. 0. 0. ... 0. 0. 0. 0. 0.
  0.   0.
     .
     .
     .
  0.   0.
0. 0. 0. 0. 0. ... 0. 0. 0. 0. 0.
```

Figure 5.31: Data file for boundary conditions and flow rates.

Initial pressure data is provided in the file `pinit.dat`. Format of this data file is shown here in Figure 5.32. First line gives the title of the file. Second line has only record indicating the number of columns available in the file. Next few lines (as many as the number of columns indicated before) have the column headers. Subsequent 64×64 lines give the initial pressure for each cell in the data grid.

```
Initial Pressure file
1
Initial Pressure (PSIA)
 3011.812
 3011.812
    .
    .
    .
 3011.812
 3011.812
```

Figure 5.32: Data file for initial grid pressures.

Format of the well data specification file `wellff.dat` is shown in Figure 5.33. The first line has two records: the number of wells and the number of producing wells. Subsequent lines have 4 records for each well: *i*- grid, *j*- grid of the well, flow rates (STB/DAYS), and the wellbore radius (ft). Specifications for all the producers must be entered first in any order, then all the injectors.

```
5  3
32 40  -200  0.33
40 40  -400  0.33
39 30  -300  0.33
10 50   400  0.33
50  8   500  0.33
```

Figure 5.33: Data file for well locations and flow rates.

Time step data for the fractional flow computation is specified in Figure 5.34. First record is the number of time steps. Subsequent lines have the time (DAYS) for watercut computation.

```
40
  2000.000
  4000.000
  6000.000
     .
     .
     .
103000.000
106500.000
110000.000
```

Figure 5.34: Data file for time steps for fractional flow computation.

N1 It should be noted that the simulation time for the fractional flow computation should be long enough to have non-zero fractional flow values at the producers. Particularly, when the wells are widely separated. The exercise given is typical of sparsely spaced wells. Thus the simulation time is quite high.

N2 The `mpsim` program does not give the pressure values for the pressure match in the next stage. User should get the pressure data using a simulator unless one is working with real data set. However the conditions should be similar. For the present problem, we have obtained using Eclipse100.

N3 Users should examine the fractional flow data and pressure data to ensure their compatibility. Fractional flow data can also be measured with any standard finite-difference simulator. Data from different sources should be coherent.

S2 Integrate well test and fractional flow data.

The `sscmp` program is used for the integration of multiple-well single-phase dynamic data inversion. Parameter file, `sscmp.par`, for `sscmp` is shown below in Figure 5.35.

```
                  Parameters for SSC
                  *******************

START OF PARAMETERS:
*******                    -file with local well conditioning ln(k) data
1  2  3  4                 -columns for X, Y coordinates, ln(k) & error
0  5                       -num of ln(k) data & num of wells with flow data
1                          -index for identifying desired histogram
../workdir/ref2D.dat       -file with ln(k) histogram (scale of SSC model)
2  0                       -columns for permeability and weight
0.73   0.6084              -mean and variance of ln(k) distribution
../workdir/wellpara.dat    -file with reservoir and well data
../workdir/flowrate.dat    -file with input flow rate and time step data
../workdir/wellpress.dat   -file with input pressure data
../workdir/boundary.dat    -file with boundary conditions
../workdir/pinit.dat       -file with initial pressure for the entire field
../workdir/seed.dat        -file with input realizations
1  1  1                    -number of total, start and end realizations
```

```
-999.0  1.0e21             -trimming limits for missing values
3                          -debugging level
../workdir/ssc2d.dbg       -file for debug output
../workdir/ssc2d.out       -file for output ln(k) realizations
../workdir/obj2d.out       -file for output objective function after each iter
../workdir/prematch2d.out  -file for output matching of pressure responses
../workdir/fwmatch2d.out   -file for output matching of fractional flow rates
64  50.0  100.0            -X grid size: nx, xmn, xsiz
64  50.0  100.0            -Y grid size: ny, ymn, ysiz
38774                      -random number seed
5  5                       -number of master points in X and Y
3                          -number of outer iterations to update master points
3.0                        -factor for defining constraint interval for optim.
15  0.3  0.01              -max num of outer iter, dumping para & min tol
50  5.e-4  5.e-4  5.e-3  40 -optimization parameters
2000.                      -search radius for kriging
1  24                      -min and max num of samples for kriging
0                          -type of kriging
2  0.0                     -number of nested structures, nugget effect
1  0.5  0.0  900.0  1400.0  -type, sill, azm, max range, min range
1  0.5  0.0  1500.0  3200.0 -type, sill, azm, max range, min range
0.2  100.  0.3  5.5e-5     -porosity, thickness,viscosity and compressibility
5  3                       -number of wells, number of producers
../workdir/wellff.dat      -well locations and flow rates
../workdir/fraction.dat    -fractional flow data at wells
1000                       -number of streamlines
```

Figure 5.35: Parameter file for `sscmp`.

No conditioning data was used in this inversion exercise. However, there is an option to incorporate it. Some of the data files used in the previous step are also required for the `sscmp` program. They are `ref2D.dat`, `pinit.dat`, `boundary.dat`, `wellff.dat`, `fraction.dat`. Other new files are `wellpara.dat`, `flowrate.dat`, `wellpress.dat` and `seed.dat`. Format of these files will be discussed later. The values for the geometric mean of the reference permeability field and the variance are required. These values are 0.73 and 0.6084 respectively. The realization numbers, grid specifications should be the same as that used in the previous step. A random number seed is needed. This seed should be changed from one realization to other, otherwise this might create some artifact in the inversion responses. The number of "master points" used here is 25 (=5 × 5). Maximum number of outer iterations to update the master points is 3. A factor of 3.0 is used for defining constraint interval for optimization. Maximum number of outer iteration, relaxation parameter and minimum tolerance are 15, 0.3 and 0.01 respectively. Optimization parameters are 50, 5.0×10^{-4}, 5.0×10^{-4}, 5.0×10^{-3} and 40. These are minimum number of iterations, tolerances for checks of norm 1, norm 2 and difference in objective functions in two consecutive iterations, and number of times the differences of two consecutive objective functions becomes less than the tolerance specified, respectively. A search radius of 2000 ft is used for kriging. Minimum and maximum number of samples for kriging are 1 and 24. Type of kriging used is "ordinary kriging" indicated by 0. The other option available is "simple kriging" indicated by 1. The variogram model from the reference distribution is used.

Reservoir and well data are given in `wellpara.dat`, which is shown below in Figure 5.36. First line in the data file has 5 records. These are number of wells: 5, ϕ 0.2, thickness 100 ft, μ 0.3 cp, and c 5.5×10^{-5} 1/psia. The subsequent 5 lines give i, j locations and wellbore radius of each well.

```
5  0.2  100.0  0.3  5.5e-5
10  50  0.33
32  40  0.33
40  40  0.33
39  30  0.33
50   8  0.33
```

Figure 5.36: Data file for reservoir and well parameters.

Flow rate data to be used for pressure solver are given in data file `flowrate.dat`. Format of this data file is excerpted here in Figure 5.37. The only record in the first line is the number of time steps (31). Number of time steps for the pressure match can be different than that for the fractional flow rates match. For each time step, 6 records must be there in the subsequent lines. These records are time in days, and flow rates of the five wells in appropriate order.

```
          31
   0.050   -200.00   -500.00   -300.00    500.00    500.00
   0.100   -200.00   -500.00   -300.00    500.00    500.00
   0.150   -200.00   -500.00   -300.00    500.00    500.00
    ...        ...        ...        ...        ...
  73.250   -200.00   -500.00   -300.00    500.00    500.00
  83.250   -200.00   -500.00   -300.00    500.00    500.00
 108.250   -200.00   -500.00   -300.00    500.00    500.00
```

Figure 5.37: Data file for flow rates.

Well pressure data are in the data file `wellpress.dat`. The format of this file is shown below in Figure 5.38. The two records in the first line are number of wells (5) and number of time steps (31). Following lines have 11 records: time in days, and pressure (psia) and weight data for the five wells.

```
  5    31
  0.05   2946.459  1  2858.672  1  2936.361  1  3137.493  1  3186.552  1
  0.10   2942.027  1  2848.395  1  2930.264  1  3144.553  1  3195.262  1
  0.15   2938.360  1  2840.412  1  2925.454  1  3150.012  1  3202.450  1
    ...       ...         ...         ...         ...         ...
 73.25   2807.779  1  2669.026  1  2788.330  1  3480.633  1  3699.485  1
 83.25   2799.394  1  2660.556  1  2780.258  1  3482.374  1  3700.966  1
108.25   2780.776  1  2641.672  1  2762.157  1  3481.644  1  3697.354  1
```

Figure 5.38: Data file for well pressures.

The `sscmp` program requires an initial seed file for the permeability. This has the same format as the file `ref2D.dat` with reference permeability data.

N4 Users should determine histograms, variograms of the generated realizations and check how good are the histogram, variogram reproduction. Adjustments should be done by tuning different parameters in order to get better reproductions.

N5 One might be interested in exploring the cases for increased maximum number of outer iterations, or finer tolerances.

N6 The objective function values, the pressure match, the fractional flow match should be inspected to check whether a good optimization is obtained.

S3 Generate fine scale models with simulated annealing technique.

One can downscale coarse grid inverted permeability distributions to higher resolution fine scale models with the program, `sasim`. Specifications are almost similar to `sasim` program used in Chapter 4. Information about the parameter file and the code can also be found in GSLIB [61]. Interested readers can perform the downscaling; programs and parameter files are supplied here.

S4 Suggested sensitivity analyses.

- Sensitivity to number of master points, search radius for kriging, number of samples used for kriging can be performed.
- Sensitivity to initial seed of $\ln(k)$ distributions can be interesting.
- It is often difficult to get a good variogram model. One logical sensitivity study can focus on variogram structures. With different variogram models, the inversion process can be repeated and uncertainty due to variograms can be estimated.
- Sensitivity to initial pressures, fluid properties, reservoir dimensions can be analyzed.

Chapter 6

Future Developments

Since the eighties, the industry has recognized the need for reservoir characterization with dynamic data. Dynamic data integration, in the name of history matching, has been existent for a long time. Of course, there are basic differences between the two. In dynamic data integration, the primary objective is to construct geologically realistic high resolution reservoir models. The uncertainty due to insufficient data should be reduced to a reasonable extent by differences in the constructed reservoir models.

This monograph presents some recent methods of dynamic data integration in reservoir characterization. Current methods appear to be quite promising with their efficiency and ability to integrate a variety of data. Uncertainty analysis by constructing equiprobable multiple realizations has not been considered in many of the techniques available. The methods discussed here obviate such limitation. Another notable feature, is the ability to construct geological facies into the models.

Notwithstanding these versatile features, there is still a lot to achieve in this field of research. Complex reservoir scenarios with changing conditions are yet to be characterized properly or efficiently. Moreover, commercial applications are still rare. Even the available techniques are devoid of the level of sophistication and versatility required for realistic application.

As described in Chapter 5, the multiphase inversion responses illustrate that the spatial permeability variation can be identified with less uncertainty by integrating more production data. While pressure data contain information on relatively large scale trends around the wells, fractional flow rate data provide additional information on the spatial connectivity between pairs of wells. Matching pressure or fractional data alone resulted in higher uncertainty in the inverse results than were obtained by integrating both pressure and fractional flow rate data jointly. The joint inversion significantly improved the representation of reservoir heterogeneity. Matching only production data without the benefit of extensive seismic, geologic and petrophysical data, performance predictions were made beyond the period of matched data. It reveals that matching pressure data only, although the predictions are improved, is not that reliable for prediction of fractional flow, even at the same wells in which the pressure data were matched. However, good reservoir performance predictions can be obtained when the early time production data at the same wells with similar flows and well conditions are matched. Also, poor predictions can be obtained when the early time production data at the wells being predicted are not matched, or well and flow conditions are changed between the calibration stage and the prediction stage.

Envisaging the limitations and the range of applicability of the methods, the future course of research requires to focus on the following avenues:

- Extension of the techniques to true multiphase flow that can handle mobility changes during the course of production is needed. In such cases, for streamline method, the pressure solution and thus streamline geometry need to be updated with time through the simulation. However, it has been found that streamline methods are inadequate to simulate true multiphase situations with complex heterogeneities. Adopting finite-difference, finite-element or finite-volume formulation into the inversion algorithm will be more realistic approach. The counterbalance between computational cost and realistic simulation features needs to be resolved.

- The SSC mothodology is not limited to streamline-based simulator. It applies to any type of flow simulators. For finite-difference or finite-element methods, efficient ways of computing required sensitivity coefficients are needed. This remains to be a future challenge.

- Extensive 3D reservoir characterization with dynamic data has not yet found its place in practice. It is necessary for more practical use of this method to model separated-layer geology when production data such as production rate profiles along the boreholes are available. Most of the studies to date encompass some averaged 2D reservoir models which are subsequently downscaled to higher resolution 3D models.

  However, it is impractical to invert reservoir models directly at fine scale due to the computational intensity. Yet, most production data usually inform large scale variation features in the reservoir. It is important to invert reservoir models at a scale appropriate to the production data [178].

- Provision for changing well conditions through time, e.g. new drilling, recompletions, workovers, infills, etc. In case of streamline-based simulators, as new wells are drilled, old wells shut in or recompleted, etc. the streamlines change, hence necessitating significant coding and testing to handle such situations. For finite-difference simulators, although adding these features will not increase algorithmic complexities, the rate of convergence will be reduced.

- Similar situations arise for reservoirs with complex wells. Inversion of production data from complex wells, e.g. deviated, horizontal, multiply completed, partially penetrated, gas-lift, etc. needs to be investigated.

- Inversion of saturation data, although discussed in brief in Section 5.9, needs further investigation. It was also pointed out in Chapter 5 that incorporation of saturation data reduces uncertainty in reservoir performance prediction. The streamline-based method was applied to invert saturation data made available from well logs or 4D seismic data (see also [118]). Incorporation of saturation data in the finite-difference formulation may require larger storage and more intensive computation.

- The inverse problem being solved here pertains to highly nonlinear coupled systems of equations. Simultaneous techniques are more appropriate for such coupled problems. Based on the similar philosophy, simultaneous inversion of porosity, permeability and lithofacies will generate more realistic reservoir models. This will account for the interrelationships between the variables to be projected. However, this is only possible at the expense of the solutions of the problems involving even larger matrices.

- Honoring soft information (e.g., seismic data) during inversion is an important issue in reservoir charcterization. One solution is to use "p-field" concept and the SSC method can be used to update probability field of a reservoir model where the prior distribution conditional to the soft data has been determined [23].

- With the depletion of most onshore petroleum reserves, exploitation of the off-shore reserves is in the offing. It is typical, in these situations, to have sparse information about a large extent of the reservoirs. In the presence of such sparse data, the major issues are the boundary delineations and conditions for example amount of aquifer influx, etc. Also complex stratigraphy and structures including partially transmissible faults exist in many reservoir environment. Characterization of these reservoirs with the dynamic data is challenging as the space of uncertainty is enormous. Future research in the field should expound these issues.

  One technique to tackle these problems partly is the incorporation of probabilistic determination of faults, structures, reservoir volumes, etc. Ideas and experiences from domain decomposition techniques, multilevel adaptive techniques, fast adaptive composite grid techniques, local defect correction methods may also be explored. It must be noted that analogies can be substantiated with all these techniques and the techniques discussed in this monograph within some suitable framework. Abstractly, one can analogize the master point concept as a "restriction" on the domain, while the spreading of the optimal perturbation field in the SSC method as a "prolongation" from the restricted space to the original domain.

- Although it was briefly discussed in Chapter 3, incorporation of hydraulic anisotropy with k_x, k_y and k_z has not been properly implemented in the inversion algorithm. Heterogeneous hydraulic anisotropy is a rigor which must be adopted in the inversion techniques to obtain more realistic reservoir models. It must be remarked that incorporation of the diagonal permeability tensor will be sufficient in most cases.

- The inversion techniques should be able to handle process specific reservoir situations. Provision for different reservoir drive mechanisms, e.g. reservoirs with gravity segregation drive, bottom-water drive, edge-water drive, steam assisted gravity drainage mechanism, waterflooding, etc. will be more rationalistic. From reservoir simulation experience, it can be said that finite-difference formulation will be more appropriate than the streamline-based formulation.

- With a few exceptions, almost all the inversion techniques available to date suppress the time variation in the phase relative permeabilities and other fluid properties. A more realistic algorithm will account for such variations.

- Outreach for the inversion of compositional production data is in the foreseeable future. The reason for this is that there exists a growing tendency in the industry to use compositional flow simulation in more and more practical cases. However, ideas are yet to be carved in a concrete manner.
- Most importantly, extensive field application and testing is required, which will stimulate research into problems not yet investigated.

Appendix A

Acronyms and Notations

A.1 Acronyms

CPU: central processing unit

GOR: gas oil ratio

GPST: generalized pulse spectrum technique

MDH: Miller-Dyes-Hutchinson plot (a plot of drawdown versus the logarithm of time)

mNAD: mean normalized absolute deviation

mNE: mean normalized error

pdf: probability density function

SGI: Silicon Graphics, Inc.

SSC: sequential self-calibration

STB: stock tank barrel

VTP: vertical tracer profile

WIPP: Waste Isolation Pilot Plant

A.2 Common Notation

a_s^{sl}**:** flow rate associated with the streamline, s

A**:** a constant defining volume of averaging (in Equation 3.9, dependent on the definition of $r(t)$)

A**:** a scaling factor defining volume of averaging (in Equation 3.17)

$[A]$**:** transmissibility matrix (which accounts for spatial and time discretizations, as well as boundary conditions)

B: formation volume factor (res vol/std vol)

$[B]$: right hand side matrix in the flow equation (accounts for time discretization and flow boundary conditions)

c: fluid compressibility (1/psi)

c_t: total compressibility (1/psi)

$\mathbf{d}$: a measurement of model response (nonlinear function of the parameter vector, $\mathbf{a}$)

E_i: exponential integral function

f: fractional flow rate

$\{f\}^t$: fractional flow rate matrix at time t

$f_j(t)$: fractional flow rate at location j and time t

$f'_j(t)$: induced fractional flow rate at location j and time t due to permeability perturbation

$f_j^{cal}(t)$: numerically calculated fractional flow rate value at well j and time t

$f_j^{obs}(t)$: measured fractional flow rate data at well j and time t

$f_s^{sl}(t)$: fractional flow of sreamline s at time t

ft: feet

$g(\mathbf{a})$: a nonlinear function of vector $\mathbf{a}$

$\Gamma(k)$: Gamma function of argument k

h: thickness of the reservoir (ft)

k: absolute permeability (md)

$\overline{k}$: average permeability

k': perturbed permeability field

Δk_m: permeability perturbation due to master point location m

k_e: effective permeability

$K(r_D, t_D)$: weighting function

L: half domain size

L_D: dimensionless half domain size

λ_j^0 and λ_j^g: kriging weights attributed to master point j, cells 0 and g

λ_1: correlation length of maximum continuity

λ_2**:** correlation length of minimum continuity

$\frac{\lambda_1}{\lambda_2}$**:** anisotropy ratio of permeability field

m**:** slope of the semilog plot

μ**:** viscosity (cp)

$_{\max}$**:** maximum

$_{\min}$**:** minimum

N**:** number of values

N_t**:** number of time levels for simulation

n_m**:** total number of master points

$n_{s,c}$**:** number of cells crossed by a streamline s from injector to producer

n_{tf}**:** number of time steps for fractional flow measurements

n_{tp}**:** number of time steps for pressure measurements

n_{wf}**:** number of wells that have fractional flow data

n_{wf}^{sl}**:** total number of streamlines arriving to well w_f

n_{wp}**:** number of wells that have pressure data

O**:** objective function

ω**:** average power parameter defining type of averaging

p**:** pressure (psi)

$\{p\}^t$**:** pressure matrix at time t

Δp**:** pressure drawdown

p_i**:** initial reservoir pressure (psi)

$p_i(t)$**:** pressure at location i at time t

$p_i^{cal}(t)$**:** numerically calculated pressure value at well i and time t

p_D**:** dimensionless pressure

$p_i^{obs}(t)$**:** measured pressure data at well i and time t

p_{wf}**:** well flowing pressure

$p(r,t)$**:** pressure at radial distance r (ft) and time t (hours)

$p(t)$**:** observed well pressure at time t

$p(\mathbf{u},t)$: observed pressure at well location $\mathbf{u}$ and time t

$p(\mathbf{u}',t)$: observed pressure at well location $\mathbf{u}'$ and time t

p_{wf}: well bore flowing pressure

$P_i^j, j=1,\ldots,N_i$: calibrated relationship of facies proportion

ϕ: porosity (pore vol/bulk vol)

$\Psi(k)$: Euler's Psi function of argument k

q: flow rate (STB/d)

$q(\mathbf{u},t)$: observed well flow rate at location $\mathbf{u}$ and time t

$q(\mathbf{u}',t)$: observed well flow rate at location $\mathbf{u}'$ and time t

q_o: oil flow rate (STB/d)

q_g: gas flow rate (STB/d)

q_w: water flow rate (STB/d)

q_s^{sl}: flow rate associated with streamline s

r: radial distance from the well bore (ft)

r_D: dimensionless radius

r_w: well bore radius (ft)

ρ: correlation coefficient

S: sensitivity coefficient matrix, also saturation

$s_{f,m,t}(j)$: sensitivity coefficient of fractional flow rate at point j due to permeability perturbation at master point location m

$s_{p,m,t}(i)$: sensitivity coefficient of pressure at point i due to permeability perturbation at master point location m

σ^2: variance

t: time (hours)

t_i: time level for simulation

t_D: dimensionless time

T: transmissibility

τ_s: time-of-flight of streamline s

$\Delta\tau_{s,c}$: associated time-of-flight for streamline s to pass through cell c

$\mathbf{u}, \mathbf{u} \in A$: a location within the entire space, A

V: annular region

w: number of well locations ($w = 1, \ldots, n_w$)

$W_{1/2,1/2}(z)$: Whittaker's function of arguments z, 1/2 and 1/2

$W_f(j,t)$: weight assigned to fractional flow rate data at well j and time t

$W_p(i,t)$: weight assigned to pressure data at well i and time t

x, y, z: dimensions of cell (Cartesian coordinate system)

$\Delta x, \Delta y, \Delta z$: set out changes in cell dimensions

Appendix B

Computer Codes

This appendix presents brief explanations of the main parameters required for all the supplied programs. The programs are arranged in order as one will come across while pursuing the inversion exercises. First four programs are for single-well single-phase inversion: **spsim**, **wtperm**, **swspcali** and **swsasim**. Next two programs are for multiple-well single-phase inversion: **ssc** and **sasim**. Finally, last two programs are for multiple-well multi-phase inversion: **mpsim** and **ssc_mp**.

The source code, parameter files, data files for the exercises, and output files are provided on the distribution compact disk.

B.1 Program: spsim

The `spsim` program is for single-well single-phase flow simulation. It assumes constant rock and fluid properties: formation volume factor, porosity, reservoir thickness, fluid viscosity and fluid compressibility. This program also allows more than one well (at most 5, here). The flow rates are considered to be same for all the wells. The rates must be constant over the entire simulation period. Locations for all the wells with their radius should be specified. Time step control is possible with the code. The parameters required are documented below:

- **datafl:** the data file with $\ln(k)$ distribution in GEOEAS format.
- **ivar:** the column number of $\ln(k)$ data.
- **idbg:** an integer debugging level between 0 and 3. The larger the debugging level,the more information written out.
- **dbgfl:** the file for the debugging output.
- **outfl:** the pressure solution is written in this file. The output file will contain time and pressure columns.
- **nx, xmn, xsiz:** the definition of the grid system (x axis).
- **ny, ymn, ysiz:** the definition of the grid system (y axis).

- **pinit:** the initial pressure (psia).
- **fvf, poro, thick, visco, comp:** formation volume factor, porosity, reservoir thickness (ft), fluid viscosity (cp) and fluid compressibility (1/psia).
- **nwell, rate:** the number of wells and flow rate (STB/DAYS).
- **iw, jw, rw:** for each of the **nwell** wells one must define the x and y locations and wellbore radius (ft).
- **tsmin, tsmax, tmax, tfact, ntcon:** the minimum time step, the maximum time step, the maximum total time, the factor for time increase/decrease, and the number of time step control.
- **nsp, tsp:** for each **ntcon** time step control one must define number of steps and length of time step (DAYS).

B.2 Program: wtperm

The `wtperm` program is for the interpretation of well test pressure decline data to effective permeability. It uses the output data from a single-well single-phase reservoir flow simulation. The format of the input data is discussed in the exercise problems. All the reservoir and fluid properties must correspond to the input data. The parameters required are shown below:

- **datafl:** the data file with single-well single-phase well test data.
- **ivt, ivp:** the column numbers of time (DAYS) and pressure (psia) data.
- **outfl:** the file for output well pressure drawdown and effective permeability. There are 6 columns: time (DAYS), pressure (psia), logarithm of time (DAYS), pressure drawdown (psia), slope, and effective permeability (md).
- **nsim, nstep:** the number of realizations and time steps.
- **nx, xmn, xsiz:** the definition of the grid system (x axis).
- **ny, ymn, ysiz:** the definition of the grid system (y axis).
- **pinit:** the initial pressure (psia).
- **rate, fvf, phi, thick, visco, comp:** flow rate (STB/DAYS), formation volume factor, porosity, reservoir thickness (ft), fluid viscosity (cp) and fluid compressibility (1/psia).
- **iw, jw, rw:** x and y locations and wellbore radius (ft).

B.3 Program: swspcali

The `swspcali` program is for calibrating the optimal (A,ω) to fit the effective permeability and time data for any angled-anisotropic case. Effective permeability data are those obtained from the program, `wtperm`. User-specified resolution for the optimal parameters is possible through the discretization of the corresponding ranges. Reservoir and fluid properties must be the same as before. User has to specify the time limits, which should be interpreted from the "semilog" plots of drawdowns or slopes. The required parameters are explained below:

- **datafl:** the data file with ln(k) in GEOEAS format.
- **iv:** the column number of ln(k).
- **effkfl:** the data file for effective permeability.
- **ivt, ivk:** the column numbers of time (DAYS) and effective permeability (md).
- **outfl:** the output file for errors. There are 5 columns: log(A), ω, normalized absolute deviation, normalized error, and sum of normalized absolute deviation and normalized error.
- **outfl2:** the output file for weighted averages. There are 3 columns: logarithm of time (DAYS), well test derived effective permeability (md), and weighted averages of permeability (md).
- **indwei:** the index option for outputting kernel weights. If set to 1, kernel weights output will be written.
- **weightfl:** the output file for kernel weights. This file will be generated only if **indwei** is set to 1.
- **nx, xmn, xsiz:** the definition of the grid system (x axis).
- **ny, ymn, ysiz:** the definition of the grid system (y axis).
- **clx, cly:** the correlation lengths for anisotropy annular region.
- **angcl:** the angle of maximum correlation length.
- **iw, jw, rw:** the well location and wellbore radius (ft).
- **tmin, tmax:** the minimum and the maximum values of logarithm of time (DAYS) from well test data.
- **ami, amx, nloga:** the minimum, the maximum and the number of discretizations for log(A).
- **omgmin, omgmax, nomg:** the minimum, the maximum and the number of discretizations for ω.

- **mcn, nstep, tgmean:** the number of realizations, the number of time step, and the geometric mean of permeability (md).
- **invstep:** the step interval for fitting effective permeability.
- **flow, fvf, visc, phi, thic, comp:** flow rate (STB/DAYS), formation volume factor, fluid viscosity (cp), porosity, reservoir thickness (ft) and fluid compressibility (1/psia).
- **id_pk:** the option for quickly picking log(A) and ω.
- **alg_pk, omg_pk:** quickly picked log(A) and ω.

B.4 Program: swsasim

The `swsasim` program is a simulated annealing based simulation program to generate high resolution permeability distribution. The method can use up to seven different objective functions: histogram, variogram, indicator variogram (useful lithofacies or other soft data), correlation coefficient, conditional distributions, coarse grid distributions, and well test effective permeability data. Any combination may be considered in a total objective function. Although the relative weighting is determined automatically, it is often necessary to adjust the weights to arrive at the weights to arrive at solutions where all components tend to zero. The parameters required for the program are shown below:

- **val:** indices for considering histogram, variogram, indicator variogram, correlation coefficient, conditional distributions, coarse grid distributions, and well test effective permeability. Activated when the indices are to 1.
- **userfac:** user defined weights for each of the seven objective functions.
- **ilog:** the log transform flag. If set to 1, log transformation will be performed.
- **nsim:** the number of simulations.
- **nx, xmn, xsiz:** the definition of the grid system (x axis).
- **ny, ymn, ysiz:** the definition of the grid system (y axis).
- **nz, zmn, zsiz:** the definition of the grid system (z axis).
- **ixv:** the random number seed.
- **idbg:** an integer debugging level between 0 and 3. The larger the debugging level, the more information written out.
- **dbgfl:** the file for the debugging output.
- **outfl:** the output file for ln(k) distribution in GEOEAS format.
- **isas:** flag for automatic schedule. If set to 0, the annealing schedule will be automatic. If set to 1, one must define the annealing schedule in the subsequent line.

- **t0, redfac, kasas, ksas, num, omin:** user set annealing schedule. The parameters are: initial temperature, reduction factor, maximum number of perturbations at any one given temperature, target number of acceptable perturbations at a given temperature, the stopping number (maximum number of times that **kasas** is reached), and a low objective function value indicating convergence.

- **maxswap,rreport:** maximum number of perturbations (will be scaled by $nx \cdot ny \cdot nz$). After a fixed number of perturbations (**rreport** scaled by $nx \cdot ny \cdot nz$) the objective function is written to the screen and the debugging file.

- **maxnochange:** the simulated annealing will be halted after **maxnochange** perturbations without a change.

- **icond:** set to 1 if there is conditioning data (0 implies no conditioning data).

- **condfl:** an input data file with the conditioning data in simplified GEOEAS format. If this file does not exist, then an unconditional simulation is generated.

- **ixloc, iyloc, izloc, ivrl:** the column numbers for the x, y, and z coordinates and the variable to be simulated. One or two of the coordinate column numbers can be set to zero, which indicates that the simulation is 2D or 1D.

- **tmin, tmax:** all values strictly less than **tmin** and strictly greater than **tmax** are ignored.

- **ihist:** set to 1 if the histogram should be taken from the following file (set to 0 if not).

- **histfl:** an input data file with histogram in simplified GEOEAS format.

- **ihvr, ihwt:** the column numbers for the variable to be simulated and a declustering weight.

- **nhist:** number of quantiles for the histogram objective function.

- **nicut:** number of indicator variograms to consider. The threshold values (in units of the primary variable) are input next and the variograms are input directly after the direct variogram of the primary variable with the same format.

- **icut:** the threshold values (in units of the primary variable) for each of the **nicut** indicator variograms.

- **secfl:** an input data file with the secondary variable model (needed if cosimulation is being performed).

- **icsecmod:** the column number for the secondary variable in **secfl**.

- **ivavg:** if set to 1, then the correlation applies to the secondary variable and a vertical average of the variable being simulated. Otherwise, the secondary variable is considered at each grid node location.

- **corr:** the correlation coefficient (used if the fourth component objective function is turned on).
- **datafl:** an input file with bivariate data to define the conditional distributions in simplified GEOEAS format.
- **icpri, icsec, icwt:** the column numbers for the primary, secondary variables and the declustering weights in **datafl**.
- **zmin, zmax:** all values strictly less than **zmin** and strictly greater than **zmax** are ignored.
- **npricut:** number of thresholds to define the conditional distributions of the primary variable within a class of the secondary variable.
- **nseccut:** number of thresholds to define the classes of secondary variable.
- **nlag:** the number of variogram lags to consider in the objective function. The closest **nlag** lags, measured in terms of variogram distance, are retained.
- **isill:** a flag specifying whether or not to standardize the sill of the semi-variogram to the variance of the univariate distribution (**isill=1** will standardize).
- **nst** and **c0:** the number of variogram structures and the isotropic nugget effect.
- For each of the **nst** nested structures one must define **it**, the type of structure; **cc**, the c parameter; **ang1, ang2, ang3**, the angles defining the geometric anisotropy; **aa**, the maximum horizontal range; **aa1**, the minimum horizontal range, **aa2**, the vertical range.
- Indicator variograms follow the definition of the direct primary variable variogram.
- **itemp, ntmp:** option for local updating (0 = global update, 1 = local update) and number of cells in template.
- **ltail, ltpar:** lower tail option for local conditional `pdf`.
- **middle, mpar:** middle option for local conditional `pdf`.
- **utail, utpar:** upper tail option for local conditional `pdf`.
- **fnkbar:** file with desired coarse scale k field.
- **nxcs, xmncs, xsizcs:** definition of the coarse grid system (x axis).
- **nycs, ymncs, ysizcs:** definition of the coarse grid system (y axis).
- **nzcs, zmncs, zsizcs:** definition of the coarse grid system (z axis).
- **omega, id_csag:** power omega and index to conform average permeability at initial.
- **wtkefl:** file with well test derived effective permeability.

- **ivt, ivk:** the column numbers for time and effective permeability in **wtkefl**.
- **alg, omega_wt:** the optimal $\log(A)$ and ω from calibration.
- **iw_wt, jw_wt, rw:** the location of testing well and wellbore radius (ft).
- **clx, cly:** the correlation lengths for anisotropic annular region.
- **angcl:** the angle of maximum correlation length.
- **wttmin, wttmax:** the minimum and the maximum values of logarithm of time (DAYS) in well test.
- **flow, fvf, visc, phi, thic, comp:** the flow rate (STB/DAYS), formation volume factor, fluid viscosity (cp), porosity, reservoir thickness (ft), and fluid compressibility (1/psia).

B.5 Program: ssc

The sequential self-calibration (SSC) method is extended for integrating dynamic multiwell production data [189]. A FORTRAN program, **ssc**, has been developed implementing the SSC methodology. The flowchart of **ssc** code is shown in Figure 4.1 in Chapter 4. This **ssc** code allows to generate a series of permeability realizations that honor a specified spatial variation structure defined by histogram and variogram, yet match dynamic multiple well production data.

The reservoir model is assumed 2-D rectangular discretized into N_x by N_y square cells with the size of each cell being $d_x = d_y$. The grid cells are numbered as shown in Figure B.1. Parameters required for **ssc** are given below:

- **datafl:** the file with local well conditioning $\ln(k)$ data.
- **ixl, iyl, ivrl, ivrrl:** the column numbers for x, y coordinates, $\ln(k)$ and error.
- **ntmed, nwell:** the number of $\ln(k)$ data and the number of wells with flow data.
- **itrans:** the index for identifying desired histogram.
- **transfl:** the file with $\ln(k)$ histogram. Should be of the same scale as the SSC model.
- **ihv, ihwt:** the column numbers for $\ln(k)$ and weight.
- **tms0, vtms0:** the mean and the variance of $\ln(k)$ distribution.
- **wellpmfl:** the data file with reservoir and well parameters. Records in this file are discussed in the exercise.
- **flowrtfl:** the data file with input flow rate (STB/DAYS) and time step data. Records in this file are discussed in the exercise.
- **wellprfl:** the data file with input pressure data (psia). Records in this file are discussed in the exercise.

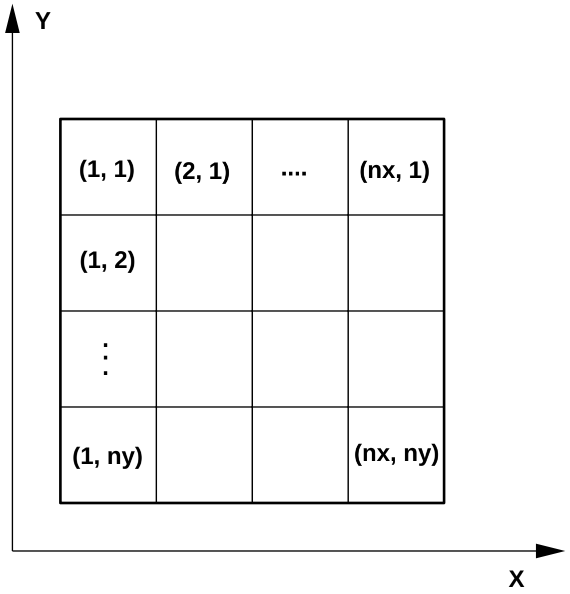

Figure B.1: Discretization and numbering of numerical reservoir model used in the **ssc** code.

- **boundfl:** the data file boundary data. Records in this file are discussed in the exercise.
- **initprfl:** the data file with initial pressure (psia) for the entire reservoir in GEOEAS format.
- **seedfl:** the data file with initial ln(k) field in GEOEAS format.
- **nsim, nsim1, nsim2:** the number of total, start and end realizations.
- **tmin, tmax:** all values strictly less than **tmin** and strictly greater than **tmax** are ignored.
- **idbg:** an integer debugging level between 0 and 3. The larger the debugging level, the more information written out.
- **dbgfl:** the file for the debugging output.
- **outfl:** the output file for ln(k) distribution in GEOEAS format.
- **objfl:** the output file for normalized objective function after each iteration . The first two records and the last records are total number iteration, initial normalized objective function, final objective function value.
- **prmtchfl:** the output file for pressure match responses. This gives the observed, the initial and the updated pressures at each time step in GEOEAS format.
- **nx, xmn, xsiz:** the definition of the grid system (x axis).
- **ny, ymn, ysiz:** the definition of the grid system (y axis).

- **iseed:** the random number seed.
- **nmpx, nmpy:** the number of master points in x and y directions.
- **it_gmp:** the number of iterations to update master points.
- **am_y:** the factor for defining the constraint interval for optimization.
- **nitera, relax, dconve:** the maximum number of outer iterations, dumping parameter and minimum tolerance.
- **it_min, eps3, eps4, eps5, ifobj:** the optimization parameters.
- **radius:** the search radius (ft) in kriging.
- **ndmin, ndmax:** the minimum and the maximum number of samples for kriging.
- **ktype:** the type of kriging. (**ktype=0** ordinary kriging, **ktype=1:** simple kriging).
- **nst** and **c0:** the number of variogram structures and the isotropic nugget effect.
- **it, cc, ang, aa1, aa2:** For each of the **nst** nested structures one must define the type of structure, the c parameter, the angle defining the geometric anisotropy, the maximum horizontal range, the minimum horizontal range.

B.6 Program: sasim

The `sasim` program is a simulated annealing based simulation program to generate high resolution permeability distribution. The method can use upto six different objective functions: histogram, variogram, indicator variogram (useful lithofacies or other soft data), correlation coefficient, conditional distributions, and coarse grid distributions. The parameters required for the program are shown below:

- **val:** indices for considering histogram, variogram, indicator variogram, correlation coefficient, conditional distributions, coarse grid distributions, and well test effective permeability. Activated when the indices are to 1.
- **userfac:** user defined weights for each of the seven objective functions.
- **ilog:** the log transform flag. If set to 1, log transformation will be performed.
- **nsim:** the number of simulations.
- **nx, xmn, xsiz:** the definition of the grid system (x axis).
- **ny, ymn, ysiz:** the definition of the grid system (y axis).
- **nz, zmn, zsiz:** the definition of the grid system (z axis).
- **ixv:** the random number seed.

- **idbg:** an integer debugging level between 0 and 3. The larger the debugging level, the more information written out.
- **dbgfl:** the file for the debugging output.
- **outfl:** the output file for $\ln(k)$ distribution in GEOEAS format.
- **isas:** flag for automatic schedule. If set to 0, the annealing schedule will be automatic. If set to 1, one must define the annealing schedule in the subsequent line.
- **t0, redfac, kasas, ksas, num, omin:** user set annealing schedule. The parameters are: initial temperature, reduction factor, maximum number of perturbations at any one given temperature, target number of acceptable perturbations at a given temperature, the stopping number (maximum number of times that **kasas** is reached), and a low objective function value indicating convergence.
- **maxswap,rreport:** maximum number of perturbations (will be scaled by $nx \cdot ny \cdot nz$). After a fixed number of perturbations (**rreport** scaled by $nx \cdot ny \cdot nz$) the objective function is written to the screen and the debugging file.
- **maxnochange:** the simulated annealing will be halted after **maxnochange** perturbations without a change.
- **icond:** set to 1 if there is conditioning data (0 implies no conditioning data).
- **condfl:** an input data file with the conditioning data (simplified GEOEAS format). If this file does not exist, then an unconditional simulation is generated.
- **ixloc, iyloc, izloc, ivrl:** the column numbers for the x, y, and z coordinates and the variable to be simulated. One or two of the coordinate column numbers can be set to zero, which indicates that the simulation is 2D or 1D.
- **tmin, tmax:** all values strictly less than **tmin** and strictly greater than **tmax** are ignored.
- **ihist:** set to 1 if the histogram should be taken from the following file (set to 0 if not).
- **histfl:** an input data file with histogram in simplified GEOEAS format.
- **ihvr, ihwt:** the column numbers for the variable to be simulated and a declustering weight.
- **nhist:** number of quantiles for the histogram objective function.
- **nicut:** number of indicator variograms to consider. The threshold values (in units of the primary variable) are input next and the variograms are input directly after the direct variogram of the primary variable with the same format.
- **icut:** the threshold values (in units of the primary variable) for each of the **nicut** indicator variograms.

- **secfl:** an input data file with the secondary variable model (needed if cosimulation is being performed).
- **icsecmod:** the column number for the secondary variable in **secfl**.
- **ivavg:** if set to 1, then the correlation applies to the secondary variable and a vertical average of the variable being simulated. Otherwise, the secondary variable is considered at each grid node location.
- **corr:** the correlation coefficient (used if the fourth component objective function is turned on).
- **datafl:** an input file with bivariate data to define the conditional distributions in simplified GEOEAS format.
- **icpri, icsec, icwt:** the column numbers for the primary, secondary variables and the declustering weights in **datafl**.
- **zmin, zmax:** all values strictly less than **zmin** and strictly greater than **zmax** are ignored.
- **npricut:** number of thresholds to define the conditional distributions of the primary variable within a class of the secondary variable.
- **nseccut:** number of thresholds to define the classes of secondary variable.
- **nlag:** the number of variogram lags to consider in the objective function. The closest **nlag** lags, measured in terms of variogram distance, are retained.
- **isill:** a flag specifying whether or not to standardize the sill of the semi-variogram to the variance of the univariate distribution (**isill=1** will standardize).
- **nst** and **c0:** the number of variogram structures and the isotropic nugget effect.
- For each of the **nst** nested structures one must define **it**, the type of structure; **cc**, the c parameter; **ang1, ang2, ang3**, the angles defining the geometric anisotropy; **aa**, the maximum horizontal range; **aa1**, the minimum horizontal range, **aa2**, the vertical range.
- Indicator variograms follow the definition of the direct primary variable variogram.
- **itemp, ntmp:** option for local updating (0 = global update, 1 = local update) and number of cells in template.
- **ltail, ltpar:** lower tail option for local conditional `pdf`.
- **middle, mpar:** middle option for local conditional `pdf`.
- **utail, utpar:** upper tail option for local conditional `pdf`.
- **fnkbar:** file with desired coarse scale k field.

- **nxcs, xmncs, xsizcs:** definition of the coarse grid system (x axis).
- **nycs, ymncs, ysizcs:** definition of the coarsegrid system (y axis).
- **nzcs, zmncs, zsizcs:** definition of the coarse grid system (z axis).
- **omega, id_csag:** power omega and index to conform average permeability at initial.

B.7 Program: mpsim

The `mpsim` program solves for fractional flow rate using streamline method. This is a 2D streamline reservoir simulator. Constant reservoir and fluid properties are considered for porosity, formation volume factor, reservoir thickness, fluid viscosity and compressibility. Flowrates for all the wells must be constant and a material balance between the total production and total injection must be maintained. Time step control is possible. The parameters required are given below:

- **datafl:** the data file with $\ln(k)$ distribution in the first column in GEOEAS format.
- **boundfl:** the data file with boundary conditions. Records of this file are discussed in the exercises.
- **initprfl:** the data file with initial pressure (psia) for the entire field in GEOEAS format.
- **nsim, nsim1, nsim2:** the number of total, start and end realizations.
- **idbg:** an integer debugging level between 0 and 3. The larger the debugging level, the more information written out.
- **dbgfl:** the file for the debugging output.
- **outfl:** the output file for fractional flow rate at each producing well in GEOEAS format.
- **nx, xmn, xsiz:** the definition of the grid system (x axis).
- **ny, ymn, ysiz:** the definition of the grid system (y axis).
- **poro, thick, visco, comp:** porosity, reservoir thickness (ft), fluid viscosity (cp) and fluid compressibility (1/psia).
- **nwellf, nprod:** the total number of wells and the number of producing wells.
- **wellffl:** the data file with well locations and flow rates (STB/DAYS). Records in this file are discussed in the exercise. Records for all the producers must be specified first.
- **timespfl:** the data file with time steps. Records in this file are discussed in the exercise.
- **np:** the number of streamlines.

B.8 Program: ssc_mp

The sequential self-calibration (SSC) method discussed earlier is extended for integrating dynamic multiwell production multi-phase data [189]. This **ssc** code allows to generate a series of permeability realizations that honor a specified spatial variation structure defined by histogram and variogram, yet match dynamic multiple well production data. Reservoir and fluid properties must correspond to the input data. Fractional flow data of the producers are required. Parameters required for **ssc** are given below:

- **datafl:** the file with local well conditioning $\ln(k)$ data.
- **ixl, iyl, ivrl, ivrrl:** the column numbers for x, y coordinates, $\ln(k)$ and error.
- **ntmed, nwell:** the number of $\ln(k)$ data and the number of wells with flow data.
- **itrans:** the index for identifying desired histogram.
- **transfl:** the file with $\ln(k)$ histogram. Should be of the same scale as the SSC model.
- **ihv, ihwt:** the column numbers for $\ln(k)$ and weight.
- **tms0, vtms0:** the mean and the variance of $\ln(k)$ distribution.
- **wellpmfl:** the data file with reservoir and well parameters. Records in this file are discussed in the exercise.
- **flowrtfl:** the data file with input flow rate (STB/DAYS) and time step data. Records in this file are discussed in the exercise.
- **wellprfl:** the data file with input pressure data (psia). Records in this file are discussed in the exercise.
- **boundfl:** the data file boundary data. Records in this file are discussed in the exercise.
- **initprfl:** the data file with initial pressure (psia) for the entire reservoir in GEOEAS format.
- **seedfl:** the data file with initial $\ln(k)$ field in GEOEAS format.
- **nsim, nsim1, nsim2:** the number of total, start and end realizations.
- **tmin, tmax:** all values strictly less than **tmin** and strictly greater than **tmax** are ignored.
- **idbg:** an integer debugging level between 0 and 3. The larger the debugging level, the more information written out.
- **dbgfl:** the file for the debugging output.
- **outfl:** the output file for $\ln(k)$ distribution in GEOEAS format.

- **objfl:** the output file for normalized objective function after each iteration . The first two records and the last records are total number iteration, initial normalized objective function, final objective function value.
- **prmtchfl:** the output file for pressure match responses. This gives the observed, the initial and the updated pressures at each time step in GEOEAS format.
- **fwmtchfl:** the output file for fractional flow rate matching responses. This gives the observed, the initial and the updated fractional flow rates at each time step in GEOEAS format.
- **nx, xmn, xsiz:** the definition of the grid system (x axis).
- **ny, ymn, ysiz:** the definition of the grid system (y axis).
- **iseed:** the random number seed.
- **nmpx, nmpy:** the number of master points in x and y directions.
- **it_gmp:** the number of iterations to update master points.
- **am_y:** the factor for defining the constraint interval for optimization.
- **nitera, relax, dconve:** the maximum number of outer iterations, dumping parameter and minimum tolerance.
- **it_min, eps3, eps4, eps5, ifobj:** the optimization parameters.
- **radius:** the search radius (ft) in kriging.
- **ndmin, ndmax:** the minimum and the maximum number of samples for kriging.
- **ktype:** the type of kriging. (**ktype=0** ordinary kriging, **ktype=1:** simple kriging).
- **nst** and **c0:** the number of variogram structures and the isotropic nugget effect.
- **it, cc, ang, aa1, aa2:** for each of the **nst** nested structures one must define the type of structure, the c parameter, the angle defining the geometric anisotropy, the maximum horizontal range, the minimum horizontal range.
- **poro, thick, visco, comp:** porosity, reservoir thickness (ft), fluid viscosity (cp) and fluid compressibility (1/psia).
- **nwellf, nprod:** the number of wells and production wells.
- **wellffl:** the data file with well locations and flow rates. Records in this file are discussed in the exercise.
- **fractfl:** the data file with fractional flow data at production wells. Records in this file are discussed in the exercise.
- **np:** the number of streamlines.

Bibliography

[1] Y. Abacioglu, A. C. Reynolds, and D. S. Oliver. Estimating heterogeneous anisotropic permeability fields from multiwell interference tests: A field example. In *SPE Annual Technical Conference and Conference*, San Antonio, TX, October 1997. SPE Paper Number 38654.

[2] F. G. Alabert. Constraining description of randomly heterogeneous reservoirs to pressure test data: a Monte Carlo study. In *SPE Annual Conference and Exhibition*, pages 307–321, San Antonio, TX, October 1989. Society of Petroleum Engineers. SPE Paper Number 19600.

[3] F. G. Alabert and G. J. Massonnat. Heterogeneity in a complex turbiditic reservoir: Stochastic modelling of facies and petrophysical variability. In *65th Annual Technical Conference and Exhibition*, pages 775–790. Society of Petroleum Engineers, September 1990. SPE Paper Number 20604.

[4] F. G. Alabert and V. Modot. Stochastic models of reservoir heterogeneity: Impact on connectivity and average permeabilities. In *67th Annual Technical Conference and Exhibition*, pages 355–370. Society of Petroleum Engineers, October 1992. SPE Paper Number 24893.

[5] F. Anterion, R. Eymard, and B. Karcher. Use of parameter gradients for reservoir history matching. In *Tenth SPE Symposium on Reservoir Simulation*, pages 339–354, Houston, TX, February 1990. Society of Petroleum Engineers. SPE Paper Number 18433.

[6] H. Ates and M. G. Kelkar. Incorporation of two-phase production data into reservoir characterization. In *SPE Annual Technical Conference and Conference*, New Orleans, LA, September 1998. SPE Paper Number 48970.

[7] D. Bandiziol and G. Massonnat. Horizontal permeability anisotropy characterization by pressure transient testing and geological data. In *1992 SPE Annual Technical Conference and Exhibition*, pages 39–52, Washington, DC, October 1992. Society of Petroleum Engineers. SPE Paper Number 24667.

[8] K. C. Bard, J. F. Arestad, A. Al-Bastaki, T. L. Davis, and R. D. Benson. Integrated reservoir characterization of a complex carbonate field. In *1995 SPE Annual Technical Conference and Exhibition*, pages 915–925, Dallas, TX, October 1995. Society of Petroleum Engineers. SPE Paper Number 30617.

[9] R. P. Batycky. *A Three-Dimensional Two-Phase Field Scale Streamline Simulator*. PhD thesis, Stanford University, Stanford, CA, 1997.

[10] R. P. Batycky, M. J. Blunt, and M. R. Thiele. A 3D field streamline simulator with gravity and changing well conditions. In *SPE 71st Annual Technical Conference and Exhibition*, Denver, CO, October 1996. Society of Petroleum Engineers. SPE Paper Number 36726.

[11] R. P. Batycky, M. J. Blunt, and M. R. Thiele. A 3D field-scale streamline-based reservoir simulator. *SPE Reservoir Engineering*, pages 246–254, November 1997.

[12] R. A. Beier. Pressure transient model of a vertically fractured well in a fractal reservoir. In *SPE Annual Technical Conference and Exhibition*, pages 557–566, New Orleans, LA, September 1990. Society of Petroleum Engineers. SPE Paper Number 20582.

[13] J. P. Benkendorfer, C. V. Deutsch, P. D. LaCroix, L. H. Landis, Y. A. Al-Askar, A. A. Al-AbdulKarim, and J. Cole. Integrated reservoir modeling of a major Arabian carbonate reservoir. In *SPE Middle East Oil Show*, Bahrain, March 1995. Society of Petroleum Engineers. SPE Paper Number 29869.

[14] R. C. Bissell, O. Dubrule, P. Lamy, P. Swaby, and O. Lepine. Combining geostatistical modelling with gradient information for history matching: the Pilot Point method. In *SPE Annual Technical Conference and Conference*, San Antonio, TX, October 1997. SPE Paper Number 38730.

[15] R. C. Bissell, J. E. Killough, and Y. Sharma. Reservoir history matching using the methods of gradients on a workstation. In *European Petroleum Computer Conference*, Stavanger, Norway, May 1992. Society of Petroleum Engineers. SPE Paper Number 24265.

[16] R. C. Bissell, Y. Sharma, and J. E. Killough. History matching using the method of gradients: Two case studies. In *SPE 69th Annual Conference and Exhibition*, pages 275–290, New Orleans, LA, September 1994. Society of Petroleum Engineers. SPE Paper Number 28590.

[17] G. Blanc, D. Huérillot, R. Rahon, and F. Roggero. Building geolostatistical models constrained by dynamic data - a posteriori constraints. In *SPE/NPF European Conference*, Stavanger, Norway, April 1995. Society of Petroleum Engineers. SPE Paper Number 35478.

[18] M. J. Blunt, K. Liu, and M. R. Thiele. A generalized streamline method to predict reservoir flow. In *8th European Symposium on Improved Oil Recovery*, pages 269–278, Vienna, Austria, May 1995.

[19] P. R. Britto and A. S. Grader. The effects of size, shape, and orientation of an impermeable region on transient pressure testing. *Formation Evaluation*, pages 595–606, September 1988.

[20] G. F. Bunn, M. J. Wittmann, W. D. Morgan, and R. C. Curnutt. Distributed pressure measurements allow early quantification of reservoir dynamics in the jene field. *SPE Formation Evaluation*, pages 55–62, March 1991.

[21] J. J. Butler, Jr. *Pumping Tests in Non-uniform Aquifers: a Deterministic/Stochastic Analysis*. PhD thesis, Stanford University, Stanford, CA, 1987.

[22] J. E. Capilla, J. J. Gómez-Hernández, and A. Sahuquillo. Stochastic simulation of transmissivity fields conditioning to both transmissivity and piezometric data, 2. demonstration in a synthetic case. *Journal of Hydrology*, 302:175–188, 1998.

[23] J. E. Capilla, J. Rodrigo, and J. J. Gómez-Hernández. Geostatistical structure of simulated transmissivity fields that honor piezometric data. In *Second European Conference on Geostatistics for Environmental Applications*, Nomeber 18-20 1998.

[24] J. Carrera, A. Medina, and X. S.-Vila. Geostatistical formulations of groundwater coupled inverse problems. In *Fourth International Geostatistics Congress*, pages 779–792, Troia, September 1992.

[25] J. Carrera and S. Neuman. Estimation of aquifer parameters under transient and steady state conditions: 1. maximum likelihood method incorporating prior information. *Water Resources Research*, 22(2):199–210, 1986.

[26] J. Carrera and S. Neuman. Estimation of aquifer parameters under transient and steady state conditions: 2. uniqueness, stability, and solution algorithms. *Water Resources Research*, 22(2):211–227, 1986.

[27] J. Carrera and S. P. Neuman. Estimation of aquifer parameters under transient and steady state conditions: Conditions: 3. application to synthetic and field data. *Water Resources Research*, 22(2):228–242, 1986.

[28] R. D. Carter, L. Kemp, A. Pierce, and D. Williams. Performance matching with constraints. *SPE Journal*, pages 187–196, April 1974.

[29] J. Chang and Y. C. Yortsos. Pressure transient analysis of fractal reservoirs. In *SPE Annual Conference and Exhibition*, Houston, TX, October 1988. Society of Petroleum Engineers. SPE Paper Number18170.

[30] M. M. Chang, M. Szpakiewicz, R. schatzinger, S. Jackson, B. Sharma, M. Tham, and F. H. Lim. Integration of a geological-engineering model with production performance: A case study at patrick draw field, wyoming. In *1993 SPE Annual Technical Conference and Exhibition*, pages 829–842, Houston, TX, October 1993. Society of Petroleum Engineers. SPE Paper Number 26499.

[31] G. Chavent, M. Dupuy, and P. Lemonnier. History matching by use of optimal theory. *SPE Journal*, pages 74–86, February 1975.

[32] W. H. Chen, G. Gavalas, J. Seinfeld, and M. L. Wasserman. A new algorithm for automatic history matching. *SPE Journal*, pages 593–608, December 1974.

[33] Y. M. Chen. Parallelism by hierarchy of GPST inversion algorithm for elastic wave equation. *Appl. Numer. Math.*, 4:83–95, 1988.

[34] Y. M. Chen and J. Q. Liu. A numerical algorithm for remote sensing of thermal conductivity. *J. Comput. Phys.*, 43:315–326, 1981.

[35] Y. M. Chen and J. Q. Liu. A numerical algorithm for solving inverse problems of two-dimensional wave equations. *J. Computational Physics*, 50:193–208, 1983.

[36] Y. M. Chen and J. Q. Liu. An iterative numerical algorithm for solving multi-parameter inverse problems of evolutional partial differential equations. *J. Comput. Phys.*, 53:429–442, 1984.

[37] Y. M. Chen and J. Q. Liu. Efficiency improvement of GPST inversion algorithm. *J. Comput. Phys.*, 72:372–382, 1987.

[38] Y. M. Chen and F. G. Zhang. Hierarchical multigrid strategy for efficiency improvement of the GPST inversion algorithm. *Appl. Numer. Math.*, 6:431–446, 1989.

[39] L. Chu, A. C. Reynolds, and D. S. Oliver. Computation of sensitivity coefficients for conditioning the permeability field to well-test pressure data. *In Situ*, 19(2):179–223, 1995.

[40] P. M. Clifton and S. P. Neuman. Effects of kriging and inverse modeling on conditional simulation of the avra valley aquifer in southern arizona. *Water Resources Research*, 18(4):1215–1234, 1982.

[41] K. H. Coats, J. R. Dempsey, and J. H. Henderson. A new technique for determining reservoir description from field performance data. *SPE Journal*, pages 66–74, March 1968.

[42] R. L. Cooley. Incorporation of prior information on parameters into nonlinear regression groundwater flow models, 1. theory. *Water Resources Research*, 18(4):965–976, 1982.

[43] L. B. Cunha, D. S. Oliver, R. A. Redner, and A. C. Reynolds. A Hybrid Markov Chain Monte Carlo method for generating permeability fields conditioned to multi-well pressure data and prior information. In *SPE Annual Technical Conference and Exhibition*, Denver, CO, October 1996. Society of Petroleum Engineers. SPE Paper Number 36566.

[44] G. Dagan. Statistic modeling of groundwater flow by unconditional and conditional probabilities: The inverse problem. *Water Resources Research*, 21(1):65–72, 1985.

[45] E. Damsleth, C. B. Tjolsen, K. H. Omre, and H. H. Haldorsen. A two-stage stochastic model applied to a north sea reservoir. In *65th Annual Technical Conference and Exhibition*, pages 791–802, New Orleans, LA, September 1990. Society of Petroleum Engineers.

[46] A. Datta-Gupta and M. J. King. A semianalytic approach to tracer flow modeling in heterogeneous permeable media. *Adv. in Water Resources*, 18(1):9–24, 1995.

[47] A. Datta-Gupta, L. W. Lake, and G. A. Pope. Characterizing heterogeneous permeability media with spatial statistics and tracer data using sequential simulation annealing. *Math. Geology*, 27(6):763–787, 1995.

[48] A. Datta-Gupta, L. W. Lake, G. A. Pope, and M. J. King. A type-curve approach to analyzing two-well tracer tests. *SPE Formation Evaluation*, March 1995.

[49] A. Datta-Gupta, D. W. Vasco, J. C. S. Long, and S. Vomvoris. Stochastic modeling of spatial heterogeneities conditioned to hydraulic and tracer tests. In *Proc. 5th Annual International Conference on High Level Radioactive Waste Management*, volume 4, pages 2624–2632, 1994.

[50] G. de Marsily, G. Lavedau, M. Boucher, and G. Fasanino. Interpretation of interference test in a well field using geostatistical techniques to fit the permeability distribution in a reservoir model. In G. Verly, M. David, A. G. Journel, and A. Marechal, editors, *Geostatistics for Natural Resources Characterization, Proceedings of the NATO Advanced Study Institute*, pages 831–849. Dordrecht, Holland, 1984.

[51] J. P. Delhomme. Spatial variability and uncertainty in groundwater flow parameters: A geostatistical approach. *Water Resources Research*, 15(2):269–280, 1979.

[52] X. Deng. *Description of Heterogeneous Reservoirs Using Pressure and Tracer Data.* PhD thesis, Stanford University, Stanford, CA, 1996.

[53] X. Deng and R. Horne. Description of heterogeneous reservoir using tracer and pressure data simultaneously. In *1995 SPE Annual Technical Conference and Exhibition*, pages 639–652, Dallas, TX, October 1995. Society of Petroleum Engineers. SPE Paper Number 30590.

[54] C. V. Deutsch. Calculating effective absolute permeability in sandstone/shale sequences. *SPE Formation Evaluation*, pages 343–348, September 1989.

[55] C. V. Deutsch. *Annealing Techniques Applied to Reservoir Modeling and the Integration of Geological and Engineering (Well Test) Data.* PhD thesis, Stanford University, Stanford, CA, 1992.

[56] C. V. Deutsch and A. G. Journel. The application of simulated annealing to stochastic reservoir modeling. In *Report 4, Stanford Center for Reservoir Forecasting*, Stanford, CA, May 1991.

[57] C. V. Deutsch and A. G. Journel. Annealing techniques applied to the integration of geological and engineering data. In *Report 5, Stanford Center for Reservoir Forecasting*, Stanford, CA, May 1992.

[58] C. V. Deutsch and A. G. Journel. *GSLIB: Geostatistical Software Library and User's Guide.* Oxford University Press, New York, 1992.

[59] C. V. Deutsch and A. G. Journel. The application of simulated annealing to stochastic reservoir modeling. *SPE Advanced Techology Series*, 2(2), April 1994.

[60] C. V. Deutsch and A. G. Journel. Integrating well test-derived absolute permeabilities. In J. M. Yarus and R. L. Chambers, editors, *Stochastic Modeling and Geostatistics: Principles, Methods, and Case Studies*, pages 131–142. AAPG Computer Applications in Geology, No. 3, 1995.

[61] C. V. Deutsch and A. G. Journel. *GSLIB: Geostatistical Software Library and User's Guide*. Oxford University Press, New York, 2nd edition, 1998.

[62] C. V. Deutsch and S. Srinivasan. Improved reservoir management through ranking stochastic reservoir models. In *SPE/DOE Tenth Symposium on Improved Oil Recovery, Tulsa, OK*, pages 105–113, Washington, DC, April 1996. Society of Petroleum Engineers. SPE Paper Number 35411.

[63] C. V. Deutsch and L. Wang. Hierarchical object-based stochastic modeling of fluvial reservoirs. *Math Geology*, 28(7):857–880, 1996.

[64] R. C. Earlougher. *Advances in Well Test Analysis*. Society of Petroleum Engineers, New York, NY, 1977.

[65] Y. Emsellem and G. de Marsily. An automatic solution for the inverse problem. *Water Resources Research*, 7(5):1264–1283, 1971.

[66] R. Ewing and T. Lin. A class of parameter estimation techniques for fluid flow in porous media. *Adv. in Water Resources*, 14(2):89–97, 1991.

[67] G. Fasanino, J.-E. Molinard, G. de Marsily, and V. Pelcé. Inverse modeling in gas reservoirs. In *1986 SPE Annual Technical Conference and Exhibition*, New Orleans, LA, October 1986. Society of Petroleum Engineers. SPE Paper Number 15592.

[68] E. Feinerman, G. Dagan, and E. Bresler. Statistical inference of spatial random functions. *Water Resources Research*, 22(6):935–942, 1986.

[69] G. S. Feitosa, L. Chu, L. G. Thompson, and A. C. Reynolds. Determination of reservoir permeability distributions from pressure buildup data. In *1993 SPE Annual Technical Conference and Exhibition*, pages 417–429, Houston, TX, October 1993. Society of Petroleum Engineers. SPE Paper Number 26457.

[70] G. S. Feitosa, L. Chu, L. G. Thompson, and A. C. Reynolds. Determination of reservoir permeability distributions from well test pressure data. In *1993 SPE Western Regional Meeting*, pages 189–204, Anchorage, Alaska, May 1993. Society of Petroleum Engineers. SPE Paper Number 26047.

[71] G. R. Gavalas, P. C. Shah, and J. H. Seinfeld. Reservoir history matching by Bayesian estimation. *SPE Journal*, pages 337–349, December 1976.

[72] F. Georgsen and H. Omre. Combining fibre processes and Gaussian random functions for modeling fluvial reservoirs. In A. Soares, editor, *Geostatistics Troia 1992*, volume 2, pages 425–440. Kluwer, 1993.

[73] J. J. Gómez-Hernández, A. Sahuquillo, and J. E. Capilla. Stochastic simulation of transmissivity fields conditioning to both transmissivity and piezometric data, 1. the theory. *Journal of Hydrology*, 302:162–174, 1998.

[74] J. J. Gómez-Hernández and X. H. Wen. To be or not to be multiGaussian: A reflection on stochastic hydrology. *Adv. of Water Resources*, 21(1):47–61, 1998.

[75] P. Goovaerts. *Geostatistics for Natural Resources Evaluation.* Oxford University Press, New York, 1997. In Press.

[76] P. Grindrod and M. D. Impey. Fractal field simulations of tracer migration with in the WIPP culebra dolomite. Technical report, Intera Information Tech., U. K., December 1991.

[77] P. Grindrod, P. Robinson, and M. Williams. The art of noise: Self-affinity, flow and transport. Technical report, Intera Sciences, Henley-on-Thames, U. K., 1991.

[78] D. Guerillot and F. Roggero. Matching the future for the evaluation of extreme reservoir development scenarios. In *8th European Symposium on Improved Oil Recovery*, Vienna, Austria, May 1995.

[79] A. L. Gutjahr. Fast Fourier transforms for random fields. Technical Report No. 4-R58-2690R, Los Alamos, NM, 1989.

[80] A. L. Gutjahr and J. L. Wilson. Co-Kriging for stochastic models. *Transport in Porous Media*, 4(6):585–598, 1989.

[81] H. H. Haldorsen and E. Damsleth. Stochastic modeling. *Journal of Petroleum Technology*, pages 404–412, April 1990.

[82] C. Harvey and S. Gorelick. Mapping hydraulic conductivity: Sequential conditioning with measurements of solute arrival time, hydraulic head, and local conductivity. *Water Resources Research*, 31(7):1615–1626, 1995.

[83] R. P. Hatcher and Y. M. Chen. An iterative method for solving inverse problems of a nonlinear wave equation. *SIAM J. Sci. Stat. Comput.*, 4(2):149–163, 1983.

[84] A. S. Hatløy. Numerical facies modeling combining deterministic and stochastic method. In J. M. Yarus and R. L. Chambers, editors, *Stochastic Modeling and Geostatistics: Principles, Methods, and Case Studies*, pages 109–120. AAPG Computer Applications in Geology, No. 3, 1995.

[85] G. W. Haws and N. F. Hurley. Applications of pressure-interference data in reservoir characterization studies, big jorn basin, wyoming. In *1992 SPE Annual Technical Conference and Exhibition*, pages 53–62, Washington, DC, October 1992. Society of Petroleum Engineers. SPE Paper Number 24668.

[86] N. He, D. S. Oliver, and A. C. Reynolds. Conditioning stochastic reservoir models to well-test data. In *SPE Annual Technical Conference and Conference*, San Antonio, October 1997. SPE Paper Number 38655.

[87] N. He, A. C. Reynolds, and D. S. Oliver. Three-dimensional reservoir description from multiwell pressure data and prior information. In *SPE Annual Technical Conference and Exhibition*, pages 151–166, Denver, CO, October 1996. SPE Paper Number 36509.

[88] E. L. Head, J. J. Pop, and F. E. Bettis. Reservoir anisotropy determination using multiple probe pressures. In *SPE Western Regional Meeting*, pages 205–219, Anchorage, Alaska, May 1993. Society of Petroleum Engineers. SPE Paper Number 26048.

[89] B. K. Hegstad and H. Omre. Uncertainty assessment in history matching and forecasting. In *Fifth International Geostatistics Congress*, Wollongong, September 1996.

[90] K. B. Hird and O. Dubrule. Quantification of reservoir connectivity for reservoir description applications. In *1995 SPE Annual Technical Conference and Exhibition*, pages 415–424, Dallas, TX, October 1995. Society of Petroleum Engineers. SPE Paper Number 30571.

[91] K. B. Hird and M. G. Kelkar. Conditional simulation method for reservoir description using spatial and well-performance constraints. *SPE Reservoir Engineering*, pages 145–152, May 1994.

[92] R. J. Hoeksema and P. K. Kitanidis. An application of the geostatistical approach to the inverse problem in two-dimensional groundwater modeling. *Water Resources Research*, 20(7):1003–1020, 1984.

[93] L. Holden, R. Madsen, K. A. Jakobsen, C. B. Tjølsen, and S. Vik. Use of well test data in stochastic reservoir modelling. In *1995 SPE Annual Technical Conference and Exhibition*, pages 653–661, Dallas, TX, October 1995. Society of Petroleum Engineers. SPE Paper Number 30591.

[94] R. N. Horne. *Modern Well Test Analysis. A Computer-Aided Approach.* Petroway Inc, 926 Bautista Court, Palo Alto, CA, 94303, 1995. Second Edition.

[95] L. Y. Hu, G. Blanc, and B. Noetinger. Estimation of lithofacies proportions using well and well test data. In *SPE 71st Annual Technical Conference and Exhibition*, Denver, CO, October 1996. Society of Petroleum Engineers. SPE Paper Number 36571.

[96] X. Huang, A. Gajraj, and M. G. Kelkar. The impact of integrating static and dynamic data in quantifying uncertainties in the future prediction of multi-phase systems. In *SPE 71st Annual Technical Conference and Exhibition*, Denver, CO, October 1996. Society of Petroleum Engineers. SPE Paper Number 36570.

[97] X. Huang and M. G. Kelkar. Integration of dynamic data for reservoir characterization in the frequency domain. In *SPE 71st Annual Technical Conference and Exhibition*, Denver, CO, October 1996. Society of Petroleum Engineers. SPE Paper Number 36513.

[98] X. Huang and M. G. Kelkar. Reservoir characterization by integration of seismic and dynamic data. In *SPE/DOE Tenth Symposium on Improved Oil Recovery*, Tulsa, OK, April 1996. Society of Petroleum Engineers. SPE Paper Number 35415.

[99] X. Huang, L. Meister, and R. Workman. Reservoir characterization by integration of time-lapse and production data. In *SPE Annual Technical Conference and Conference*, San Antonio, TX, October 1997. SPE Paper Number 38695.

[100] X. Huang, L. Meister, and R. Workman. Improvement and sensitivity of reservoir characterization derived from time-lapse seismic data. In *SPE Annual Technical Conference and Conference*, New Orleans, LA, September 1998. SPE Paper Number 49146.

[101] Intera ECL Petroleum Technologies, Highlands Farm, Greys Road, Henley-on-Thames, Oxon, UK. *ECLIPSE 100 Reference Manual*, 1991.

[102] P. Jacquard and C. Jain. Permeability distribution from field pressure data. *SPE Journal*, pages 281–294, December 1965.

[103] H. O. Jahns. A rapid method for obtaining a two-dimensional reservoir description from well pressure response data. *SPE Journal*, pages 315–327, December 1966.

[104] F. E. Jansen and M. G. Kelkar. Applications of wavelets to production data in describing inter-well relationships. In *Parmian Basin Oil and Gas Recovery Conference*, Midland, TX, March 1996. SPE Paper Number 35184.

[105] F. E. Jansen and M. G. Kelkar. Applications of wavelets to production data in describing inter-well relationships. In *SPE Annual Technical Conference and Conference*, San Antonio, TX, October 1997. SPE Paper Number 38876.

[106] F. E. Jansen and M. G. Kelkar. Non-stationary estimation of reservoir properties using production data. In *SPE Annual Technical Conference and Conference*, San Antonio, TX, October 1997. SPE Paper Number 38729.

[107] P. W. Johnson. The relationship between radius of drainage and cumulative production. *SPE Formation Evaluation*, pages 267–270, March 1988.

[108] A. G. Journel. Geostatistics for conditional simulation of orebodies. *Economic Geology*, 69:673–680, 1974.

[109] A. G. Journel. *Fundamentals of Geostatistics in Five Lessons*. Volume 8 Short Course in Geology. American Geophysical Union, Washington, D. C., 1989.

[110] A. G. Journel, C. V. Deutsch, and A. J. Desbarats. Power averaging for block effective permeability. In *56th California Regional Meeting*, pages 329–334. Society of Petroleum Engineers, April 1986. SPE Paper Number 15128.

[111] A. G. Journel and J. J. Gómez-Hernández. Stochastic imaging of the Wilmington clastic sequence. SPE Paper Number 19857, 1989.

[112] A. G. Journel and C. J. Huijbregts. *Mining Geostatistics*. Academic Press, New York, 1978.

[113] A. G. Journel and E. H. Isaaks. Conditional indicator simulation: Application to a Saskatchewan uranium deposit. *Mathematical Geology*, 16(7):685–718, 1984.

[114] P. K. Kitanidis and E. G. Vomvoris. A geostatistical approach to the inverse problem in groundwater modeling (steady state) and one-dimensional simulations. *Water Resources Research*, 19(3):677–690, 1983.

[115] C. Kravaris and J. H. Seinfeld. Identification of parameters in distributed parameter systems by regularization. *SIAM J. Control and Optimization*, 23(2):217–241, 1985.

[116] C. Kravaris and J. H. Seinfeld. Identifiability of spatially-varying conductivity from point observation as an inverse sturm-liouville problem. *SIAM J. Control and Optimization*, 24(3):522–542, 1986.

[117] C. Kravaris and J. H. Seinfeld. Identification of spatially varying parameters in distributed parameter systems by discrete regularization. *J. Mathematical Analysis and Appl.*, 119:128–152, 1986.

[118] J. L. Landa. *Reservoir Parameter Estimation Constrained to Pressure Transients, Performance History and Distributed Saturation Data.* PhD thesis, Stanford University, Stanford, CA, 1997.

[119] J. L. Landa and R. N. Horne. Procedure to integrate well test data, reservoir performance history and 4-d seismic information into a reservoir description. In *SPE Annual Technical Conference and Conference*, San Antonio, TX, October 1997. SPE Paper Number 38653.

[120] J. L. Landa, M. M. Kamal, C. D. Jenkins, and R. N. Horne. Reservoir characterization constrained to well test data: A field example. In *1996 SPE Annual Technical Conference and Exhibition*, pages 177–192, Denver, CO, October 1996. Society of Petroleum Engineers. SPE Paper Number 36511.

[121] A. M. LaVenue and J. F. Pickens. Application of a coupled adjoint sensitivity and kriging approach to calibrate a groundwater flow model. *Water Resources Research*, 28(6):1543–1569, 1992.

[122] A. M. LaVenue, B. S. RamaRao, G. de Marsily, and M. G. Marietta. Pilot Point methodology for automated calibration of an ensemble of conditionally simulated transmissivity fields, 2. application. *Water Resources Research*, 31(3):495–519, 1995.

[123] B. O. Lee. Evaluation of devonian shale reservoirs using multiwell pressure transient testing data. In *SPE/DOE Unconventional Gas Recovery Symposium*, Pittsburgh, PA, May 1982. Society of Petroleum Engineers. SPE/DOE Paper Number 10838.

[124] T. Lee, C. Kravaris, and J. H. Seinfeld. History matching by spline approximation and regrlarization in single-phase areal reservoirs. *SPE Reservoir Engineering*, 1:??, 1986.

[125] T. Lee and J. H. Seinfeld. Estimation of two-phase petroleum reservoir properties by regularization. *J. Computational Physics*, 69:397–419, 1987.

[126] P. M. Lemouzy, R. Eschard, and H. Beucher. An integrated approach EOR evaluation of production scenarios in the field delineation phase. In *66th SPE Annual Technical Conference and Exhibition*, pages 209–219, Dallas, TX, October 1991. Society of Petroleum Engineers. SPE Paper Number 22906.

[127] J. Q. Liu and Y. M. Chen. An iterative algorithm for solving inverse problems of two-dimensional diffusion equations. *SIAM J. Sci. Stat. Comput.*, 5(2):255–269, 1984.

[128] X. Y. Liu and Y. M. Chen. A generalized pulse-spectrum technique (gpst) for determining time-dependent coefficients of one-dimensional diffusion equations. *SIAM J. Sci. Stat. Comput.*, 8(3):436–445, 1987.

[129] X. Y. Liu and Y. M. Chen. Convergence of a generalized pulse-spectrum technique (gpst) for inverse problems of i-d diffusion equations in space-time domain. *Math. Comp.*, 51(184):477–489, 1988.

[130] M. E. Lord and R. E. Collins. Detecting compartmented gas reservoirs through production performance. In *1991 SPE Annual Technical Conference and Exhibition*, pages 575–581, Dallas, TX, October 1991. Society of Petroleum Engineers. SPE Paper Number 22941.

[131] E. M. Makhlouf, W. H. Chen, M. L. Wasserman, and J. H. Seinfeld. A general history matching algorithm for three-phase, three-dimensional petroleum reservoirs. *SPE Advanced Technology Series*, 1(2):83–92, 1993.

[132] V. Maroongroge, N. Saad, and G. A. Pope. Use of inverse modeling for conditioning geostatistical models to vertical tracer profiles. In *1995 SPE Annual Technical Conference and Exhibition*, pages 661–672, Dallas, TX, October 1995. Society of Petroleum Engineers. SPE Paper Number 30592.

[133] G. Matheron, H. Beucher, H. de Fouquet, A. Galli, D. Guerillot, and C. Ravenne. Conditional simulation of the geometry of fluvio-deltaic reservoirs. SPE Paper Number 16753, 1987.

[134] C. D. McElwee. Sensitivity analysis of groundwater models. In *Advances in Transport Phenomena in Porous Media*. NATO Advanced Science Institute, Series E, No. 82, 1984.

[135] L. Nazareth. A conjugate direction algorithm without line searchers. *Journal of Optimization Theory and Applications*, pages 373–387, November 1977.

[136] S. P. Neuman and S. Yakowitz. A stochastic approach to the inverse problem of aquifer hydrology, 1. theory. *Water Resources Research*, 15(4):845–860, 1979.

[137] B. Noetinger and A. Haas. Permeability averaging for well tests in 3D stochastic reservoir models. In *1996 SPE Annual Technical Conference and Exhibition*, pages 919–925, Denver, CO, October 1996. Society of Petroleum Engineers. SPE Paper Number 36653.

[138] D. S. Oliver. The averaging process in permeability estimation from well test data. *SPE Formation Evaluation*, pages 319–324, September 1990.

[139] D. S. Oliver. Estimation of radial permeability distribution from well test data. In *SPE Annual Technical Conference and Exhibition*, pages 243–250, New Orleans, LA, September 1990. Society of Petroleum Engineers. SPE Paper Number 20555.

[140] D. S. Oliver. Estimation of radial permeability distribution from well test pressure data. *SPE Formation Evaluation*, pages 290–296, December 1992.

[141] D. S. Oliver. Incorporation of transient pressure data into reservoir characterization. *In Situ*, 18(3):243–275, 1994.

[142] D. S. Oliver. A comparsion of the value of interference and well-test data for mapping permeability and porosity. *In Situ*, 20(1):41–59, 1996.

[143] D. S. Oliver, L. B. Cunha, and A. C. Reynolds. Markov Chain Monte Carlo methods for conditioning a permeability field to a pressure data. *Math. Geology*, 29(1):61–91, 1997.

[144] D. S. Oliver, N. He, and A. C. Reynolds. Conditioning permeability fields to pressure data. In *5th European Conference on the Mathematics of Oil Recovery*, Leoben, Austria, September 1996.

[145] A. Ouenes, S. Bhagavan, P. H. Bunge, and B. J. Travis. Application of simulated annealing and other global optimization methods to reservoir description: Myths and realities. In *SPE 69th Annual Conference and Exhibition*, pages 547–561, Washington, DC, September 1994. Society of Petroleum Engineers. SPE Paper Number 28415.

[146] A. Ouenes, G. Fasanino, and R. L. Lee. Simulated annealing for interpreting gas/water laboratory corefloods. In *1992 SPE Annual Technical Conference and Exhibition*, pages 43–55, Washington, DC, October 1992. Society of Petroleum Engineers. SPE Paper Number 24870.

[147] R. Parish, V. Calderbank, A. Watkins, A. Muggeridge, A. Goode, and P. Robinson. Effective history matching: The application of advanced software techniques to the history-matching process. *SPEJ*, pages 187–196, 1993.

[148] Petroleum Society of CIM / Society of Petroleum Engineers. *Pressure Transient Field Data Showing Fractal Reservoir Structure*, Calgary, AB, June 10-13 1990.

[149] D. W. Pollock. Documentation of computer programs to compute and display pathline results from the us geological survey modular three-dimansional finite-difference ground-water flow model. Technical report, U.S. Geological Survey, 1989. Open File Report 89-381.

[150] R. Raghavan. *Well Test Analysis*. PTR Prentice-Hall, Inc., New Jersey, NJ, 1993.

[151] D. Rahon, G. Blanc, and D. Guérillot. Gradients method constrained by geological bodies for history matching. In *SPE Annual Technical Conference and Exhibition*, pages 841–850, Denver, CO, October 1996. Society of Petroleum Engineers. SPE Paper Number 36568.

[152] D. Rahon, P. F. Edoa, and M. Masmoudi. Identification of geological shapes in reservoir engineering by history matching production data. In *SPE Annual Technical Conference and Conference*, New Orleans, LA, September 1998. SPE Paper Number 48969.

[153] D. Rahon and M. Masmoudi. Inversion of geological shapes in reservoir engineering using well-tests and history matching of production data. In *SPE Annual Technical Conference and Conference*, pages 141–153, San Antonio, TX, October 1997. SPE Paper Number 38656.

[154] B. S. RamaRao, A. M. LaVenue, G. de Marsily, and M. G. Marietta. Pilot Point methodology for automated calibration of an ensemble of conditionally simulated transmissivity fields, 1. theory and computational experiments. *Water Resources Research*, 31(3):475–493, 1995.

[155] A. C. Reynolds, N. He, L. Chu, and D. S. Oliver. Reparamerterization techniques for generating reservoir descriptions conditioned to variograms and well-test pressure. In *1995 SPE Annual Technical Conference and Exhibition*, pages 609–624, Dallas, TX, October 1995. Society of Petroleum Engineers. SPE Paper Number 30588.

[156] F. Roggero. Direct selection of stochastic model realizations constrained to historical data. In *SPE Annual Technical Conference and Conference*, San Antonio, TX, October 1997. SPE Paper Number 38731.

[157] F. Roggero and L. Hu. Gradual deformation of continuous geostatistical models for history matching. In *SPE Annual Technical Conference and Conference*, New Orleans, LA, September 1998. SPE Paper Number 49004.

[158] A. J. Rosa and R. N. Horne. Reservoir description by well test analysis using cyclic flow rate variation. In *1991 SPE Annual Technical Conference and Exhibition*, pages 433–448, Dallas, TX, October 1991. Society of Petroleum Engineers. SPE Paper Number 22698.

[159] A. J. Rosa and R. N. Horne. Pressure transient behavior in reservoirs with an internal circular discontinuity. In *1993 SPE Annual Technical Conference and Exhibition*, pages 389–401, Houston, TX, October 1993. Society of Petroleum Engineers. SPE Paper Number 26455.

[160] Y. Rubin and G. Dagan. Stochastic identification of transmissivity and effective recharge in steady groundwater flow, 1. theory. *Water Resources Research*, 23(7):1185–1192, 1987.

[161] Y. Rubin and G. Dagan. Stochastic identification of transmissivity and effective recharge in steady groundwater flow, 2. case study. *Water Resources Research*, 23(7):1193–1200, 1987.

[162] M. A. Sabet. *Well Test Analysis*, volume 8 of *Contributions in Petroleum Geology and Engineering.* Gulf Publishing Company, Houston, 1991.

[163] R. K. Sagar, B. G. Kelkar, and L. G. Thompson. Reservoir description by integration of well test data and spatial statistics. In *1993 SPE Annual Technical Conference and Exhibition*, pages 475–489, Houston, TX, October 1993. Society of Petroleum Engineers. SPE Paper Number 26462.

[164] R. K. Sagar, B. G. Kelkar, and L. G. Thompson. Reservoir description by integration of well test data and spatial statistics. *SPE Formation Evaluation*, pages 267–274, December 1995.

[165] P. C. Shah, G. R. Gavalas, and J. H. Seinfeld. Error analysis in history matching: The optimum level of parametrization. *SPE Journal*, pages 219–228, June 1978.

[166] S. Srinivasan and A. G. Journel. Simulation of permeability field conditioned to well test data. In *SPE Annual Technical Conference and Conference*, New Orleans, LA, September 1998. SPE Paper Number 49289.

[167] A. J. Sultan, A. Ouenes, and W. W. Weiss. Reservoir description by inverse modeling: Application to EVGSAU field. In *1993 SPE Annual Technical Conference and Exhibition*, pages 637–652, Houston, TX, October 1993. Society of Petroleum Engineers. SPE Paper Number 26478.

[168] J. E. Sykes, J. L. Wilson, and R. W. Andrews. Sensitivity analysis for steady-state groundwater flow using adjoint operators. *Water Resources Research*, 21(3):359–371, 1985.

[169] T. Tan and N. Kalogerakis. Improved reservoir characterization using automatic history matching procedures. *Journal of Canadian Petroleum Technology*, 32(6):26–33, May-June 1993.

[170] Y. N. Tang, Y. M. Chen, W. H. Chen, and M. L. Wasserman. Generalized pulse-spectrum technique for 2-d and 2-phase history matching. *Appl. Numer. Math.*, 5:529–539, 1989.

[171] A. Tarantola. *Inverse Problem Theory: Methods for Data Fitting and Model Parameter Estimation.* Elsevier, Amsterdam, The Netherlands, 1987.

[172] E. Tauzin. Integration of well test data into stochastic modeling. Master's thesis, Stanford University, Stanford, CA, 1995.

[173] M. R. Thiele. *Modeling Multiphase Flow in Heterogeneous Media Using Streamtubes.* PhD thesis, Stanford University, Stanford, CA, 1994.

[174] M. R. Thiele, M. J. Blunt, and F. M. Orr, Jr. Predicting multicomponent, multiphase flow in heterogeneous systems using streamtubes. In *4th European Conference on the Mathematics of Oil Recovery*, Roros, Norway, June 1994.

[175] M. R. Thiele, M. J. Blunt, and F. M. Orr, Jr. Simulating flow in heterogeneous systems using streamtubes. *SPE Reservoir Engineering*, pages 5–12, February 1996.

[176] H. Tjelmeland and H. Omre. Semi-Markov random fields. In A. Soares, editor, *Geostatistics Troia 1992*, volume 2, pages 493–504. Kluwer, 1993.

[177] H. Tjelmeland and H. Omre. A complex sand-shale facies model conditioned on observations from wells, seismics, and production. In *Fifth International Geostatistics Congress*, Wollongong, September 1996.

[178] T. T. Tran, X.-H. Wen, and R. A. Behrens. Efficient conditioning of 3D fine-scale reservoir model to multiphase production data using streamline-based coarse-scale inversion and geostatistical downscaling. In *SPE Annual Technical Conference and Conference*, Houston, TX, October 1999. SPE Paper Number 56518.

[179] D. S. Tsien and Y. M. Chen. Computational methods in nonlinear mechanics. In *Proc. Int. Conf. Comput. Meth. Nonlinear Methods*, pages 935–943, Austin, TX, 1974. The University of Texas, Austin.

[180] K. Tyler, A. Henriquez, F. Georgsen, L. Holden, and H. Tjelmeland. A program for 3D modeling of heterogeneities in a fluvial reservoir. In *3rd European Conference on the Mathematics of Oil Recovery*, pages 31–40, Delft, June 1992.

[181] K. Tyler, T. Svanes, and A. Henriquez. Heterogeneity modelling used for production simulation or fluvial reservoir. *SPE Formation Evaluation*, pages 85–92, June 1992.

[182] H. K. van Poollen. A hard look at radius of drainage and stabilization-time equations. *Oil and Gas Journal*, pages 139–147, September 1964.

[183] D. W. Vasco, A. Datta-Gupta, and J. C. S. Long. Integrating field production history in stochastic reservoir characterization. In *SPE 71st Annual Technical Conference and Exhibition*, Denver, CO, October 1996. Society of Petroleum Engineers. SPE Paper Number 36567.

[184] N. Vashist, R. N. Dennis, A. K. Rajvanshi, H. R. Taneja, R. K. Walia, and P. K. Sharma. Reservoir facies and their distribution in a heterogeneous carbonate reservoir: An integrated approach. In *1993 SPE Annual Technical Conference and Exhibition*, pages 819–828, Houston, TX, October 1993. Society of Petroleum Engineers. SPE Paper Number 26498.

[185] M. L. Wasserman, A. S. Emanuel, and J. Seinfeld. Practical applications of optimal-control theory to history-matching multiphase simulator models. *SPE Journal*, pages 347–355, August 1975.

[186] A. T. Watson, J. H. Seinfeld, G. R. Gavalas, and P. T. Woo. History matching in two-phase petroleum reservoirs. *SPE Journal*, pages 521–532, December 1980.

[187] X. H. Wen. *Geostatistical Methods for Prediction of Mass Transport in Groundwater*. PhD thesis, Royal Institute of Technology, Stockholm, Sweden, Stockholm, Sweden, 1995.

[188] X. H. Wen. *Stochastic Simulation of Groundwater Flow and Mass Transport in Heterogeneous Aquifers: Conditioning and Problem of Scales.* PhD thesis, Polytechnic University of Valencia, Spain, Valencia, Spain, 1996.

[189] X. H. Wen, J. E. Capilla, C. V. Deutsch, J. J. Gómez-Hernández, and S. A. Cullick. SSC: A FORTRAN program to create permeability fields that honor single-phase flow rate. *Computers & Geosciences*, 25:217–230, 1999.

[190] X. H. Wen, A. S. Cullick, and C. V. Deutsch. Constraints on the spatial distribution of permeability due to a single well pressure transient test. In *Report 10*, Stanford, CA, May 1997. Stanford Center for Reservoir Forecasting.

[191] X. H. Wen, C. V. Deutsch, and A. S. Cullick. High resolution reservoir models integrating multiple-well production data. In *1997 SPE Annual Technical Conference and Exhibition*, pages 9–19, San Antonio, TX, October 1997. Society of Petroleum Engineers. SPE Paper Number 38728.

[192] X. H. Wen, C. V. Deutsch, and A. S. Cullick. High-resolution reservoir models integrating multiple-well production data. *SPE J*, pages 344–355, December 1998.

[193] X.-H. Wen, C. V. Deutsch, and A. S. Cullick. Integrating pressure and fractional flow data in reservoir modeling with fast streamline-based inverse method. In *SPE Annual Technical Conference and Conference*, pages 161–175, New Orleans, LA, September 1998. SPE Paper Number 48971.

[194] X. H. Wen and J. J. Gómez-Hernández. Upscaling of hydraulic conductivity in heterogeneous media: An overview. *Journal of Hydrology*, 183:ix–xxxii, 1996.

[195] X. H. Wen, J. J. Gómez-Hernández, J. E. Capillo, and A. Sahuquillo. Significance of conditioning on piezometric head data for predictions of mass transport in groundwater modeling. *Math. Geology*, 28(7):951–968, 1996.

[196] Z. Wu, A. C. Reynolds, and D. S. Oliver. Conditioning geostatistical models to two-phase production data. In *SPE Annual Technical Conference and Conference*, New Orleans, LA, September 1998. SPE Paper Number 49003.

[197] W. Xu and A. G. Journel. GTSIM: Gaussian truncated simulations of reservoir units in a west texas carbonate field. SPE Paper Number 27412, 1993.

[198] G. Xue and A. Datta-Gupta. A new approach to seismic data integration during reservoir characterization using optimal non-parametric transformations. In *SPE 71st Annual Technical Conference and Exhibition*, Denver, CO, October 1996. Society of Petroleum Engineers. SPE Paper Number 36500.

[199] S. K. Yadavalli, J. R. Jones, L. D. Krase, N.-S. Yeh, and R. D. Roadifer. Use of pressure transient data to estimate permeability variograms. In *1995 SPE Annual Technical Conference and Exhibition*, pages 597–608, Dallas, TX, October 1995. Society of Petroleum Engineers. SPE Paper Number 30587.

[200] S. K. Yadavalli, R. D. Roadifer, J. R. Jones, L. D. Krase, and N.-S. Yeh. Use of pressure transient data to obtain geostatistical parameters for reservoir characterization. In *1994 SPE Annual Technical Conference and Exhibition*, New Orleans, LA, September 1994. Society of Petroleum Engineers. SPE Paper Number 28432.

[201] S. Yakowitz and L. Duckstein. Instability in aquifer identification: Theory and case studies. *Water Resources Research*, 16(9):1045–1064, 1980.

[202] T.-C. J. Yeh, M. Jin, and S. Hanna. An iterative stochastic inverse method: Conditional effective transmissivity and hydraulic head fields. *Water Resources Research*, 32(1):85–92, 1996.

[203] W. W.-G. Yeh. Review of parameter identification procedures in groundwater hydrology: The inverse problem. *Water Resources Research*, 22(2):95–108, 1986.

[204] D. A. Zimmerman, C. L. Axness, G. de Marsily, M. G. Marietta, and C. A. Gotway. Some results from a comparison study of geostatistically-based inverse techniques. Sandia National Laboratories, Albuquerque, NM, 1995.